Nonlinear Stability and Control of Gliding Vehicles

Pradeep Bhatta

A Dissertation
Presented to the Faculty
of Princeton University
in Candidacy for the Degree
of Doctor of Philosophy

Recommended for Acceptance
by the Department of
Mechanical and Aerospace Engineering

September, 2006

Prepared By: ______________________________

Pradeep Bhatta

Dissertation Advisor: ______________________________

Naomi E. Leonard

Dissertation Readers: ______________________________

Clarence W. Rowley

____

Robert F. Stengel

Abstract

In this thesis we use nonlinear systems analysis to study dynamics and design control solutions for vehicles subject to hydrodynamic or aerodynamic forcing. Application of energy-based methods for such vehicles is challenging due to the presence of energy-conserving lift and side forces. We study how the lift force determines the geometric structure of vehicle dynamics. A Hamiltonian formulation of the integrable phugoid-mode equations provides a Lyapunov function candidate, which is used throughout the thesis for deriving equilibrium stability results and designing stabilizing control laws.

A strong motivation for our work is the emergence of underwater gliders as an important observation platform for oceanography. Underwater gliders rely on buoyancy regulation and internal mass redistribution for motion control. These vehicles are attractive because they are designed to operate autonomously and continuously for several weeks. The results presented in this thesis contribute toward the development of systematic control design procedures for extending the range of provably stable maneuvers of the underwater glider.

As the first major contribution we derive conditions for nonlinear stability of longitudinal steady gliding motions using singular perturbation theory. Stability is proved using a composite Lyapunov function, composed of individual Lyapunov functions that prove stability of rotational and translational subsystem equilibria. We use the composite Lyapunov function to design control laws for stabilizing desired relative equilibria in different actuation configurations for the underwater glider.

We propose an approximate trajectory tracking method for an aircraft model. Our method uses exponential stability results of controllable steady gliding motions, derived by interpreting the aircraft dynamics as an interconnected system of rotational and translational subsystems. We prove bounded position error for tracking prescribed, straight-line trajectories, and demonstrate good performance in tracking

unsteady trajectories in the longitudinal plane.

We present all possible relative equilibrium motions for a rigid body moving in a fluid. Motion along a circular helix is a practical relative equilibrium for an underwater glider. We present a study of how internal mass distribution and buoyancy of the underwater glider influence the size of the steady circular helix, and the effect of a vehicle bottom-heaviness parameter on its stability.

Acknowledgements

Foremost I would like to thank my advisor, Professor Naomi Ehrich Leonard, for her enduring guidance, encouragement and support throughout my PhD program. I am very fortunate and honored to be able to work with Naomi. She has been an inspiring role model during the last six years, and I look forward to learning more from her for much longer.

My sincere thanks to the principal readers of this dissertation, Professor Clarence Rowley and Professor Robert Stengel. I highly appreciate their comments and guidance, which has greatly helped improve the quality of this presentation and increased my knowledge of the subject. Thanks also to Professor Phil Holmes and Professor Jeremy Kasdin for agreeing to serve as examiners of my thesis presentation.

I would like to thank all my instructors at Princeton University for sharing their insights and enthusiasm, and being generous with their time. Thanks also to many administrators who have helped me in numerous ways. I would like to particularly thank Jessica O'Leary in the Department of Mechanical and Aerospace Engineering and Jennifer McNabb in the Office of Visa Services, who have repeatedly helped me in complex situations.

Several fellow students and lab members have been wonderful work-mates and great friends. Life in the Engineering Quadrangle has been bright and cheerful thanks to the company of Ralf Bachmayer, Spring Berman, Eddie Fiorelli, Josh Graver, Nilesh Kulkarni, Francois Lekien, David Luet, Luc Moreau, Heloise Muller, Benjamin Nabet, Sujit Nair, Petter Ögren, Derek Paley, Laurent Pueyo, Maaike Schilthuis, Troy Smith and Fumin Zhang.

Thanks to Eliane Geren for providing me a wonderful room for a year in Princeton, and introducing me to great housemates. I thank David, Eliane, Marcela Hernandez and Frank Scharnowski for all the lively conversations. Thanks also to Shoba Narayan and Narayan Iyengar for their wonderful hospitality and support.

My wife's parents, Shobha and Yajaman Bhushan, and brother, Shreyas, have wholeheartedly supported me and cheered me during my PhD. I thank them immensely for their love and encouragement. Many thanks also to Ashok, Anita, Anjali and Ananya Murthy for their humor, hospitality and support.

My parents, Vijaya and Hiranya Bhatta, and my grandmother, Gundamma, cannot be thanked enough. I would like to express my deepest appreciation for their hard work and sacrifices in motivating me to pursue good education. Their unbounded love, support and encouragement has always been a great source of strength.

Finally, no words can completely describe how grateful I am to my wife, Shruthi Bhushan, for riding this roller coaster with me from the beginning till the end. Shruthi, your presence, care and understanding were very critical, stabilizing inputs during this highly nonlinear ride. You make everything joyful.

This thesis carries the designation 3159T in the records of the Department of Mechanical and Aerospace Engineering, Princeton University.

for

Shruthi

Contents

List of Figures

Chapter 1

Introduction

In this thesis we focus on using nonlinear systems tools to study dynamics of vehicles subject to hydrodynamic or aerodynamic forces and moments. Our work is largely motivated by the emergence of a new class of autonomous underwater vehicles (AUVs) called underwater gliders [1, 2]. Underwater gliders are autonomous vehicles that rely on changes in vehicle buoyancy and internal mass redistribution for regulating their motion. They do not carry thrusters or propellers and have limited external moving control surfaces. They are underactuated and difficult to maneuver. On the other hand, underwater gliders are extremely energy efficient and have already demonstrated high endurance, making them very attractive for oceanographic surveys requiring long-term deployment and autonomous operation [3, 4].

The motion of an underwater glider is determined by its shape, size, total mass and distribution of mass, as well as properties of the surrounding fluid. In this thesis we consider a physics-based model derived from rigid body equations of motion for describing underwater glider dynamics. The model we use incorporates important viscous effects in the form of added mass and added inertia caused by a heavy surrounding fluid, and in the form of external hydrodynamic forces and moments caused by the motion of the rigid body relative to the fluid. The equations of motion are derived in [5, 6] and have the same structure as the US Navy standard submarine equations of motion. The latter set of equations were first presented in [7] and revised in [8]. The model we consider has fewer number of external moment and force coefficients than those present in the most general set of equations for an underwater vehicle. A high-fidelity coefficient-based vehicle model would require a detailed parameter estimation and experimental validation, which is not a focus of this thesis. Detailed estimation of parameters was performed in [9] for underwater gliders; similar work on other underwater vehicles includes [10] for the REMUS vehicle, [11] (a propeller driven low-cost AUV), and [12] for the NPS AUV II. On the other hand, in this thesis we attempt to understand underwater glider dynamics by employing approximations that focus our attention on certain dynamical structures. These dynamical structures play a critical role in determining many important modes of motion and the associated stability properties.

1.1 Motivation

Since underwater gliders are underactuated and it is very desirable to design controllers that contribute towards high endurance for these vehicles, we devote a considerable amount of attention towards understanding their natural dynamics. The goal is to be able to beneficially use natural dynamics in designing control algorithms that demand minimal on-board energy consumption. Our approach involves the application of several tools from nonlinear systems theory [13]. We seek to derive analytical results that identify parameters responsible for certain useful properties of the system. As a consequence, our results characterize the qualitative properties of the underwater glider across a wide range of vehicle parameters. For example, one of our stability results for longitudinal plane steady gliding (proved using a composite Lyapunov function in Chapter 5) depends critically only on the signs of certain vehicle parameters. Furthermore, the stability results, although mostly local in nature, cover a wider range of operating conditions.

The nonlinear systems based approach taken in our work complements various vehicle specific studies that typically focus on designing and implementing control systems for regulating a specific set of motions. Linearized dynamics are commonly used in such studies. Examples of vehicle specific studies include work related to three commercially available underwater gliders: the Slocum glider (shown in Figure 1.1) [14] developed by Webb Research Corporation, the Spray glider [15] of Scripps Institute of Oceanography and the Seaglider [16] developed at University of Washington. Examples of similar work on design and control system development of other AUVs are [11, 17, 10] for the REMUS vehicle, [18] for the Starbug AUV developed for environmental monitoring on the Great Barrier Reef off the Australian coast, [19] for the SeaBED AUV developed for high resolution optical and acoustic sensing, [20, 21] for a line of low-cost miniature AUV's developed at Virginia Polytechnic Institute and State University and the United States Naval Academy. Many of these vehicles incorporate separate proportional-integral-derivative (PID) type control loops for regulating motion along different motion axes or for regulating a desired vehicle behavior. For instance, the Slocum glider uses proportional control to regulate the position of an internal movable mass in order to achieve a desired vehicle pitch. The controller gains are tuned on the basis of user experience, experimental testing and linear analysis.

Nonlinear systems analysis and control design attempt to exploit inherent system nonlinearities, and develop solutions that require low control effort and guarantee performance over a wide operating regime. We present work that attempts to cast important elements of glider dynamics in a modern geometric framework of mechanics [22]. The geometric framework provides various tools that determine the properties of a system based on its dynamic structure. There is a growing body of litera-

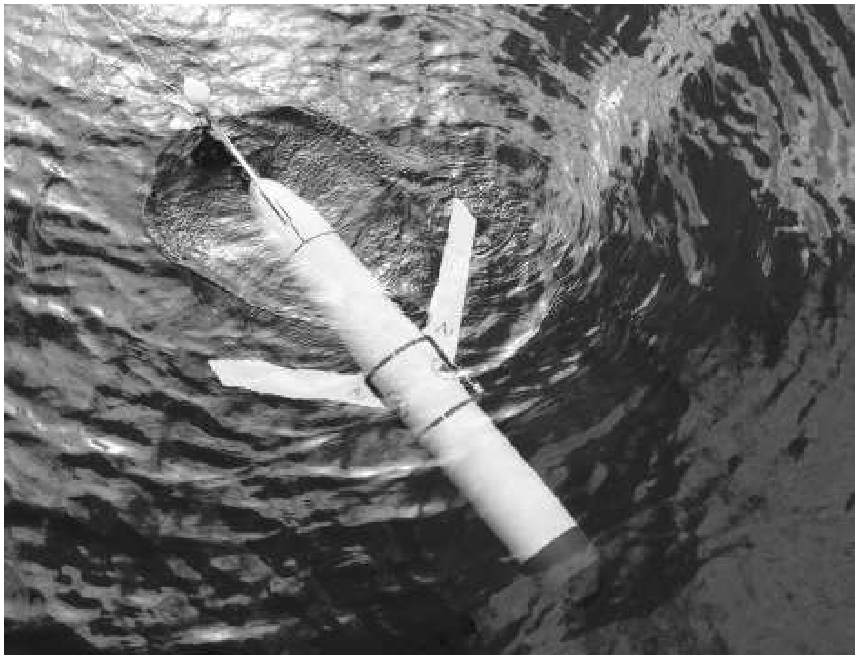

Figure 1.1: A Slocum underwater glider in Monterey Bay, off the California coast during the Autonomous Ocean Sampling Network-II experiment in August 2003. The glider was operated by David Fratantoni of Woods Hole Oceanographic Institution.

ture on applying geometric tools for dynamical systems analysis and control design. For example, systematic nonlinear control design techniques like the method of controlled Lagrangians [23] and the equivalent method of interconnection and damping assignment [24] are emerging. There are technical challenges in directly applying such tools to systems involving the aero/hydrodynamic forces due to the presence of energy-conserving lift and side-force components, but these tools are very attractive especially in the light of a demand for low-energy control solutions for underwater gliders and other AUVs.

Although the results we present in this thesis pertain mainly to the underwater glider application, the methods and approaches we use are applicable to other AUVs and to other types of vehicles such as airships and sailplanes. Airships in particular have strong similarities in their dynamics with underwater gliders. Both operate in a surrounding fluid whose relative density is comparable to their own. Added mass effects are important in both cases. The reference [25] presents a dynamic model of the airship and analysis of various modes of motion. References [26, 27, 28, 29, 30] present control system development and numerical simulation studies for airships.

1.2 Thesis Overview

Motivated by the emergence of underwater gliders as a promising technology and by the strength of nonlinear systems analysis and control design methodologies, we focus on the following set of problems in this thesis:

1. Characterize the parameter dependence and nonlinear stability of underwater glider relative equilibrium motions that may be utilized for nonlinear control synthesis.

2. Design low-energy control solutions that may be applicable to the general class of vehicles subject to aerodynamic forces and moments.

We study dynamic models of underwater gliders and aircraft of different orders of complexity. We calculate the associated relative equilibrium motions and study their stability properties. We design control laws to regulate desired steady motions and also to track desired unsteady trajectories.

Chapter 2 presents background information about development of underwater glider technology as well as study of their dynamics and control design. We briefly describe commercially available underwater gliders and important elements of their construction that help generate controllable gliding motions. We present a mathematical model [6] that describes glider dynamics and discuss the properties of this model, including the inherent approximations. We specialize this model to the longitudinal plane of the vehicle and survey linear systems analysis results for a laboratory scale underwater glider ROGUE [31], developed at Princeton University. We also discuss various nonlinear control design approaches that have been employed for aerospace and underwater vehicles, and highlight the important aspects of our approach.

In Chapter 3 we present results from the Autonomous Ocean Sampling Network II (AOSN II) project [32], in which underwater gliders played a pivotal role in ocean sampling. Underwater gliders are expected to play an increasingly important role in oceanography in the forthcoming decades. This motivates further research in vehicle design and control synthesis. As we already noted, control laws that demand low energy are critical for underwater gliders. We further discuss various ways in which nonlinear systems analysis may contribute towards development of underwater glider technology.

The hydrodynamic lift force is an important characteristic of the underlying structure of underwater glider dynamics. Since lift is an energy conserving force, it can potentially be incorporated within a Hamiltonian framework. In Chapter 4 we present such a framework for the conservative part of the translational dynamics of the underwater glider in the longitudinal plane. The system we describe is the phugoid mode of underwater glider dynamics, much like the phugoid mode of aircraft [33, 34]. We discuss connections between the phugoid-mode dynamics and Hamiltonian descriptions of some well known, planar mechanical systems.

In Chapter 5 we use singular perturbation theory [13, 35] to study the dynamics of underwater gliders. We identify slow and fast subsystems, and reduce the glider dynamics to the slow subsystem. This slow subsystem is a generalization of the phugoid-mode model of Chapter 4. We derive Lyapunov functions to prove exponential stability of the equilibria of slow and fast subsystems, and use these functions to construct a composite Lyapunov function for proving the asymptotic stability of the relative equilibrium of the underwater glider. The composite Lyapunov function is also used to derive estimates of the region of attraction of glider relative equilibria.

Chapter 6 presents application of results from Chapter 5 to design control laws for stabilizing desired steady gliding motions of underwater gliders. We consider three different control actuation configurations: pure torque control, buoyancy control, and elevator control. The elevator control model incorporates a moment-to-force coupling term that renders control synthesis challenging. For all three control configurations, our control synthesis is based on the composite Lyapunov function constructed in Chapter 5.

In Chapter 7 we apply gliding stability results to the position tracking problem for a Conventional Take Off and Landing (CTOL) aircraft. The CTOL aircraft model considered in [36] has been widely studied as a prototypical aircraft model for nonlinear control design. Common nonlinear control approaches have been based on feedback linearization techniques. Such methods have to deal with the nonminimum phase nature of the problem and may yield large control inputs. We present an alternative method, based on exponential stability of steady gliding motions. We first prove exponential stability of CTOL steady glides by interpreting the aircraft as an interconnected system of translational and rotational subsystems. We then propose an approximate trajectory tracking methodology in which a desired trajectory is approximated using a set of steady glides.

Chapter 8 focuses on the three-dimensional steady motions of underwater gliders. We first describe all possible relative equilibrium motions for a rigid body moving through a fluid in three-dimensional space. Only a subset of these relative equilibria may be realized by underwater gliders, and they correspond to motion along circular helices and straight lines. Furthermore, the range of properties of possible circular helices and straight lines depends on vehicle parameters. We present a simulation of circular helical motion using model parameters corresponding to a Slocum underwater glider. We also calculate a subset of the envelope of attainable circular helical motions by adjusting the vehicle mass and internal mass redistribution. We investigate the stability of motion along a circular helix. In particular we discuss how stability changes with respect to a bottom-heaviness parameter.

Chapter 9 summarizes the methods and results presented in this thesis, and indicates some avenues for related future work.

Chapter 2

Underwater Glider Modelling and Control

Our development of nonlinear stability results and control methodologies is largely motivated by the emergence of a new class of ocean vehicles called underwater gliders. These vehicles are rapidly becoming important assets in ocean sampling and have strong potential for applications in environmental monitoring and real-time assessment of ocean dynamics. The high endurance of underwater gliders enable their long-term deployment in the oceans. Being autonomous they have lower operating costs, making them ideal candidates for large scale ocean sampling tasks. In Chapter 3 we discuss results from an experimental ocean sampling project in which underwater gliders demonstrated their capabilities and played an important role in collecting valuable data for ocean scientists. Underwater gliders are also inspiring development of similar technologies for exploring extra-terrestrial dense environments such as the atmosphere of Venus or the speculated oceans of Europa, one of Jupiter's moons [37].

In §2.1 we introduce a set of underwater gliders that have been successfully deployed in the oceans. We discuss important elements of underwater glider configuration and how they determine the nominal motion of the vehicle. In §2.2 we present a mathematical model that describes the dynamics of underwater gliders. We describe what aspects of underwater glider dynamics have been accounted for in the model and the inherent approximations. We specialize the dynamics to the longitudinal plane in §2.3 and summarize linear stability and control results for a laboratory scale underwater glider developed at Princeton University. In §2.4 we briefly survey different nonlinear control methods for underwater and aerospace vehicles, and indicate the main characteristics of our approach.

2.1 Ocean-Class Underwater Gliders

The development of ocean-class underwater gliders has been primarily driven by a need to develop low-cost observational platforms that can efficiently and autonomously gather a wide range of scientific data from the ocean for long periods of time. This need is being addressed by a set of multi-institutional research programs supported by the United States Office of Naval Research (ONR), including the Autonomous Ocean Sampling Network (AOSN) [3] and Adaptive Sampling and Prediction (ASAP) [4] projects discussed in Chapter 3.

The vision of underwater gliders playing an important role in efficient data gathering of the ocean was laid out in an article written by Henry Stommel [38]. This vision was recognized in the establishment of the AOSN research initiative [39]. The AOSN project has led to the development of three sea-faring underwater gliders - the *Slocum* [14] developed by Webb Research Corporation, the *Spray* [15] developed by Scripps Institution of Oceanography and the *Seaglider* [16] developed at University of Washington. A review of operation of these gliders, their design considerations and technical specifications, including a discussion of the navigational and science sensors they carry and their communication capabilities, is provided by Rudnick et al [1]. Below we discuss the most important features pertaining to their dynamics and control.

The Seaglider, Slocum, and Spray propel themselves by changing their buoyancy and redistributing internal mass. The basic principle of operation is very simple: a rigid body immersed in a fluid sinks, floats or rises depending on whether it is negatively buoyant (i.e., heavier with respect to the surrounding fluid), neutrally buoyant or positively buoyant. If such a rigid body is also equipped with lifting surfaces, such as wings, it can achieve motion in the horizontal plane in addition to the vertical motion due to buoyancy. A purely horizontal displacement may be obtained by combining a series of downward and upward straight gliding motions as shown in Figure 2.1.

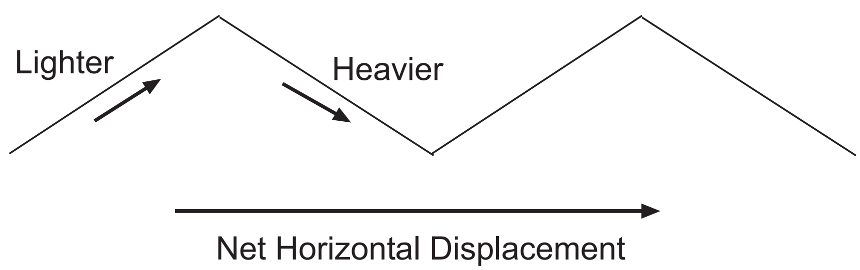

Figure 2.1: Nominal Underwater Glider Motion

The mechanism on the underwater glider that effects the change in buoyancy is called the "buoyancy engine". All three gliders mentioned in this section pump a fluid (oil or water) between an internal reservoir and an external bladder in order to change the vehicle volume, thus changing their relative density with respect to the surrounding fluid and their buoyancy. The pumping energy is typically derived from electric batteries. There is also a version of the Slocum glider that utilizes the thermal gradient of the ocean (deeper water is cooler) to derive the pumping energy. The *thermal* Slocum has an external bladder, which contains a working fluid that undergoes a volume change due to a change of state caused by the difference in temperatures between the near-surface water and deep-sea water.

The battery pack (or an alternative internal mass) is moved fore and aft to move the center of gravity of the underwater glider fore and aft, and consequently to adjust vehicle attitude and flight path angle. An effective lateral displacement of the center of gravity that causes a rolling motion may be achieved by rotating an asymmetric portion of the battery pack about the longitudinal axis. In Seaglider and Spray, the roll induces a yawing moment that is used to steer the underwater glider. The Slocum has a dedicated external rudder for steering control.

2.2 Mathematical Model for Underwater Glider Dynamics

A mathematical model for describing underwater glider dynamics is presented in [6, 5]. In this section we present the equations of motion of this model. The reader is referred to [5] for a derivation of equations of motion. The underwater glider is modelled as a homogeneous rigid body containing two internal point masses. The vehicle hull is considered to be homogenous with a total mass of m_h. One internal point mass, whose (controllable) value we denote by m_b, models the buoyancy regulating mechanism of the underwater glider. Although m_b may be distributed within the internal volume of the vehicle, rotational inertia of this mass is negligible. This point mass is fixed at the center of buoyancy (CB) of the vehicle. The other internal point mass, whose constant value we denote by $\bar{m}$, models the internal moving battery packs of the glider. The (controllable) position of $\bar{m}$ with respect to the CB of the rigid body is denoted by $\boldsymbol{r}_P = (r_{P1}, r_{P2}, r_{P3})^T \in \mathbb{R}^3$. See Figure 2.2 for an illustration of the positions of the point masses within the hull of the underwater glider.

We assume the rigid body to be ellipsoidal for the sake of simplicity. The CB of the glider is located at the center of the ellipsoid. We attach a frame of reference at the CB. This is the *body fixed frame.* We align the body fixed frame such that body

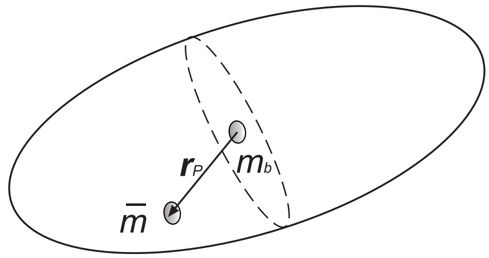

Figure 2.2: Point mass locations within the hull of the underwater glider.

1 axis lies along the long axis of the glider, positive in the direction of the nose. The body 2 axis lies in the plane of the wings and is orthogonal to the body 1 axis. The body 3 axis is orthogonal to the body 1 and 2 axes, as shown in Figure 2.3.

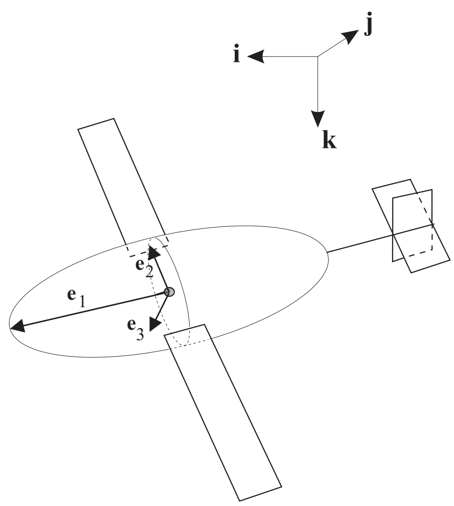

Figure 2.3: Body frame assignment

The position of the origin of the body fixed frame with respect to an *inertial frame* (fixed-to-earth frame) is $\boldsymbol{b} \in \mathbb{R}^3$. The orientation of the body fixed frame is specified by a rotation matrix $R \in SO(3)$, where $SO(3)$ is a *Lie group* (see Appendix A for the definition of Lie group) containing all 3×3 orthogonal matrices whose determinant is equal to 1. Rotation matrices have certain special properties that we will use in our analysis and control design.

We denote the inertial velocity of the underwater glider in body-fixed frame coordinates by the vector $\boldsymbol{v} = (v_1, v_2, v_3)^T \in \mathbb{R}^3$ and in inertial frame coordinates by $\dot{\boldsymbol{b}} \in \mathbb{R}^3$. The angular velocity is $\boldsymbol{\Omega} = (\Omega_1, \Omega_2, \Omega_3)^T \in \mathbb{R}^3$ in body coordinates and $\boldsymbol{\omega} \in \mathbb{R}^3$ in inertial coordinates. The rotation matrix R transforms vectors in body coordinates to corresponding vectors in inertial coordinates. Thus, $\dot{\boldsymbol{b}} = R\boldsymbol{v}$ and $\boldsymbol{\omega} = R\boldsymbol{\Omega}$.

2.2.1 Kinematics

The configuration of the underwater glider system can be completely described by specifying the following variables: $(\boldsymbol{b}, R, \boldsymbol{r}_P) \in \mathbb{R}^3 \times SO(3) \times \mathbb{R}^3$. We do not impose any restrictions on how the underwater glider moves in space or the way $\bar{m}$ moves internally. Thus, the kinematics of the system are described by the following equations:

$$\frac{d\boldsymbol{b}}{dt} = R\boldsymbol{v} \tag{2.1}$$

$$\frac{dR}{dt} = R\hat{\boldsymbol{\Omega}} \tag{2.2}$$

$$\frac{d\boldsymbol{r}_P}{dt} = \dot{\boldsymbol{r}}_P. \tag{2.3}$$

The $\hat{}$ operator used in equation (2.2) maps vectors $\boldsymbol{x} = (x_1, x_2, x_3)^T \in \mathbb{R}^3$ to 3×3 skew symmetric (cross-product-equivalent) matrices as follows:

$$\hat{\boldsymbol{x}} = \begin{bmatrix} 0 & -x_3 & x_2 \\ x_3 & 0 & -x_1 \\ -x_2 & x_1 & 0 \end{bmatrix}.$$

For any $\boldsymbol{x}, \boldsymbol{y} \in \mathbb{R}^3$, $\boldsymbol{x} \times \boldsymbol{y} = \hat{\boldsymbol{x}}\boldsymbol{y}$.

2.2.2 Dynamics

Before we present the equations of motion describing the dynamics of the underwater glider, we need to introduce the inertia and mass matrices. We consider the contributions of the rigid body plus buoyancy point mass (m_b) separately from the internal moving point mass ($\bar{m}$). Let the total stationary mass of the underwater glider be $m_s = m_h + m_b$, where m_h is the mass of the rigid body. $J_s = J_h$ is the moment of inertia matrix corresponding to the stationary mass. The mass/inertia matrix corresponding to the stationary mass of the vehicle is

$$I_s = \begin{bmatrix} m_s \mathbb{I}_3 & 0 \\ 0 & J_s \end{bmatrix},$$

where $\mathbb{I}_3$ is the 3×3 identity matrix.

The motion of the underwater glider induces a flow of the surrounding fluid, which in turn affects the glider dynamics. For example, in order to accelerate the underwater glider it is also necessary to accelerate some of the surrounding fluid. Thus, a greater force or moment is required to change the linear or angular momentum of the underwater glider compared to an identical vehicle operating in a vacuum. This effect is captured through an *added mass/inertia matrix*

$$I_f = \begin{bmatrix} M_f & D_f^T \\ D_f & J_f \end{bmatrix},$$

where M_f, J_f and D_f are the added mass, added inertia and the added cross term matrices respectively. The elements of I_f depend on the external shape of the rigid body and the density of the surrounding fluid. Their computation is described in standard hydrodynamics textbooks such as [40, 41]. If we neglect the added mass and inertia contributions of the wings and tail of the underwater glider assuming that at low angles of attack the contribution of the wings and tail is dominated by lift, drag and associated moments, the matrices M_f and J_f can be taken to be diagonal and $D_f = 0$. This approximation is used throughout this thesis. With this approximation we can define the total mass, M, and inertia, J, matrices corresponding to the stationary mass of the underwater glider system as follows:

$$\begin{aligned} M &= m_s\mathbb{I}_3 + M_f &&= \mathrm{diag}(m_1, m_2, m_3) \\ J &= J_s + M_f &&= \mathrm{diag}(J_1, J_2, J_3) \end{aligned}$$

References [6, 5] consider more general arrangements of internal point masses. The arrangement we consider in this thesis is sufficient for describing the most important aspects of underwater glider dynamics.

The dynamical equations of motion are:

$$\dot{\boldsymbol{v}} = M^{-1}\bar{\boldsymbol{F}} \tag{2.4}$$

$$\dot{\boldsymbol{\Omega}} = J^{-1}\bar{\boldsymbol{T}} \tag{2.5}$$

$$\dot{\boldsymbol{P}}_P = \bar{\boldsymbol{u}}, \tag{2.6}$$

where,

$$\begin{aligned} \boldsymbol{P}_P &= \bar{m}(\boldsymbol{v} + \dot{\boldsymbol{r}}_P + \boldsymbol{\Omega} \times \boldsymbol{r}_P) \\ \bar{\boldsymbol{F}} &= (M\boldsymbol{v} + \boldsymbol{P}_P) \times \boldsymbol{\Omega} + m_0 g R^T \boldsymbol{k} + \boldsymbol{F_{ext}} - \bar{\boldsymbol{u}} \\ \bar{\boldsymbol{T}} &= (J\boldsymbol{\Omega} + \hat{\boldsymbol{r}}_P \boldsymbol{P}_P) \times \boldsymbol{\Omega} + M\boldsymbol{v} \times \boldsymbol{v} + \bar{m} g \hat{\boldsymbol{r}}_P R^T \boldsymbol{k} + \boldsymbol{T_{ext}} - \hat{\boldsymbol{r}}_P \bar{\boldsymbol{u}}. \end{aligned}$$

In the above equations m_0 is the buoyancy of the vehicle. It is the total mass of the vehicle minus the mass of the displaced fluid: $m_0 = m_h + m_b + \bar{m} - m_{df}$, where m_{df} is the mass of the displaced fluid. The vector $\boldsymbol{k} = (0, 0, 1)^T$ represents the direction of gravity in the inertial reference frame. The vector $\boldsymbol{P}_P = (P_{P1}, P_{P2}, P_{P3})^T$ represents the momentum of the internal moving point mass in body coordinates. The vector $\bar{\boldsymbol{u}} = (u_1, u_2, u_3)^T$ is the total force acting on the internal moving point mass, and is equal to

$$\bar{\boldsymbol{u}} = \boldsymbol{P}_P \times \boldsymbol{\Omega} + \bar{m}g\left(R^T\boldsymbol{k}\right) + \tilde{\boldsymbol{u}}, \tag{2.7}$$

where $\tilde{\boldsymbol{u}} = R^T \sum_k^K \boldsymbol{f}_{int_k}$ in the total internal force exerted by the rigid body on the internal point mass, expressed in body coordinates. $\tilde{\boldsymbol{u}}$ may be considered to be a control force that can be specified. Alternatively, we can use relation (2.7) to interpret $\bar{\boldsymbol{u}}$ as the control force, which is the interpretation used in [6]. $\boldsymbol{F_{ext}}$ includes all the external forces acting on the underwater glider system except gravity, and $\boldsymbol{T_{ext}}$ are external moments. The non-gravitational external forces we consider are the hydrodynamic lift, drag and side forces, and external moments are the hydrodynamic moments about the three body axes.

2.2.3 Buoyancy Control

The buoyancy engine of the glider is modelled using a control signal, u_4, which represents the rate of change of the buoyancy point mass:

$$\dot{m}_b = u_4. \tag{2.8}$$

2.2.4 Further Discussion of Model Components

Equations (2.1)-(2.8) completely describe the motion of the underwater glider system. Below we list the important components of the model.

1. The added mass and added inertia effects are included in the matrices M_f and J_f, embedded in M and J respectively. We have made an assumption that M_f and J_f are diagonal and neglected the cross term D_f. These are reasonable

assumptions for the purpose of studying the dynamics and the use of feedback control compensates the perturbations due to the terms that have been ignored.

2. The buoyancy engine is modelled by equation (2.8). Typically there is a limit on the magnitude of the control signal u_4. The saturation of u_4 is considered in the control laws that we design: the control laws do not require a rapid change in the vehicle buoyancy.

3. The viscous forces and moments are included in $\boldsymbol{F_{ext}}$ and $\boldsymbol{T_{ext}}$,

$$\boldsymbol{F_{ext}} = \begin{pmatrix} -D \\ SF \\ -L \end{pmatrix} \quad \text{and} \quad \boldsymbol{T_{ext}} = \begin{pmatrix} M_{DL_1} \\ M_{DL_2} \\ M_{DL_3}, \end{pmatrix}$$

   where D, L, and SF represent the hydrodynamic lift, drag, and side forces respectively. M_{DL_i} are the hydrodynamic moments. We use a coefficient-based model for the hydrodynamic forces and moments, similar to the models used in the aircraft dynamics literature [42, 43], but considerably simpler. Our goal is to include important aspects of vehicle dynamics using a small set of parameters so that the resulting model is amenable to tools of nonlinear systems and control. While the model we consider does not include all dynamical effects, the control laws and design insights gained from the analysis will be useful in analytical or numerical analysis of more detailed models. Furthermore, use of feedback control is expected to provide robustness to unmodelled dynamics. The hydrodynamic force and moment model described below fulfills the objective of encoding important dynamical effects as well as having a reasonably small set of vehicle parameters:

$$
\begin{aligned}
D &= (K_{D0} + K_D \alpha^2) V^2 && (2.9)\\
SF &= K_\beta \beta V^2 && (2.10)\\
L &= (K_{L0} + K_L \alpha) V^2 && (2.11)\\
M_{DL_1} &= K_{MR} \beta V^2 + K_{q1} \Omega_1 V^2 && (2.12)\\
M_{DL_2} &= (K_{M0} + K_M \alpha + K_{q2} \Omega_2) V^2 && (2.13)\\
M_{DL_3} &= K_{MY} \beta V^2 + K_{q3} \Omega_3 V^2, && (2.14)
\end{aligned}
$$

where $\alpha = \tan^{-1}\left(\frac{v_3}{v_1}\right)$ is the angle of attack and $\beta = \sin^{-1}\left(\frac{v_2}{V}\right)$ is the sideslip angle. See Figure 2.4 for a pictorial representation of angles α and β; α is the angle from the projection of the velocity vector on the body 1-3 plane to the body 1 axis and β is the angle from the projection of the velocity vector on the body 1-3 plane to the velocity vector. The hydrodynamic coefficients appearing in the above equations may be estimated by using reference data for generic aerodynamic bodies [44], and verified either by wind tunnel tests or parameter identification techniques. Reference [45] presents estimates of lift, drag and pitching moment coefficients based on wind tunnel experiments for a scaled model of a Slocum glider. Estimates of hydrodynamic coefficients calculated using steady gliding data collected during sea trials of a Slocum underwater glider are presented in [46].

4. The coupling between the position and momentum of the internal moving point mass $\bar{m}$ and the rigid body motion appears in the terms containing $\boldsymbol{r}_P$, $\boldsymbol{P}_P$ and $\bar{\boldsymbol{u}}$. Equation (2.6) describes the dynamics governing the motion of $\bar{m}$. We recall that $\bar{m}$ is free to move inside the rigid body. However, in most glider designs the motion is constrained by some sort of internal mechanism such as a railing

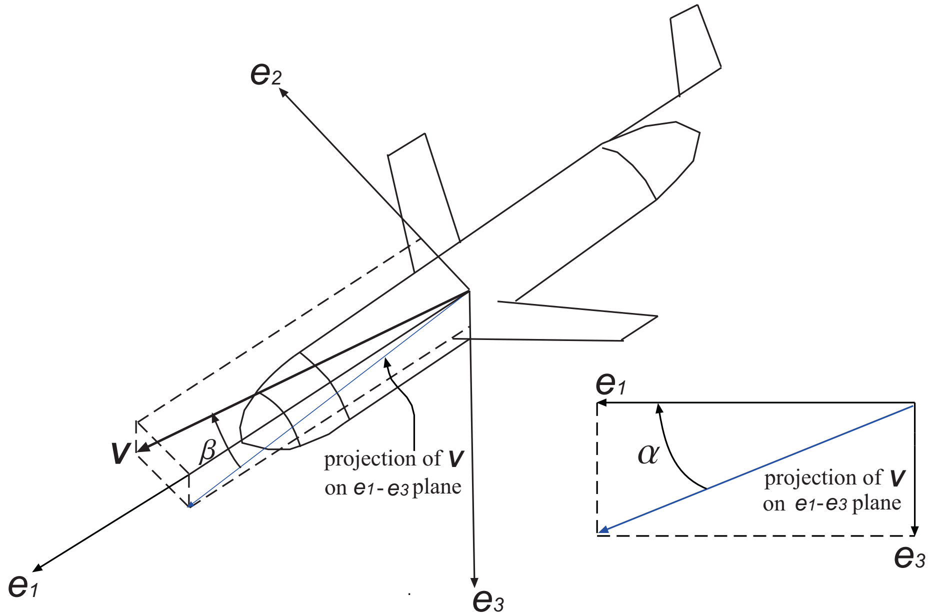

Figure 2.4: Schematic showing the angle of attack α and side slip angle β for a torpedo-shaped underwater glider (like the Slocum [14]).

or a screw. The constraint forces causing such a motion must be included in $\bar{\boldsymbol{u}}$.

2.3 Longitudinal Plane Equations of Motion

The plane formed by the 1 and 3 body axes of the underwater glider is longitudinal plane. The longitudinal plane is an invariant plane under the dynamics represented by equations (2.1)-(2.8) provided that the vehicle is symmetric about the same plane. If such a vehicle starts with a set of initial conditions that correspond to motion in the longitudinal plane (the required conditions are $v_2 = 0$, $\Omega_1 = \Omega_3 = 0$, $r_{P2} = 0$, $P_{P2} = 0$ and $R^T k \cdot j = 0$) and if $u_2 = 0$ the vehicle will remain in the longitudinal plane for all time. The last condition listed within parentheses implies that the gravity vector must be in the longitudinal plane of the vehicle. Further assuming (without loss of generality) that the invariant longitudinal plane of the underwater glider coincides with the x-z plane in the inertial reference frame, we can write the equations describing the motion of the underwater glider as follows:

$$
\begin{aligned}
\dot{x} &= v_1 \cos\theta + v_3 \sin\theta && (2.15)\\
\dot{z} &= -v_1 \sin\theta + v_3 \cos\theta && (2.16)\\
\dot{\theta} &= \Omega_2 && (2.17)\\
\dot{v}_1 &= \frac{1}{m_1}\Big\{-m_3 v_3 \Omega_2 - P_{P3}\Omega_2 - m_0 g \sin\theta + L\sin\alpha - D\cos\alpha \\
&\qquad - u_1\Big\} && (2.18)\\
\dot{v}_3 &= \frac{1}{m_3}\Big\{m_1 v_1 \Omega_2 + P_{P1}\Omega_2 + m_0 g \cos\theta - L\cos\alpha - D\sin\alpha \\
&\qquad - u_3\Big\} && (2.19)\\
\dot{\Omega}_2 &= \frac{1}{J_2}\Big\{(m_3 - m_1)\, v_1 v_3 - \bar{m} g\,(r_{P1}\cos\theta + r_{P3}\sin\theta) + M_{DL_2} \\
&\qquad + r_{P1} u_3 - r_{P3} u_1 - \Omega_2\,(r_{P1} P_{P1} + r_{P3} P_{P3})\Big\} && (2.20)\\
\dot{r}_{P1} &= \frac{1}{\bar{m}} P_{P1} - v_1 - r_{P3}\Omega_2 && (2.21)\\
\dot{r}_{P3} &= \frac{1}{\bar{m}} P_{P3} - v_3 + r_{P1}\Omega_2 && (2.22)\\
\dot{P}_{P1} &= u_1 && (2.23)\\
\dot{P}_{P3} &= u_3 && (2.24)\\
\dot{m}_0 &= u_4, && (2.25)
\end{aligned}
$$

where θ is the pitch angle, equal to the sum of the angle of attack α and flight path angle γ, as shown in Figure 2.5. We note that equation (2.4) and the above set of equations assume a constant acceleration due to gravity (the flat-earth assumption). Table 2.3 summarizes definitions of all variables used in equations (2.15)-(2.25).

If the controls u_1, u_3 and u_4 do not depend on the translational position (x, z), the longitudinal dynamics are invariant with respect to the position of the underwater glider. This implies that the longitudinal dynamics can be further reduced to equations (2.17)-(2.25). The fixed points of this reduced system are the relative equilibria

α	angle of attack
D	drag force component
g	acceleration due to gravity
L	lift force component
m_0	vehicle heaviness
m_1	added mass along body-1 direction
m_3	added mass along body-3 direction
$\bar{m}$	internal moving mass
M_{DL_2}	pitching moment
J_2	added moment of inertia along the body-2 direction
Ω_2	pitch rate
(P_{P1}, P_{P3})	total momentum of $\bar{m}$ in body coordinates
(r_{P1}, r_{P3})	position of $\bar{m}$ with respect to CB in body coordinates
θ	pitch angle
(u_1, u_3)	components of total force on $\bar{m}$ in body coordinates
u_4	buoyancy control
(v_1, v_3)	velocity components in body coordinates
(x, z)	inertial position coordinates of the CB

Table 2.1: Definitions of all variables appearing in the underwater glider longitudinal equations of motion (2.15)-(2.25).

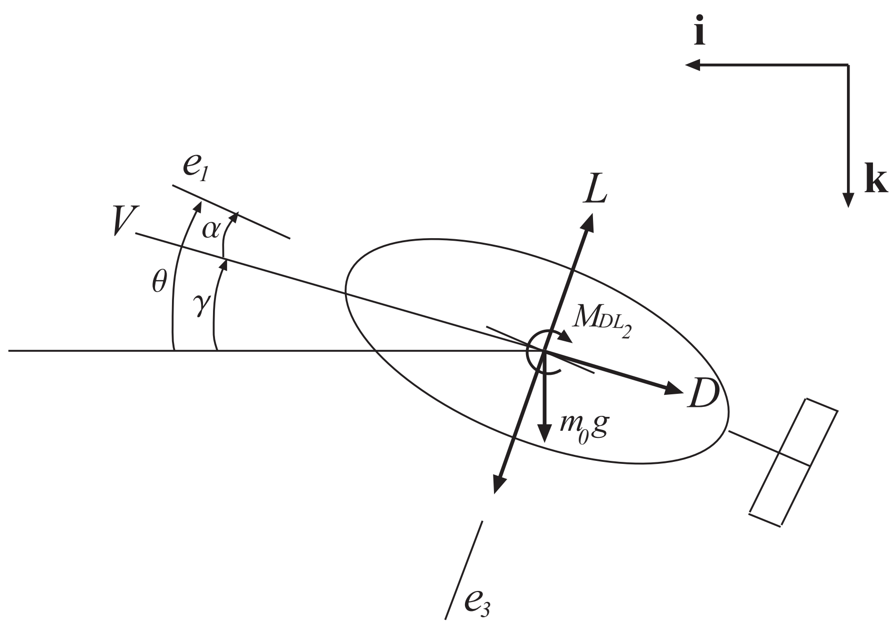

Figure 2.5: External forces and moment in the longitudinal plane.

of the longitudinal dynamics, and they correspond to steady gliding motions of the underwater glider.

The vehicle speed $V = \sqrt{v_1^2 + v_3^2}$ and flight path angle γ are constant during a steady gliding motion. In [6] steady gliding paths corresponding to a prescribed equilibrium speed V_e and equilibrium flight path angle γ_e were computed. The hydrodynamic lift and drag coefficients determine the permissible values of γ_e within the interval $(-\frac{\pi}{2}, \frac{\pi}{2})$. In [6] it was shown that γ_e must lie within the following set:

$$\begin{aligned}\gamma_e \in & \left\{ \tan^{-1}\left[2\frac{K_D}{K_L}\left(\frac{K_{L0}}{K_L} + \sqrt{\left(\frac{K_{L0}}{K_L}\right)^2 + \frac{K_{D0}}{K_D}}\right)\right], \frac{\pi}{2} \right\} \bigcup \\ & \left\{ -\frac{\pi}{2}, \tan^{-1}\left[2\frac{K_D}{K_L}\left(\frac{K_{L0}}{K_L} - \sqrt{\left(\frac{K_{L0}}{K_L}\right)^2 + \frac{K_{D0}}{K_D}}\right)\right] \right\}\end{aligned} \tag{2.26}$$

The magnitude of the shallowest steady flight path angle is smaller for lower values of $K_D (> 0)$. Given V_e and a permissible γ_e, reference [6] computes the corresponding equilibrium values of m_0, α, r_{P1} and r_{P3}. It is shown that in general there exists a one-parameter family of solutions for equilibrium internal mass position (r_{P1_e}, r_{P3_e}) corresponding to a steady gliding motion. The projection of (r_{P1_e}, r_{P3_e}) along the direction of gravity determines the "bottom-heaviness" [47] of the vehicle, which affects the stability of the equilibrium motion.

For a given (r_{P1_e}, r_{P3_e}) and equilibrium buoyancy m_{0e}, the equilibrium speed and flight path angle are given by the following equations.

$$V_e = \frac{\sqrt{|m_{0e}|g}}{\{L_e(\alpha_e)^2 + D_e(\alpha_e)^2\}^{\frac{1}{4}}} \tag{2.27}$$

$$\gamma_e = \tan^{-1}\frac{L_e(\alpha_e)\sin\alpha_e - D_e(\alpha_e)\cos\alpha_e}{L_e(\alpha_e)\cos\alpha_e + D_e(\alpha_e)\sin\alpha_e}, \tag{2.28}$$

where $L_e(\alpha_e) = (K_{L0} + K_L\alpha_e)\,V_e^2$, $D_e(\alpha_e) = (K_{D0} + K_D\alpha_e^2)\,V_e^2$ and α_e is the solution of the following nonlinear equation:

$$
\begin{aligned}
& m_{0e}(m_3 - m_1)\sin\alpha_e\cos\alpha_e + m_{0e}\left(K_{M0} + K_M\alpha_e\right) \\
- \; & \bar{m}r_{P3_e}\left\{(K_{L0} + K_L\alpha_e)\sin\alpha_e - \left(K_{D0} + K_D\alpha_e^2\right)\cos\alpha_e\right\} \\
- \; & \bar{m}r_{P1_e}\left\{(K_{L0} + K_L\alpha_e)\cos\alpha_e + \left(K_{D0} + K_D\alpha_e^2\right)\sin\alpha_e\right\} = 0 \qquad (2.29)
\end{aligned}
$$

2.3.1 Linear Stability and Control Analysis for a Laboratory Scale Underwater Glider

The stability of steady glides can be determined by linearizing the longitudinal equations of motion. The linearization is carried out in [6, 48] with equations (2.15)-(2.16) for x and z replaced by a single equation for the variable z', which represents the perpendicular component of the vector to the underwater glider from a certain desired steady glide path, as shown in Figure 2.6. The evolution of z' is given by the following equation:

$$
\dot{z}' = \sin\gamma_e\left(v_1\cos\theta + v_3\sin\theta\right) + \cos\gamma_e\left(-v_1\sin\theta + v_3\cos\theta\right), \qquad (2.30)
$$

where γ_e is the steady flight path angle corresponding to the desired path.

Linear stability, controllability and observability of four steady glides were determined in [6, 48] for a laboratory scale underwater glider ROGUE [31] built at Princeton University. Following parameter values were used in the analysis: $m_1 = 13.22$ kg, $m_3 = 25.22$ kg, $\bar{m} = 2$ kg, $J_2 = 0.1$ Nm^2, $K_{D0} = 18$ N(s/m)^2, $K_D = 109$ N(s/m)^2, $K_L = 306$ N(s/m)^2, $K_M =$ -36.5 Nm(s/m)^2, $K_q = 0$ Nms(s/m)^2. Two of the steady glides investigated were downward gliding motions at flight path angles of -30^o and -45^o, and the other two were upward gliding motions at flight path angles of 30^o and 45^o. All of them had a slow unstable mode caused by the motion of $\bar{m}$ relative to the body of the glider.

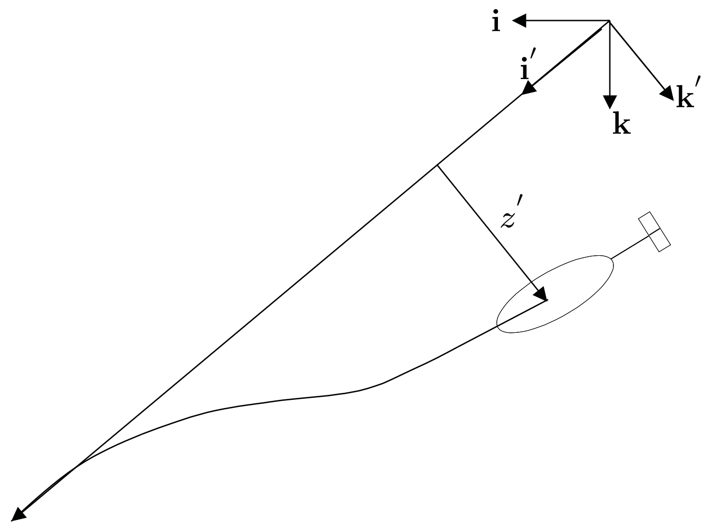

Figure 2.6: Planar gliding controlled to a line.

For example, we consider the steady gliding motion with a flight path angle of -45^o and a speed of 0.3 m/s. The linearized dynamics of the uncontrolled (i.e., $u_1 = u_3 = u_4 = 0$) ROGUE glider about this equilibrium has a pair of eigenvalues at $0.099 \pm 2.325i$. Recall that glider dynamics were derived by considering $\bar{m}$ to be able to freely move within the glider body. Also recall that (u_1, u_3) represents the total force acting on $\bar{m}$, including the interaction force between the rigid body and $\bar{m}$. Setting $u_1 = u_3 = 0$ amounts to setting the momentum of $\bar{m}$ constant, i.e., setting the interaction force between $\bar{m}$ and the rigid body such that the momentum of $\bar{m}$ remains constant. This interaction force causes the unstable mode observed in the linearized dynamics. The instability is similar to the fuel slosh instability observed in aircraft and space vehicles [49]. We can study the dependence of the unstable mode on the value of the internal mass $\bar{m}$. The unstable pair of eigenvalues crosses over to the left half plane when $\bar{m}$ is made sufficiently small. For the equilibrium under consideration this happens when $\bar{m}$ is smaller than 0.257 kg.

The steady glides reported in [6, 48] are locally controllable, with controllability extending to the z' state as well. Thus, it is possible to design a linear control law for $(u_1, u_3, u_4)^T$ to regulate the motion of the glider to a prescribed straight line. Interestingly, full state controllability is preserved even when the internal mass motion is restricted to be along just one of the body axes. However, for large motions, such as switching from an upward glide to a downward glide path, care needs to be taken if restricting the degrees of freedom of the movable mass. For instance, while the motion of the movable mass restricted to the body 1 axis is sufficient for sawtooth maneuvers, motion restricted to the body 3 axis does not allow for both upward and downward steady glide motions.

All states except z' are observable for the linear models computed in [6, 48] with measurements restricted to internal mass position (r_{P1}, r_{P3}) and the vehicle heaviness m_0. All states except z' are also observable with measurements limited to the pitch angle θ, r_{P1} (or r_{P3}) and m_0.

2.3.2 Transformation from Force to Acceleration Control

The motion of the internal point mass $\bar{m}$ in most glider designs is restricted by some sort of supporting mechanism (for example a railing). Such a mechanism also makes it possible to directly control the acceleration of the point mass relative to the vehicle body, and consequently the relative velocity and position of $\bar{m}$. This situation can be realized in the underwater glider model by performing a coordinate and feedback control transformation [50].

We consider the coordinate transformation derived from equations (2.21)-(2.22):

$$\begin{pmatrix} P_{P1} \\ P_{P3} \end{pmatrix} \mapsto \begin{pmatrix} \dot{r}_{P1} \\ \dot{r}_{P3} \end{pmatrix} = \begin{pmatrix} \frac{1}{\bar{m}} P_{P1} - v_1 - r_{P3}\Omega_2 \\ \frac{1}{\bar{m}} P_{P3} - v_3 + r_{P1}\Omega_2 \end{pmatrix}. \tag{2.31}$$

Differentiating the above equation once gives equations for $\ddot{r}_{P1}$ and $\ddot{r}_{P3}$ in terms of control inputs u_1 and u_3:

$$\begin{pmatrix} \ddot{r}_{P1} \\ \ddot{r}_{P3} \end{pmatrix} = \boldsymbol{Z} + F \begin{bmatrix} u_1 \\ u_3 \end{bmatrix}, \tag{2.32}$$

where

$$\begin{aligned}
\boldsymbol{Z} &= \begin{bmatrix} \frac{1}{m_1} X_1 + \dot{r}_{P3}\Omega_2 + \frac{r_{P3} Y}{J_2} \\ \frac{1}{m_3} X_3 - \dot{r}_{P1}\Omega_2 - \frac{r_{P1} Y}{J_2} \end{bmatrix} \\
F &= \begin{bmatrix} \left(\frac{1}{\bar{m}} + \frac{1}{m_1} + \frac{r_{P3}^2}{J_2}\right) & -\frac{r_{P1} r_{P3}}{J_2} \\ -\frac{r_{P1} r_{P3}}{J_2} & \left(\frac{1}{\bar{m}} + \frac{1}{m_3} + \frac{r_{P1}^2}{J_2}\right) \end{bmatrix} \\
X_1 &= -m_3 v_3 \Omega_2 - \bar{m}(v_3 + \dot{r}_{P3} - r_{P1}\Omega_2)\Omega_2 - m_0 g \sin\theta + L \sin\alpha - D\cos\alpha \\
X_3 &= m_1 v_1 \Omega_2 + \bar{m}(v_1 + \dot{r}_{P1} + r_{P3}\Omega_2)\Omega_2 + m_0 g \cos\theta - L\cos\alpha - D\sin\alpha \\
Y &= (m_3 - m_1) v_1 v_3 - \bar{m} g (r_{P1}\cos\theta + r_{P3}\sin\theta) + M_{DL_2} \\
&\quad - \Omega_2 \left(r_{P1} P_{P1} + r_{P3} P_{P3}\right).
\end{aligned}$$

The above equations are linear in u_1 and u_3, and we can check that the determinant of F is always nonzero. Thus, we can choose the following control law:

$$\begin{bmatrix} u_1 \\ u_3 \end{bmatrix} = F^{-1} \left(-\boldsymbol{Z} + \begin{bmatrix} w_1 \\ w_3 \end{bmatrix} \right), \tag{2.33}$$

where w_1 and w_3 are acceleration inputs. We also set

$$u_4 = w_4. \tag{2.34}$$

Now, if we define $\boldsymbol{\eta} = (x, z, \theta, \Omega_2, v_1, v_3)^T$, $\boldsymbol{\zeta} = (r_{P1}, \dot{r}_{P1}, r_{P3}, \dot{r}_{P3}, m_0)^T$, $\boldsymbol{w} = (w_1, w_3, w_4)^T$

the resulting equations of motion of the underwater glider are

$$\begin{aligned}\dot{\boldsymbol{\eta}} &= \boldsymbol{q}(\boldsymbol{\eta}, \boldsymbol{\zeta}, \boldsymbol{w}) \\ \dot{\boldsymbol{\zeta}} &= A\boldsymbol{\zeta} + B\boldsymbol{w},\end{aligned}$$

where,

$$A = \begin{bmatrix} 0 & 1 & 0 & 0 & 0 \\ 0 & 0 & 0 & 0 & 0 \\ 0 & 0 & 0 & 1 & 0 \\ 0 & 0 & 0 & 0 & 0 \\ 0 & 0 & 0 & 0 & 0 \end{bmatrix}, \quad B = \begin{bmatrix} 0 & 0 & 0 \\ 1 & 0 & 0 \\ 0 & 0 & 0 \\ 0 & 1 & 0 \\ 0 & 0 & 1 \end{bmatrix},$$

and $\boldsymbol{q}$ is the vector field obtained by substituting the mapping (2.31) and the equation (2.33) in equations (2.15)-(2.20). To study the stability of the relative equilibria we only consider the states of a reduced system: $(\boldsymbol{\eta}_r, \boldsymbol{\zeta})$, where $\boldsymbol{\eta}_r = (\theta, \Omega_2, v_1, v_3)$. This reduction is possible since the dynamics (2.35)-(2.36) are invariant with respect to the glider position (x, z). The equations of motion for this reduced system are:

$$\dot{\boldsymbol{\eta}}_{\boldsymbol{r}} = \boldsymbol{q}_r(\boldsymbol{\eta}_r, \boldsymbol{\zeta}, \boldsymbol{w}) \tag{2.35}$$

$$\dot{\boldsymbol{\zeta}} = A\boldsymbol{\zeta} + B\boldsymbol{w}, \tag{2.36}$$

where $\boldsymbol{q}_r$ is the vector of last four components of $\boldsymbol{q}$.

We note that the gliding relative equilibria are not changed due to the coordinate and feedback transformation, but the nature of the system stability at these equilibria is altered. Linearization of the dynamics about the steady glides for the laboratory scale glider ROGUE in [50] shows that the steady gliding equilibria that were unstable before the feedback (2.33)-(2.34) may be rendered stable for the feedback controlled system by simply choosing an appropriate equilibrium (r_{P1}, r_{P3}). As in [6, 5] there is a one-parameter family of internal mass positions (r_{P1}, r_{P3}) corresponding to a desired, permissible steady gliding speed and flight path angle, and as before this family may be parameterized by a bottom-heaviness parameter r_{bh}, which describes the component of (r_{P1}, r_{P3}) in the direction of gravity. Thus, we can always choose (r_{P1}, r_{P3}) for a desired equilibrium such that r_{bh} is large enough (i.e., the vehicle is sufficiently bottom-heavy) for the equilibrium of the feedback controlled system to be stable. We choose

$$\boldsymbol{w} = K\left(\boldsymbol{\zeta} - \boldsymbol{\zeta_e}\right), \tag{2.37}$$

where K is a control gain matrix such that all eigenvalues of the matrix $A + BK$ have negative real parts. Now, the Jacobian matrix of (2.35)-(2.37) has the following upper block-triangular form:

$$\begin{bmatrix} \left(\frac{\partial \boldsymbol{q}_r}{\partial \boldsymbol{\eta}_r}\right)_e & \left(\frac{\partial \boldsymbol{q}_r}{\partial \boldsymbol{\zeta}}\right)_e \\ 0 & A + BK \end{bmatrix}.$$

The set eigenvalues of the above Jacobian matrix are the union of eigenvalues of $A+BK$ and the eigenvalues of $\left(\frac{\partial \boldsymbol{q}_r}{\partial \boldsymbol{\eta}_r}\right)_e$. Thus, if all eigenvalues of $\left(\frac{\partial \boldsymbol{q}_r}{\partial \boldsymbol{\eta}_r}\right)_e$ have negative real parts (which will be true for a sufficiently bottom-heavy glider, as illustrated in an example discussed below), the gliding equilibrium will be linearly stable. This condition further implies that the same equilibrium for the underwater glider with (r_{P1}, r_{P3}) and m_0 set to their equilibrium values is also stable since the dynamics of $\boldsymbol{\eta}_r$ (equation (2.35)) does not influence $\boldsymbol{\zeta}$ (equation (2.36)). This conclusion is consistent with experimental observations of stable, gliding motions observed for ROGUE and other underwater gliders with fixed internal mass position and constant buoyancy.

To illustrate the effect of bottom-heaviness on the stability of straight gliding motions we plot the dependence of eigenvalues of $\left(\frac{\partial \boldsymbol{q}_r}{\partial \boldsymbol{\eta}_r}\right)_e$ on r_{bh}. We consider the equilibrium corresponding to steady gliding with a flight path angle of -45^o and speed 0.3 m/s with the same vehicle parameters as those considered in [6, 5]. Figure 2.7 shows the variation of eigenvalues of $\left(\frac{\partial \boldsymbol{q}_r}{\partial \boldsymbol{\eta}_r}\right)_e$ with respect to r_{bh}. The real part of one of the eigenvalues becomes positive when r_{bh} is approximately -0.0068 m. Thus the internal point mass $\bar{m}$ needs to be sufficiently low so that the vehicle is sufficiently bottom-heavy to ensure the stability of the steady gliding motion. We note that to the left of point A there is a pair of complex conjugate eigenvalues and two real eigenvalues. The latter come together at point A and go apart at point B. Points A and B correspond break in and break away points respectively of a root locus plot of the system with r_{bh} interpreted as the adjustable control gain.

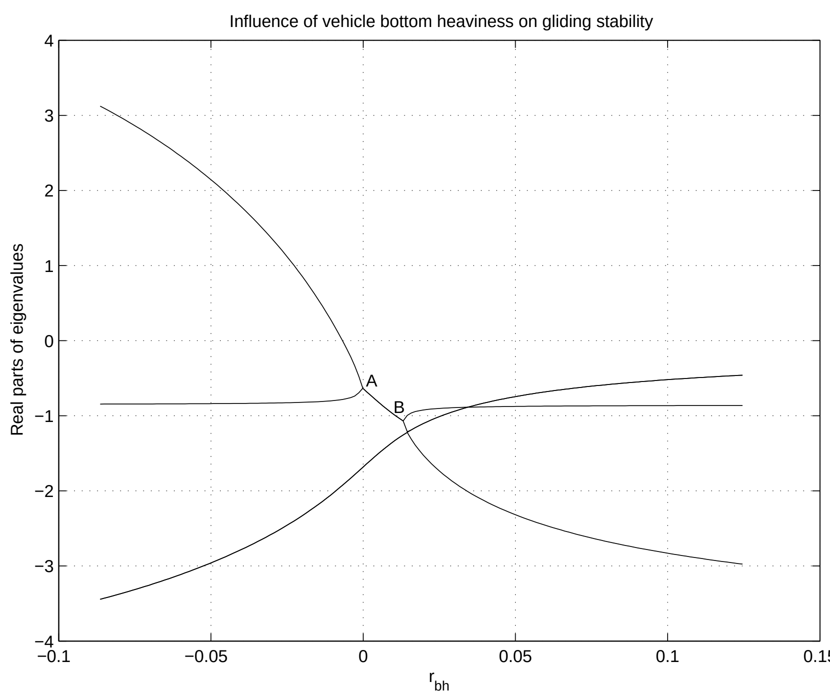

Figure 2.7: Dependence of stability of longitudinal plane steady glides on vehicle bottom-heaviness

Simulations of the closed-loop system (2.35)-(2.37) suggest a very large region of attraction. This is illustrated by a switch from a downward 45^o glide to an upward

45^o glide for the ROGUE, as shown in Figure 2.8. In this simulation we have chosen the matrix K to be a diagonal matrix with the following diagonal vector: 1exp(2).[1 3 1 3 0.5]. The simulation is started with the underwater glider moving along a -45^o steady glide. At $t = 5$ s the glider is commanded to switch to a $+45^o$ steady glide.

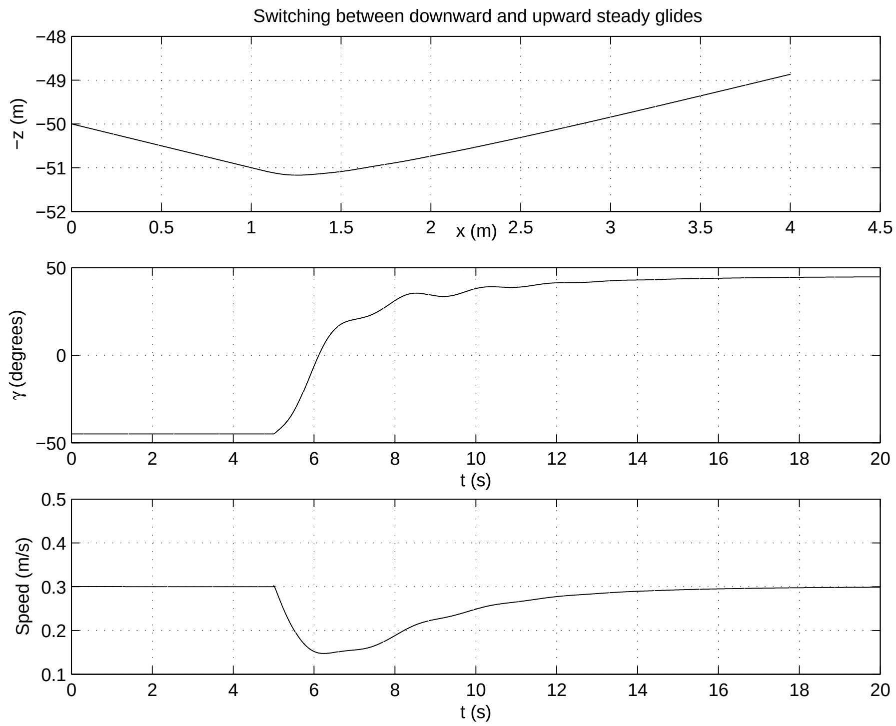

Figure 2.8: Switching between downward and upward steady glides

2.4 Nonlinear Control of Underwater and Aerospace Vehicles

Several nonlinear systems tools have been brought to bear in the last couple of decades for aircraft control problems. Methods applied to aircraft control include feedback linearization [51, 52, 53, 54, 55], backstepping [56, 57] and passivity [58] based techniques. These tools have been applied to the design of nonlinear control laws for simple models that incorporate salient features of aircraft dynamics and, in some instances, to models that incorporate elaborate, empirically determined dependence of external forces and moments on aircraft velocity and orientation. Examples of simple models that have been extensively studied are the Conventional Take-Off and Landing (CTOL) model considered in [36] and the Vertical Take-Off and Landing (VTOL) model considered in [59].

The nature of aerodynamic forcing makes the application of nonlinear systems tools challenging. The problem is complex due to the strong coupling between force and moment generation mechanisms inherent in aerodynamic control using external moving surfaces. For instance, in order to increase the angle of attack a pitch-up moment needs to be created. This is achieved by generating an appropriate force on the control surface. If an aft control surface (such as an elevator on the aft tail) is used, a negative lift generation is necessary to produce a pitch-up moment. Such a coupling between moment and force generation is responsible for the longitudinal dynamics being non-minimum phase in the problem of flight trajectory tracking. One way to work around this problem is to simply neglect the coupling terms in designing the control law by inversion of dynamics. This method was considered in [51] and good performance was demonstrated for the full system. Another approach is to make use of method for stable inversion of dynamics [60, 61, 62]. Input and state trajectories that achieve a desired output trajectory are calculated. These inputs are fedforward in conjunction with a feedback control law that locally stabilizes the inverse state trajectory. Alternative methods achieve approximate tracking by neglecting the coupling between moment and force generation [63, 64]. Some of these methods are applied to the CTOL aircraft model in [36].

Our approach in this thesis is based on designing control laws that beneficially use the natural dynamics of the system. The control actions are sometimes chosen deliberately to mimic the effects of hydrodynamic forces and moments so that we can design hydrodynamic effects to our advantage. For example, in Chapter 6 we use torque control proportional to the underwater glider angle of attack so that we can design a closed-loop pitching moment coefficient. The motivation is to design control laws that demand minimal on board energy. Our approach allows us to use theoretical results about stability of the uncontrolled system for designing control laws to achieve desired closed-loop motions.

Chapter 3

Underwater Glider Operations

The Autonomous Ocean Sampling Network II (AOSN-II) [3] sea trials performed in Monterey Bay during July-August, 2003 provided a demonstration of underwater gliders cooperatively collecting data from the ocean. During AOSN-II underwater gliders travelled along nominal steady gliding paths between waypoints in the ocean. We give a brief description of the AOSN-II project in §3.1. We present a summary of results from two control demonstrations in §3.2. These results were presented in [65, 32]. In §3.3 we discuss problems and scenarios where underwater glider dynamics and control become important for either performing or optimizing ocean sampling tasks. The AOSN-II and its successor projects, such as the Adaptive Sampling and Prediction (ASAP) project [4], provide strong motivation for the study of underwater glider dynamics and control design. Energy efficient control laws will further enhance underwater glider capabilities, useful for adaptive ocean sampling and other applications.

3.1 Autonomous Ocean Sampling Network-II

The Autonomous Ocean Sampling Network [3] research initiative aims to develop a sustainable, integrated observation-modeling system for the oceans. It constitutes a major effort towards improving the state of the art in sustainable, ocean state prediction technology. The initiative promotes research and development in several disciplines ranging from marine ecology to underwater glider dynamics and control. Important foci are in (a) developing components of a mostly autonomous adaptive sampling infrastructure, (b) designing adaptive sampling methods that are intended to provide optimal data to ocean models so that the models can accurately predict interesting scientific phenomena in the ocean and (c) improving understanding of ocean science through data collected by various platforms.

The sea trials conducted in Monterey Bay during July-August 2003, called AOSN-II, demonstrated the feasibility of an integrated system. During AOSN-II sampling patterns of various mobile observational assets such as ships, airplanes, propeller driven autonomous underwater vehicles (for example, the REMUS [66] and the Dorado [67]) and underwater gliders (Slocum [14] and Spray [15]) were planned and, in some cases, adapted using predictions from independently running ocean models. The ocean models used in AOSN-II were the Harvard Ocean Prediction System [68], the Regional Ocean Modeling System [69] and the Innovative Coastal-Ocean Observing Network model [70]. These models were in turn supplied with data coming from mobile assets, as well as other sources such as CODAR (COntinental raDAR) data, satellites, fixed moorings and surface drifters. Further details about the operational scenario during AOSN-II can be found in [1, 71, 65].

Underwater gliders collected a vast amount of data during the AOSN-II experiment. The Spray gliders operated tens of kilometers away from the shore while Slocum gliders collected data closer to the shore. For most part of the experiment both types of gliders traversed along preplanned sampling paths. These sampling paths were 80-100 km long lines perpendicular to the shore for the Spray gliders whereas for the Slocum gliders they were closed polygons that were formed by connecting predetermined waypoints by straight lines.

Figure 3.1 shows a schematic of different levels of control implementation in a typical multi-glider operation such as AOSN-II. The gliders have on-board "low-level" control implementation that regulate their motion in accordance with commands supplied by a "high-level" control module. The low-level control is typically designed to yield a finite set of "behaviors". Example behaviors include station keeping and waypoint tracking. More advanced behaviors could include trajectory tracking or maneuver regulation. In the AOSN-II demonstrations described in §3.2 the high-level control was in the form of waypoint specification. The waypoint lists were determined centrally for all gliders based on data from navigational sensors of gliders, as well as environmental data (such as temperature, salinity, flow fields, etc.) from all observation platforms and forecast from ocean models. The on-board low-level control ensured that the gliders travelled to the specified waypoints.

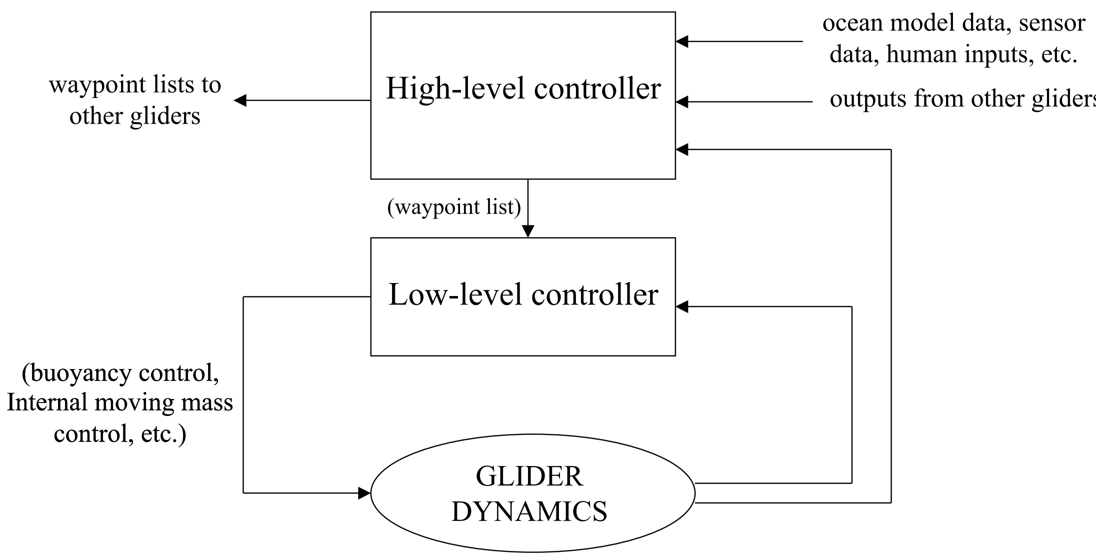

Figure 3.1: Glider Control Architecture in a Multi-Vehicle Fleet.

In AOSN-II the Slocum underwater gliders, operated by David Fratantoni of Woods Hole Oceanographic Institution, were used to demonstrate multi-vehicle formation control and real time particle (drifter) tracking capabilities. We present a summary of results from these demonstrations in the following section. Further details regarding implementation of high level control algorithms on Slocums during AOSN-II, including a discussion of communication and navigation constraints can be found in [72, 65].

3.2 High-Level Control Demonstrations

Underwater gliders make extremely useful mobile observation platforms for oceanographic sampling. Their utility is further enhanced when they collect data cooperatively. Cooperation amongst underwater gliders and between other sensor platforms and gliders yield many valuable adaptive sampling strategies. For instance a cooperative group of vehicles can measure and climb gradients in fields of scalar variables such as temperature or chlorophyll concentration more efficiently than a group of independently operating vehicles [73, 74]. An adaptable formation of vehicles makes it possible to gather data about oceanographic process occurring at various spatial and temporal scales [75].

3.2.1 AOSN-II Formation Control Demonstration

During AOSN-II formation control strategies were designed based on the method of Virtual Bodies and Artificial Potentials (VBAP). The VBAP method is developed in [76, 77, 73] and adapted to operational constraints of the AOSN-II Slocum underwater gliders in [72]. The central theme of the VBAP methodology involves inducing cooperation in a group of vehicles through forces derived from artificial potential energy functions. Artificial potentials are introduced between vehicles as well as between vehicles and moving reference points called *virtual leaders*. The forces induced by artificial potentials are similar to those due to a nonlinear spring. They vanish when the two interacting agents are a certain (desired) distance apart. The force is attractive if the agents are farther and repulsive if they are closer than the desired distance.

A desired formation motion can be obtained by choosing appropriate potential functions and virtual leaders, and group mission objectives can be realized by directing the motion of virtual leaders appropriately. For instance a group of three vehicles can be controlled to move in an equilateral triangle formation with the centroid of the group climbing the temperature gradient in a plane, calculated using temperature measurements from the vehicles. Convergence of the group to the desired formation is independent of the collective mission objective of the group. The stability of a formation may be proved using Lyapunov functions constructed from artificial potentials employed to achieve the formation [76, 73].

During AOSN-II, in a demonstration conducted on August 16, 2003, a group of three vehicles was controlled to move in an equilateral triangle formation with its centroid required to follow a predetermined path. The desired triangle side length was changed from 6 km to 3 km in the middle of the demonstration. Figures 3.2 and 3.3 show the path followed by the vehicle group and the average distance between vehicles during the course of the demonstration respectively. The performance of the group was good especially in light of strong, unknown currents present during the demonstration. Further analysis of the results of the demonstration is given in [65, 74, 32].

3.2.2 Real-time Drifter Tracking Demonstration

A demonstration of a Slocum underwater glider tracking a surface drifter was performed during AOSN-II on August 23, 2003. A surface drifter moves approximately according to the ocean flow. Ocean flow transports water bodies containing interesting biology, which can be followed by drifters. Drifters are also often used to track major ocean currents or oil, and other pollutant spills in the ocean.

During this demonstration the surface drifter transmitted its position every 30

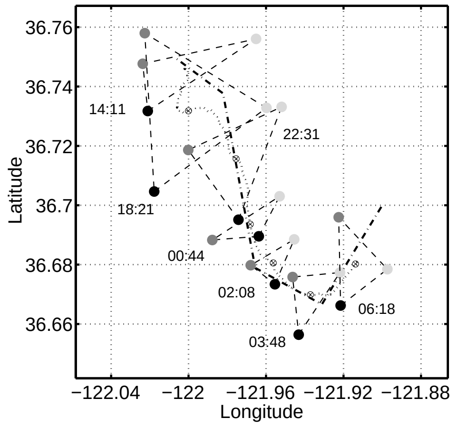

Figure 3.2: Triangle formation snapshots at various UTC times on August 16, 2003. Dotted line is the path of formation centroid; Piecewise linear dash-dotted line is the desired virtual leader path [65, 74, 32].

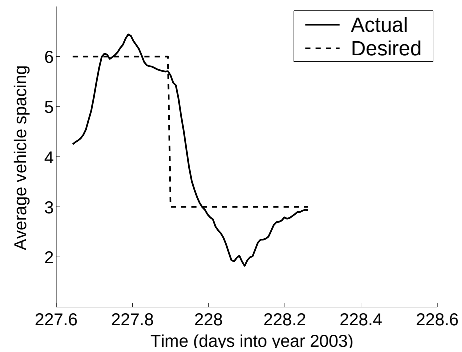

Figure 3.3: Actual average of the three inter-vehicle distances and the desired inter-vehicle spacing as a function of time during the August 16, 2003 formation control demonstration [65, 74, 32].

minutes. This data arrived at the central planning station with a time lag of 15 minutes. In order to follow the drifter in real time it was necessary to predict the future trajectory of the drifter. More details regarding the prediction scheme used and time delays inherent in the control implementation are described in [65, 32].

The goal of the demonstration was to have a Slocum glider travel back and forth along a chord of a circle, of a certain specified radius, with respect to the drifter as described in Figure 3.4. The actual tracks followed by the drifter and the underwater glider are shown in Figure 3.5.

The underwater glider approximately followed the drifter during the demonstration. Various factors, including limited sensitivity of drifter position measurements and uncertainty in ocean currents, contributed to errors in drifter tracking. The performance of tracking may be vastly improved if the underwater glider is allowed to track the drifter with a small time delay such that the glider crisscrosses the actual path traced by the drifter, instead of tracking a predicted drifter path in real time.

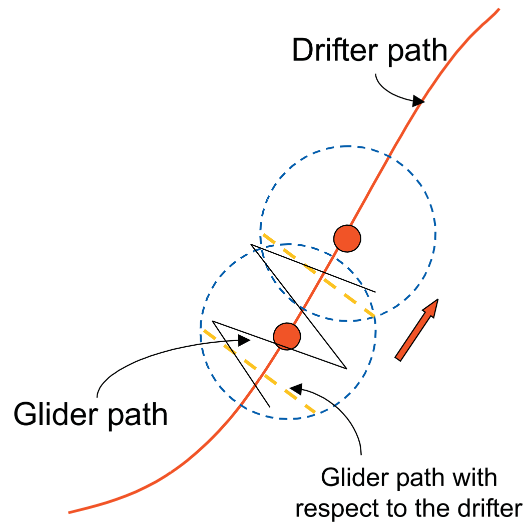

Figure 3.4: Drifter tracking demonstration plan: The solid circles indicate drifter positions at two time instants, and the line connecting the solid circles is the drifter path. The solid line crossing the drifter path is the desired glider path. The glider path relative to the drifter is a chord (dashed lines) of a circle (dashed circles) of specified radius about the drifter [65, 32].

3.2.3 Synoptic Area Coverage

A focus of the Adaptive Sampling And Prediction (ASAP) [4] project is the design of coordinated glider control algorithms for groups of underwater gliders operating in a specified region of the ocean such that the gliders collect optimal data of certain ocean processes, specified by their spatial and temporal scales, for input to ocean models. The goal is to cover as large an area of the ocean and as broad a spectrum of spatial and temporal frequencies of ocean process as possible with a given group of underwater gliders. A methodology for this purpose, developed in [78, 79, 80], relies on a sampling metric based on Objective Analysis [81, 82], a linear data assimilating scheme. A summary of developments toward designing mobile sensor networks that optimize the sampling metric is provided in [75]. Demonstrations of the application of synoptic area coverage sampling methods on underwater glider groups in the ASAP project are scheduled to take place in Monterey Bay in August 2006.

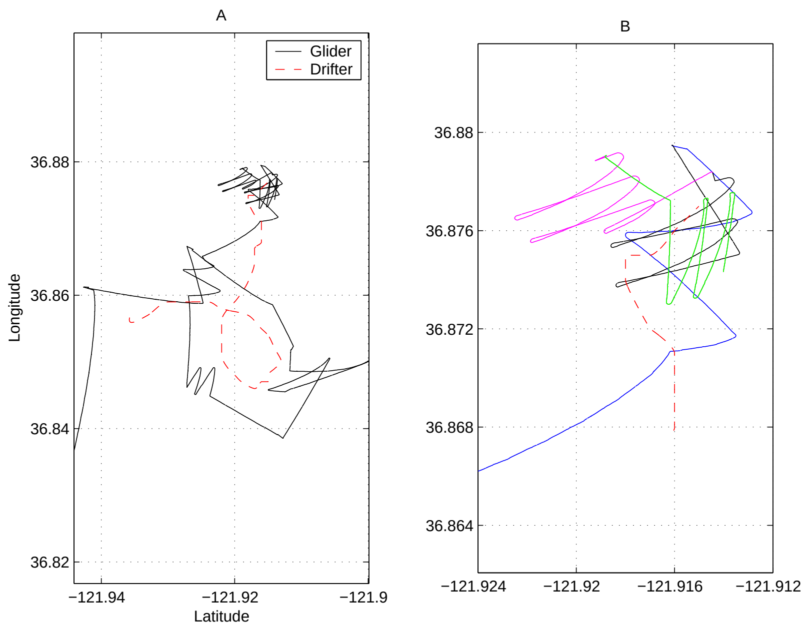

Figure 3.5: Tracks followed by the Slocum glider and the drifter during the AOSN-II drifter tracking demonstration. (A) The complete experiment (B) The last four glider dive cycles - the dashed line is the drifter track and the solid line is the glider track [65, 32].

3.3 Low-Level Underwater Glider Control

AOSN-II and ASAP projects demonstrate strong potential for extensive application of underwater gliders for ocean sampling tasks. Underwater glider operation in these projects rely on inherent stability of steady gliding motions. Active low-level control laws employed are fairly simple at the moment. They are limited to bang-bang control or proportional-derivative control of buoyancy, center of gravity position and vehicle heading. These control laws are adequate for current operations but more advanced techniques that pay attention to the nonlinear underwater glider dynamics will increase the variety of tasks that the vehicles can accomplish. Some applications where control laws and strategies designed using nonlinear systems analysis may be important are discussed below:

1. Applications involving underwater gliders collecting data related to processes

with very small spatial scales require careful attention to vehicle dynamics. We may consider a group of tiny underwater gliders whose longest length dimension may be a few inches. Such vehicles equipped with sensors could locate interesting features cooperatively in small domains. For such tasks, collision avoidance methods based on vehicle dynamics are important.

2. Study of underwater glider dynamics allows us to compute optimal gliding motions for a given glider design as well as to compute optimal designs for given mission and vehicle size requirements. A discussion regarding optimal motions and optimal glider design can be found in [9] and in Chapter 7 of [5].

3. Analysis of nonlinear dynamics throws light on certain nontrivial motions that may be efficiently accomplished by underwater gliders. Some desirable maneuvers may be small perturbations of natural vehicle trajectories. Such maneuvers may be stably realized with minimal control by utilizing inherent vehicle dynamics.

4. We can classify different steady motions of a glider. Unstable steady motions that cannot be observed in laboratory tests can be identified and stabilized using active control. We may combine different stable or stabilizable steady motions to yield useful maneuvers. For instance we may use a steady circular helical motion, studied in Chapter 8, to switch between (invariant) vertical planes of steady straight-line glides.

5. Tracking of desired trajectories may be accomplished in an energy efficient and stable manner using nonlinear control laws. Trajectory tracking methods using steady gliding motions are discussed in Chapter 7.

6. Since underwater gliders have limited control authority their motion is significantly influenced by ocean currents. Controlled current compensation by

adjusting underwater glider trajectories may improve sampling accuracy.

The remainder of this thesis addresses several issues pertaining to underwater glider dynamics and control that may be directly or indirectly useful in the context of the above mentioned, motivating applications. The stability analysis and control methodologies discussed in this thesis are presented mostly with respect to underwater glider models, but are also applicable to other vehicles moving through a fluid.

Chapter 4

Hamiltonian Description of Phugoid-Mode Dynamics

In this chapter we formulate underwater glider dynamics in a modern geometric framework of mechanics [22]. We focus on how the hydrodynamic lift plays an important role in determining the motion of the underwater glider by studying the phugoid-mode dynamics. The phugoid-mode equations we consider are energy conserving, which suggests a Hamiltonian formulation. We present several Hamiltonian formulations, including one using 2-dimensional canonical Hamilton's equations. For the latter formulation the Hamiltonian function of the system is not the energy of the underwater glider, but a scalar multiple of Lanchester's second conserved quantity [34, 33], commonly used to parameterize different classes of motion corresponding to phugoid-mode dynamics. This Hamiltonian function is used in Chapter 5 to derive the Lyapunov function candidate for proving the stability of longitudinal dynamics of the underwater glider. The other Hamiltonian formulations are derived by comparing phugoid-mode dynamics with the equations of motion of a charged particle in a magnetic field, and using the notion of the vector potential [83, 22]. We also investigate connections between the phugoid-mode dynamics and two (equivalent) conservative, planar systems that may be interpreted as Hamiltonian systems: the simple pendulum and the thin elastic rod. The results of this chapter motivate further investigation of glider dynamics in a geometric framework. The results presented in this chapter and future work on the analysis of underwater glider dynamics in a geometric framework are motivated by the potential of emerging tools such as [23, 24] for the development of low-energy nonlinear control solutions.

For our analysis in this chapter we consider an energy-conserving model of underwater glider dynamics. The underwater glider model of Chapter 2 considers a number of factors including added mass effects, internal moving mass dynamic coupling and viscous external forces and moments. In this chapter we consider dynamics in the longitudinal plane and ignore contributions from added mass and internal moving mass. We also do not include the nonconservative drag force and the nonconservative pitching moment. The above simplifications yield a model, which is at the core of underwater glider dynamics. This model is equivalent to Lanchester's phugoid-mode model [34] for aircraft longitudinal dynamics after a time scaling [5]. Although the model considered in this chapter only approximates underwater glider longitudinal dynamics, it serves the purpose of focusing on the effect of an important dynamical structure caused by the lift force component. The energy conserving lift force component always acts perpendicular to the direction of velocity and is responsible for a nontrivial geometric structure for underwater glider dynamics.

In §4.1 we present the phugoid-mode model for an underwater glider and show how the equations describing the model can be written as Hamilton's equations. For comparison, we present Hamiltonian equations of motion for three other dynamic systems in §4.2: a charged particle moving in a magnetic field, a simple pendulum and a thin elastic rod (the elastica). Connections between these systems and the phugoid-mode model are established in §4.3. Lagrangian and canonical Hamiltonian formulations for the phugoid-mode model are also presented.

4.1 Phugoid-Mode Model

The phugoid-mode model for an underwater glider is derived following Lanchester [34, 33] by restricting the motion of the glider to the longitudinal plane and making the following assumptions or simplifications:

1. A large moment of inertia pitching coefficient (K_M) coupled with a small moment of inertia about the pitching axis (J_2) enables the angle of attack to quickly converge to a constant value.

2. The effect of hydrodynamic drag is not considered.

3. Added masses along the body 1 and body 3 axes are considered to be equal. This implies that $m_1 = m_3$, which corresponds to a spherically-shaped underwater glider.

4. The internal movable mass is fixed at the center of buoyancy, i.e., $\boldsymbol{r}_P = 0$.

In Chapter 5 we use singular perturbation theory to rigorously show under what conditions simplification 1 is indeed justified. Drag is excluded in our present analysis in order to make the underwater glider model conservative. Including drag annihilates some natural classes of motion of the phugoid-mode model. Drag is included in subsequent analyses of glider dynamics in later chapters, and its significance described. Assumptions 3 and 4 are not necessary for energy conservation but are required for the Hamiltonian formulations presented in this chapter. The Hamiltonian function used in the formulation presented in §4.1 is used in §5.2 to construct a Lyapunov function to prove exponential stability of gliding motions in the presence of drag.

Applying the above assumptions in the equations of motion (2.15)-(2.25) presented in §2.3, and using inertial velocity coordinates $(\dot{x}, \dot{z})$ instead of body velocities (v_1, v_3), we get the following equations of motion for the phugoid-mode model of an underwater glider:

$$\frac{dx}{dt} = \dot{x} \tag{4.1}$$

$$\frac{dz}{dt} = \dot{z} \tag{4.2}$$

$$\frac{d\dot{x}}{dt} = \frac{K}{m_1 + \bar{m}}(\dot{x}^2 + \dot{z}^2)^{\frac{1}{2}}\dot{z} \tag{4.3}$$

$$\frac{d\dot{z}}{dt} = \frac{1}{m_1 + \bar{m}}\left(m_0 g - K(\dot{x}^2 + \dot{z}^2)^{\frac{1}{2}}\dot{x}\right), \tag{4.4}$$

where K is a constant lift coefficient, equal to $K_{L0} + K_L\alpha$. The definitions of masses m and $\bar{m}$ are the same as those in §2.2.2. Equations (4.1)-(4.4) are identical in structure to the phugoid-mode dynamical equations of an aircraft. The aircraft phugoid-mode equations may be derived from the above equations by replacing both m_0 and $m_1 + \bar{m}$ by the mass of the aircraft.

Equations (4.1)-(4.4) represent a conservative system. The total energy of the underwater glider in the phugoid-mode model, $E = \frac{1}{2}(m_1 + \bar{m})(\dot{x}^2 + \dot{z}^2) - m_0 g z$, remains constant.

The phugoid-mode dynamics are invariant with respect to the position of the underwater glider, i.e., we have full $\mathbb{R}^2$ symmetry. This implies that we only need to consider a reduced system consisting of equations for $\dot{x}$ and $\dot{z}$, i.e., equations (4.3)-(4.4). The solutions $x(t)$ and $z(t)$ can be reconstructed by integration of $\dot{x}$ and $\dot{z}$. The relative equilibria of phugoid-mode dynamics are solutions of equations (4.1)-(4.4) with constant velocity, i.e., $\dot{x}(t) = \dot{x}_e$, $\dot{z}(t) = \dot{z}_e$. We have one such relative equilibrium solution,

$$\begin{aligned} \dot{x}_e &= \sqrt{\frac{m_0 g}{K}} \\ \dot{z}_e &= 0. \end{aligned}$$

The above relative equilibrium corresponds to a steady, horizontal motion of the underwater glider. We note that the steady horizontal motion is not a feasible solution for a real underwater glider but is present in this model as a consequence of the absence of drag.

Lanchester [34, 33] showed that the phugoid-mode model has a second conserved quantity C, in addition to energy:

$$C = \frac{\dot{x}}{|\dot{x}_e|} - \frac{1}{3}\left(\frac{\dot{x}^2 + \dot{z}^2}{\dot{x}_e^2}\right)^{3/2} \tag{4.5}$$

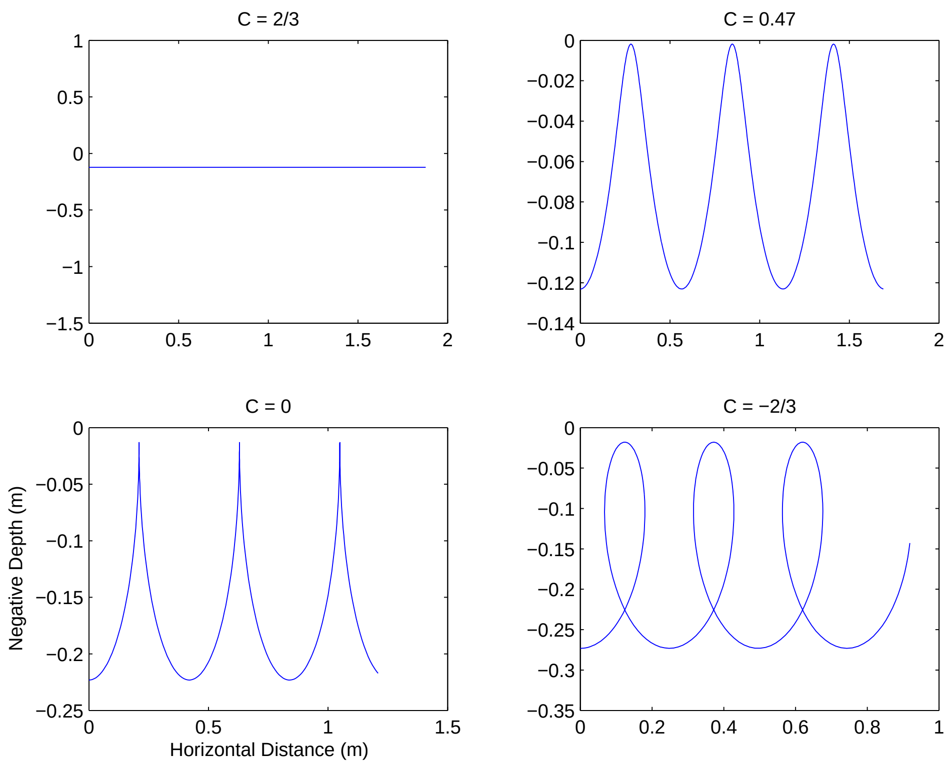

Figure 4.1: Phugoid-mode trajectories

Thus, the phugoid-mode model is integrable, and the quantity C parameterizes the trajectories of the model as shown by Lanchester [34, 33]. Figure 4.1 shows simulations run for 6 s for the four different classes of trajectories of a phugoid-mode model with the following parameters: $m_1 + \bar{m} = 14$ kg, $m_0 = 1$ kg and $K = 100$ kg/m.

$C = 2/3$ corresponds to the relative equilibrium motion (steady level flight path). Values of C between 0 and 2/3 yield wavy trajectories. This is the most common phugoid mode observed in commercial aircraft. Negative values of C correspond to trajectories with loops. This mode may be observed in the flight of a paper airplane. Figures 1.3-2a and 1.3-2b of reference [42] show simulations illustrating the above modes in the longitudinal motions of a paper airplane. For values of C near 0, we get trajectories with a sharp cusp. $C = 0$ corresponds to a singular trajectory, a single flight with the flight path angle varying between - 90^o and $+90^o$ over an infinite time interval. We note that C may be set by picking an appropriate initial velocity for the underwater glider.

The reduced phugoid-mode dynamics, i.e., equations (4.3)-(4.4) may be written as Hamilton's equations if we interpret the generalized coordinate to be $q = \dot{x}$ and the momentum to be $p = \dot{z}$, as noted in [84]. Interestingly, a similar Hamiltonian formulation appears in the case of point-vortex models [85]. Consider the Hamiltonian function $H = -\frac{m_0 g}{m_1+\bar{m}}|\dot{x}_e|C$, i.e.,

$$\begin{aligned} H &= \frac{-m_0 g}{m_1+\bar{m}}|\dot{x}_e|C \\ &= \frac{-m_0 g}{m_1+\bar{m}}|\dot{x}_e|\left(\frac{\dot{x}}{|\dot{x}_e|} - \frac{1}{3}\left(\frac{\dot{x}^2+\dot{z}^2}{\dot{x}_e^2}\right)^{\frac{3}{2}}\right) \\ &= \frac{K}{3(m_1+\bar{m})}(\dot{x}^2+\dot{z}^2)^{\frac{3}{2}} - \frac{m_0 g}{m_1+\bar{m}}\dot{x}. \end{aligned} \tag{4.6}$$

In deriving the last equality of equation (4.6) we have used the relation $m_0 g = K\dot{x}_e^2$. Using H, equations (4.3)-(4.4) can be rewritten as Hamilton's equations:

$$\frac{d\dot{x}}{dt} = \frac{\partial H}{\partial \dot{z}} \tag{4.7}$$

$$\frac{d\dot{z}}{dt} = -\frac{\partial H}{\partial \dot{x}}. \tag{4.8}$$

4.2 Three Related Systems: Charged Particle, Pendulum, and Elastic Rod

In the Hamiltonian system given by equations (4.7)-(4.8) both state variables are velocities. Thus, it is not clear how to interpret the geometric structure of the system. The system is Hamiltonian on the cotangent bundle (a symplectic manifold) $T^*\mathbb{R}$ with the Hamiltonian function H given by equation (4.6), but there is ambiguity in choosing between $\dot{x}$ or $\dot{z}$ for the base and fiber variables.[1] However, the Hamiltonian function H leads us to a Lyapunov function candidate for proving the stability of the equilibrium of longitudinal dynamics of the underwater glider in Chapter 5. A complete understanding of the geometric structure of the phugoid-mode model may provide us with better insight for dynamical system analysis and control design, and facilitate application of tools such as [23, 24] to the underwater glider system. With this motivation we study comparisons between the phugoid-mode system and three conservative, planar systems whose Hamiltonian structures are well understood. The latter systems are described in this section and the comparisons are discussed in §4.3.

4.2.1 Charged Particle in a Magnetic Field

Consider a particle of mass m carrying a charge q moving in a magnetic field $\boldsymbol{B} = (B_x, B_y, B_z)^T$, as shown in Figure 4.2. Let $\boldsymbol{r} = (x, y, z)^T$ be the position of the particle, with z increasing in the direction of gravity. Let $\boldsymbol{V} = (V_x, V_y, V_z)^T$ be its velocity with respect to a laboratory-fixed frame of reference. The dynamics of the charged

[1] See Appendix B for a brief introduction to Hamiltonian systems and the associated geometry, including the definition of a symplectic manifold. Appendix A provides the definition of a cotangent bundle such as $T^*\mathbb{R}$. The cotangent bundle is essentially a phase space associated to any configuration manifold. If a configuration manifold Q has coordinates $(q_1, q_2, \ldots, q_n)$, the cotangent manifold has coordinates $(q_1, q_2, \ldots, q_n, p_1, p_2, \ldots, p_n)$, where $(p_1, p_2, \ldots, p_n)$ belongs to the dual space of the tangent space at $(q_1, q_2, \ldots, q_n)$.

particle, governed by the Lorentz law, are described by the following equations:

$$\frac{d\boldsymbol{r}}{dt} = \boldsymbol{V} \tag{4.9}$$

$$\frac{d\boldsymbol{V}}{dt} = \frac{q}{m}\boldsymbol{B} \times \boldsymbol{V}. \tag{4.10}$$

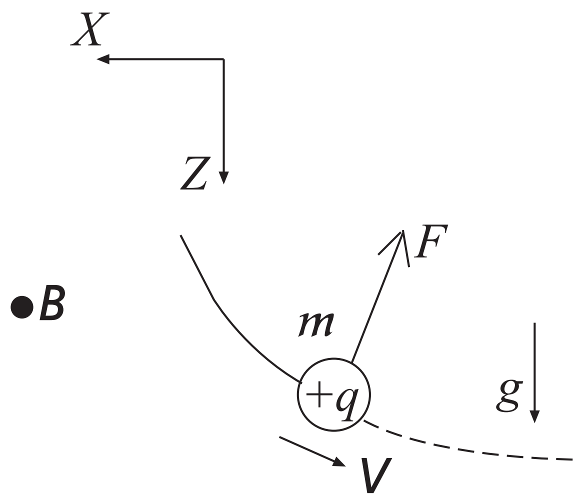

Figure 4.2: Schematic of the motion of a charged particle in a magnetic field.

The above dynamics can be represented as a (noncanonical) Hamiltonian system on the cotangent bundle $T^*\mathbb{R}^3$, which is interpreted as a symplectic manifold endowed with the following symplectic 2-form [22]:

$$\Omega_B = m\,(dx \wedge dp_x + dy \wedge dp_y + dz \wedge dp_z) \tag{4.11}$$

$$- q(B_x dy \wedge dz + B_y dz \wedge dx + B_z dx \wedge dy), \tag{4.12}$$

where $(p_x, p_y, p_z)^T = \boldsymbol{p} = m\boldsymbol{V}$ is the momentum of the charged particle, and the symbol $\wedge$ denotes the wedge product[2]. In the matrix formulation, the symplectic

[2]The general definition of the wedge product of two 1-forms is given in Appendix A. As an example, if we represent the one forms dx by $a = [1\;0\;0\;0\;0\;0]$ and dp_x by $b = [0\;0\;0\;1\;0\;0]$, then the wedge product $dx \wedge dp_x$ may be represented as a 6×6 matrix $a^T b - b^T a$.

2-form Ω_B may be written as the skew-symmetric matrix

$$\Omega_B = \begin{bmatrix} 0 & -qB_z & qB_y & m & 0 & 0 \\ qB_z & 0 & -qB_x & 0 & m & 0 \\ -qB_y & qB_x & 0 & 0 & 0 & m \\ -m & 0 & 0 & 0 & 0 & 0 \\ 0 & -m & 0 & 0 & 0 & 0 \\ 0 & 0 & -m & 0 & 0 & 0 \end{bmatrix}. \tag{4.13}$$

Consider the Hamiltonian function H to be the sum of the kinetic and potential energies of the charged particle:

$$H = \frac{1}{2}m(\dot{x}^2 + \dot{y}^2 + \dot{z}^2) - mgz. \tag{4.14}$$

The Hamiltonian vector field $X_H = (X_{H_1}, X_{H_2}, X_{H_3}, X_{H_4}, X_{H_5}, X_{H_6})^T$ that governs the motion of the charged particle is implicitly defined using

$$dH = \boldsymbol{i}_{X_H}\Omega_B, \tag{4.15}$$

where $\boldsymbol{i}_{X_H}\Omega_B$ is the interior product of X_H and Ω_B. Using this definition we have, in matrix form,

$$\begin{aligned} \boldsymbol{i}_{X_H}\Omega_B &= X_H^T\Omega_B && (4.16) \\ &= \begin{bmatrix} q(B_zX_{H_2} - B_yX_{H_3}) - mX_{H_4} \\ q(B_xX_{H_3} - B_zX_{H_1}) - mX_{H_5} \\ q(B_yX_{H_1} - B_xX_{H_2}) - mX_{H_6} \\ mX_{H_1} \\ mX_{H_2} \\ mX_{H_3} \end{bmatrix}^T. && (4.17) \end{aligned}$$

We compute

$$dH = \begin{bmatrix} 0 & 0 & -mg & m\dot{x} & m\dot{y} & m\dot{z} \end{bmatrix}. \tag{4.18}$$

Now, we can readily check that equation (4.15) represents dynamics of the charged particle described by equations (4.9)-(4.10). Thus, the charged particle dynamics is Hamiltonian on the symplectic manifold $(T^*\mathbb{R}^3, \Omega_B)$, and can be derived using the with the Hamiltonian function H defined by equation (4.14).

4.2.2 Simple Pendulum

Consider a point mass m suspended by a massless rigid rod of length l, as in Figure 4.3. Let (x, y, z) describe the position of the mass in a laboratory-fixed reference frame. We consider the motion of the pendulum in the $x - z$ plane $(y = 0)$. The equations of motion are

$$\begin{aligned} \frac{dx}{dt} &= \dot{x} && (4.19)\\ \frac{dz}{dt} &= \dot{z} && (4.20)\\ \frac{d\dot{x}}{dt} &= -T\cos\theta && (4.21)\\ \frac{d\dot{z}}{dt} &= mg - T\sin\theta, && (4.22) \end{aligned}$$

where $T = (m/l)(\dot{x}^2 + \dot{z}^2) + mg\cos\theta$ is the tension in the rod and θ is the angle made by the rod with the z-axis of the reference frame. We have $\cos\theta = z/l$ and $\sin\theta = x/l$. Thus, due to the rigidity of the rod, we have the constraint equation: $x^2 + z^2 = l^2$. Due to this constraint, the simple pendulum dynamics can be completely described by the equation governing the evolution of θ:

$$ml\frac{d^2\theta}{dt^2} + mg\sin\theta = 0 \tag{4.23}$$

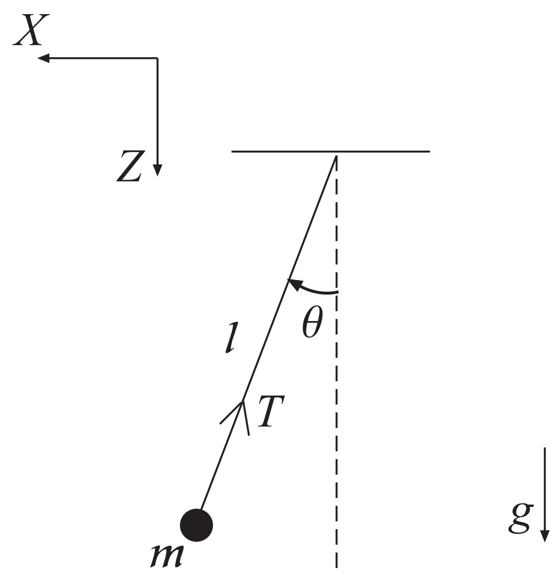

Figure 4.3: Planar Simple Pendulum

The above dynamics can be expressed as Hamilton's equations on the cotangent bundle $T^*\mathbb{R}$ endowed with the canonical symplectic structure, using the total energy

$$E = \frac{1}{2m} p_\theta^2 - mgl\cos\theta$$

as the Hamiltonian function, with θ as the configuration variable and the corresponding conjugate momentum $p_\theta = ml\dot{\theta}$. The Hamilton's equations are:

$$\frac{d\theta}{dt} = \frac{\partial H}{\partial p_\theta} = \frac{p_\theta}{m} \tag{4.24}$$

$$\frac{dp_\theta}{dt} = -\frac{\partial H}{\partial \theta} = -mgl\sin\theta, \tag{4.25}$$

equivalent to equation (4.23), describing the simple pendulum dynamics.

4.2.3 Elastic Rod

The problem of elastica [86] considers shapes of a thin rod under the action of forces and couples applied at its ends. The rod is assumed to be straight in the unstressed state. It is also assumed that the rod undergoes a planar deformation without any twist.

Let equal and opposite forces of magnitude R be applied at each end of the rod so that the total external force is zero. Figure 4.4 shows the forces and moment acting on a section of the rod. Let s represent the path length from one end of the rod and $\theta(s)$ be the angle made by the tangent to the center line with the line of action of R at the end from which s is measured. Let $T(s)$ and $N(s)$ respectively represent the tension and normal forces at the section taken at s. Let $M(s)$ be the bending moment.

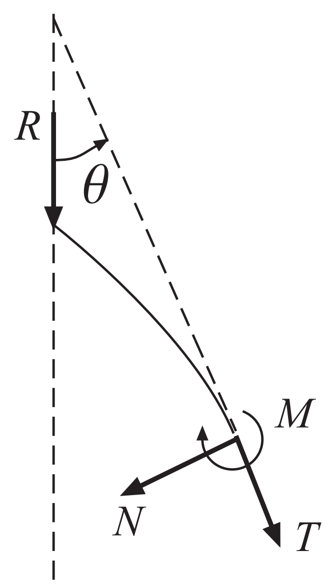

Figure 4.4: Forces acting on a section of the elastic rod. [86]

A linear constitutive relation between the bending moment and the curvature $\kappa(s) = \frac{d\theta(s)}{ds}$ of the rod is assumed:

$$M(s) = EAr_g^2\kappa(s), \tag{4.26}$$

where E is the Young's modulus for the material of the rod, A is the area of cross section (assumed to be uniform over s) and r_g is the radius of gyration of the cross-section about a principal axis in the plane of the cross-section.

The equations of equilibrium of the rod are

$$\begin{aligned} T &= -R\cos\theta && (4.27) \\ N &= -R\sin\theta && (4.28) \\ \frac{dM}{ds} + N &= 0. && (4.29) \end{aligned}$$

Kirchhoff [87] noticed that the governing equations of the shape of elastica are identical to the equations describing the motion of a simple pendulum. This can be readily seen by substituting the constitutive relation (4.26) in equation (4.29) to get equation (4.30) and comparing with pendulum dynamics described by equation (4.23).

$$EAr_g^2\frac{d^2\theta}{ds^2} + R\sin\theta = 0. \tag{4.30}$$

We note that the analogue of time evolution is the progression of distance in the problem of elastica. Thus, the various shapes of the elastic rod (presented in [86] for example) are similar to the shapes of θ-trajectories (plots of θ versus t) of the planar simple pendulum. The analogy between the elastic rod and the pendulum can be extended to the Hamiltonian structure; the equations of a thin elastic rod can also be described using canonical Hamilton's equations.

4.3 Alternative Representations of the Phugoid-Mode Model

In this section we study the similarities between the phugoid-mode model and the Hamiltonian systems presented in the previous section. This allows us to interpret the action of the lift force in the phugoid-mode model in terms of forces present in other Hamiltonian systems and also to derive alternative Hamiltonian formalisms.

4.3.1 A Noncanonical Hamiltonian Formulation

We note that a charged particle in a magnetic field experiences a force (Lorentz force) that always acts perpendicular to the particle's velocity, quite like the lift force on the underwater glider. The magnitude of the force is proportional to speed in both cases. In the case of the charged particle it is a linear dependence on speed, but the common hydrodynamic lift model calls for a quadratic dependence on speed. However, we can induce a quadratic dependence of the Lorentz force by considering a varying magnetic field, whose strength depends on the speed of the particle.

If we consider a magnetic field with $B_x = B_z = 0$ and with $B_y = -(K/q)\sqrt{\dot{x}^2 + \dot{z}^2}$, and if we restrict to planar motion of the charged particle (i.e., $\dot{y} = 0$), we recover the equations of motion of the phugoid mode for an underwater glider with $m_1 + \bar{m} = m$. This also implies that we can interpret the phugoid-mode dynamics as being Hamiltonian on the cotangent bundle $T^*\mathbb{R}^2$, endowed with the noncanonical symplectic form,

$$\begin{aligned} \Omega_B &= m\,(dx \wedge d\dot{x} + dz \wedge d\dot{z}) + K\sqrt{\dot{x}^2 + \dot{z}^2}\, dz \wedge dx \\ &\equiv \begin{bmatrix} 0 & K\sqrt{\dot{x}^2+\dot{z}^2} & m & 0 \\ -K\sqrt{\dot{x}^2+\dot{z}^2} & 0 & 0 & m \\ -m & 0 & 0 & 0 \\ 0 & -m & 0 & 0 \end{bmatrix}. \end{aligned} \tag{4.31}$$

The Hamiltonian function is the the total energy of the underwater glider

$$H = \frac{1}{2}(m_1 + \bar{m})(\dot{x}^2 + \dot{z}^2) - m_0 g z. \tag{4.32}$$

The Hamiltonian vector field $X_H = (X_{H_1}, X_{H_2}, X_{H_3}, X_{H_4})^T$ that represents the phugoid-mode dynamics is implicitly defined by

$$dH = \boldsymbol{i}_{X_H}\Omega_B. \tag{4.33}$$

We compute

$$\boldsymbol{i}_{X_H}\Omega_B = X_H^T\Omega_B = \begin{bmatrix} -K\sqrt{\dot{x}^2+\dot{z}^2} - mX_{H_3} \\ K\sqrt{\dot{x}^2+\dot{z}^2} - mX_{H_4} \\ mX_{H_1} \\ mX_{H_2} \end{bmatrix}^T, \tag{4.34}$$

$$dH = \begin{bmatrix} 0 & -m_0 g & m\dot{x} & m\dot{z} \end{bmatrix}. \tag{4.35}$$

Now, we can readily check that equation (4.33) represents the phugoid-mode dynamics described by equations (4.3)-(4.4). Thus, the phugoid-mode dynamics is Hamiltonian on the symplectic manifold $(T^*\mathbb{R}^2, \Omega_B)$, where Ω_B is a noncanonical symplectic form defined by equation (4.31), derived using the Hamiltonian function H given by equation (4.32).

4.3.2 A Lagrangian Formulation

Inspired by the similarity between the Lorentz force and the hydrodynamic lift, we describe a Lagrangian formulation for the phugoid-mode dynamics using the notion of the vector potential function used for describing the dynamics of a charged particle in a magnetic field [83, 22].

We consider a Lagrangian system on the tangent bundle $T\mathbb{R}^2$. The coordinates on $T\mathbb{R}^2$ are the position and velocity of the underwater glider: $(x, z, \dot{x}, \dot{z})$. The Euler-

Lagrange equations are

$$\frac{d}{dt}\left(\frac{\partial L}{\partial \dot{\boldsymbol{q}}}\right) = \frac{\partial L}{\partial \boldsymbol{q}}, \tag{4.36}$$

where,

$$\boldsymbol{q} \;=\; (x,z)^T, \quad \dot{\boldsymbol{q}} = (\dot{x},\dot{z})^T.$$

We take the Lagrangian function to be

$$L(\boldsymbol{q},\dot{\boldsymbol{q}}) = \frac{1}{2}\,(m_1+\bar{m})\|\dot{\boldsymbol{q}}\|^2 + K\boldsymbol{A}\cdot\dot{\boldsymbol{q}} + m_0 g z, \tag{4.37}$$

where,

$$\boldsymbol{A} \;=\; (A_1,A_2)^T = \left(\frac{-\,(2m_0gz)^{\frac{3}{2}}}{3m_0g\sqrt{m_1+\bar{m}}}, 0\right)^T.$$

We interpret $\boldsymbol{A}$ to be a vector potential as in [83, 22].

The conjugate momenta are

$$\begin{aligned}
\boldsymbol{p} \;=\; (p_1,p_2)^T \;&=\; \frac{\partial L}{\partial \dot{\boldsymbol{q}}} \qquad (4.38)\\
&=\; (m_1+\bar{m})\dot{\boldsymbol{q}} + K\boldsymbol{A}\\
&=\; \left((m_1+\bar{m})\dot{x} + \frac{-K\,(2m_0gz)^{\frac{3}{2}}}{3m_0g\sqrt{m_1+\bar{m}}}, (m_1+\bar{m})\dot{z}\right)^T.
\end{aligned}$$

We calculate,

$$\frac{d}{dt}\left(\frac{\partial L}{\partial \dot{x}}\right) \;=\; (m_1+\bar{m})\ddot{x} - K\left(\frac{2m_0gz}{m_1+\bar{m}}\right)^{\frac{1}{2}}\dot{z}, \quad \frac{\partial L}{\partial x} \;=\; 0 \tag{4.39}$$

$$\frac{d}{dt}\left(\frac{\partial L}{\partial \dot{z}}\right) \;=\; (m_1+\bar{m})\ddot{z}, \quad \frac{\partial L}{\partial z} \;=\; -K\left(\frac{2m_0gz}{m_1+\bar{m}}\right)^{\frac{1}{2}}\dot{x} + m_0 g. \tag{4.40}$$

The Euler-Lagrange equations (4.36) for L may be written as follows

$$(m_1 + \bar{m})\ddot{x} = K \left(\frac{2m_0 g z}{m_1 + \bar{m}} \right)^{\frac{1}{2}} \dot{z} \tag{4.41}$$

$$(m_1 + \bar{m})\ddot{z} = m_0 g - K \left(\frac{2m_0 g z}{m_1 + \bar{m}} \right)^{\frac{1}{2}} \dot{x}. \tag{4.42}$$

The total energy E for the above Lagrangian system is conserved, i.e.,

$$E = \frac{1}{2}(m_1 + \bar{m})(\dot{x}^2 + \dot{z}^2) - m_0 g z = \text{constant}. \tag{4.43}$$

For the zero-energy trajectory ($E = 0$) we have

$$\frac{2m_0 g z}{m_1 + \bar{m}} = \dot{x}^2 + \dot{z}^2.$$

Thus, the zero-energy trajectory of the above Lagrangian system (equations (4.41)-(4.42)) is identical to a trajectory of the phugoid-mode model (equations (4.1)-(4.4)). Furthermore, all trajectories of the above Lagrangian system can be mapped to a zero-energy trajectory by appropriate change of coordinates: $z \to z_n = z + E/(m_0 g)$. This change of coordinates does not affect the form of the Euler-Lagrange equations. Thus, there is a one-to-one correspondence between the trajectories of the Lagrangian system described by equations (4.41)-(4.42) and those of the phugoid-mode model described by equations (4.1)-(4.4).

4.3.3 A Canonical Hamiltonian Formulation

In this subsection we use the Legendre transform to derive a canonical Hamiltonian system from the Lagrangian system described in the previous subsection.

The Legendre transform maps $\dot{\boldsymbol{q}} \in T_{\boldsymbol{q}}\mathbb{R}^2$ to $\boldsymbol{p} \in T^*_{\boldsymbol{q}}\mathbb{R}^2$ according to equation (4.38), and the Lagrangian L defined on the tangent bundle $T\mathbb{R}^2$ to the Hamiltonian

H (equal to the total energy) defined on cotangent bundle $T^*\mathbb{R}^2$ according to

$$\begin{aligned} H(\boldsymbol{q},\boldsymbol{p}) &= \boldsymbol{p}\,.\,\dot{\boldsymbol{q}} - L(\boldsymbol{q},\dot{\boldsymbol{q}}) \\ &= \frac{1}{2}\,(m_1+\bar{m})\|\dot{\boldsymbol{q}}\|^2 - m_0 g z \\ &= \frac{1}{2(m_1+\bar{m})}\|\boldsymbol{p} - K\boldsymbol{A}\|^2 - m_0 g z. \end{aligned} \tag{4.44}$$

The zero-energy trajectory of the canonical Hamiltonian system on $T^*\mathbb{R}^2$ with the above Hamiltonian function is equivalent to a trajectory of the phugoid-mode model. To see that let us evaluate Hamilton's equations corresponding to the above Hamiltonian function with generalized coordinates $\boldsymbol{q}$ and the corresponding conjugate momenta $\boldsymbol{p}$. Hamilton's first equation,

$$\dot{\boldsymbol{q}} = \frac{\partial H}{\partial \boldsymbol{p}} = \frac{1}{m_1+\bar{m}}\,(\boldsymbol{p} - K\boldsymbol{A})\,, \tag{4.45}$$

is consistent with the definition of the conjugate momentum $\boldsymbol{p}$ given by equation (4.38). Hamilton's second equation is

$$\begin{aligned} \dot{\boldsymbol{p}} = -\frac{\partial H}{\partial \boldsymbol{q}} &= -\frac{1}{m_1+\bar{m}}\begin{bmatrix} \frac{\partial A_1}{\partial x} & \frac{\partial A_1}{\partial z} \\ \frac{\partial A_2}{\partial x} & \frac{\partial A_2}{\partial z} \end{bmatrix}^T (\boldsymbol{p} - K\boldsymbol{A}) + (0, m_0 g)^T \\ &= \left(0, -\frac{(2m_0 g z)^{\frac{1}{2}}}{\sqrt{m_1+\bar{m}}}(p_1 - KA_1)\right)^T + (0, m_0 g)^T\,. \end{aligned} \tag{4.46}$$

Using the definition of $\boldsymbol{p}$ (equation 4.38) we evaluate

$$\dot{p}_1 = (m_1+\bar{m})\,\ddot{x} - \frac{K(2m_0 g z)^{\frac{1}{2}}\dot{z}}{\sqrt{m_1+\bar{m}}} \tag{4.47}$$

$$\dot{p}_2 = (m_1+\bar{m})\,\ddot{z}. \tag{4.48}$$

Substituting the above expressions as well as the zero-energy condition ($E = \frac{1}{2}(m_1 + \bar{m})\,(\dot{x}^2 + \dot{z}^2) - m_0 g z = 0$) in equation (4.46), and solving for $\ddot{x}$ and $\ddot{z}$ we recover the phugoid-mode equations (4.3)-(4.4).

Furthermore, as in the previous subsection, we can induce a coordinate mapping to establish a one-to-one correspondence between the trajectories of the canonical Hamiltonian system of this section and those of the phugoid-mode dynamics.

4.3.4 Connections to Simple Pendulum and Elastic Rod

We have seen that the dynamics of a planar simple pendulum and a thin elastic rod are analogous in §4.2.3. The connection between these analogous systems and the phugoid-mode model is less direct. The tension force in the simple pendulum is similar to the lift force in the phugoid mode but the tension has a different functional dependence. The magnitude of tension in the pendulum has a quadratic dependence on speed but it also depends on the position of the mass:

$$T = (m/l)(\dot{x}^2 + \dot{z}^2) + mg\cos\theta. \tag{4.49}$$

The magnitude of lift force on the underwater glider just depends on the speed of the glider:

$$L = K(\dot{x}^2 + \dot{z}^2). \tag{4.50}$$

It is *not* possible to interpret the motion of the phugoid-mode glider as being analogous to a simple pendulum of varying length without recourse to infinite lengths - a straight line motion of the phugoid-mode glider would require to be interpreted as analogous to the motion of an infinite length pendulum.

On the other hand we could interpret the phugoid-mode motion as the motion of a simple pendulum motion with respect to a base driven with a certain prescribed acceleration. Equations (4.21)-(4.22), which represent the dynamics of a pendulum with respect to a fixed base may be rewritten as follows:

$$\frac{d\dot{x}}{dt} = -\left(\frac{mV^2}{l} + mg\cos\theta\right)\sin\theta \tag{4.51}$$

$$\frac{d\dot{z}}{dt} = mg - \left(\frac{mV^2}{l} + mg\cos\theta\right)\cos\theta, \tag{4.52}$$

where we have substituted the expression for tension $T = \left(\frac{mV^2}{l} + mg\cos\theta\right)$. We recall that, by definition, $x = l\sin\theta$ and $z = l\cos\theta$. We also have $V\cos\theta = \dot{x}$ and $V\sin\theta = -\dot{z}$. Using these relations we may rewrite the pendulum dynamics (for a fixed base) as follows:

$$\frac{d\dot{x}}{dt} = \frac{mV}{l}\dot{z} - mg\frac{xz}{l^2} \tag{4.53}$$

$$\frac{d\dot{z}}{dt} = mg - \frac{mV}{l}\dot{x} - mg\frac{z^2}{l^2}. \tag{4.54}$$

Now, if the base is driven with the following acceleration,

$$\frac{d\dot{x}_b}{dt} = -mg\frac{xz}{l^2} \tag{4.55}$$

$$\frac{d\dot{z}_b}{dt} = -mg\frac{z^2}{l^2}, \tag{4.56}$$

the dynamics of the pendulum in the base-frame coordinates is identical to the phugoid-mode dynamics:

$$\frac{d\dot{x}}{dt} = \frac{mV}{l}\dot{z} \tag{4.57}$$

$$\frac{d\dot{z}}{dt} = mg - \frac{mV}{l}\dot{x}, \tag{4.58}$$

where x and z are (still) the position of the pendulum mass in base frame coordinates. For an observer on such a base frame, the pendulum motion will appear identical to the phugoid-mode glider motion observed by an observer who is travelling along the

$x-$direction with a constant speed equal to the average speed of the glider.

4.3.5 Summary

The analogies between the underwater glider phugoid-mode model and the Hamiltonian structures of well studied, conservative, planar systems presented in this chapter indicate avenues for further investigation of the dynamics of vehicles subject to aero/hydrodynamic forcing in a geometric framework. For the application of tools of the geometric framework it is critical to formulate and understand the implications of the dynamical structure of the system. The phugoid-mode dynamics can be modelled by Hamilton's equations as presented in §4.1, but it is not clear how to usefully interpret the structure or the Hamiltonian function of this formulation. Both the configuration variable and the corresponding conjugate momentum are velocity components, and the Hamiltonian function is not the energy of the system. A similar formulation appears in the context of point vortex models [85] and it will be interesting to draw from insights developed in the related analytical fluid mechanics literature.

As an alternative to the Hamiltonian model in §4.1, the Hamiltonian formulations for the phugoid-mode dynamics presented in §4.3 use energy as the Hamiltonian function and they are defined on a larger cotangent bundle ($T^*\mathbb{R}^2$). In this case the Hamiltonian function is invariant with respect to one of the configuration directions (the x-position). This means that we can reduce these Hamiltonian systems, which is a subject of future work. The Lagrangian formulation of §4.3.2 and the corresponding canonical Hamiltonian formulation of §4.3.3 use the idea of a vector potential, drawn from the analogy with the motion of a charged particle in a magnetic field. Such analogies may be useful in developing interpretations of the dynamical structure due to the lift force component.

The constructions presented in this chapter may be further extended to incorporate added mass effects (which is straightforward for the formulations of §4.3) as well as coupling with internal mass dynamics. This would get us closer to the real underwater glider system. The next step would be to incorporate the effects of non-conservative external forces and moment components, and control design to regulate desirable motions. The results presented in this chapter and future work on the analysis of underwater glider dynamics in a geometric framework are motivated by the potential of emerging tools such as [23, 24] for the development of low-energy, nonlinear control solutions.

Chapter 5

Singular Perturbation Analysis

In this chapter we use singular perturbation theory for the study of longitudinal dynamics of the underwater glider. Singular perturbation theory, which exploits the multiple time-scale structure of a system, has been widely used in the aircraft guidance and control literature. The survey paper [88] provides an exhaustive listing of references on this subject.

There is a vast body of literature concerning flight path optimization using singular perturbation theory, starting with the works of Kelley and Edelbaum [89], Kelley [90, 91, 92] (summarized in [93]), Ardema [94, 95], Calise [96, 97, 98, 99] and Breakwell [100, 101]. The above references consider planar or 3D point-mass models for vehicle dynamics with different control configurations. They seek control solutions that optimize objective functions encoding costs related to time-of-flight, fuel consumption, or other performance metrics. The approach taken in calculating a (near) optimal solution uses the multiple time-scale structure of the problem to reduce a high-order, two-point boundary value problem to several lower order ones by the application of singular perturbation theory. This reduction is motivated by the need for computing onboard real-time feedback control solutions. Most of the above cited references only postulate the existence of a multiple time-scale structure in the system, and introduce an artificial small parameter (ϵ) for stretching time scales related to the postulated fast states so that a multiple time-scale structure is forced - hence the term *forced singularly perturbed system* used in the literature. The actual vehicle dynamics correspond to $\epsilon = 1$ but the singular perturbation reduction is carried out by considering ϵ to be much smaller than 1. The resulting solutions are checked for multiple time-scale behavior to ensure consistency with the assumptions of the analysis. With the exception of [99, 101] (and some later references such as [102]), ϵ is not defined in terms of vehicle parameters. The choice of slow and fast states for singular perturbation analysis is usually made on the basis of user experience and insight.

Application of singular perturbation theory to flight path optimization problems was further considered in the works of Calise and collaborators [103, 104, 102], Shinar and collaborators [105, 106], van Buren, Kremer, and Mease [107, 108, 109, 110, 111] (for aerospace planes), Vinh and collaborators [112, 113], and several others. These latter references also considered point-mass vehicle models. Point-mass models were sufficient because the focus was on computing solutions that optimized performance.

The focus in this thesis is on studying the stability of motion and designing stabilizing control laws using singular perturbation theory. We consider rigid body models and take into account the effects of rotational dynamics. This amounts to considering the angle of attack and pitch rate dynamics in the case of longitudinal plane motion. We identify a multiple time-scale structure inherent in the vehicle dynamics and compute the different time scales in terms of vehicle parameters for applying singular perturbation theory. There has been a recent resurgence of interest in determining slow and fast time scales of linearized longitudinal dynamics of aircraft, and deriving new phugoid-mode approximations [114, 115, 116]. Stability analysis and stabilizing control design for linear systems using singular perturbation theory has been extensively studied in [117, 118, 119, 120, 121, 122, 123, 124, 35, 125] and references therein. But there have been fewer results and case studies on nonlinear stability analysis and stabilizing control design using singular perturbation theory [126, 127, 128, 35]. We consider nonlinear, longitudinal dynamics in this chapter.

We apply the method of constructing composite Lyapunov functions for singularly perturbed systems originally presented in [127, 128] and summarized in [35] to a rigid body model of an underwater glider, restricted to the longitudinal plane. The main goals of the analysis presented here are to rigorously derive conditions under which we can simplify glider dynamics, prove asymptotic stability of steady gliding motions as a function of vehicle parameters, and derive estimates of the corresponding region of attraction.

Slow and fast subsystems of the underwater glider are identified, and the glider dynamics are reduced to the slow subsystem in §5.1. This reduced model is a generalization of the phugoid-mode model of Chapter 4. We include drag in our analysis in this chapter. The presence of drag is critical for singular perturbation theory to be applicable for the glider model.

The Lyapunov functions derived to prove stability of equilibria of the slow and fast subsystems are used to construct a composite Lyapunov function for the full underwater glider dynamics. This construction and the proof of asymptotic stability of relative equilibria are presented in §5.2. The composite Lyapunov function is also used to derive estimates of the region of attraction in §5.3. The analysis in §5.1-§5.3 follows the presentation in [129, 130].

We noted in §2.3 that relative equilibria of the longitudinal dynamics of the underwater glider correspond to steady, straight-line glides. This motion requires the internal movable mass of the glider to be fixed with respect to the glider center of mass. Furthermore, the buoyancy mass must be constant. In this chapter we keep the internal movable mass fixed at the center of buoyancy of the vehicle such that the centers of buoyancy and gravity are coincident. In the analysis presented in §5.1-§5.3 we also assume that the glider added mass along body-1 and body-3 axes are equal (corresponding to a spherically shaped vehicle). This assumption simplifies the analysis considerably and aids in the presentation of the methodology. We extend the singular perturbation reduction result to the case of unequal added masses in §5.4. We summarize the results of the chapter in §5.5

5.1 Singular Perturbation Reduction

In this section we present the singular perturbation reduction of underwater glider dynamics. We make the following assumptions (that are relaxed in the later sections or chapters) in order to simplify the analysis:

1. The internal moving mass $\bar{m}$ is assumed to be fixed at the center of buoyancy, thus making the center of buoyancy coincident with the center of gravity ($\boldsymbol{r}_P = 0$).

2. The buoyancy mass is held constant at a nonzero value ($m_0 \neq 0 =$ constant).

3. Added masses along body-1 and body-3 directions are taken to be equal. Thus, $m_1 = m_3$. We note that we continue to assume that the added mass and inertia contributions of the wings and tail are small because at low angles of attack and angular rate, their contribution is dominated by lift, drag, and associated moments.

We apply the above assumptions to equations (2.35)-(2.36) that describe the longitudinal dynamics of underwater glider. We also change the velocity coordinates from body velocities (v_1, v_3) to (V, γ), and the orientation coordinate from θ to α, where V is glider speed, γ is the flight path angle, and α is the angle of attack:

$$V = \sqrt{v_1^2 + v_3^2} \tag{5.1}$$

$$\alpha = \tan^{-1}\left(\frac{v_3}{v_1}\right) \tag{5.2}$$

$$\gamma = \theta - \alpha. \tag{5.3}$$

All states of equation (2.36), describing the evolution of $(r_{P1}, \dot{r}_{P1}, r_{P3}, \dot{r}_{P3}, m_0)$, remain constant due to our assumptions. We do not explicitly consider the evolution of position components (x, z) because the dynamics are invariant with respect to glider position.

The equations describing the longitudinal dynamics of the underwater glider in the new coordinates are

$$\dot{V} = -\frac{1}{m_1}\left\{m_0 g \sin\gamma + D\right\} \tag{5.4}$$

$$\dot{\gamma} = \frac{1}{m_1 V}\left\{L - m_0 g \cos\gamma\right\} \tag{5.5}$$

$$\dot{\alpha} = \Omega_2 - \frac{1}{m_1 V}\left\{L - m_0 g \cos\gamma\right\} \tag{5.6}$$

$$\dot{\Omega}_2 = \frac{M_{DL_2}}{J_2}, \tag{5.7}$$

for $V > 0$, where L, D and M_{DL_2} are the hydrodynamic lift, drag and pitching moment respectively, whose functional dependence on the vehicle states is described by equations (2.11), (2.9) and (2.13), respectively.

The relative equilibrium (steady glide) state values of the underwater glider model may be computed to be

$$V_e = \left(\frac{|m_0| g}{\sqrt{K_{D_e}^2 + K_{L_e}^2}}\right)^{\frac{1}{2}} \tag{5.8}$$

$$\gamma_e = \tan^{-1}\frac{-K_{D_e}/m_0}{K_{L_e}/m_0} \tag{5.9}$$

$$\alpha_e = -\frac{K_{M0}}{K_M} \tag{5.10}$$

$$\Omega_{2e} = 0, \tag{5.11}$$

where $K_{D_e} = K_{D0} + K_D\alpha_e^2$ and $K_{L_e} = K_{L0} + K_L\alpha_e$ are equilibrium values of the drag and lift coefficients respectively.

We take $(V,\ \gamma)$ to be the states of the slow time-scale subsystem and $(\alpha,\ \Omega_2)$ to be the states of the fast time-scale subsystem. We transform the state variables $(V, \gamma, \alpha, \Omega_2)$ to nondimensional states $(\bar{V}, \bar{\gamma}, \bar{\alpha}, \bar{\Omega}_2)$ such that the relative equilibrium solution corresponds to the origin in the new coordinates:

$$\bar{V} = \frac{V - V_e}{V_e} \tag{5.12}$$

$$\bar{\gamma} = \gamma - \gamma_e \tag{5.13}$$

$$\bar{\alpha} = \alpha - \alpha_e \tag{5.14}$$

$$\bar{\Omega}_2 = \frac{K_q}{K_M}\Omega_2. \tag{5.15}$$

We define two nondimensional parameters, ϵ_1 and ϵ_2 that quantify the degree of time-scale separation:

$$\epsilon_1 = \left(\frac{K_q}{K_M}\right)\frac{1}{\tau_s} \tag{5.16}$$

$$\epsilon_2 = -\left(\frac{J_2}{K_q V_e^2}\right)\frac{1}{\tau_s}, \tag{5.17}$$

where,

$$\tau_s = \frac{m_1}{K_{D_e}V_e}. \tag{5.18}$$

The reference time scale τ_s is of the same order of magnitude as the time periods associated with the eigenvalues of the linearization of equations (5.4)-(5.5) about (V_e, γ_e) (after setting $\alpha = \alpha_e$, $\Omega_2 = \Omega_{2e} = 0$). In fact, the sum of the reciprocals of eigenvalues of the linearization mentioned is exactly equal to $3\tau_s$. We note that equations (5.4)-(5.5) with $\alpha = \alpha_e$, $\Omega_2 = \Omega_{2e} = 0$ are the dimensional analog of the (nondimensional) reduced system defined in §5.1.2. Thus, the reference time scale is of the same order of magnitude as the time-constants of the reduced system.

The parameters ϵ_i are small positive numbers for a typical underwater glider (such as ROGUE [6], as will be shown in §5.3). Smaller values of ϵ_i imply a greater degree of separation between the slow and fast time scales of the underwater glider. Physically this means that the rotational dynamics are much faster than the translational dynamics.

We also define a nondimensional time variable t_n using the reference time scale τ_s:

$$t_n = \frac{t}{\tau_s}\,. \tag{5.19}$$

We can rewrite the equations of motion of the underwater glider (5.4)-(5.7) in terms of the new nondimensional variables as follows:

$$\begin{aligned}
\frac{d\bar{V}}{dt_n} &= -\frac{1}{K_{D_e}V_e^2}\left(m_0 g \sin(\bar{\gamma}+\gamma_e) + D\right) && (5.20)\\
\frac{d\bar{\gamma}}{dt_n} &= \frac{1}{K_{D_e}V_e^2(1+\bar{V})}\left(-m_0 g \cos(\bar{\gamma}+\gamma_e) + L\right) =: \bar{E}_2 && (5.21)\\
\epsilon_1\frac{d\bar{\alpha}}{dt_n} &= \bar{\Omega}_2 - \epsilon_1\bar{E}_2 && (5.22)\\
\epsilon_2\frac{d\bar{\Omega}_2}{dt_n} &= -\left(\bar{\alpha}+\bar{\Omega}_2\right)\left(1+\bar{V}\right)^2. && (5.23)
\end{aligned}$$

In terms of the nondimensional variables, the expressions for lift and drag forces are

$$\begin{aligned}
D &= \left(K_{D0} + K_D(\bar{\alpha}+\alpha_e)^2\right)V_e^2\left(1+\bar{V}\right)^2 && (5.24)\\
L &= \left(K_{L0} + K_L(\bar{\alpha}+\alpha_e)\right)V_e^2\left(1+\bar{V}\right)^2. && (5.25)
\end{aligned}$$

The presence of two small parameters ϵ_1 and ϵ_2 indicates the presence of three (possibly) different time scales in the above system: the slow time scale t_n, and two fast time scales $\epsilon_1 t_n$ and $\epsilon_2 t_n$. Singular perturbation reduction of such a system may be performed in stages: first, a reduction from the whole system to an intermediate system containing dynamics in the slow time scale and the slower of the two fast time scales and then a reduction from this intermediate system to a system containing only the slow time scale. Such a reduction in stages would require sufficient separation between the two fast time scales.

We adopt an alternative approach, presented in [128]. We do not make any assumptions about the relative magnitudes of ϵ_1 and ϵ_2, i.e., we do not require any separation between the two fast time scales. Instead we simply consider one *fast subsystem* that contains both fast time scales. To do so we define

$$\mu := \max\{\epsilon_1, \epsilon_2\}, \tag{5.26}$$

and assume that

$$r_1 := \frac{\mu}{\epsilon_1}, \quad r_2 := \frac{\mu}{\epsilon_2} \tag{5.27}$$

are $O(1)$.[1] We note that μ is a constant for an underwater glider with a constant set of vehicle parameters.

We also restrict the domain of our system to a local neighborhood of the equilibrium. The size of this neighborhood, along with μ, affects the region of attraction estimates that we compute in §5.3, but it does not change the result qualitatively. In other words the singular perturbation reduction procedure presented here works irrespective of the size of the domain for a correspondingly small value of μ. The domain is given by $(\boldsymbol{p}, \boldsymbol{q}) \in B_{\boldsymbol{p}} \times B_{\boldsymbol{q}}$, where $\boldsymbol{p} := (\bar{V}, \bar{\gamma})$ and $\boldsymbol{q} := (\bar{\alpha}, \bar{\Omega}_2)$. $B_{\boldsymbol{p}} \in \mathbb{R}^2$

[1] $f_1(\delta) = O(f_2(\delta))$ if $\exists$ positive constants k, c such that $|f_1(\delta)| \leq k\,|f_2(\delta)| \;\; \forall \; |\delta| < c$. [13]

is a neighborhood of the origin such that $-1 < \bar{V}_{min} \leq \bar{V} \leq \bar{V}_{max}$, $-\pi \leq \bar{\gamma} < \pi$, and $B_{\boldsymbol{q}} \in \mathbb{R}^2$ is also a neighborhood of the origin such that $-2\pi \leq \bar{\alpha}_{min} \leq \bar{\alpha} \leq \bar{\alpha}_{max} \leq 2\pi$, $-\bar{\Omega}_{2,min} \leq \bar{\Omega}_2 \leq \bar{\Omega}_{2,max}$.

Multiplying equation (5.22) by $\frac{\mu}{\epsilon_1}$ and equation (5.23) by $\frac{\mu}{\epsilon_2}$, and using our new definitions we can rewrite equations (5.20)-(5.23) in a compact form as follows:

$$\frac{d\boldsymbol{p}}{dt_n} = \boldsymbol{f}(\boldsymbol{p}, \boldsymbol{q}) \tag{5.28}$$

$$\mu \frac{d\boldsymbol{q}}{dt_n} = A\,\boldsymbol{g}\,(\boldsymbol{p}, \boldsymbol{q}, \boldsymbol{\epsilon}) \tag{5.29}$$

where,

$$\begin{aligned}
\boldsymbol{\epsilon} &= \begin{bmatrix} \epsilon_1 \\ \epsilon_2 \end{bmatrix}, \quad A = \begin{bmatrix} \frac{\mu}{\epsilon_1} & 0 \\ 0 & \frac{\mu}{\epsilon_2} \end{bmatrix}, \quad \boldsymbol{f} = \begin{bmatrix} f_1 \\ f_2 \end{bmatrix}, \quad \boldsymbol{g} = \begin{bmatrix} g_1 \\ g_2 \end{bmatrix} \\
f_1 &= -\frac{1}{K_{D_e} V_e^2} \left(m_0 g \sin(\bar{\gamma} + \gamma_e) + D \right) \\
f_2 &= \frac{1}{K_{D_e} V_e^2 (1 + \bar{V})} \left(-m_0 g \cos(\bar{\gamma} + \gamma_e) + L \right) \\
g_1 &= \bar{\Omega}_2 - \frac{\epsilon_1}{K_{D_e} V_e^2 (1 + \bar{V})} \left(-m_0 g \cos(\bar{\gamma} + \gamma_e) + L \right) \\
g_2 &= -\left(\bar{\alpha} + \bar{\Omega}_2 \right) \left(1 + \bar{V} \right)^2 .
\end{aligned}$$

In the following two subsections, §5.1.1 and §5.1.2, we identify the *boundary-layer* (fast) subsystem and the *reduced* (slow) subsystem, and also construct Lyapunov functions to prove that their equilibria are exponentially stable. In §5.1.3 we reduce the full system dynamics to the dynamics of the reduced subsystem.

5.1.1 Boundary-Layer Susbystem

The boundary-layer subsystem describes the fast time-scale dynamics that are required to be exponentially stable for singular perturbation reduction. The fast convergence of these dynamics allows us to approximate the states of the fast subsystem by their equilibrium values in order to derive the reduced subsystem.

The fast dynamics of (5.28)-(5.29) are described by the latter equation. Singular perturbation theory allows us to derive results by studying the limiting case of the small parameter $\mu \to 0$. This limit is taken by first changing the time variable t_n to

$$\tau := \frac{t_n}{\mu},$$

which defines a *stretched* time scale. Then, we set $\mu = 0$ in equation (5.29). This leads to the following equation for the fast subsystem dynamics:

$$\frac{d\boldsymbol{q}}{d\tau} = A\boldsymbol{g}(\boldsymbol{p}, \boldsymbol{q}, \boldsymbol{0}). \tag{5.30}$$

Furthermore, this limiting approximation allows us to consider the states of the slow dynamics (described by equation (5.28)) to be constant in the analysis of the fast subsystem.

We state a proposition that provides sufficient conditions for uniform (in $\boldsymbol{p}$) exponential stability of the origin ($\boldsymbol{q} = \boldsymbol{0}$) of the boundary-layer subsystem.

Proposition 1. *[130] The origin is an exponentially stable equilibrium of the boundary layer subsystem (5.30) if there is a Lyapunov function $\hat{W}$ that satisfies*

1. $k_3\|\boldsymbol{q}\|^2 \leq \hat{W}(\boldsymbol{p}, \boldsymbol{q}) \leq k_4\|\boldsymbol{q}\|^2$ *for some* $k_3, k_4 > 0$.

2. $\frac{\partial \hat{W}}{\partial \boldsymbol{q}} A\boldsymbol{g}(\boldsymbol{p}, \boldsymbol{q}) \leq -a_2\sigma^2(\boldsymbol{q}) \leq -b_2\|\boldsymbol{q}\|^2$ *where* $\sigma(.)$ *is a positive definite function on* $\mathbb{R}^2$, *that vanishes only at* $\boldsymbol{q} = 0$, *and* a_2, b_2 *are positive constants.*

Proof This proposition is a result of the application of Theorem 4.10 of [13] to the boundary-layer subsystem (5.30). $\square$

We propose a quadratic Lyapunov function candidate for the boundary layer subsystem:

$$\hat{W} = \frac{1}{2}\boldsymbol{q}^T C_W \boldsymbol{q} = \frac{1}{2}\left[\begin{array}{cc} \bar{\alpha} & \bar{\Omega}_2 \end{array}\right]\left[\begin{array}{cc} c_1 & c_3 \\ c_3 & c_2 \end{array}\right]\left[\begin{array}{c} \bar{\alpha} \\ \bar{\Omega}_2 \end{array}\right]. \tag{5.31}$$

The matrix C_W is a constant matrix with $c_1 = r_1 + r_1 a + r_2 a$, $c_2 = 1 + \frac{r_1}{r_2 a}$ and $c_3 = 1$, where $a = \left(1 + \bar{V}\right)^2$ (recall that $\bar{V}$ may be considered to be constant in the boundary-layer system). The above choice of C_W assures that $\hat{W}$ is a positive-definite matrix. Condition (1) of Proposition 1 is satisfied with k_3 and k_4 equal to the smaller and greater of the two eigenvalues of C_W respectively. Furthermore, this choice of C_W ensures that the coefficient of the cross-term ($\bar{\alpha}\bar{\Omega}_2$) in the derivative of $\hat{W}$ with respect to τ is zero.

We compute the derivative of $\hat{W}$ with respect to τ:

$$\frac{d\hat{W}}{d\tau} = \frac{\partial \hat{W}}{\partial \boldsymbol{q}} A\boldsymbol{g}(\boldsymbol{p}, \boldsymbol{q}) = -r_2 a \left(\bar{\alpha}^2 + \bar{\Omega}_2^2\right).$$

Thus, condition (2) of Proposition 1 is satisfied with $a_2 = r_2$, $b_2 = a_2 \left(1 + \bar{V}_{min}\right)^2$ and

$$\sigma = \left(1 + \bar{V}\right)\sqrt{\bar{\alpha}^2 + \bar{\Omega}_2^2}\,. \tag{5.32}$$

Proposition 1 provides the stability of the boundary-layer subsystem. Validity of singular perturbation reduction for infinite time intervals requires the reduced (slow) subsystem to exponentially converge to its equilibrium. This is proven in the following subsection.

5.1.2 Reduced Subsytem

The reduced subsystem for the underwater glider is obtained by assuming that the states of the boundary-layer subsystem have reached their equilibrium values. This amounts to setting $\boldsymbol{q} = \mathbf{0}$ in equation (5.28)[2]:

$$\frac{d\boldsymbol{p}}{dt_n} = f(\boldsymbol{p}, \mathbf{0}). \tag{5.33}$$

The following proposition provides sufficient conditions for the exponential stability of the origin for the reduced subsystem.

Proposition 2. *[130] The origin is an exponentially stable equilibrium point of the reduced model (5.33) if there is a Lyapunov function Φ that satisfies*

1. $k_1\|\boldsymbol{p}\|^2 < \Phi(\boldsymbol{p}) < k_2\|\boldsymbol{p}\|^2$ *for some* $k_1, k_2 > 0$.
2. $\frac{\partial\Phi}{\partial\boldsymbol{p}}\boldsymbol{f}(\boldsymbol{p}, \mathbf{0}) \leq -a_1\psi^2(\boldsymbol{p}) \leq -b_1\|\boldsymbol{p}\|^2$ *where* $\psi(.)$ *is a scalar positive-definite function of* $\boldsymbol{p}$ *that vanishes only at* $\boldsymbol{p} = \mathbf{0}$, *and* a_1, b_1 *are positive constants.*

Proof This proposition is a result of the application of Theorem 4.10 of [13] to the reduced subsystem (5.33). □

In order to prove the exponential stability of the equilibrium $\boldsymbol{p} = \mathbf{0}$ of (5.33), we use a Lyapunov function candidate derived from the conserved quantity C of the phugoid-mode model of the underwater glider, discussed in §4.1. In terms of the nondimensional states we can rewrite C as follows:

$$C = (1 + \bar{V})\cos(\bar{\gamma} + \gamma_e) - \frac{1}{3}(1 + \bar{V})^3. \tag{5.34}$$

We modify C such that the modified function is positive definite and zero at the origin. We consider the Lyapunov function candidate Φ:

$$\Phi = \frac{2}{3} - (1 + \bar{V})\cos\bar{\gamma} + \frac{1}{3}\left(1 + \bar{V}\right)^3 . \tag{5.35}$$

[2]This is a generalization of the procedure of *residualization* used in linear systems (for example, see chapter 4 of [42]) to the case of nonlinear systems with multiple time scales.

In order to show that Φ satisfies condition (1) of Proposition 2 in any compact domain $B_{\boldsymbol{p}}$ we employ the power series expansions. Using the expansion of $\cos\bar{\gamma}$ we can write Φ as follows:

$$\begin{aligned}\Phi &= \frac{2}{3} - (1+\bar{V})\left(1 - \frac{\bar{\gamma}^2}{2!} + \frac{\bar{\gamma}^4}{4!} - \frac{\bar{\gamma}^6}{6!} + \frac{\bar{\gamma}^8}{8!} + \ldots\right) + \frac{1}{3} + \bar{V} + \bar{V}^2 + \frac{\bar{V}^3}{3} \\ &= \left(1 + \frac{\bar{V}}{3}\right)\bar{V}^2 + \frac{(1+\bar{V})}{2}\left[\left\{1 - \frac{\bar{\gamma}^2}{4\times 3}\right\} + \frac{2\,\bar{\gamma}^4}{6!}\left\{1 - \frac{\bar{\gamma}^2}{8\times 7}\right\} + \ldots\right]\bar{\gamma}^2. \quad (5.36)\end{aligned}$$

We note that since $-\pi \leq \bar{\gamma} < \pi$ in our domain, every term within braces $\{.\}$ in the above expression is greater than 0. Furthermore, since $\bar{V} > \bar{V}_{min} > -1$, $\left(1 + \frac{\bar{V}}{3}\right) > 0$. Thus, we can conclude

$$\begin{aligned}\Phi &\geq \left(1 + \frac{\bar{V}}{3}\right)\bar{V}^2 + \frac{(1+\bar{V})}{2}\left\{1 - \frac{\bar{\gamma}^2}{4\times 3}\right\}\bar{\gamma}^2 \\ &\geq k_1\left(\bar{V}^2 + \bar{\gamma}^2\right), \quad (5.37)\end{aligned}$$

where,

$$k_1 = \min\left\{1 + \frac{\bar{V}_{min}}{3}, \left(\frac{1+\bar{V}_{min}}{2}\right)\left(1 - \frac{\pi^2}{12}\right)\right\}. \quad (5.38)$$

We can rewrite the expansion for Φ as follows:

$$\begin{aligned}\Phi = &\left(1 + \frac{\bar{V}}{3}\right)\bar{V}^2 + \frac{(1+\bar{V})}{2}\bar{\gamma}^2 \\ &- \frac{(1+\bar{V})}{4!}\left[\left\{1 - \frac{\bar{\gamma}^2}{6\times 5}\right\} + \frac{4!\,\bar{\gamma}^4}{8!}\left\{1 - \frac{\bar{\gamma}^2}{10\times 9}\right\} + \ldots\right]\bar{\gamma}^4 \quad (5.39)\end{aligned}$$

Once again since $-\pi \leq \bar{\gamma} < \pi$ in our domain, every term within braces $\{.\}$ in the above expression is greater than 0. Thus, we have

$$\begin{aligned}\Phi &\leq \left(1 + \frac{\bar{V}}{3}\right)\bar{V}^2 + \frac{(1+\bar{V})}{2}\bar{\gamma}^2 \\ &\leq k_2\left(\bar{V}^2 + \bar{\gamma}^2\right), \quad (5.40)\end{aligned}$$

where,

$$k_2 = \max\left\{1 + \frac{\bar{V}_{max}}{3}, \frac{1+\bar{V}_{max}}{2}\right\}. \tag{5.41}$$

Thus, condition (1) of Proposition 2 is satisfied.

We compute the derivative of Φ with respect to t_n:

$$\begin{aligned}
\frac{d\Phi}{dt_n} &= \left(-\cos\bar{\gamma} + \left(1+\bar{V}\right)^2\right)\left[-\frac{1}{K_{D_e}V_e^2}\left(m_0 g \sin\left(\bar{\gamma}+\gamma_e\right) + K_{D_e}V_e^2\left(1+\bar{V}\right)^2\right)\right] \\
&\quad + \left(1+\bar{V}\right)\sin\bar{\gamma}\left(\frac{-1}{K_{D_e}V_e^2\left(1+\bar{V}\right)}\right)\left\{m_0 g\cos\left(\bar{\gamma}+\gamma_e\right) - K_{L_e}V_e^2\left(1+\bar{V}\right)^2\right\} \\
&= \frac{-1}{K_{D_e}V_e^2}\Big[m_0 g\left(\sin\bar{\gamma}\cos\left(\bar{\gamma}+\gamma_e\right) - \cos\bar{\gamma}\sin\left(\bar{\gamma}+\gamma_e\right)\right) - K_{L_e}V_e^2\left(1+\bar{V}\right)^2\sin\bar{\gamma} \\
&\qquad - K_{D_e}V_e^2\left(1+\bar{V}\right)^2\cos\bar{\gamma} + m_0 g\sin\left(\bar{\gamma}+\gamma_e\right)\left(1+\bar{V}\right)^2 \\
&\qquad + K_{D_e}V_e^2\left(1+\bar{V}\right)^4\Big] \\
&= \frac{-1}{K_{D_e}V_e^2}\Big[-m_0 g\sin\gamma_e - K_{L_e}V_e^2\left(1+\bar{V}\right)^2\sin\bar{\gamma} - K_{D_e}V_e^2\left(1+\bar{V}\right)^2\cos\bar{\gamma} \\
&\qquad + m_0 g\sin\left(\bar{\gamma}+\gamma_e\right)\left(1+\bar{V}\right)^2 + K_{D_e}V_e^2\left(1+\bar{V}\right)^4\Big]
\end{aligned} \tag{5.42}$$

We note that $m_0 g\sin\gamma_e = -K_{D_e}V_e^2$ and $K_{L_e}V_e^2 = m_0 g\cos\gamma_e$. Substituting these two relations in the first two terms of the above equality we get

$$\begin{aligned}
\frac{d\Phi}{dt_n} &= \frac{-1}{K_{D_e}V_e^2}\Big[K_{D_e}V_e^2 - m_0 g\cos\gamma_e\left(1+\bar{V}\right)^2\sin\bar{\gamma} - K_{D_e}V_e^2\left(1+\bar{V}\right)^2\cos\bar{\gamma} \\
&\qquad + m_0 g\sin\left(\bar{\gamma}+\gamma_e\right)\left(1+\bar{V}\right)^2 + K_{D_e}V_e^2\left(1+\bar{V}\right)^4\Big] \\
&= \frac{-1}{K_{D_e}V_e^2}\Big[K_{D_e}V_e^2 - K_{D_e}V_e^2\left(1+\bar{V}\right)^2\cos\bar{\gamma} \\
&\qquad + m_0 g\sin\gamma_e\cos\bar{\gamma}\left(1+\bar{V}\right)^2 + K_{D_e}V_e^2\left(1+\bar{V}\right)^4\Big]
\end{aligned} \tag{5.43}$$

Once again using the relation $m_0 g\sin\gamma_e = -K_{D_e}V_e^2$ - this time in the third term of the above equation - and also substituting $1-2\sin^2\frac{\bar{\gamma}}{2}$ for $\cos\bar{\gamma}$ we compute

$$\begin{aligned}
\frac{d\Phi}{dt_n} &= \frac{-1}{K_{D_e}V_e^2}\left[K_{D_e}V_e^2 - 2K_{D_e}V_e^2\left(1+\bar{V}\right)^2\left(1-2\sin^2\frac{\bar{\gamma}}{2}\right) + K_{D_e}V_e^2\left(1+\bar{V}\right)^4\right] \\
&= -\left[1-2\left(1+\bar{V}\right)^2\left(1-2\sin^2\frac{\bar{\gamma}}{2}\right)+\left(1+\bar{V}\right)^4\right] \\
&= -\left[\left(\left(1+\bar{V}\right)^2-1\right)^2+4\left(1+\bar{V}\right)^2\sin^2\frac{\bar{\gamma}}{2}\right] \\
&= -\left\{\left(\bar{V}(\bar{V}+2)\right)^2+4(1+\bar{V})^2\sin^2\left(\frac{\bar{\gamma}}{2}\right)\right\}. \qquad (5.44)
\end{aligned}$$

Let us examine the above expression carefully. First, we note that $\sin^2(\bar{\gamma}/2) = \sin^2(|\bar{\gamma}|/2)$. The power series expansion of the sine function gives us

$$\begin{aligned}
\sin\left(\frac{|\bar{\gamma}|}{2}\right) &= \frac{|\bar{\gamma}|}{2} - \frac{1}{3!}\left(\frac{|\bar{\gamma}|}{2}\right)^3 + \frac{1}{5!}\left(\frac{|\bar{\gamma}|}{2}\right)^5\left(1-\frac{(|\bar{\gamma}|/2)^2}{7\times 6}\right)+\dots \\
&\geq \frac{|\bar{\gamma}|}{2} - \frac{1}{3!}\left(\frac{|\bar{\gamma}|}{2}\right)^3 \text{ because } -\pi \leq \bar{\gamma} < \pi \\
&= \frac{|\bar{\gamma}|}{2}\left(1-\frac{|\bar{\gamma}|^2}{24}\right) \\
&\geq \frac{|\bar{\gamma}|}{2}\,e, \qquad (5.45)
\end{aligned}$$

where,

$$e = \left(1-\frac{\pi^2}{24}\right) > 0. \qquad (5.46)$$

Thus, we have

$$-\sin^2\left(\frac{\bar{\gamma}}{2}\right) \leq -e^2\left(\frac{\bar{\gamma}}{2}\right)^2. \qquad (5.47)$$

Substituting relation (5.47) in equation (5.44) we can conclude that

$$\frac{d\Phi}{dt_n} \leq -\left\{\left(\bar{V}+2\right)^2\bar{V}^2+(1+\bar{V})^2e^2\bar{\gamma}^2\right\}. \qquad (5.48)$$

This implies,

$$
\begin{aligned}
\frac{d\Phi}{dt_n} &\leq -\min\left(\left(\bar{V}_{min}+2\right)^2, (1+\bar{V}_{min})^2e^2\right)\left(\bar{V}^2+\bar{\gamma}^2\right) \\
&= -\left(1+\bar{V}_{min}\right)^2 e^2\left(\bar{V}^2+\bar{\gamma}^2\right). \qquad (5.49)
\end{aligned}
$$

Thus, condition (2) of Proposition 2 is satisfied with $a_1 = 1$, $b_1 = e^2\left(1+\bar{V}_{min}\right)^2$ and

$$
\psi = \sqrt{(\bar{V}^2+2\bar{V})^2 + 4(1+\bar{V})^2\sin^2\left(\frac{\bar{\gamma}}{2}\right)}. \qquad (5.50)
$$

Proposition 2 provides the stability of the reduced (slow) subsystem. This result is used along with the result of Proposition 1 to derive the singular perturbation reduction of underwater glider dynamics in the following subsection. The result of the following subsection is consistent with the phugoid-mode approximations based on eigenvalues of linearized models, commonly used in aircraft control literature.

5.1.3 Reduction of Dynamics

Since the equilibria of both the boundary-layer and reduced subsystems are exponentially stable, the reduced system dynamics approximate the dynamics of the full system. More precisely we can state the following result:

Theorem 1. *[130] Let $R^A_{\boldsymbol{q}} \subset B_{\boldsymbol{q}}$ be the region of attraction of (5.30) about $\boldsymbol{q} = \boldsymbol{0}$ and $\Lambda_{\boldsymbol{q}}$ be a compact subset of $R^A_{\boldsymbol{q}}$. Let the set $\{\|\boldsymbol{p}\|^2 \leq k_5\}$, where $k_5 > 0$, be a compact subset of $B_{\boldsymbol{p}}$. For each compact set $\Lambda_{\boldsymbol{p}} \subset \{\|\boldsymbol{p}\|^2 \leq \rho k_5, 0 < \rho < 1\}$ there is a positive constant μ^* such that for all initial conditions $(\bar{V}_0, \bar{\gamma}_0) \in \Lambda_{\boldsymbol{p}}$, $(\bar{\alpha}_0, \bar{\Omega}_{2,0}) \in \Lambda_{\boldsymbol{q}}$, $0 < \mu < \mu^*$ and $t_n \in [t_{n,0}, \infty)$,*

$$
\boldsymbol{p}(t_n,\mu) - \boldsymbol{p}_r(t_n) = O(\mu) \qquad (5.51)
$$

$$
\boldsymbol{q}(t_n,\mu) - \hat{\boldsymbol{q}}(t_n/\mu) = O(\mu) \qquad (5.52)
$$

where $\boldsymbol{p}_r(t_n)$ and $\hat{\boldsymbol{q}}(\tau)$ are the solutions of the reduced (5.33) and boundary layer (5.30) systems respectively.

Proof This theorem follows by applying Theorem 11.2 of [13] to the system described by equations (5.28)-(5.29). □

Figure 5.1 shows a simulation of the reduced system and the full system for an underwater glider of a similar size as ROGUE [31]. This simulation provides an illustration of the result of Theorem 1. The parameters used in the simulation are as follows (see §5.3 for more discussion on these parameters): $m_1 = m_3 = 28$ kg, $m_0 = 0.7$ kg, $K_{L0} = 0$ kg/m, $K_L = 75$ kg/m/rad, $K_{D0} = 2$ kg/m, $K_D = 80$ kg/m/rad^2, $K_{M0} = 1$ kg, $K_q = -2$ kg.s/rad, $K_M = -50$ kg/rad, $J_2 = 0.02$ kg.m^2. The initial conditions for the full dynamics were $V(0) = 1.730$ m/s, $\gamma(0) = -0.91$ rad, $\alpha(0) = 0.03$ rad and $\Omega_2 = 2.50$ rad/s. The initial conditions for the reduced subsystem were $V(0) = 1.765$ m/s and $\gamma(0) = -0.93$ rad. The nondimensional small parameters are $\epsilon_1 = 4.784\exp(-3)$ and $\epsilon_2 = 4.403\exp(-4)$. The eigenvalues of the linearization of the nondimensional reduced system are -1.500±0.916i and those of the boundary-layer system scaled to the time scale t_n (i.e., equation (5.30) with the left-hand-side derivative with respect to t_n instead of τ for the purpose of comparing with eigenvalues of the reduced system) are -84.582 and -363.796. We observe that the solutions of the two systems remain close to each other during the entire simulation, indicating that the reduced system dynamics well approximate the full system dynamics. The convergence of the two solutions starting at different initial conditions also demonstrates the stability of the equilibrium of the reduced system.

The result of the above theorem also makes rigorous the justification for the phugoid-mode approximation for underwater gliders and aircraft [34]. The justification for the phugoid-mode approximation is usually argued on the basis of separation of eigenvalues of the linearization of the vehicle model. The system matrix is sometimes approximated to a block triangular matrix [124] by neglecting parasitic terms.

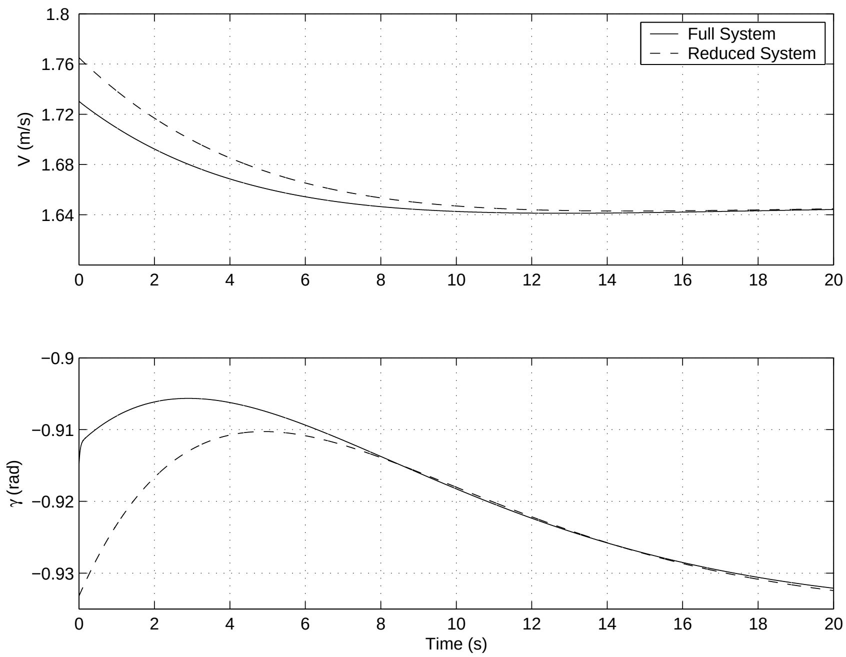

Figure 5.1: Singular Perturbation Reduction Simulation

The validity of the approximation is checked by comparing the eigenvalues of the slow and fast subsystems to the eigenvalues of the original system. If the set of eigenvalues of the original system is close to the union of the sets of eigenvalues of the slow and fast subsystems, the latter subsystems are analyzed separately. Furthermore, if all eigenvalues are on the left half plane, the original system may be approximated by the slow (reduced) subsystem. In contrast, our result is derived using the original nonlinear model of the vehicle (equations (5.20)-(5.23)). We do not ignore any coupling terms between the slow and fast subsystems. The statement of Theorem 1 provides precise conditions in terms of vehicle parameters (ϵ_i's are functions of vehicle parameters) and system domain where phugoid-mode approximation is valid. The phugoid-mode approximation holds in a compact set within a neighborhood around the equilibrium (origin) of the longitudinal dynamics. This neighborhood may be specified as follows: $-1 < \bar{V}_{min} \leq \bar{V} \leq \bar{V}_{max}$, $-\pi \leq \bar{\gamma} < \pi$, $-2\pi \leq \bar{\alpha} < 2\pi$, $-\bar{\Omega}_{2,min} \leq \bar{\Omega}_2 \leq \bar{\Omega}_{2,max}$. The size of the compact set within the above neighborhood is determined by the parameters ϵ_1 and ϵ_2 defined by equations (5.16)-(5.17). Smaller values of ϵ_i imply a larger separation between the fast and slow time scales of the system, which provides for a larger compact set around the equilibrium where the phugoid-mode approximation is valid, as illustrated in the numerical example presented in §5.3.1.

5.2 Composite Lyapunov Function

The stability of equilibria of boundary-layer and reduced subsystems guarantees stability of the equilibrium of the full system dynamics in a small enough region around the equilibrium. An estimate of the size of this region may be calculated using a Lyapunov function candidate for the full system. Such a Lyapunov function, which proves the asymptotic stability of the full system equilibrium, is constructed in this section by combining the Lyapunov functions for the boundary-layer and reduced subsystems. The composite Lyapunov function is used in §5.3 to compute (conservative) estimates of the region of attraction of the equilibrium.

We first state a result derived from [127, 128]. This result, presented in [129, 130], provides conditions under which a composite Lyapunov function candidate is valid.

Theorem 2. *[130] Consider a singularly perturbed system of the form (5.28)-(5.29). Assume the origin is the unique equilibrium in the neighborhood* $B_{\boldsymbol{p}} \times B_{\boldsymbol{q}}$*, and* $\boldsymbol{q} = 0$ *is the unique equilibrium for the boundary layer system of the form (5.30) for* $\boldsymbol{p} \in B_{\boldsymbol{p}}$*. Suppose the conditions of Propositions 1 and 2 hold as well as all other assumptions of Theorem 11.2 of [13]. Suppose further the following interconnection conditions hold for all* $(\boldsymbol{p}, \boldsymbol{q}, \epsilon_i) \in B_{\boldsymbol{p}} \times B_{\boldsymbol{q}} \times [0, \epsilon_i^*]$*,* $i = 1, 2$*;*

1. $\frac{\partial \Phi}{\partial \boldsymbol{p}} \left[\boldsymbol{f}(\boldsymbol{p}, \boldsymbol{q}) - \boldsymbol{f}(\boldsymbol{p}, \boldsymbol{0}) \right] \leq \beta_1 \psi(\boldsymbol{p}) \sigma(\boldsymbol{q}) + \mu \gamma_1 \psi^2(\boldsymbol{p})$

2. $\frac{\partial \hat{W}}{\partial \boldsymbol{q}} A \left[\boldsymbol{g}(\boldsymbol{p}, \boldsymbol{q}, \boldsymbol{\epsilon}) - \boldsymbol{g}(\boldsymbol{p}, \boldsymbol{q}, \boldsymbol{0}) \right] \leq \mu \left(\gamma_2' \sigma^2(\boldsymbol{q}) + \beta_2' \psi(\boldsymbol{p}) \sigma(\boldsymbol{q}) \right)$

3. $\left| \frac{\partial \hat{W}}{\partial \boldsymbol{p}} \boldsymbol{f}(\boldsymbol{p}, \boldsymbol{q}) \right| \leq \gamma_2'' \sigma^2(\boldsymbol{q}) + \beta_2'' \psi(\boldsymbol{p}) \sigma(\boldsymbol{q})$

where $\beta_1,\ \beta_2^{'},\ \beta_2^{''},\ \gamma_1,\ \gamma_2^{'},\ \gamma_2^{''}$ *are nonnegative constants and* $\epsilon_i^* > 0,\ i = 1, 2$*. Then, the origin is an asymptotically stable equilibrium of (5.28)-(5.29) for all* $0 < \epsilon_i < \min\{\mu^*, \epsilon_i^*\},\ i = 1, 2$*, where*

$$\mu^* = \frac{a_1 a_2}{a_1\gamma_2 + a_2\gamma_1 + \beta_1\beta_2},$$

$\beta_2 = \beta_2^{'} + \beta_2^{''},\ \gamma_2 = \gamma_2^{'} + \gamma_2^{''}$*. Moreover, for every* $0 < d < 1$*, the composite function*

$$\nu(\boldsymbol{p}, \boldsymbol{q}) = (1 - d)\Phi(\boldsymbol{p}) + d\hat{W}(\boldsymbol{p}, \boldsymbol{q}) \tag{5.53}$$

is a Lyapunov function that proves the asymptotic stability of the origin of (5.28)-(5.29) for all $0 < \epsilon_i < \min\{\mu_d, \epsilon_i^*\},\ i = 1, 2$*, where*

$$\mu_d = \frac{a_1 a_2}{a_1\gamma_2 + a_2\gamma_1 + \frac{1}{4(1-d)d}\left[(1 - d)\beta_1 + d\beta_2\right]^2}\,. \tag{5.54}$$

Furthermore,

$$\frac{d\nu}{dt_n} \leq -c\left\{\|\boldsymbol{p}\|^2 + \|\boldsymbol{q}\|^2\right\}, \tag{5.55}$$

for some positive constant c.

Proof This theorem follows by applying Theorem 1 of [128] to the system described by equations (5.28)-(5.29). The interconnection conditions are satisfied in a sufficiently small enough neighborhood of the equilibrium of the full system and for sufficiently small ϵ_i^*. The computation of the constants appearing in the interconnection conditions is given in §5.2.1-§5.2.3. □

The first and third conditions of the above theorem ensure that the coupling between the states of the fast and slow subsystems is small enough so that the stability of the individual subsystems leads to the stability of the full system. They may also be interpreted as conditions that require $\boldsymbol{f}$ and $\boldsymbol{g}$ to be smooth enough. As noted in [127], one way to grasp their meaning is to consider a special case when the partial derivatives of V and $\hat{W}$ are bounded by ψ and σ, respectively, and $\boldsymbol{f}_r(\boldsymbol{p})$ is bounded by ψ. In this special case, inequalities 1 and 3 (of the above theorem) follow from the Lipschitz-like condition

$$|f(\boldsymbol{p}, \boldsymbol{q}_1) - f(\boldsymbol{p}, \boldsymbol{q}_2)| \leq L\sigma(\boldsymbol{q}_1 - \boldsymbol{q}_2) \tag{5.56}$$

which simply says that the rate of growth of $\boldsymbol{f}$ in $\boldsymbol{q}$ cannot be faster than the rate of growth of $\sigma(\cdot)$. The second condition of the theorem monitors the dependence of $\boldsymbol{g}$ on $\boldsymbol{\epsilon}$.

The freedom in choosing d in the composite Lyapunov function may be used to optimize the region of attraction estimate for a given set of glider parameters. It can also be used to optimize the estimates of the upper bound of small parameters ϵ_1 and ϵ_2 to guarantee a certain specified region of attraction.

In the following subsections we show that the underwater glider system satisfies the conditions of Theorem 2, and we derive the expressions for various coefficients that appear in the theorem.

5.2.1 Interconnection Condition 1

Let us denote the left-hand-side of condition 1 of Theorem 2 by C_1. We calculate

$$\begin{aligned} C_1 \;\; = \;\; & \frac{1}{K_{D_e}} \Bigg\{ K_D \left[(\bar{\alpha} + \alpha_e)^2 - \alpha_e^2 \right] \left[\left(1 + \bar{V}\right)^2 - \cos(\bar{\gamma}) \right] \\ & \qquad + K_L \bar{\alpha} \sin \bar{\gamma} \Bigg\} \left(1 + \bar{V}\right)^2 . \end{aligned} \tag{5.57}$$

We note that $(\bar{\alpha} + \alpha_e)^2 - \alpha_e^2 = (\bar{\alpha} + 2\alpha_e)\,\bar{\alpha} \leq (|\bar{\alpha}|_{max} + 2|\alpha_e|)\,|\bar{\alpha}|$, where $|\bar{\alpha}|_{max} = \max\{-\bar{\alpha}_{min}, \bar{\alpha}_{max}\}$. We further note that $\bar{\alpha} \sin \bar{\gamma} = \bar{\alpha}\, 2 \sin \frac{\bar{\gamma}}{2} \cos \frac{\bar{\gamma}}{2} \leq |\bar{\alpha}| \left|2 \sin \frac{\bar{\gamma}}{2}\right|$.

Substituting these results in equation (5.57), using the identities $\cos\bar{\gamma} = 1 - 2\sin^2\frac{\bar{\gamma}}{2}$, $\sin\bar{\gamma} = 2\sin\frac{\bar{\gamma}}{2}\cos\frac{\bar{\gamma}}{2}$ and using the fact that $\left(1+\bar{V}\right) = |1+\bar{V}|$ (since $\bar{V} > -1$) we get

$$\begin{aligned} C_1 \quad \leq \quad & \frac{1}{K_{D_e}}\Bigg\{K_D\Big[\left(|\bar{\alpha}|_{max} + 2|\alpha_e|\right)\left(1+\bar{V}\right)|\bar{\alpha}|\Big] \\ & \qquad \times \left[\left(1+\bar{V}\right)\left|\bar{V}^2 + 2\bar{V} + 2\sin^2(\frac{\bar{\gamma}}{2})\right|\right] \\ & \qquad + K_L\left(1+\bar{V}\right)|\bar{\alpha}|\left|\left(1+\bar{V}\right)2\sin(\frac{\bar{\gamma}}{2})\right|\Bigg\}. \end{aligned} \tag{5.58}$$

In order to express the right-hand-side of the above expression in terms of σ defined by equation (5.32) and ψ defined by equation (5.50) we make the following observations:

- $|\bar{\alpha}| \leq \sqrt{\bar{\alpha}^2 + \bar{\Omega}_2^2}$. Thus, $\left(1+\bar{V}\right)|\bar{\alpha}| \leq \sigma$.
- $\left|\left(1+\bar{V}\right)2\sin(\frac{\bar{\gamma}}{2})\right| = \sqrt{\left(\left(1+\bar{V}\right)2\sin(\frac{\bar{\gamma}}{2})\right)^2} \leq \psi$.
- $\left|\bar{V}^2 + 2\bar{V} + 2\sin^2(\frac{\bar{\gamma}}{2})\right| = \left|\bar{V}^2 + 2\bar{V} + 2\left(1+\bar{V}\right)\sin^2(\frac{\bar{\gamma}}{2}) - 2\,\bar{V}\sin^2(\frac{\bar{\gamma}}{2})\right|$ $\leq \left|\bar{V}^2 + 2\bar{V} + 2\left(1+\bar{V}\right)\sin^2(\frac{\bar{\gamma}}{2})\right| + \left|2\,\bar{V}\sin^2(\frac{\bar{\gamma}}{2})\right|$. For any two numbers x_1 and x_2, $|x_1 + x_2| \leq \sqrt{2\left(x_1^2 + x_2^2\right)}$. Setting $x_1 = \left(\bar{V}^2 + 2\bar{V}\right)$ and $x_2 = 2\left(1+\bar{V}\right)\sin^2(\frac{\bar{\gamma}}{2})$, we find

$$\begin{aligned} \left|\bar{V}^2 + 2\bar{V} + 2\left(1+\bar{V}\right)\sin^2(\frac{\bar{\gamma}}{2})\right| \quad & \leq \quad \sqrt{2}\sqrt{\left(\bar{V}^2 + 2\bar{V}\right)^2 + 4\left(1+\bar{V}\right)^2\sin^4(\frac{\bar{\gamma}}{2})} \\ & \leq \quad \sqrt{2}\sqrt{\left(\bar{V}^2 + 2\bar{V}\right)^2 + 4\left(1+\bar{V}\right)^2\sin^2(\frac{\bar{\gamma}}{2})} \\ & = \quad \sqrt{2}\psi \end{aligned} \tag{5.59}$$

The second inequality above follows from the fact that $\sin^4(\cdot) \leq \sin^2(\cdot)$. Furthermore, we can see that

$$\begin{aligned}
\left(1+\bar{V}\right)\left|2\,\bar{V}\sin^2(\frac{\bar{\gamma}}{2})\right| &\leq \bar{V}_{max}\left|2\,\left(1+\bar{V}\right)\sin^2(\frac{\bar{\gamma}}{2})\right| \\
&= \bar{V}_{max}\sqrt{4\,\left(1+\bar{V}\right)^2\sin^4(\frac{\bar{\gamma}}{2})} \\
&\leq \bar{V}_{max}\sqrt{4\,\left(1+\bar{V}\right)^2\sin^2(\frac{\bar{\gamma}}{2})} \\
&\leq \bar{V}_{max}\psi. \qquad (5.60)
\end{aligned}$$

Using the above observations in the inequality (5.58) we get

$$C_1 \leq \frac{1}{K_{D_e}}\Big[K_D\left(|\bar{\alpha}|_{max}+2|\alpha_e|\right)\left(\sqrt{2}+(\sqrt{2}+1)\bar{V}_{max}\right)+K_L\Big]\sigma\psi. \qquad (5.61)$$

Thus, interconnection condition 1 is satisfied with

$$\begin{aligned}
\beta_1 &= \frac{1}{K_{D_e}}\Big[K_L+K_D\left(|\bar{\alpha}|_{max}+2|\alpha_e|\right)\left(\sqrt{2}+(\sqrt{2}+1)\bar{V}_{max}\right)\Big] \qquad (5.62) \\
\gamma_1 &= 0. \qquad (5.63)
\end{aligned}$$

5.2.2 Interconnection Condition 2

Let us denote the left-hand-side of condition 2 of Theorem 2 by C_2. We compute

$$\begin{aligned}
C_2 &= \frac{\mu\left(c_1\bar{\alpha}+c_3\bar{\Omega}_2\right)}{K_{D_e}V_e^2\left(1+\bar{V}\right)}\Big\{m_0 g\cos(\bar{\gamma}+\gamma_e) \\
&\qquad -\left(K_{L0}+K_L(\bar{\alpha}+\alpha_e)\right)V_e^2\left(1+\bar{V}\right)^2\Big\}. \qquad (5.64)
\end{aligned}$$

Using the equilibrium relation $m_0 g\cos\gamma_e = K_{L_e}V_e^2$ from equation (5.21) (where $K_{L_e} = K_{L0}+K_L\alpha_e$) and recalling that $c_3 = 1$ we can rewrite C_2 as follows:

$$C_2 = -p_1 s_1\bar{\Omega}_2 - p_2\bar{\alpha}\bar{\Omega}_2 - p_3 s_1\bar{\alpha} - p_4\bar{\alpha}^2, \qquad (5.65)$$

where

$$
\begin{aligned}
p_1 &= \frac{\mu}{\left(1+\bar{V}\right)}\left(\frac{K_{L_e}}{K_{D_e}\cos\gamma_e}\right), \\
p_2 &= \frac{\mu K_L\left(1+\bar{V}\right)}{K_{D_e}} > 0 \qquad \text{(assuming } K_L > 0\text{)}, \\
p_3 &= p_1\left\{r_1 + (r_1+r_2)\left(1+\bar{V}\right)^2\right\}, \\
p_4 &= \frac{p_2 p_3}{p_1} = p_2\left\{r_1 + (r_1+r_2)\left(1+\bar{V}\right)^2\right\} > 0, \\
s_1 &= \left(\bar{V}^2 + 2\bar{V}\right)\cos\gamma_e + 2\sin\frac{\bar{\gamma}}{2}\sin\left(\frac{\gamma+\gamma_e}{2}\right).
\end{aligned}
$$

Since $p_4\bar{\alpha}^2 \geq 0$, we have

$$
\begin{aligned}
C_2 &\leq -p_1 s_1\bar{\Omega}_2 - p_2\bar{\alpha}\bar{\Omega}_2 - p_3 s_1\bar{\alpha} \\
&\leq |p_1||s_1|\left|\bar{\Omega}_2\right| + p_2\left|\bar{\alpha}\,\bar{\Omega}_2\right| + |p_3||s_1||\bar{\alpha}|. \qquad (5.66)
\end{aligned}
$$

We closely examine the terms appearing on the right-hand-side of the last inequality.

- $|s_1|$: Inspecting the expression for s_1 we can conclude that

$$
|s_1| \leq \left|\left(\bar{V}^2+2\bar{V}\right)\right| + 2\left|\sin\frac{\bar{\gamma}}{2}\right| = s_1^1 + s_1^2, \qquad (5.67)
$$

  where,

$$
\begin{aligned}
s_1^1 &= \left|\left(\bar{V}^2+2\bar{V}\right)\right| + 2\left(1+\bar{V}\right)\left|\sin\frac{\bar{\gamma}}{2}\right| \leq \sqrt{2}\psi, \\
s_1^2 &= -2\bar{V}\left|\sin\frac{\bar{\gamma}}{2}\right|.
\end{aligned}
$$

We can further calculate that

$$\begin{aligned} s_1^2 &\leq 2\left|\bar{V}\right|\left|\sin\frac{\bar{\gamma}}{2}\right| \\ &= \frac{1}{\left(1+\bar{V}\right)}|\bar{V}|\left|\left(1+\bar{V}\right)2\sin\frac{\bar{\gamma}}{2}\right| \\ &\leq \frac{|\bar{V}|}{\left(1+\bar{V}\right)}\psi. \end{aligned} \tag{5.68}$$

Thus,

$$|s_1| \leq \sqrt{2}\psi + \frac{|\bar{V}|}{\left(1+\bar{V}\right)}\psi. \tag{5.69}$$

- $\left|\bar{\alpha}\,\bar{\Omega}_2\right|$: We start by multiplying and dividing by $\left(1+\bar{V}\right)$:

$$\left|\bar{\alpha}\,\bar{\Omega}_2\right| = \frac{1}{\left(1+\bar{V}\right)}\left(1+\bar{V}\right)\left|\bar{\alpha}\,\bar{\Omega}_2\right| \tag{5.70}$$

For any two numbers x_1 and x_2, $|x_1x_2| \leq \frac{1}{2}\left(x_1^2+x_2^2\right)$. Setting $x_1 = \bar{\alpha}$ and $x_2 = \bar{\Omega}_2$ we have

$$\left|\bar{\alpha}\,\bar{\Omega}_2\right| \leq \frac{1}{2}\left(\bar{\alpha}^2+\bar{\Omega}_2^2\right). \tag{5.71}$$

Multiplying and dividing the relation 5.71 by $\left(1+\bar{V}\right)^2$ we get

$$\begin{aligned} \left|\bar{\alpha}\,\bar{\Omega}_2\right| &\leq \frac{1}{2\left(1+\bar{V}\right)^2}\left(1+\bar{V}\right)^2\left(\bar{\alpha}^2+\bar{\Omega}_2^2\right) \\ &= \frac{1}{2\left(1+\bar{V}\right)^2}\sigma^2. \end{aligned} \tag{5.72}$$

- $|\bar{\alpha}|$, $\left|\bar{\Omega}_2\right|$: Multiplying and dividing $|\bar{\alpha}| = \sqrt{\bar{\alpha}^2}$ by $\left(1+\bar{V}\right)$ we get

$$\begin{aligned} |\bar{\alpha}| &= \frac{1}{\left(1+\bar{V}\right)}\left(1+\bar{V}\right)\sqrt{\bar{\alpha}^2} \\ &\leq \frac{1}{\left(1+\bar{V}\right)}\left(1+\bar{V}\right)\sqrt{\bar{\alpha}^2+\bar{\Omega}_2^2} \\ &= \frac{1}{\left(1+\bar{V}\right)}\sigma. \end{aligned} \tag{5.73}$$

Similarly,

$$\left|\bar{\Omega}_2\right| \leq \frac{1}{\left(1+\bar{V}\right)}\sigma. \tag{5.74}$$

Using the above results as well as expressions for p_1, p_2 and p_3 in inequality (5.66) we calculate

$$\begin{aligned} C_2 &\leq \frac{\mu|K_{L_e}|}{K_{D_e}|\cos(\gamma_e)|}\left\{\sqrt{2}+\frac{|\bar{V}|}{\left(1+\bar{V}\right)}\right\}\left\{\frac{(1+r_1)}{\left(1+\bar{V}\right)^2}+r_1+r_2\right\}\sigma\psi \\ &\quad + \frac{\mu K_L}{2K_{D_e}\left(1+\bar{V}\right)}\sigma^2 \qquad (5.75) \\ &\leq \mu\beta_2'\psi\sigma+\mu\gamma_2'\sigma^2, \qquad (5.76) \end{aligned}$$

where,

$$\begin{aligned} \beta_2' &= \frac{|K_{L_e}|}{K_{D_e}|\cos(\gamma_e)|}\left\{\sqrt{2}+\frac{\max\{-\bar{V}_{min},\bar{V}_{max}\}}{\left(1+\bar{V}_{min}\right)}\right\}\left\{\frac{(1+r_1)}{\left(1+\bar{V}_{min}\right)^2}+r_1+r_2\right\} \qquad (5.77) \\ \gamma_2' &= \frac{K_L}{2K_{D_e}\left(1+\bar{V}_{min}\right)}. \qquad (5.78) \end{aligned}$$

Thus, condition 2 of Theorem 2 is satisfied.

5.2.3 Interconnection Condition 3

Let us denote the left-hand-side of condition 3 of Theorem 2 by C_3. We compute

$$\begin{aligned} C_3 &= \frac{1}{K_{D_e}V_e^2}\Bigg|\left\{\frac{m_0 g\left(\sin\gamma-\sin\gamma_e\right)}{\left(1+\bar{V}\right)^3}+\frac{K_D\left(\bar{\alpha}+2\alpha_e\right)\bar{\alpha}V_e^2}{\left(1+\bar{V}\right)}\right. \\ &\quad \left.+\frac{K_{D_e}V_e^2\left(\bar{V}^2+2\bar{V}\right)}{\left(1+\bar{V}\right)^3}\right\}\frac{r_1\bar{\Omega}_2^2}{r_2} \\ &\quad -\left(r_1+r_2\right)\left\{m_0 g\left(\sin\gamma-\sin\gamma_e\right)+K_D\left(\bar{\alpha}+2\alpha_e\right)\bar{\alpha}V_e^2\left(1+\bar{V}\right)^2\right. \\ &\quad \left.+K_{D_e}V_e^2\left(\bar{V}^2+2\bar{V}\right)\right\}\left(1+\bar{V}\right)\bar{\alpha}^2\Bigg|. \end{aligned} \tag{5.79}$$

In deriving equation (5.79) we have used the following computation:

$$\begin{aligned} f_1 &= \frac{1}{K_{D_e}}\left(-m_0 g\sin\gamma-\left(K_{D0}+K_D\left(\bar{\alpha}+\alpha_e\right)^2V_e^2\left(1+\bar{V}\right)^2\right)\right) \\ &= \frac{1}{K_{D_e}}\left\{-m_0 g\sin\gamma_e+m_0 g(\sin\gamma_e-\sin\gamma)-(K_{D_0}+K_D\alpha_e^2)V_e^2(1+\bar{V})^2\right. \\ &\quad \left.-K_D(\bar{\alpha}^2+2\bar{\alpha}\alpha_e)V_e^2\left(1+\bar{V}\right)^2\right\} \\ &= \frac{1}{K_{D_e}}\left\{-m_0 g(\sin\gamma-\sin\gamma_e)-(K_{D_0}+K_D\alpha_e^2)V_e^2(\bar{V}^2+2\bar{V})\right. \\ &\quad \left.-K_D(\bar{\alpha}^2+2\bar{\alpha}\alpha_e)V_e^2\left(1+\bar{V}\right)^2\right\}. \end{aligned}$$

From equation (5.79) we can derive the following relation,

$$C_3 \le \gamma_2^{''}\sigma^2, \tag{5.80}$$

where,

$$C_3 = \max\{C_3^{t1}, C_3^{t2}\}, \tag{5.81}$$

where

$$
\begin{aligned}
C_3^{t1} &= \frac{2|m_0|g}{\left(1+\bar{V}_{min}\right)^3} + \frac{K_D\left(\bar{\alpha}+2\alpha_e\right)_{max}\bar{\alpha}_{max}V_e^2}{\left(1+\bar{V}_{min}\right)} + \frac{K_{D_e}V_e^2\left(\bar{V}^2+2\bar{V}\right)_{max}}{\left(1+\bar{V}_{min}\right)^3}, \\
C_3^{t2} &= \Big\{2|m_0|g + K_D\left(\bar{\alpha}+2\alpha_e\right)_{max}\bar{\alpha}_{max}V_e^2\left(1+\bar{V}_{max}\right)^2 \\
&\quad + K_{D_e}V_e^2\left(\bar{V}^2+2\bar{V}\right)_{max}\Big\}\left(1+\bar{V}_{max}\right).
\end{aligned}
$$

The term $(\bar{\alpha}^2+2\bar{\alpha}\alpha_e)_{max}$ denotes the maximum value of $(\bar{\alpha}^2+2\bar{\alpha}\alpha_e)$ in $B_{\boldsymbol{q}}$. We note that we have also used the fact that $|\sin\gamma - \sin\gamma_e| \leq 2$ in the above computations.

Thus, we satisfy condition 3 of Theorem 2 with

$$
\beta_2^{''} = 0, \tag{5.82}
$$

and $\gamma_2^{''}$ given by equation (5.81).

By satisfying all conditions of Theorem 2 we have shown that the Lyapunov function,

$$
\begin{aligned}
\nu &= \frac{d}{2}\Bigg\{\Big[r_1+\left(1+\bar{V}\right)^2(r_1+r_2)\Big]\bar{\alpha}^2 + \left[1+\frac{r_1}{r_2\left(1+\bar{V}\right)^2}\right]\bar{\Omega}_2^2 + 2\bar{\alpha}\bar{\Omega}_2\Bigg\} \\
&\quad + (1-d)\left\{\frac{2}{3} - (1+\bar{V})\cos(\bar{\gamma}) + \frac{1}{3}\left(1+\bar{V}\right)^3\right\},
\end{aligned} \tag{5.83}
$$

where $0 < d < 1$, proves the asymptotic stability of the steady glides of the underwater glider for all $0 < \epsilon_i < \min\{\mu_d, \epsilon_i^*\}$, where μ_d is given by equation (5.54) and ϵ_i^*, $i = 1, 2$, are bounds on the positive constants ϵ_i, as defined in Theorem 2.

5.3 Region of Attraction Estimates

In this section we use the results of [127] to compute estimates of the region of attraction of the steady motions of the underwater glider. The material of this section follows the results presented in [129].

In §5.2 we noted that d, the weighting factor of the composite Lyapunov function ν given by equation 5.53, can be chosen such that the size of the region of attraction is optimized. The reference [127] calculates the optimal value of d for the largest estimate of the region of attraction in terms of the bounds of Lyapunov functions of the boundary-layer and reduced subsystems, $\hat{W}$ and Φ, in the domain $B_{\boldsymbol{p}} \times B_{\boldsymbol{q}}$. According to this calculation, if $L_R = \{(\bar{V}, \bar{\gamma}) \in B_{\boldsymbol{p}} \,|\, 0 \leq \Phi \leq v_0\}$ is in the region of attraction of the reduced subsystem and $L_B = \{(\bar{V}, \bar{\gamma}, \bar{\alpha}, \bar{\Omega}_2) \in B_{\boldsymbol{p}} \times B_{\boldsymbol{q}} \,|\, 0 \leq \hat{W} \leq w_0\}$ is in the region of attraction of the boundary layer subsystem, the value of d that yields the largest region of attraction estimate for the full system dynamics is

$$d = \frac{v_0}{v_0 + w_0}. \tag{5.84}$$

The corresponding region of attraction estimate L^* is defined as follows:

$$L^* = \left\{ \left(\bar{V}, \bar{\gamma}, \bar{\alpha}, \bar{\Omega}_2\right) \in B_{\boldsymbol{p}} \times B_{\boldsymbol{q}} \,\middle|\, 0 \leq \nu \leq \frac{v_0 w_0}{v_0 + w_0} \right\}. \tag{5.85}$$

5.3.1 Numerical Example

In this subsection we compute region of attraction estimates for an underwater glider and illustrate how changing certain design parameters will affect the stability guarantees provided by the composite Lyapunov function ν. We consider an underwater glider of a similar hull mass and size as the ROGUE [31], but with a different hull shape. ROGUE had an ellipsoidal shape whereas the glider under consideration here has a spherical shape (since we consider the case of equal added masses). Further, we consider a glider with significantly smaller wings (for lower lift) and moment of inertia than ROGUE. The parameter values for this model are: $m_1 = m_3 = 28$ kg, $m_0 = 0.7$ kg, $K_{L0} = 0$ kg/m, $K_L = 75$ kg/m/rad, $K_{D0} = 2$ kg/m, $K_D = 80$ kg/m/rad^2,

$K_{M0} = 1$ kg, $K_q = -2$ kg.s/rad, $K_M = -50$ kg/rad, $J_2 = 0.02$ kg.m^2. We calculate $\epsilon_1 = 4.784\exp(-3)$, $\epsilon_2 = 4.403\exp(-4)$. Thus, $\mu = \max\{\epsilon_1, \epsilon_2\} = 4.784\exp(-3)$. The reference time scale for the slow dynamics is $\tau_s = 8.361$ s.

The above parameters lead to an equilibrium glide at speed $V_e = 1.684$ m/s and flight path angle $\gamma_e = -53.566$ degrees. We consider a neighborhood of the equilibrium, $B_{\boldsymbol{p}} \times B_{\boldsymbol{q}}$, such that $|\bar{V}| \leq 0.4$ and $|\bar{\alpha}| \leq 0.2$. For this neighborhood the corresponding $\mu_d = 3.635\exp(-3)$, with $d = 0.4423$. Since $\mu > \mu_d$, ν given by equation (5.83) does not guarantee asymptotic stability of the equilibrium in the chosen domain.

If we consider an alternative glider design such that $K_M = -100$ kg/rad *and/or* $J_2 = 0.01$ kg.m^2, with other parameters remaining unchanged, we find $\mu < \mu_d$, and ν can be used to prove asymptotic stability of the equilibrium in the same domain. Note that different values of K_M yield different equilibria whereas changing the value of J_2 does not affect the equilibrium. A higher value of K_M may be realized by considering a larger horizontal tail. A lower J_2 would require a different mass distribution in the spherical hull, with a larger concentration of mass near the center.

We consider $K_M = -100$ kg/rad, $J_2 = 0.02$ kg.m^2, and plot projections of an estimate of the region of attraction of the equilibrium of the glider, provided by ν, onto $(\bar{V}, \bar{\alpha})$ space in Figure 5.2 [129]. The guaranteed region of attraction can be increased by decreasing J_2 or increasing K_M. Decreasing J_2 yields a lower ϵ_2, and increasing K_M yields a lower ϵ_1 (but changing K_M also changes the equilibrium speed and flight path angle). Both help towards increasing the separation between the fast time scales and the slow time scale, decreasing the coupling between the corresponding dynamics. This results in the composite Lyapunov function providing a stability guarantee over a larger domain around the equilibrium point.

We note that the region of attraction estimate provided by the Lyapunov function is rather conservative. For example, simulations suggest that for all $(\bar{\gamma}, \bar{\Omega}_2)$ sections of the phase space shown in Figure 5.2, the projection of the region of attraction spans the $(\bar{V}, \bar{\alpha})$ space. However, the Lyapunov function provides a *stability guarantee* as a function of vehicle parameters, which is useful in control system design presented in Chapter 6.

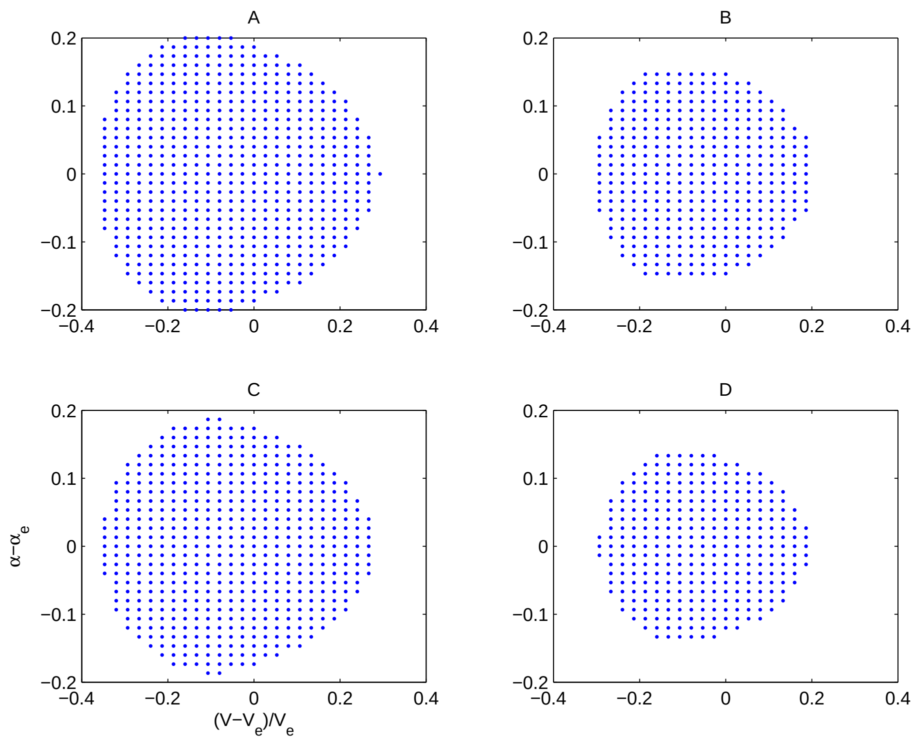

Figure 5.2: Projections of an estimate of the region of attraction on the $(\bar{V}, \bar{\alpha})$ space. The four plots represent projections given different ranges on the other two states. (A) $|\bar{\gamma}| \leq \frac{\pi}{12}, |\bar{\Omega}_2| \leq 0.01$, (B) $|\bar{\gamma}| \leq \frac{\pi}{8}, |\bar{\Omega}_2| \leq 0.01$, (C) $|\bar{\gamma}| \leq \frac{\pi}{12}, |\bar{\Omega}_2| \leq 0.1$, (D) $|\bar{\gamma}| \leq \frac{\pi}{8}, |\bar{\Omega}_2| \leq 0.1$. For the sake of reference we note that $|\bar{V}| = 0.2$ amounts to a deviation of V from equilibrium speed by about 0.36 m/s. [129]

5.4 Extension of Results

In this section we extend singular perturbation reduction to the case of underwater gliders with unequal added masses. This case presents additional technical difficulties due to the stronger coupling between translational and rotational dynamics.

Denoting the difference in added masses $m_3 - m_1$ by Δm, the equations of motion of the underwater glider with unequal added masses may be written as follows for $V > 0$, analogous to equations (5.4)-(5.7):

$$
\begin{aligned}
\dot{V} &= -\frac{\Delta m \cos\alpha}{m_1 m_3}\Big\{m_0 g \sin\theta - L\sin\alpha + D\cos\alpha + (m_1+m_3)\,V\Omega_2\sin\alpha\Big\} \\
&\quad -\frac{1}{m_3}\,(m_0 g\sin\gamma + D) \qquad (5.86)\\
\dot{\gamma} &= -\frac{\Delta m}{m_1 m_3 V}\Big\{(m_0 g\sin\theta - L\sin\alpha + D\cos\alpha)\sin\alpha \\
&\qquad\qquad + \left(m_3\sin^2\alpha - m_1\cos^2\alpha\right)V\Omega_2\Big\} \\
&\qquad\qquad + \frac{1}{m_3 V}\,(-m_0 g\cos\gamma + L) \\
&=: E_2^{'} \qquad (5.87)\\
\dot{\alpha} &= \Omega_2 - E_2^{'} \qquad (5.88)\\
\dot{\Omega}_2 &= \frac{1}{J_2}\Big\{(K_{M0} + K_M\alpha + K_q\Omega_2)\,V^2 + \Delta m V^2\sin\alpha\cos\alpha\Big\}. \qquad (5.89)
\end{aligned}
$$

The equilibrium pitch rate $\Omega_{2e} = 0$ and the equilibrium speed and flight path angle, V_e and γ_e respectively, are given by the same expressions as for the case with equal added masses: equations (5.8)-(5.9). However, the equilibrium angle of attack α_e is a function of Δm. α_e is computed as the solution of the following equilibrium equation:

$$
K_{M0} + K_M\alpha_e + \Delta m\sin\alpha_e\cos\alpha_e = 0. \qquad (5.90)
$$

We define nondimensional state variables $(\bar{V}, \bar{\gamma}, \bar{\alpha}, \bar{\Omega}_2)$, time variable t_n and parameters $\epsilon_1, \epsilon_2, \mu$ exactly as in the case of equal added masses. Equations of motion (5.86)-(5.89) may be expressed in the same compact form as equations (5.28)-(5.29), but the expressions for f and g are correspondingly different.

The boundary-layer subsystem is given by equation (5.30). The component equations contained in (5.30) are expanded for the sake of illustration:

$$\begin{aligned}
\frac{d\bar{\alpha}}{d\tau} &= r_1\bar{\Omega}_2 && (5.91)\\
\frac{d\bar{\Omega}_2}{d\tau} &= -r_2\left\{\bar{\alpha}+\frac{\Delta m}{K_M}\sin\left(\bar{\alpha}+2\alpha_e\right)\cos\bar{\alpha}+\bar{\Omega}_2\right\}\left(1+\bar{V}\right)^2. && (5.92)
\end{aligned}$$

We seek a Lyapunov function candidate of the form,

$$\begin{aligned}
\hat{W} &= \frac{h_1}{2r_2}\bar{\Omega}_2^2+\frac{h_2}{2r_1}\bar{\alpha}^2\left(1+\bar{V}\right)^2+\frac{h_3}{\sqrt{r_1r_2}}\bar{\Omega}_2\bar{\alpha}\left(1+\bar{V}\right)\\
&\quad -\frac{h_1\Delta m}{2K_Mr_1}\left(\frac{\cos 2\left(\bar{\alpha}+\alpha_e\right)}{2}+\bar{\alpha}\sin 2\alpha_e\right)\left(1+\bar{V}\right)^2, && (5.93)
\end{aligned}$$

where h_1, h_2, h_3 are positive constants that will be chosen later.

The gradient of $\hat{W}$ with respect to $\boldsymbol{q}=\left(\bar{\alpha},\bar{\Omega}_2\right)^T$ is

$$\nabla\hat{W}=\begin{pmatrix}\frac{h_2}{r_1}\bar{\alpha}+\frac{h_3}{\sqrt{r_1r_2}\left(1+\bar{V}\right)}\bar{\Omega}_2+\frac{h_1\Delta m}{2K_Mr_1}\left(\sin 2\left(\bar{\alpha}+\alpha_e\right)-\sin 2\alpha_e\right)\\ \frac{h_1}{r_2\left(1+\bar{V}\right)^2}\bar{\Omega}_2+\frac{h_3}{\sqrt{r_1r_2}\left(1+\bar{V}\right)}\bar{\alpha}\end{pmatrix}\left(1+\bar{V}\right)^2. \quad (5.94)$$

Evaluated at the equilibrium, the gradient is equal to the zero vector. The Hessian matrix evaluated at the equilibrium is

$$\nabla^2\hat{W}\Big|_{\left(\bar{\alpha}=0,\,\bar{\Omega}_2=0\right)}=\begin{bmatrix}\frac{h_2}{r_1}+\frac{h_1\Delta m}{K_Mr_1}\cos 2\alpha_e & \frac{h_3}{\sqrt{r_1r_2}}\\ \frac{h_3}{\sqrt{r_1r_2}} & \frac{h_1}{r_2}\end{bmatrix}. \quad (5.95)$$

For the above Hessian matrix to be positive definite we require $h_1>0$ and

$$h_1\left(h_2+\frac{h_1\Delta m}{K_M}\cos 2\alpha_e\right)-h_3^2>0.$$

In that case we satisfy condition (1) of Proposition 1 in a sufficiently small neighborhood $B_{\boldsymbol{q}}$ with k_3 and k_4 equal to the smaller and larger of the two eigenvalues of the above Hessian matrix, respectively.

The derivative of the Lyapunov function $\hat{W}$ with respect to τ is

$$\begin{aligned}\frac{d\hat{W}}{d\tau} &= \left(h_2 - h_1 - h_3\sqrt{\frac{r_2}{r_1}}\left(1+\bar{V}\right)\right)\bar{\alpha}\bar{\Omega}_2 - h_3\sqrt{\frac{r_2}{r_1}}\left(1+\bar{V}\right)^3\bar{\alpha}^2 \\ &\quad - \left(h_1\left(1+\bar{V}\right) - h_3\sqrt{\frac{r_1}{r_2}}\right)\left(1+\bar{V}\right)\bar{\Omega}_2^2 \\ &\quad - h_3\sqrt{\frac{r_2}{r_1}}\left(1+\bar{V}\right)^3\frac{\Delta m}{K_M}\bar{\alpha}\sin\left(\bar{\alpha}+2\alpha_e\right)\cos\bar{\alpha}. \qquad (5.96)\end{aligned}$$

We set

$$h_2 = h_1 + h_3\sqrt{\frac{r_2}{r_1}}\left(1+\bar{V}\right), \qquad (5.97)$$

and assume that $|\alpha_e| \leq \pi/4$ and $|\bar{\alpha}| \leq \alpha_m$, where α_m is some positive number less than or equal to $\sqrt{3}$. Then, it is possible to satisfy condition (2) of Proposition 1 with

$$\begin{aligned}\sigma &= \left(1+\bar{V}\right)\sqrt{\bar{\alpha}^2+\bar{\Omega}_2^2} && (5.98)\\ a_2 &= \min\{a_{21}, a_{22}\} && (5.99)\\ b_2 &= a_2\left(1+\bar{V}_{min}\right)^2, && (5.100)\end{aligned}$$

where,

$$\begin{aligned}a_{21} &= h_3\left(1+\bar{V}_{min}\right)\sqrt{\frac{r_2}{r_1}}\left(1-\left|\frac{\Delta m}{2K_M}\alpha_m\tan 2\alpha_e\right|\right) && (5.101)\\ a_{22} &= h_1 - h_3\sqrt{\frac{r_1}{r_2}}\frac{1}{\left(1+\bar{V}_{min}\right)}. && (5.102)\end{aligned}$$

We omit the details of the above calculation for the sake of brevity. By picking a large enough h_1 we can ensure that $a_{22} > 0$. For $a_{21} > 0$, we require Δm to be small enough. Thus, we are able to prove local exponential stability of the equilibrium of the boundary layer model for sufficiently small Δm and $|\alpha_e| \leq \pi/4$.

The reduced subsystem is given by equation (5.33). The component equations contained in (5.33) are:

$$\frac{d\bar{V}}{dt_n} = \frac{-\tau_s}{m_3 V_e}\left[m_0 g \sin\left(\bar{\gamma}+\gamma_e\right) + K_{D_e} V_e^2 \left(1+\bar{V}\right)^2 + \frac{\Delta m \cos\alpha_e}{m_1} f\right] \quad (5.103)$$

$$\frac{d\bar{\gamma}}{dt_n} = \frac{\tau_s}{m_3 V_e \left(1+\bar{V}\right)}\left[K_{L_e} V_e^2 \left(1+\bar{V}\right)^2 - m_0 g \cos\left(\bar{\gamma}+\gamma_e\right) + \frac{\Delta m \sin\alpha_e}{m_1} f\right], \quad (5.104)$$

where,

$$f = m_0 g \left\{\sin\theta_e \left(1+\bar{V}\right)^2 - \sin\left(\bar{\gamma}+\theta_e\right)\right\}. \quad (5.105)$$

We consider the same Lyapunov function candidate that we used for the case of equal added masses:

$$\Phi = \frac{2}{3} - \left(1+\bar{V}\right)\cos\bar{\gamma} + \frac{1}{3}\left(1+\bar{V}\right)^3. \quad (5.106)$$

Condition (1) of Proposition 2 is satisfied as in §5.1.2.

We compute the derivative of Φ:

$$\frac{d\Phi}{dt_n} = -\left\{\left(\bar{V}+2\right)^2 \bar{V}^2 + 4\left(1+\bar{V}\right)^2 \sin^2\frac{\bar{\gamma}}{2}\right\} + R, \quad (5.107)$$

where,

$$R = \frac{\Delta m}{m_1 K_{D_e} V_e^2}\left(2\sin\left(\frac{\bar{\gamma}+2\alpha_e}{2}\right)\sin\frac{\bar{\gamma}}{2} + \cos\alpha_e\left(\bar{V}^2 + 2\bar{V}\right)\right) f. \quad (5.108)$$

It can be shown that

$$R \leq \frac{2\Delta m|m_0 g|}{m_1 K_{D_e} V_e^2 \left(1+\bar{V}_{min}\right)^2} \left\{ \left(\bar{V}+2\right)^2 \bar{V}^2 + 4\left(1+\bar{V}\right)^2 \sin^2 \frac{\bar{\gamma}}{2} \right\}. \qquad (5.109)$$

We omit the details of the above calculation for the sake of brevity. For Φ to be a valid Lyapunov function, we require

$$\frac{2|\Delta m\, m_0 g|}{m_1 K_{D_e} V_e^2 \left(1+\bar{V}_{min}\right)^2} < 1, \qquad (5.110)$$

which can be satisfied with a small enough Δm or a small enough domain $B_{\boldsymbol{p}}$ (so that $\bar{V}_{min}$ is large enough). Figure 5.3 shows a plot of allowable $|\Delta m|/m_1$ and $\bar{V}_{min}$ combinations for which the Lyapunov function Φ given by equation (5.106) can be used to prove the stability of the equilibrium for $\frac{m_0 g}{K_{D_e} V_e^2} = 1.243$ (corresponding to the equilibrium m_0, K_{D_e} and V_e of the numerical example of §5.3.1).

Thus, the equilibrium of the reduced subsystem is locally exponentially stable. This also means that the solutions of the reduced system described by equations (5.103)-(5.104) approximate solutions of the full model of the underwater glider described by equations (5.86)-(5.89) for an infinite time-interval, for all initial conditions starting in the domain $B_{\boldsymbol{p}} \times B_{\boldsymbol{q}}$. We can also in principle construct a composite Lyapunov function for the case of equal added masses to prove local asymptotic stability of the equilibrium of the full model.

5.5 Summary

In this chapter we use time-scale separation between the slow and fast subsystems of the underwater glider to reduce the dynamics to the slow subsystem using singular perturbation theory. The slow subsystem is a generalization of the phugoid-mode model of Chapter 4. In fact, the Lyapunov function used to prove the stability

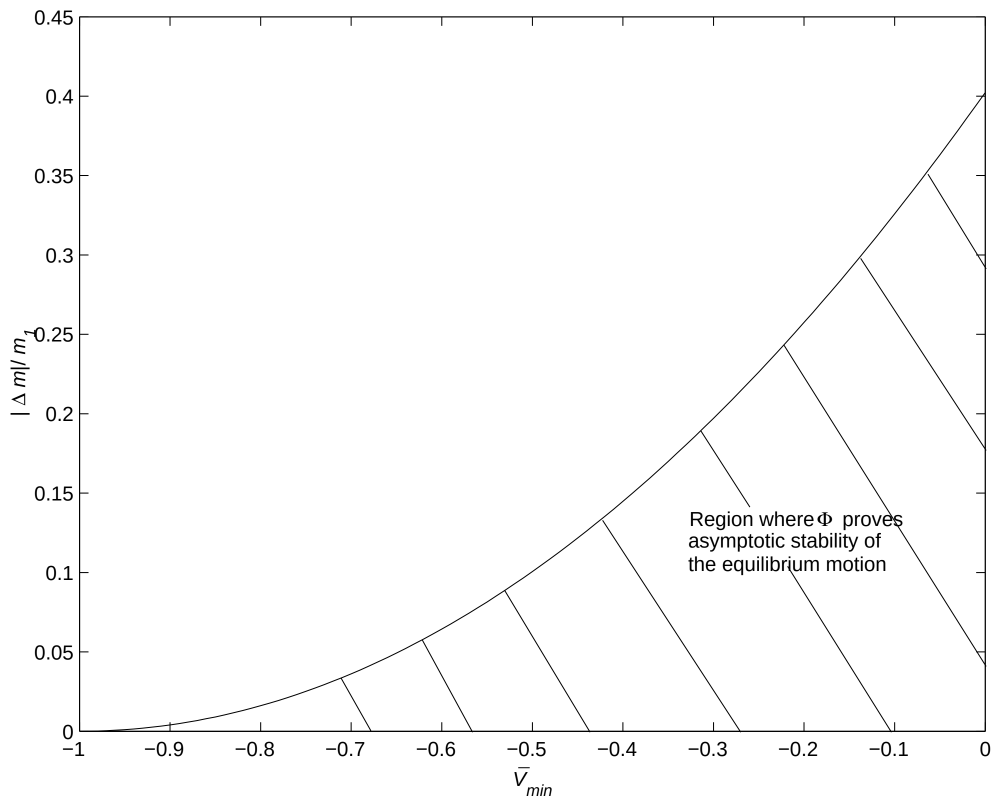

Figure 5.3: Trade off between domain size (determined by $\bar{V}_{min}$) and $|\Delta m|/m_1$ for using Lyapunov function Φ to prove asymptotic stability of the equilibrium.

of the equilibrium of the slow subsystem is derived from the Hamiltonian function presented in §4.1. The Lyapunov functions for the slow and fast subsystems are used to construct a composite Lyapunov function for proving the stability of the equilibrium of the full underwater glider system. The composite Lyapunov function is used to derive equilibrium region-of-attraction guarantees.

Chapter 6

Underwater Glider Control

In this chapter we use results of Chapter 5 to design control laws for stabilizing steady gliding motions of underwater gliders. We consider the case of equal added masses to better elucidate the steps of the design process. Using the results of §5.4, the design procedure may be readily extended to the more general case of unequal added masses, although this would involve significantly more algebra than for equal added masses considered in this chapter. We present control designs for three different underwater glider control configurations. In §6.1 control actuation is in the form of a pure torque. Buoyancy control is considered in §6.2. Elevator-type control configuration, commonly employed in aircraft, is presented in §6.3. The elevator, used primarily to regulate the angle of attack, induces a moment-to-force coupling, which makes the control problem challenging. We take this coupling into account in our analysis. In all three configurations we design control laws using the composite Lyapunov function constructed in the previous chapter. The results of this chapter are based on the presentation in [130].

6.1 Pure Torque Control

In this section we consider an underwater glider equipped with torque control, which is used to regulate the equilibrium angle of attack. The torque control in an operational underwater glider is realized by redistributing internal mass. With respect to the model presented in Chapter 2, this amounts to controlling the position ($\boldsymbol{r}_P$) of the moving mass $\bar{m}$. In the present section, we approximate the effect of this control action by a pure torque.

The above simplification is partly motivated by the fact that a different position of $\bar{m}$ at equilibrium results in a different pure torque acting on the system. This may be readily seen by inspecting equations (2.15)-(2.20). Since $\Omega_2 = 0$ at equilibrium the terms r_{P1} and r_{P3} appear only in the torque balance equation (2.20).

We also note that torque control may be realized by using external moving surfaces, such as an elevator, on the underwater glider. Such a control mechanism typically induces significant additional external forces, coupled to torque generation. We consider elevator control action with moment-to-force coupling in §6.3.

The equations of motion of the underwater glider with a pure torque control actuation are:

$$\dot{V} = -\frac{1}{m_1}\left(m_0 g \sin\gamma + D\right) \tag{6.1}$$

$$\dot{\gamma} = \frac{1}{m_1 V}\left(-m_0 g \cos\gamma + L\right) \tag{6.2}$$

$$\dot{\alpha} = \Omega_2 - \frac{1}{m_1 V}\left(-m_0 g \cos\gamma + L\right) \tag{6.3}$$

$$\dot{\Omega}_2 = \frac{1}{J_2}\Big[\left(K_{M0} + K_M\alpha + K_q\Omega_2\right)V^2 + u\Big], \tag{6.4}$$

where u represents the control torque.

Choosing u appropriately gives a desired equilibrium angle of attack α_e. α_e may be determined on the basis of either a desired equilibrium speed V_e or a desired equilibrium flight path angle γ_e. We cannot design u to achieve both a desired V_e and a desired γ_e but can achieve the desired value of one of these two states. Furthermore, we can design u to improve the region of attraction estimate provided by the composite Lyapunov function constructed in §5.2. We choose u to mimic the moment due to lift:

$$u = (K_{M0u} + K_{Mu}\alpha + K_{qu}\Omega_2)\, V^2 \tag{6.5}$$

The controlled dynamics look like the uncontrolled underwater glider dynamics, except that the net moment coefficients are modified by K_{M0u}, K_{Mu}, and K_{qu} to achieve desired values. They may be chosen to increase the separation between the time scales of the fast and slow subsystems of the closed-loop dynamics. As we noted in the previous chapter, greater separation implies weaker coupling between the two subsystems, which leads to larger estimates of the region of attraction of the closed-loop equilibrium. We note that (6.5) and the other feedback control laws presented in this thesis assume perfect, lag-free measurements of all system states. Practical implementations of these control laws must take into consideration measurement errors as well as lag between measurements and control actuation.

With feedback control, the closed-loop equilibrium angle of attack, α_e is

$$\alpha_e = -\left(\frac{K_{M0} + K_{M0u}}{K_M + K_{Mu}}\right),$$

and the closed-loop small parameters ϵ_i are,

$$\begin{aligned}
\epsilon_1 &= \frac{K_{D_e} V_e}{m_1} \frac{(K_q + K_{qu})}{(K_M + K_{Mu})} \\
\epsilon_2 &= -\frac{K_{D_e} V_e^3}{m_1} \frac{J_2}{(K_q + K_{qu})},
\end{aligned}$$

where V_e refers to the closed-loop equilibrium speed. We choose K_{Mu} and K_{qu} to ensure that $\epsilon_1 > 0$ and $\epsilon_2 > 0$. The constants K_{Mu} and K_{qu} may be chosen to set small enough ϵ_i. After picking ϵ_i we may pick K_{M0u} to obtain a desired α_e. The desired α_e itself may be calculated using equations (5.8)-(5.9) such that we achieve a specified V_e or γ_e.

6.1.1 Improving Region of Attraction Guarantee

In this subsection we further elaborate on how various factors determine the region of attraction estimate, and how we can systematically pick the control constants K_{Mu} and K_{qu} to obtain a larger guaranteed region of attraction.

The region of attraction guarantee is strongly influenced by $\mu = \max\{\epsilon_1, \epsilon_2\}$. This can be seen by the following argument: for obtaining a larger region of attraction guarantee we need to start by considering the system dynamics in a correspondingly larger domain $B_p \times B_q$. The domain must necessarily be larger than the desired region of attraction guarantee. In fact, we must consider a domain which is a large enough superset of the required guarantee, i.e., we need to consider large enough values of $\bar{V}_{max}$ and $\bar{\alpha}_{max}$, and small enough values of $\bar{V}_{min}$ and $\bar{\alpha}_{min}$. These bounds influence the constants β_1, $\beta_2^{'}$, $\beta_2^{''}$, γ_1, $\gamma_2^{'}$, $\gamma_2^{''}$ of Theorem 2. Less conservative bounds lead to larger values for the above constants, which imply a smaller μ_d, evident by inspecting equation (5.54). Furthermore, Theorem 2 also requires $\mu < \mu_d$ for the composite Lyapunov function ν given by equation (5.53) to prove asymptotic stability of the equilibrium. Consequently, a larger guarantee of region of attraction requires μ to be smaller, i.e., ϵ_i to be smaller. In other words, we require a greater separation between the fast and slow time scales.

We propose to pick K_{Mu} and K_{qu} that determine ϵ_i in a way that does not influence a given choice of $r_1 = \frac{\mu}{\epsilon_1}$ and $r_1 = \frac{\mu}{\epsilon_2}$. This is because r_1 and r_2 also influence $\beta_2^{'}$, $\gamma_2^{'}$, and $\gamma_2^{''}$, which determine μ_d. By keeping the r_i's invariant we will have a simple way of adjusting K_{Mu} and K_{qu} to improve the region of attraction estimate.

Keeping r_i's constant amounts to keeping the ratio ϵ_1/ϵ_2 constant. Thus, we pick K_{Mu} and K_{qu} such that the following constraint equation is satisfied,

$$J_2 \frac{\epsilon_1}{\epsilon_2} = \frac{(K_q + K_{qu})^2}{(K_M + K_{Mu})} V_e^2 = \frac{K_q^2}{K_M} V_{e,ol}^2, \tag{6.6}$$

where V_e and $V_{e,ol}$ are the closed-loop and the open-loop equilibrium speeds respectively.

To summarize, given a desired size of the region of attraction we can pick K_{Mu} and K_{qu} such that equation (6.6) is satisfied and $\mu < \mu_d$. This condition ensures that the separation of time scales between the fast rotational dynamics and the slow translational dynamics is large enough so that composite Lyapunov function ν proves closed-loop stability. As in Chapter 5, ν gives us an analytical, nonlinear stability result consistent with the standard phugoid-mode approximation based on sufficient separation between (stable) eigenvalues of short-period and phugoid-modes. We note that larger values of K_{Mu} and K_{qu} that give larger separation of time scales lead to larger control signals. An upper bound on the control signal will determine the largest possible region of attraction guarantee provided by the control law (6.5) and the composite Lyapunov function ν.

6.2 Buoyancy Control

Underwater gliders use buoyancy control along with internal mass redistribution to change their gliding speed and flight path angle. In this section we continue to keep the center of mass fixed at the center of buoyancy and study the buoyancy control action.

Changing buoyancy alone does not affect the equilibrium angle of attack α_e, which is determined entirely by pitching moment coefficients. Thus we cannot alter the equilibrium flight path angle of the underwater glider using just buoyancy control.

However, we may design a buoyancy control law that stably changes the equilibrium gliding speed.

First, given a desired steady gliding speed V_e, we determine the corresponding equilibrium value of the buoyancy mass m_{0e} using equation (5.8):

$$m_{0e} = \pm \left(\frac{1}{g}\right) \sqrt{K_{D_e}^2 + K_{L_e}^2} V_e^2, \tag{6.7}$$

where the sign of m_{0e} is determined by the sign of γ_e. m_{0e} is positive for negative γ_e and vice-versa.

Following [6], the buoyancy control action is simply modelled as follows:

$$\frac{d\bar{m}_0}{dt_n} = u, \tag{6.8}$$

where $\bar{m}_0 := \frac{m_0 - m_{0e}}{m_e}$ represents a nondimensional buoyancy mass. m_e is the total equilibrium mass of the glider.

We pick the following proportional buoyancy control law to achieve the calculated m_{0e}:

$$u = -K_b \bar{m}_0. \tag{6.9}$$

It remains to be shown that the above control law yields a stable closed-loop system. This is done by modifying the composite Lyapunov function of §5.2.

Equations (5.20)-(5.23) appended with equation (6.8), along with the control law (6.9), describe the dynamics of our closed-loop system. We note that we define the nondimensional state variables using equilibrium values of the closed-loop system. We propose the following Lyapunov function candidate to prove asymptotic stability of the equilibrium:

$$\nu_b = \nu + \frac{1}{2}\bar{m}_0^2, \tag{6.10}$$

where ν is given by equation (5.83) from §5.2.

The derivative of ν_b is

$$\begin{aligned} \frac{d\nu_b}{dt_n} &= \frac{d\nu}{dt_n} + \frac{1}{2}\frac{d\bar{m}_0^2}{dt_n} \\ &= \frac{d\nu}{dt_n} - K_b\bar{m}_0^2. \end{aligned} \tag{6.11}$$

We note that ν is independent of $\bar{m}_0$. So $\frac{d\nu}{dt_n}$ is still given by equation (5.55) from Theorem 2 (for constant buoyancy). Substituting equation (5.55) in equation (6.11) we get

$$\frac{d\nu_b}{dt_n} \leq -c\left\{\bar{V}^2 + \bar{\gamma}^2 + \bar{\alpha}^2 + \bar{\Omega}_2^2\right\} - K_b\bar{m}_0^2, \tag{6.12}$$

for some $c > 0$. Thus, the closed-loop system is locally asymptotically stable.

The region of attraction of the closed-loop system is related to the region of attraction of the open-loop system. If the set $B_o = \{(\boldsymbol{p}, \boldsymbol{q}) \mid \|(\boldsymbol{p}, \boldsymbol{q})\| \leq r_o\}$ is in the region of attraction of the open-loop system, an estimate of the closed-loop region of attraction is given by,

$$B_c = \left\{(\boldsymbol{p}, \boldsymbol{q}, \bar{m}_0)\middle| \|(\boldsymbol{p}, \boldsymbol{q})\|^2 + \bar{m}_0^2 \leq r_o^2\right\}. \tag{6.13}$$

6.3 Elevator Control

In this section we consider an underwater glider equipped with an external control surface, an aft elevator, in addition to the buoyancy control of the previous section.

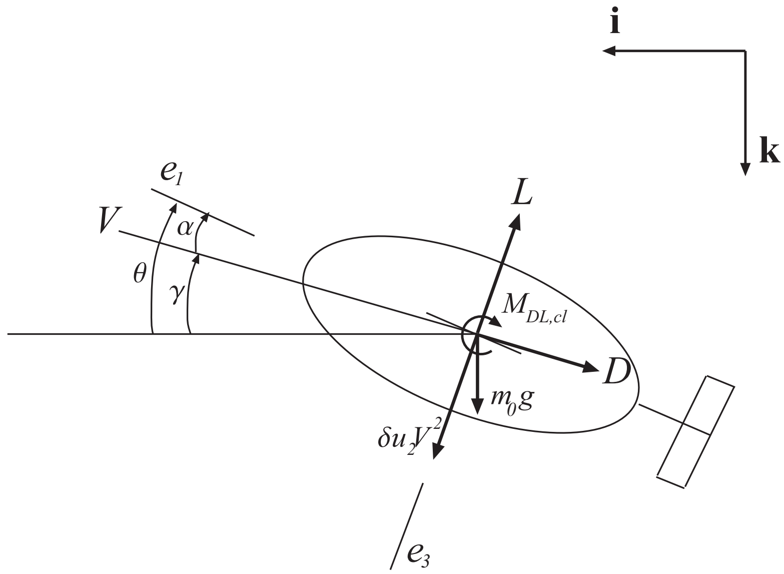

Figure 6.1: All external forces and moments acting on the underwater glider equipped with elevator and buoyancy controls. $\boldsymbol{V}$ is the velocity vector. Forces D and L are the hydrodynamic lift and drag. M_{DL} is the hydrodynamic pitching moment, $K_M u_2 V^2$ is the pitching moment due to elevator control, $\delta u_2 V^2$ is the elevator induced force, and $m_0 g$ is the net force due to gravity.

We now denote the buoyancy control by u_1. We model the elevator action as application of an external torque $K_M u_2 V^2$, quite like the control action considered in §6.1. However, in this section we also consider a coupling force induced by the elevator action. The magnitude of the coupling force is $\delta u_2 V^2$, where δ is a coupling factor. It acts along the 3-axis of the underwater glider. Figure 6.1 shows all the forces and torques acting on the underwater glider in this control scenario.

The nondimensional equations of motion of the underwater glider (with equal added masses and coincident centers of buoyancy and gravity) equipped with elevator and buoyancy controls are:

$$\frac{d\bar{V}}{dt_n} = -\frac{1}{K_{D_e} V_e^2}\Big\{m_0 g \sin(\bar{\gamma} + \gamma_e) + D - h \sin(\bar{\alpha} + \alpha_e)\Big\} \tag{6.14}$$

$$
\begin{aligned}
\frac{d\bar{\gamma}}{dt_n} &= \frac{1}{K_{D_e}V_e^2(1+\bar{V})}\Big\{-m_0 g\cos(\bar{\gamma}+\gamma_e)+L \\
&\qquad\qquad + \; h\cos\left(\bar{\alpha}+\alpha_e\right)\Big\} \;=:\; \bar{E}_2 &(6.15)\\
\frac{d\bar{m}_0}{dt_n} &= u_1 &(6.16)\\
\epsilon_1\frac{d\bar{\alpha}}{dt_n} &= \bar{\Omega}_2-\epsilon_1\bar{E}_2 &(6.17)\\
\epsilon_2\frac{d\bar{\Omega}_2}{dt_n} &= -\left(\bar{\alpha}+\bar{\Omega}_2-\bar{u}_2\right)\left(1+\bar{V}\right)^2, &(6.18)
\end{aligned}
$$

where $h=\delta(\bar{u}_2+u_{2e})V_e^2(1+\bar{V})^2$ and $\bar{u}_2=u_2-u_{2e}$. The term u_{2e} is a reference value of the control angle of attack u_2. We take u_{2e} to be the equilibrium value of u_2.

The total closed-loop pitching moment acting on the glider is equal to

$$
M_{DL,\text{ closed loop}}=\left(K_{M_0}+K_M\alpha+K_q\Omega_2+K_M u_2\right)V^2. \qquad (6.19)
$$

At equilibrium $\Omega_2=0$. Thus, the closed-loop equilibrium angle of attack is

$$
\alpha_e=-\frac{K_{M0}}{K_M}+u_{2e}. \qquad (6.20)
$$

Since we have two control inputs we can specify both desired steady speed V_e and desired steady flight path angle γ_e. As before, control saturation limits restrict the attainable range of steady glides. Given a desired V_e and γ_e we first determine the corresponding equilibrium buoyancy mass m_{0e} and angle of attack α_e using the equilibrium equations of translational dynamics - equations (6.14)-(6.15). Then the equilibrium value of u_2 may be determined using equation (6.20). We note that u_{2e} must necessarily be within the control saturation limits.

We pick the following control laws for u_1 and u_2:

$$
\begin{aligned}
u_1 &= -K\bar{m}_0 \quad (K>0) &(6.21)\\
u_2 &= u_{2e}. &(6.22)
\end{aligned}
$$

Theorem 3. *The closed-loop equilibrium of the underwater glider system with elevator and buoyancy controls, described by equations of motion (6.14)-(6.18) and the control laws (6.21)-(6.22), is locally asymptotically stable provided the elevator moment-to-force coupling factor δ is small enough such that*

$$K'_{D_e} \ := \ K_{D0} + K_D\alpha_e^2 - \delta u_{2e} V_e^2 \sin\alpha_e \ > \ 0. \tag{6.23}$$

Proof We outline the proof in two steps. First, we prove the stability of the closed-loop system with $\bar{m}_0 = 0$. Then, we may use the same argument as that of §6.2 to conclude local asymptotic stability of the equilibrium for the system including buoyancy control.

For the first step we compare equations (6.14)-(6.15), (6.17)-(6.18), with m_0 set to m_{0e}, to equations of the uncontrolled underwater glider system of Chapter 5, represented by equations (5.28)-(5.29).

We note that the boundary-layer subsystem of the present model is identical in form to the boundary-layer subsystem represented by equation (5.30). Thus, the equilibrium of the boundary-layer subsystem is the origin, i.e., $\bar{\Omega} = \bar{\alpha} = 0$. This also implies that the reduced subsystem is of the form represented by equation (5.33). However, the expression of f is slightly different in the present case. It includes the elevator moment coupling force, and is given by the right-hand-side of the following equations:

$$\frac{d\bar{V}}{dt_n} \ = \ -\frac{1}{K'_{D_e}V_e^2}\left\{m_{0e}g\sin\left(\bar{\gamma}+\gamma_e\right) + K'_{D_e}V_e^2\left(1+\bar{V}\right)^2\right\} \tag{6.24}$$

$$\frac{d\bar{\gamma}}{dt_n} \ = \ \frac{1}{K'_{D_e}V_e^2\left(1+\bar{V}\right)^2}\left\{-m_{0e}g\cos\left(\bar{\gamma}+\gamma_e\right) + K'_{L_e}V_e^2\left(1+\bar{V}\right)^2\right\}, \tag{6.25}$$

where K'_{D_e} is the effective equilibrium drag coefficient, given by equation (6.23) and

$$K'_{L_e} = K_{L0} + K_L \alpha_e + \delta u_{2e} \cos \alpha_e, \tag{6.26}$$

is the effective equilibrium lift coefficient. We note that we have also redefined the reference time variable t_n in terms of K'_{D_e}:

$$t_n = \frac{t}{\tau_s}, \qquad \text{with} \ \ \tau_s = \frac{m_1}{K'_{D_e} V_e}. \tag{6.27}$$

Thus, the exponential stability of the equilibrium of the reduced subsystem follows from Proposition 2 provided the effective drag constant $K'_{D_e} > 0$ so that the nondimensional time variable t_n has the same sense as t. This would also ensure the exponential stability of the equilibrium of the boundary-layer subsystem through Proposition 1. The interconnection conditions of Theorem 2 are also satisfied. Thus, if $K'_{D_e} > 0$ we may use the Lyapunov function ν given by equation (5.83) to conclude the local asymptotic stability of our system given by equations (6.14)-(6.18), with $u_1 = 0$ and $m_0 = m_{0e}$.

Now, we can use the same argument as in §6.2 to conclude that the appended Lyapunov function,

$$\nu_b = \nu + \frac{1}{2}\bar{m}_0^2, \tag{6.28}$$

proves local asymptotic stability of the equilibrium of the system with $u_1 = -K\bar{m}_0$. This completes the proof of Theorem 3. $\Box$

Numerical Example

To illustrate the stability of the closed-loop system given by equations (6.14)-(6.18), (6.21)-(6.22) we present a numerical simulation for an underwater glider with the following parameters: $m = m_1 - m_0 = m_3 - m_0 = 28$ kg, $K_{L0} = 0$ N(s/m)^2, $K_L = 300$

$N(s/m)^2$, $K_{D0} = 18$ $N(s/m)^2$, $K_D = 110$ $N(s/m)^2$, $K_q = -5$ $Nms(s/m)^2$, $K_{M0} = 1$ $Nm(s/m)^2$, $K_M = -40$ $Nm(s/m)^2$, $\delta = 0.3$. We seek to stabilize the glider to an equilibrium specified by a speed $V_e = 1$ m/s and flight path angle $\gamma_e = -45^o$. The corresponding equilibrium angle of attack is $\alpha_e = 3.51^o$ and buoyancy $m_{0e} = 2.657$ kg. The time-scaling parameters are $\epsilon_1 = 0.075$ and $\epsilon_2 = 0.012$. Figure 6.2 shows the motion of the glider in the longitudinal plane as well as the evolution of the five system states for 10 s.

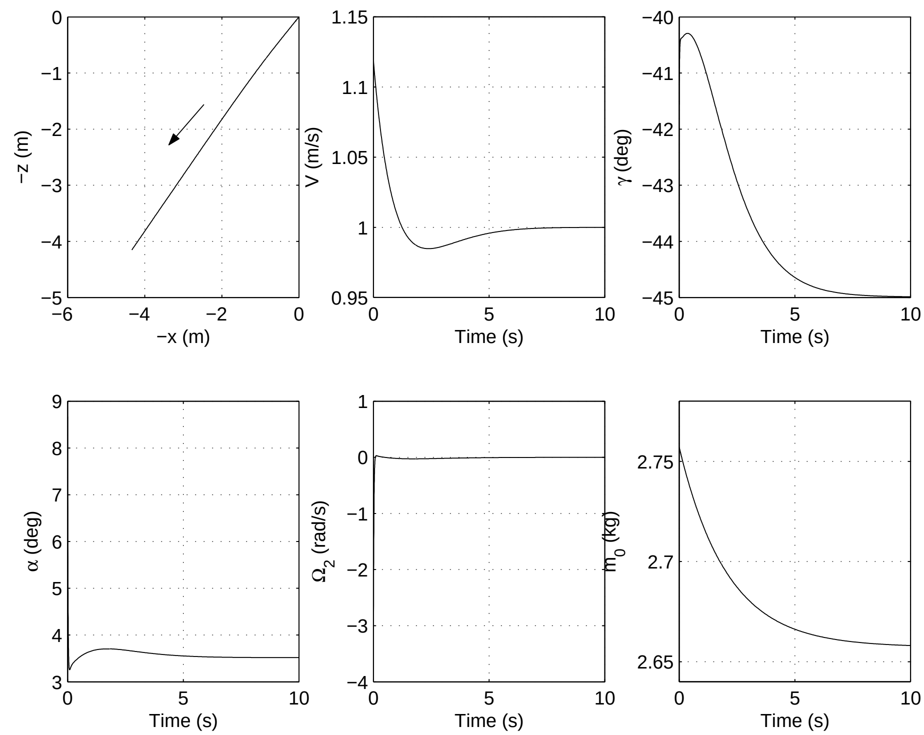

Figure 6.2: Elevator Control Simulation

In the next chapter we use controlled steady gliding results similar to those presented in this chapter to design approximate trajectory tracking methods for the Conventional Take-Off and Landing (CTOL) aircraft model introduced in [36]. One of the difficulties of exact trajectory tracking for the underwater glider and the CTOL aircraft is a consequence of the moment-to-force coupling of elevator control, which demands application of large control inputs. It may not be possible to realize such inputs on underwater gliders, and in the case of both underwater gliders and aircraft, it is desirable to use lower control inputs. An alternative trajectory tracking method that uses steady gliding segments to approximate desired trajectories may demand lower control actuation than methods that seek to track trajectories by inverting the dynamics. The results of this chapter may be combined with the approximate tracking methodology presented in the following chapter to design low-energy trajectory tracking and maneuver regulation solutions for underwater gliders.

Chapter 7

Approximate Trajectory Tracking

In this chapter we present an application of gliding stability results for the position tracking problem of a model of Conventional Take-Off and Landing (CTOL) aircraft. The eventual goal of this work is to design trajectory tracking or maneuver regulation controllers for underwater gliders. The CTOL aircraft, equipped with thrust and elevator controls, is more maneuverable than the underwater glider and makes a simpler, first application for the approximate trajectory tracking methodology presented in this chapter. We note that there is a huge amount of literature on CTOL aircraft control, many concerning more complex vehicle and actuation models than the one presented here. For example, there have been several studies concerning design of feedback control laws for optimally regulating aircraft motion through wind shear [131, 132, 133, 134, 135]. The particular model considered in this chapter has also been studied in the context of trajectory tracking and maneuver regulation in many references including [36, 62, 136, 137]. The main feature of our approach is the use of stabilizable, steady gliding motions for approximately tracking desired trajectories. Use of steady gliding motions is motivated by the underwater glider application and yields control laws that demand low actuation energy.

The CTOL aircraft model, considered in [36], is presented in §7.1. The CTOL model is a nonminimum phase system if the output is taken to be the position of the aircraft. The nonminimum phase nature of the system makes trajectory tracking by inversion of dynamics challenging, as described in §7.3.1. In §7.3.2 we propose a methodology for approximate trajectory tracking by using control laws that exponentially stabilize any desired steady glide of the CTOL aircraft, presented in §7.2. The results in §7.2-§7.3 follow the presentation of [138].

7.1 Conventional Take-Off and Landing Aircraft Model

The CTOL model, presented in [36], describes the longitudinal dynamics of a conventional aircraft. The model includes the lift and drag forces acting on the aircraft. The actuation is in the form of a thrust force control, u_1, and an elevator moment control, u_2. The model also incorporates the moment-to-force coupling: the action of an aft elevator control induces an external force on the aircraft that opposes the ultimate response. This induced force causes the CTOL model to be nonminimum phase for position tracking.

7.1.1 Equations of Motion

Let the position of the CTOL aircraft in the vertical plane be described by (x, y) with respect to an inertial frame fixed on Earth. The orientation of the aircraft is described by the aircraft pitch angle θ. The pitch angle is the angle made by the long axis of the aircraft with the horizontal.

The inertial velocity of the aircraft is $(\dot{x}, \dot{y})$, which may also be represented in terms of coordinates (V, γ), where $V = \sqrt{\dot{x}^2 + \dot{y}^2}$ is the aircraft speed and $\gamma = \tan^{-1} \frac{\dot{y}}{\dot{x}} \in (-\pi, \pi]$ is the aircraft flight path angle. The pitch angle of the aircraft is $\theta \in (-\pi, \pi]$ and the angle of attack is $\alpha = \theta - \gamma$. The rate of change of pitch angle is $\Omega_2 := \dot{\theta}$.

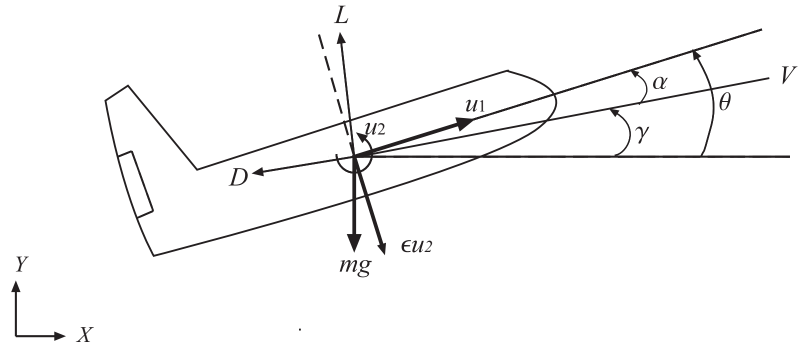

Figure 7.1: Aerodynamic forces and controls acting on the CTOL aircraft.

Figure 7.1 shows all the external forces and torques acting on the aircraft. The lift force L acts perpendicular to the velocity vector $\boldsymbol{V}$ and the drag force D acts along the direction opposite to $\boldsymbol{V}$. The thrust control is modelled by the force u_1, acting along the long axis of the aircraft. The control moment u_2 is due to the elevator actuation. This moment induces the coupling force ϵu_2, acting perpendicular to u_1. The factor ϵ describes the strength of moment-to-force coupling.

The aerodynamic lift and drag forces for the aircraft are modelled to be proportional to the square of the aircraft speed, similar to lift and drag modelling for the underwater glider in §2.2.4. However, the formulation of the aerodynamic coefficients is slightly different. The model for the lift and drag forces for the CTOL aircraft are given by the following equations:

$$L = a_L(1 + c\alpha)V^2 \cdot \frac{\rho A_W}{2} \tag{7.1}$$

$$D = a_D(1 + b(1 + c\alpha)^2)V^2 \cdot \frac{\rho A_W}{2}, \tag{7.2}$$

where a_L, a_D, b and c are non-dimensional coefficients, ρ is the density of air, and A_W is the wing (reference) area. The model for the lift force is identical to that considered for the underwater glider in §2.2.4 with the following mapping between parameters:

$$a_L = \frac{2K_{L0}}{\rho A_W} \tag{7.3}$$

$$c = \frac{K_L}{K_{L0}}. \tag{7.4}$$

The coefficient of drag force in the CTOL model includes a dependence on α in addition to a dependence on α^2 and α^0. The α dependence is not considered for the drag model of the underwater glider presented in §2.2.4.

The dynamic equations of motion for the CTOL aircraft are:

$$m\ddot{x} = -D\cos\gamma - L\sin\gamma + u_1\cos\theta + \epsilon u_2 \sin\theta \tag{7.5}$$

$$m\ddot{y} = -D\sin\gamma + L\cos\gamma + u_1\sin\theta - \epsilon u_2 \cos\theta - mg \tag{7.6}$$

$$J\ddot{\theta} = u_2, \tag{7.7}$$

where m is the aircraft mass, J is its moment of inertia and g is the acceleration due to gravity. For the rest of this section and sections 7.2-7.3 we set $\frac{\rho A_W}{2} = 1$ kg/m, $m = 1$ kg, $g = 1$ kg/m^2 and $J = 1$ kg-m^2. This choice of parameters leads us to the form of equations presented in [36] but does not affect the stability results or the tracking methodology presented in this chapter.

In the following section we design control laws u_1 and u_2 in order to obtain exponentially stable, steady gliding motions with arbitrary steady gliding speed V_e and steady flight path angle γ_e.

7.2 Stabilizing Steady Glides of Aircraft

In this section we derive control laws u_1 and u_2 for the CTOL aircraft model in order to exponentially stabilize desired, steady gliding flights. We pick our control laws independent of the aircraft position (x, y). This makes the closed-loop system invariant with respect to x and y. This allows the reduction of the CTOL aircraft dynamics, represented by equations (7.5)-(7.7), defined on the phase space $T\mathbb{R}^2 \times TS^1$, to a system defined on $(T\mathbb{R}^2 \times TS^1)/\mathbb{R}^2$. The steady glides are fixed points of the reduced system. The reduced system may be represented using just four states: $(V, \gamma, \theta, \Omega_2)$. A fixed point of the reduced system corresponds to a set of constant values of states, $(V_e, \gamma_e, \theta_e, \Omega_{2e})$, with $\Omega_{2e} = 0$. From here onwards we simply refer to the CTOL aircraft reduced system defined on $(T\mathbb{R}^2 \times TS^1)/\mathbb{R}^2$ as "CTOL aircraft dynamics" or just "CTOL dynamics".

We define nondimensional state variables to describe CTOL aircraft dynamics, analogous to those used for describing underwater glider dynamics in §5.1:

$$\bar{V} = \frac{V - V_e}{V_e} \tag{7.8}$$

$$\bar{\gamma} = \gamma - \gamma_e \tag{7.9}$$

$$\bar{\theta} = \theta - \theta_e \tag{7.10}$$

$$\bar{\Omega}_2 = T\Omega_2, \tag{7.11}$$

where T is a reference time interval. In terms of the nondimensional states the fixed point of interest of the CTOL dynamics is the origin and the equations of motion are

$$\dot{\bar{V}} = \frac{1}{V_e}\Big\{-\sin(\bar{\gamma}+\gamma_e) - K_{Dr}(\alpha)V_e^2(1+\bar{V})^2 + u_1\cos\alpha + \epsilon u_2 \sin\alpha\Big\} \tag{7.12}$$

$$\dot{\bar{\gamma}} = \frac{1}{V_e(1+\bar{V})}\Big\{-\cos(\bar{\gamma}+\gamma_e) + K_{Li}(\alpha)V_e^2(1+\bar{V})^2 + u_1\sin\alpha - \epsilon u_2 \cos\alpha\Big\} \tag{7.13}$$

$$\dot{\bar{\theta}} = \bar{\Omega}_2/T \tag{7.14}$$

$$\dot{\bar{\Omega}}_2 = Tu_2, \tag{7.15}$$

where $K_{Dr}(\alpha) = a_D(1+b(1+c\alpha)^2)$ and $K_{Li}(\alpha) = a_L(1+c\alpha)$. Recall that $\alpha = \theta - \gamma =$

$\bar{\theta} + \theta_e - (\bar{\gamma} + \gamma_e)$.

We interpret the CTOL aircraft dynamics as an interconnected system containing a rotational subsystem and a translation subsystem in §7.2.2. The control law design preserves the decoupling of the rotational dynamics but injects useful terms, defined in §7.2.4, into the translational subsystem in such a way that the two subsystems have exponentially stable equilibria. The coupling between the two subsystems is small enough for the interconnected system representing the CTOL aircraft dynamics to have an exponentially stable, desired equilibrium. We note that the approach presented here does not explicitly use singular perturbation theorems discussed in Chapters 5 and 6. However, the coupling between the interconnected subsystems is analogous to the time-scale separation in the underwater glider dynamics study: a stronger coupling between the two subsystems of the interconnected CTOL system has similar effects as a smaller time-scale separation between the slow and fast subsystems of the underwater glider described in Chapter 5.

We propose the following control laws for stabilizing desired CTOL aircraft equilibria:

$$u_1 = w_{11} \tag{7.16}$$

$$u_2 = w_{21} + w_{22}, \tag{7.17}$$

where,

$$w_{11} = -k_1 \sin(\bar{\theta} + \theta_e) - k_2 \cos(\bar{\theta} + \theta_e) \tag{7.18}$$

$$w_{21} = (k_1/\epsilon) \cos(\bar{\theta} + \theta_e) - (k_2/\epsilon) \sin(\bar{\theta} + \theta_e) \tag{7.19}$$

$$w_{22} = -(k_3/\epsilon) \sin \bar{\theta} - k_4 \bar{\Omega}_2. \tag{7.20}$$

In the above control design gains k_1 and k_2 determine the closed-loop equilibrium and also influence its stability. The positive control gains k_3 and k_4 ensure the stability of the rotational dynamics.

In the rest of this section we choose the gains in the control law and prove the exponential stability of the desired, closed-loop relative equilibrium. The calculation of k_1 and k_2 is presented in §7.2.1. Lower bounds on control gains k_3 and k_4 are computed in §7.2.3. The closed-loop system is interpreted as an interconnected system in §7.2.2. The stability of equilibria of the rotational and translational subsystems of this interconnected system is presented in §7.2.3 and §7.2.4 respectively. The coupling between the two subsystems is examined and proof of exponential stability of the CTOL aircraft relative equilibria is completed using a composite Lyapunov function in §7.2.5.

7.2.1 Relative Equilibria

The CTOL aircraft relative equilibria are fixed points of the reduced dynamics and correspond to steady gliding motions with a constant speed V_e and flight path angle γ_e. Any desired closed-loop V_e and γ_e may be realized by appropriately selecting the control gains k_1 and k_2. We compute k_1 and k_2 by solving the following equilibrium equations, obtained by setting expressions on the right-hand-side of equations (7.12), (7.13) and (7.15) evaluated at the origin to zero:

$$-(k_1+1)\sin\gamma_e - k_2\cos\gamma_e - K_{Dr_e}V_e^2 = 0 \tag{7.21}$$

$$-(k_1+1)\cos\gamma_e + k_2\sin\gamma_e + K_{Li_e}V_e^2 = 0 \tag{7.22}$$

$$k_1\cos(\gamma_e+\alpha_e) - k_2\sin(\gamma_e+\alpha_e) = 0 \tag{7.23}$$

In the above equations $K_{Dr_e} = a_D(1+b(1+c\alpha_e)^2)$ and $K_{Li_e} = a_L(1+c\alpha_e)$.

Theorem 4. *For any given V_e and γ_e there exist control gains k_1 and k_2 such that the equilibrium equations (7.21)-(7.23) are satisfied for all aircraft parameter values.*

Proof Given V_e and γ_e we need to solve for three unknowns k_1, k_2 and α_e using the equilibrium equations (7.21)-(7.23). We derive a solution to the equilibrium equations by first solving for α_e and then solving the linear equations (7.21)-(7.22) for k_1 and k_2.

Let us add $\sin\alpha_e$ times equation (7.21) to $(-\cos\alpha_e)$ times equation (7.22) to get

$$(k_1+1)\cos(\gamma_e+\alpha_e) - k_2\sin(\gamma_e+\alpha_e) - (K_{Dr_e}\sin\alpha_e + K_{Li_e}\cos\alpha_e)V_e^2 = 0. \quad (7.24)$$

Using equation (7.23), equation (7.24) may be simplified to

$$\cos(\gamma_e+\alpha_e) - (K_{Dr_e}\sin\alpha_e + K_{Li_e}\cos\alpha_e)V_e^2 = 0, \quad (7.25)$$

which implies that

$$(\cos\gamma_e - K_{Li_e}V_e^2)\cos\alpha_e = (\sin\gamma_e + K_{Dr_e}V_e^2)\sin\alpha_e. \quad (7.26)$$

Let us say $\alpha_e = \alpha_e^*$ is the unique solution of $(\cos\gamma_e - K_{Li_e}V_e^2) = 0$. If $\alpha_e^* = 0$, then $\alpha_e = 0$ is in fact the solution of equation (7.26). Next, let us consider the case when $\alpha_e^* > 0$. Now, for $\alpha_e \in [-\pi, 0]$ we have $(\cos\gamma_e - K_{Li_e}V_e^2) \neq 0$. Thus, we can rewrite equation (7.26) as

$$\cot\alpha_e = \frac{\sin\gamma_e + K_{Dr_e}V_e^2}{\cos\gamma_e - K_{Li_e}V_e^2} \quad (7.27)$$

for $\alpha_e \in [-\pi, 0]$. The left-hand-side of the above equation has a range of $(-\infty, \infty)$ whereas the right-hand-side of the equation is bounded and continuous with respect to α_e. This implies that there exists some $\alpha_e \in [-\pi, 0]$ that satisfies equation (7.26). For the last case of $\alpha_e^* < 0$ we can use similar arguments to show that there exists some $\alpha_e \in [0, \pi]$ that satisfies equation (7.26). Once α_e is computed we can substitute it in the first two equilibrium equations, rendered linear in the remaining unknowns k_1 and k_2. Furthermore these equations are always independent, thus giving us a unique set of control gains k_1 and k_2. $\square$

7.2.2 Interconnected System

We interpret the closed-loop CTOL aircraft dynamics, described by equations (7.12)-(7.15) with u_1 and u_2 defined by equations (7.16)-(7.17), as an interconnected system. The interconnected system has the following structure:

$$\dot{x}_i = f_i(x_i) + g_i(x) \quad i = 1, 2 \tag{7.28}$$

where $x = (x_1^T, x_2^T)^T$, $x_1 = (\bar{V}, \bar{\gamma})^T$, $x_2 = (\bar{\theta}, \bar{\Omega}_2)^T$, $f_i = (f_{i1}, f_{i2})^T$ and $g_i = (g_{i1}, g_{i2})^T$. The functions f_{ij}, g_{ij} are given by

$$f_{11} = \frac{1}{V_e}\{-(k_1+1)\sin\gamma - k_2\cos\gamma - (K_{Dr_e} + \delta_{Dr1})V^2\} \tag{7.29}$$

$$f_{12} = \frac{1}{V}\{-(k_1+1)\cos\gamma + k_2\sin\gamma + (K_{Li_e} + \delta_{Li1})V^2\} \tag{7.30}$$

$$g_{11} = \frac{1}{V_e}\{-\delta_{Dr2}V^2 - k_3\sin\bar{\theta}\sin\alpha - \epsilon k_4\bar{\Omega}_2\sin\alpha\} \tag{7.31}$$

$$g_{12} = \frac{1}{V}\{\delta_{Li2}V^2 + k_3\sin\bar{\theta}\cos\alpha + \epsilon k_4\bar{\Omega}_2\cos\alpha\} \tag{7.32}$$

$$f_{21} = \bar{\Omega}_2/T \tag{7.33}$$

$$f_{22} = (T/\epsilon)\{k_1\cos\theta - k_2\sin\theta - k_3\sin\bar{\theta} - k_4\epsilon\bar{\Omega}_2\} \tag{7.34}$$

$$g_{2j} = 0, \quad j = 1, 2, \tag{7.35}$$

where,

$$\begin{aligned}
\delta_{Dr1} &= a_D b(c^2\bar{\gamma}^2 - 2c^2\bar{\gamma}\alpha_e - 2c\bar{\gamma}) && (7.36)\\
\delta_{Dr2} &= a_D b(c^2\bar{\theta}^2 + 2c^2\bar{\theta}\alpha_e - 2c^2\bar{\theta}\bar{\gamma} + 2c\bar{\theta}) && (7.37)\\
\delta_{Li1} &= -a_L c\,\bar{\gamma} && (7.38)\\
\delta_{Li2} &= a_L c\,\bar{\theta}. && (7.39)
\end{aligned}$$

Recall that $V = V_e(1+\bar{V})$, $\gamma = \bar{\gamma} + \gamma_e$, $\theta = \bar{\theta} + \theta_e$ and $\alpha = \bar{\theta} + \theta_e - (\bar{\gamma} + \gamma_e)$.

We prove the stability of the equilibrium of the above interconnected system by employing the following result, derived from Theorem 9.2 of [13].

Theorem 5. *[138, 13] Consider the interconnected system given by equation (7.28) and suppose there are positive definite, decrescent Lyapunov functions $Q_i(x_i)$ that satisfy the following conditions for $i = 1, 2$,*

$$\begin{aligned}
c_{i1}\|x_i\|^2 \leq\ Q_i\ &\leq c_{i2}\|x_i\|^2 && (7.40)\\
\frac{\partial Q_i}{\partial x_i} f_i(x_i)\ &\leq\ -\lambda_i\,\|x_i\|^2 && (7.41)\\
\left\|\frac{\partial Q_i}{\partial x_i}\right\|\ &\leq\ \beta_i\,\|x_i\|, && (7.42)
\end{aligned}$$

and the functions g_i satisfy

$$\|g_i(x)\| \leq \sum_{j=1}^{2} \gamma_{ij}\,\|x_j\| \tag{7.43}$$

for $\|x\| \leq r$, for some nonnegative constants γ_{ij} and positive constants c_{ij}, λ_i, β_i and r. Further suppose that the following coupling conditions,

$$\lambda_1 - \beta_1\gamma_{11} > 0 \tag{7.44}$$

$$\lambda_1\lambda_2 + \beta_1\beta_2(\gamma_{11}\gamma_{22} - \gamma_{12}\gamma_{21}) - \lambda_1\beta_2\gamma_{22} - \lambda_2\beta_1\gamma_{11} > 0, \tag{7.45}$$

hold. Then, there exist constants $d_1, d_2 > 0$ such that the derivative with respect to time of the function $Q = d_1 Q_1 + d_2 Q_2$ along the trajectories of the interconnected system (7.28) satisfies the inequality

$$\dot{Q} \leq -\frac{\lambda}{2} \|x\|^2 \tag{7.46}$$

for some $\lambda > 0$. Thus, Q is a Lyapunov function that proves exponential stability of the origin of the interconnected system (7.28).

Proof This theorem follows by applying Theorem 9.2 of [128] to the interconnected system described by equation (7.28). The coupling conditions (7.44)-(7.45) are equivalent to necessary and sufficient conditions that make the matrix S of Theorem 9.2 in [13] an $M-$matrix. Condition (7.41) strengthens the result of Theorem 9.2 of [13] to exponential stability of the origin of the interconnected system (7.28). □

In the following two subsections, we present Lyapunov functions Q_i that satisfy conditions (7.40)-(7.42) for the rotational and translational subsystems and thus prove exponential stability of their respective equilibria.

7.2.3 Stability of Rotational Subsystem

Because $g_2 = 0$ (equation (7.35)) the rotational subsystem is simply

$$\dot{x}_2 = f_2(x_2). \tag{7.47}$$

We consider the Lyapunov function candidate Q_2:

$$Q_2 = (k_3 + k^{''})\frac{2T^2}{\epsilon}\sin^2\frac{\bar{\theta}}{2} + \frac{1}{2}\bar{\Omega}_2^2 + k^{'}\bar{\theta}\bar{\Omega}_2, \tag{7.48}$$

where $k^{'} > 0$ and $k^{''} = k_1 \sin\theta_e + k_2 \cos\theta_e$.

Proposition 3. *The Lyapunov function candidate Q_2 satisfies conditions (7.40)-*

(7.42), i.e., the origin is an exponentially stable equilibrium point of the rotational subsystem of CTOL aircraft dynamics (7.47).

Proof First we note that

$$Q_2 \;\leq\; |Q_2| \;\leq\; \left|k_3 + k^{''}\right| \frac{2T^2}{\epsilon} \sin^2 \frac{\bar{\theta}}{2} + \frac{1}{2}\bar{\Omega}_2^2 + k^{'} \left|\bar{\theta}\bar{\Omega}_2\right| . \tag{7.49}$$

We substitute the relations

$$|\bar{\theta}\,\bar{\Omega}_2| \;\leq\; \frac{\bar{\theta}^2 + \bar{\Omega}_2^2}{2} \tag{7.50}$$

$$\sin^2 \frac{\bar{\theta}}{2} \;\leq\; \frac{\bar{\theta}^2}{4} \tag{7.51}$$

in equation (7.49) and conclude that

$$Q_2 \;\leq\; \frac{1}{2}\left(\frac{|k_3 + k^{''}|T^2}{\epsilon} + k^{'}\right)\bar{\theta}^2 + \frac{1}{2}\left(1 + k^{'}\right)\bar{\Omega}_2^2. \tag{7.52}$$

Thus, we have $Q_2 \leq c_{22}(\bar{\theta}^2 + \bar{\Omega}_2^2)$, where

$$c_{22} = \frac{1}{2}\max\left\{\frac{|k_3 + k^{''}|T^2}{\epsilon} + k^{'}, 1 + k^{'}\right\} > 0. \tag{7.53}$$

For any variable $\eta \in (-\pi + \delta, \pi - \delta)$, where δ is a constant such that $\pi > \delta > 0$, we have

$$|\sin\eta| \geq \frac{\sin(\pi - \delta)}{(\pi - \delta)}\eta = \frac{\sin\delta}{(\pi - \delta)}\eta. \tag{7.54}$$

If $\eta = \bar{\theta}/2$, we may set $\delta = \pi/2$ because $\bar{\theta}/2 \in (-\pi/2, \pi/2]$ since $\theta \in (-\pi, \pi]$ as defined in §7.1.1. Thus,

$$\left|\sin\frac{\theta}{2}\right| \;\geq\; \frac{1}{\pi}\,\bar{\theta}. \tag{7.55}$$

This implies

$$\sin^2\frac{\bar\theta}{2} \quad \geq \quad \frac{1}{\pi^2}\,\bar\theta^2. \tag{7.56}$$

By substituting relation (7.56) and the following relation

$$\bar\theta\,\bar\Omega_2 \geq -\frac{\bar\theta^2+\bar\Omega_2^2}{2} \tag{7.57}$$

in equation (7.48), and by further choosing $k_3 > |k^{''}|$, we can conclude that

$$Q_2 \quad \geq \quad \frac{1}{2}\left(\frac{4(k_3+k^{''})T^2}{\epsilon\pi^2} - k^{'}\right)\bar\theta^2 + \frac{1}{2}\left(1-k^{'}\right)\bar\Omega_2^2. \tag{7.58}$$

By choosing $k^{'} < 1$ and k_3 large enough we can ensure that $Q_2 \geq c_{21}(\bar\theta^2+\bar\Omega_2^2)$, where

$$c_{21} = \frac{1}{2}\min\left\{4(k_3+k^{''})\frac{T^2}{\epsilon\pi^2} - k^{'}, 1-k^{'}\right\} > 0. \tag{7.59}$$

Thus, we satisfy condition (7.40) for Q_2 and prove that Q_2 is indeed a positive definite function for sufficiently large k_3.

Next, we compute

$$\dot{Q}_2 = -T\left[\frac{(k_3+k^{''})k^{'}}{\epsilon}\bar\theta\sin\bar\theta + \big(k_4 - \frac{k^{'}}{T^2}\big)\bar\Omega_2^2 + k_4k^{'}\bar\theta\bar\Omega_2\right] \tag{7.60}$$

using our choice of k_1, k_2 to satisfy equilibrium equations (7.21)-(7.23). We note that $\bar\theta\sin\bar\theta \geq 0$. Thus, $\bar\theta\sin\bar\theta = |\bar\theta\sin\bar\theta| = |\bar\theta|\sin|\bar\theta|$. We restrict $|\bar\theta| \leq r$ i.e., $\bar\theta \in (-r, r)$. We pick $r < \pi$ and use the inequality (7.54) with $\pi - \delta = r$ to get

$$\sin|\bar\theta| \geq \frac{\sin r}{r}\,|\bar\theta|. \tag{7.61}$$

Using the above relation and inequality (7.57) in the equation (7.60) for $\dot{Q}_2$ we get

$$\dot{Q}_2 \;\le\; -T\left[\left(\frac{(k_3+k^{''})\sin r}{\epsilon r}-\frac{k_4}{2}\right)k^{'}\bar{\theta}^2+\left(k_4\left(1-\frac{k^{'}}{2}\right)-\frac{k^{'}}{T^2}\right)\bar{\Omega}_2^2\right]. \qquad (7.62)$$

Since we have already chosen $k^{'}<1$ we can find large enough k_3 and k_4 such that the coefficients of $\bar{\theta}^2$ and $\bar{\Omega}_2^2$ in the above expression are positive. Thus we satisfy the inequality (7.41) for Q_2 with

$$\lambda_2 = k^{'}T\min\left\{\frac{(k_3+k^{''})\sin(1)}{\epsilon}-\frac{k_4}{2}, k_4\left(\frac{1}{k^{'}}-\frac{1}{2}\right)-\frac{1}{T^2}\right\}. \qquad (7.63)$$

Lastly, we compute

$$\begin{aligned}
\left\|\frac{\partial Q_2}{\partial x_2}\right\| &= \left\|\left(\frac{(k_3+k^{''})T^2}{\epsilon}\sin\bar{\theta}+k^{'}\bar{\Omega}_2, \bar{\Omega}_2+k^{'}\bar{\theta}\right)\right\| \\
&= \left\{\frac{(k_3+k^{''})^2T^4}{\epsilon^2}\sin^2\bar{\theta}+k^{'2}\bar{\theta}^2+(1+k^{'2})\bar{\Omega}_2^2\right. \\
&\qquad \left.+\,2\left(\frac{(k_3+k^{''})T^2}{\epsilon}k^{'}\sin\bar{\theta}\bar{\Omega}_2+k^{'}\bar{\theta}\bar{\Omega}_2\right)\right\}^{\frac{1}{2}} \\
&\le \left[\left\{\frac{(k_3+k^{''})^2T^4}{\epsilon^2}+\frac{(k_3+k^{''})T^2}{\epsilon}k^{'}+k^{'}+k^{'2}\right\}\bar{\theta}^2\right. \\
&\quad \left.+\left\{1+k^{'2}+\frac{(k_3+k^{''})T^2}{\epsilon}k^{'}+k^{'}\right\}\bar{\Omega}_2^2\right]^{\frac{1}{2}}
\end{aligned} \qquad (7.64)$$

For deriving the last inequality we have used the following relations:

$$2\left(\sin\bar{\theta}\right)\bar{\Omega}_2 \;\le\; 2\left(\sin\left|\bar{\theta}\right|\right)\left|\bar{\Omega}_2\right| \;\le\; \sin^2\bar{\theta}+\bar{\Omega}_2^2 \;\le\; \bar{\theta}^2+\bar{\Omega}_2^2 \qquad (7.65)$$

$$2\bar{\theta}\bar{\Omega}_2 \;\le\; \bar{\theta}^2+\bar{\Omega}_2^2. \qquad (7.66)$$

Thus, condition (7.42) is satisfied for Q_2 with

$$\beta_2 = \left[\frac{k^{'}(k_3+k^{''})T^2}{\epsilon}+k^{'}+\max\left\{\frac{(k_3+k^{''})^2T^4}{\epsilon^2}+k^{'2}, 1+k^{'2}\right\}\right]^{\frac{1}{2}}. \qquad (7.67)$$

Thus, the Lyapunov function candidate Q_2 satisfies conditions (7.40)-(7.42) for the rotational subsystem (7.47). Using Theorem 4.2 of [13] we can conclude that the origin is an exponentially stable equilibrium of the rotational subsystem. $\square$

7.2.4 Stability of Translational Subsystem

The translational subsystem is

$$\dot{x}_1 = f_1(x_1). \tag{7.68}$$

To prove stability of the translational subsystem we consider the same Lyapunov function candidate as we did for proving the stability of the reduced (slow) subsystem of the underwater glider in §5.1.2:

$$Q_1 = \frac{1}{3}(1+\bar{V})^3 - (1+\bar{V})\cos\bar{\gamma} + \frac{2}{3}. \tag{7.69}$$

We recall that the above Lyapunov function candidate is derived from the conserved quantity C of the phugoid-mode model of the underwater glider, discussed in §4.1. The CTOL aircraft phugoid-mode model is derived by using Lanchester's assumptions [34, 33]. The two phugoid-mode models have the identical structure and can be related using a simple time scaling.

Proposition 4. *The Lyapunov function candidate Q_1 satisfies conditions (7.40)-(7.42), i.e., the origin is an exponentially stable equilibrium point of the translational subsystem of CTOL aircraft dynamics.*

Proof We have already shown that Q_1 satisfies condition (7.40) in §5.1.2. Constants c_{11} and c_{12} are equal to k_1 and k_2 of §5.1.2 respectively.

In Appendix D we assume $r < 1$ in Theorem 5 and show that Q_1 satisfies condition (7.41) with

$$\lambda_1 = \min\{s_1, s_2\} > 0, \tag{7.70}$$

for small enough $b > 0$, $r > 0$, where

$$\begin{aligned} s_1 &= K_{Dr_e}(2-r)^2 - 2a_D bc|c\alpha_e + 1|(1 + 3r + r^2) && (7.71) \\ s_2 &= K_{Dr_e}(1-r)^2 \frac{\sin^2(r/2)}{(r/2)^2} + a_L c \frac{\sin r}{r}(1-r)^2 + a_d bc^2(r^2 - 2r) \\ &\quad - a_D bc|c\alpha_e + 1|((1+r)^2 r + 2). && (7.72) \end{aligned}$$

Lastly, we compute

$$\begin{aligned} \left\| \frac{\partial Q_1}{\partial x_1} \right\| &= \left\{ (\bar{V}^2 + 2\bar{V} + 2\sin^2 \frac{\bar{\gamma}}{2})^2 + (1+\bar{V})^2 \sin^2 \bar{\gamma} \right\}^{\frac{1}{2}} \\ &= \left\{ (\bar{V}^2 + 2\bar{V})^2 + 4\sin^4 \frac{\bar{\gamma}}{2} + 4(\bar{V}^2 + 2\bar{V})\sin^2 \frac{\bar{\gamma}}{2} + (1+\bar{V})^2 \sin^2 \bar{\gamma} \right\}^{\frac{1}{2}} \\ &\leq \left\{ 2(\bar{V}^2 + 2\bar{V})^2 + 8\sin^4 \frac{\bar{\gamma}}{2} + (1+\bar{V})^2 \sin^2 \bar{\gamma} \right\}^{\frac{1}{2}}. && (7.73) \end{aligned}$$

To arrive at the inequality in the above calculation we have used the fact that $2ab \leq (a^2 + b^2)$ for any $a, b \in \mathbb{R}$. We have set $a = \bar{V}^2 + 2\bar{V}$ and $b = 2\sin^2 \frac{\bar{\gamma}}{2}$. In Appendix D we show that the above inequality can be reduced to condition (7.42) for Q_1 with

$$\beta_1 = \sqrt{2}(2 + r). \tag{7.74}$$

Thus, the Lyapunov function candidate Q_1 satisfies conditions (7.40)-(7.42) for the translational subsystem (7.68). Using Theorem 4.2 of [13] we can conclude that the origin is an exponentially stable equilibrium of the translational subsystem. □

7.2.5 Composite Lyapunov Function

In this subsection we show that the interconnected system satisfies the coupling conditions (7.44)-(7.45) of Theorem 5 and complete the proof of exponential stability of its relative equilibrium.

First we compute the constants γ_{ij}. Since $g_2 = 0$ we have $\gamma_{2j} = 0$. We note that all terms of g_1 contain either $\sin\bar{\theta}$, $\bar{\theta}$ or $\bar{\Omega}_2$. This implies that we can write $\|g_1\|$ in the following form:

$$\|g_1\| = (p_1 \sin^2\bar{\theta} + p_2\bar{\theta}^2 + p_3\bar{\Omega}_2^2)^{\frac{1}{2}}, \tag{7.75}$$

where p_i's are some bounded (due to compactness of our domain) nonnegative numbers (not necessarily constant). Using the fact that $\sin^2\bar{\theta} \leq \bar{\theta}^2$ we can write

$$\|g_1\| \leq \left((p_1 + p_2)\bar{\theta}^2 + p_3\bar{\Omega}_2^2\right)^{\frac{1}{2}} \leq (\max\{p_1 + p_2,\ p_3\})^{\frac{1}{2}}\,\|x_2\|. \tag{7.76}$$

Thus, we have $\gamma_{11} = 0$ and,

$$\gamma_{12} = (\max\{p_1 + p_2,\ p_3\})^{\frac{1}{2}}\,. \tag{7.77}$$

Because $\gamma_{11} = \gamma_{21} = \gamma_{22} = 0$ the coupling conditions (7.44)-(7.45) reduce to

$$\lambda_i > 0, \quad i = 1, 2. \tag{7.78}$$

λ_i's are positive by derivation, as shown in the previous two subsections.

Since all conditions of Theorem 5 are satisfied we can conclude the existence of a composite Lyapunov function

$$Q = d_1 Q_1 + d_2 Q_2 \tag{7.79}$$

for some $d_1,\ d_2 > 0$, that proves exponential stability of the steady glides of CTOL aircraft model. The exponential stability of the relative equilibrium is guaranteed within a region of attraction specified by $\|x\| \le r_a(d_1, d_2) \le r$.

7.3 Approximate Trajectory Tracking of Aircraft

In this section we utilize the exponential stability result of the previous section to design an approximate trajectory tracking methodology for the CTOL aircraft. First, we briefly review some results from previous work on CTOL aircraft position tracking in §7.3.1. The tracking problem is challenging due to the nonminimum phase nature of the system. We describe our approximate tracking methodology based on stability of steady gliding motions in §7.3.2 and illustrate the method with a numerical simulation in §7.3.3.

7.3.1 Tracking by Feedback Linearization

A common approach for trajectory tracking involves feedback linearization techniques [139]. In the case of CTOL aircraft dynamics, if the position of the aircraft (x, y) is taken to be output of the system, we may use a feedback and control transformation such that input-output dynamics is linear. This is done by picking

$$u_1 = D\cos\alpha - L\sin\alpha + \sin\theta + w_1\cos\theta + w_2\sin\theta \tag{7.80}$$

$$u_2 = \frac{1}{\epsilon}\left(D\sin\alpha + L\cos\alpha - \cos\theta - w_2\cos\theta + w_1\sin\theta\right), \tag{7.81}$$

where w_1 and w_2 are new control inputs to be designed. Now, from equations (7.5)-(7.6) the input-output dynamics are:

$$\ddot{x} = w_1 \tag{7.82}$$

$$\ddot{y} = w_2. \tag{7.83}$$

The above input-output dynamics along with the internal dynamics,

$$\ddot{\theta} = u_2 = \frac{1}{\epsilon}\left(D\sin\alpha + L\cos\alpha - mg\cos\theta - w_2\cos\theta + w_1\sin\theta\right) \tag{7.84}$$

completely describe the motion of the CTOL aircraft.

The zero dynamics [139] of the CTOL aircraft are the internal dynamics corresponding to a prescribed realization of the input-output dynamics. We note that control law (u_1, u_2) renders the zero dynamics unobservable. The zero dynamics for a prescribed constant altitude, constant speed motion of the CTOL aircraft are analyzed in [36] and it is shown to have no exponentially stable fixed points. The equilibrium at the origin is shown to be a saddle point. This makes the CTOL dynamics *nonminimum phase*. Simply choosing w_1 and w_2 to stabilize (x, y) along a desired trajectory may cause inputs u_1 and u_2 to become unbounded.

Several approaches have been proposed to address the nonminimum phase nature of CTOL dynamics. One approach is to find the control law $(u_1(t), u_2(t))$ such that a prescribed trajectory is an exact solution of the equations of motion of the system (7.5)-(7.7). An iterative scheme for finding exact tracking solutions to nonlinear systems presented in [60] was applied to the CTOL problem in [36]. The resulting required control inputs (u_1, u_2) are very large. In order to obtain lower pitching control moment magnitude [36] also presents application of approximate linearization techniques of [63] and [64] to the CTOL problem. The approximate linearization techniques are based on a minimum phase approximation to the nonminimum phase system. These methods also result in large pitching control magnitudes, but they are lower than the pitching control magnitude for exact tracking when averaged over time. The tracking by these approximate methods is very accurate but not exact. Tracking based on inversion of approximate input-output linearization has also been applied to the Vertical Take Off and Landing (VTOL) aircraft model in [63].

In [62] the authors consider the zero dynamics to be singularly perturbed. They further assume constant angle of attack of the aircraft. This assumption, although not rigorously justified in [62], greatly simplifies the analysis of CTOL dynamics. The authors present a general framework for describing nonlinear, nonminimum phase systems with singularly perturbed zero dynamics. Using this framework and the exact tracking methods of [60], further extended in [140, 61], a bounded tracking control law for the CTOL aircraft is proposed. This control design is expected to have a smaller pitching moment control than the methods presented in [36].

An alternative approach to CTOL trajectory tracking, presented in [141, 137], utilizes a coordinate change to decompose the system into minimum phase and non-minimum phase parts. The controller for the minimum phase part is designed based on stable inversion of dynamics. The nonminimum phase part is interpreted as a system perturbed from its linearization about a desired, steady trajectory. A Linear Quadratic Regulator (LQR) controller designed for the nominal (linear) system is used for the perturbed (nonlinear) system.

Reduction of control magnitude is also achieved by posing a maneuver regulation problem instead of the trajectory tracking problem in [136]. The control design attempts to regulate the position error transverse to the desired path and maintain the desired velocity along the path. The controller ignores position error along the path. Thus, the aircraft attempts to follow just the prescribed path instead of following a prescribed trajectory.

All the approaches mentioned in this section employ inversion of dynamics demanding large control inputs. In the following two subsections we present an alternative approach for approximately tracking a desired trajectory, utilizing exponentially stabilizable relative equilibria of CTOL aircraft dynamics. We achieve similar tracking accuracy as the dynamic inversion based methods, but with significantly lower control effort.

7.3.2 Approximate Trajectory Tracking Methodology

In this section we present a method for the CTOL aircraft model to track constant velocity desired trajectories. In §7.3.3 we apply the method in simulation to a desired trajectory that is *not* constant velocity and illustrate the potential for this method beyond what is proven below. Our approach utilizes exponential stability of steady gliding motions. We compute steady glides that regulate the aircraft motion to the desired trajectory at small enough discrete time steps. These steady glides are achieved by using appropriate control laws. Recall that CTOL aircraft dynamics may be exponentially stabilized to any desired steady glide using the control law presented in §7.2.

Let $(x_d(t), y_d(t))$ describe a desired trajectory for the CTOL aircraft that has constant velocity. Let us consider the following state vector for CTOL dynamics: $z = (\dot{x}, \dot{y}, \theta, \Omega_2)$. The first two components of the state vector are the x and y components of the aircraft velocity. The constant velocity desired trajectory corresponds to the state vector z being equal to a constant z_d with $\Omega_{2d} = 0$.

At the time instant $t = t_k$ we compute a steady glide that takes the aircraft from its current position to the desired position of the aircraft at $t_{k+1} := t_k + \Delta t_k$, for some $\Delta t_k > 0$. This procedure is repeated at t_{k+1}, where we calculate a desired steady glide that takes the aircraft from its current position to the desired position of the aircraft at t_{k+2}, and so on. We refer this approach as "tracking based on steady gliding".

Theorem 6. *Tracking of a desired constant velocity trajectory* $(x_d(t), y_d(t))$ *based on steady gliding for the CTOL aircraft yields bounded position tracking error.*

Proof Let the state vector corresponding to the computed desired steady glide between t_k and t_{k+1} be equal to the constant $z_{g,k}$. We assume that we start close enough to the desired trajectory z_d in the state space. More precisely we assume that $r_1(t_k) := \|z(t_k) - z_d\| < r_{za}$ for $t_k = t_0 = 0$, where r_{za} is an estimate of the region of attraction provided by the composite Lyapunov function of §7.2.5. We choose a large enough Δt_k such that $r_2(k) := \|z_d - z_{g,k}\| < r_1(t_k)$ and $r_1(t_k) + r_2(k) \leq r_{za}$. Then,

$$\begin{aligned} \|z(t_k) - z_{g,k}\| &= \|z(t_k) - z_d + z_d - z_{g,k}\| \\ &\leq \|z(t_k) - z_d\| + \|z_d - z_{g,k}\| \\ &= r_1(t_k) + r_2(k) \\ &\leq r_{za} \quad \text{for } k = 0. \end{aligned} \tag{7.85}$$

Since our control law for the time interval $(t_k, t_{k+1}]$ exponentially stabilizes the CTOL aircraft to the steady glide specified by $z_{g,k}$, we have

$$\|z(t_{k+1}) - z_{g,k}\| \leq M r_{za} \exp(-\eta \Delta t_k), \tag{7.86}$$

for some $M, \eta > 0$. This implies that

$$\begin{aligned} \|z(t_{k+1}) - z_d\| &= \|z(t_{k+1}) - z_{g,k} + z_{g,k} - z_d\| \\ &\leq \|z(t_{k+1}) - z_{g,k}\| + \|z_{g,k} - z_d\| \\ &\leq M r_a \exp(-\eta \Delta t_k) + r_2(k). \end{aligned} \tag{7.87}$$

Since we have chosen $r_2(k) < r_1(t_k)$ we can always choose a large enough Δt_k such that $r_1(t_{k+1}) = \|z(t_{k+1}) - z_d\| < r_1(t_k) < r_{za}$.

The above procedure can be repeated for all values of k since $r_1(t_k)$ will always be less than r_{za}. Since $0 \leq r_1(t_{k+1}) < r_1(t_k)$ for all k, we can conclude that z remains close to z_d.

Now, let us see what happens to the position tracking error: let e_x and e_y be the x and y components of the position tracking error. The magnitude of the position tracking error is $e = \sqrt{e_x^2 + e_y^2}$. We have

$$\begin{aligned} |e_x(t_{k+1})| &= |x(t_{k+1}) - x_d(t_{k+1})| \\ &= |x(t_{k+1}) - x_g(t_{k+1})|, \end{aligned} \tag{7.88}$$

where $x_g(t_{k+1})$ is meant to denote the $x-$coordinate at t_{k+1} on the desired steady glide computed at t_k. The equality of $x_g(t_{k+1})$ and $x_d(t_{k+1})$ follows from our tracking methodology - the desired steady glide between t_k and t_{k+1} intersects the desired trajectory at t_{k+1}. We also note that the aircraft always starts with zero position error with respect to the desired steady glide (not the prescribed desired trajectory) when a new desired glide is computed, because the new desired glide joins the current position of the aircraft to the position on the prescribed trajectory Δt_k seconds later. Since the closed-loop steady glides are exponentially stable, using equation (7.88) we can write,

$$\begin{aligned} |e_x(t_{k+1})| &\leq \int_0^{\Delta t_k} M r_a \exp(-\eta\tau) d\tau \\ &= \frac{M r_a}{\eta}(1 - \exp(-\eta \Delta t_k)). \end{aligned} \tag{7.89}$$

The above argument may be applied to $|e_y(t_{k+1})|$ also. Thus,

$$\|e(t_{k+1})\| \leq \frac{\sqrt{2} M r_a}{\eta}(1 - \exp(-\eta \Delta t_k)) < \frac{\sqrt{2} M r_a}{\eta}, \tag{7.90}$$

i.e., the position error remains bounded at all time instants when new desired steady glides are calculated. This also implies that the position tracking error is bounded at all t. This completes the proof. $\square$

7.3.3 Aircraft Tracking Simulation

We demonstrate the performance of the methodology presented in the previous subsection by way of a numerical simulation of approximately tracking the trajectory studied in [36]. We select the same nondimensional parameters for a DC-8 aircraft as in [36]: $a_L = 30$, $a_D = 2$, $b = 0.01$, $c = 6$ and $\epsilon = 0.3$. We use mass and inertia parameter values considered in [136] for the DC-8: $m = 85000$ kg and $J_2 = 4\times 10^6$ kgm^2. The desired trajectory, shown in Figure 7.2, corresponds to constant speed motion of the aircraft in the horizontal direction, $x_d(t) = \frac{0.85}{\sqrt{a_L}} t$, and a smooth altitude climb in the vertical direction, determined by the solution of the differential equation

$$y_d^{(5)}(t) + 3.5y_d^{(4)}(t) + 4.9y_d^{(3)}(t) + 3.4y_d^{(2)}(t) + 1.2y_d^{(1)}(t) + 0.17y_d(t) - 1.7 = 0, \quad (7.91)$$

with zero initial conditions.

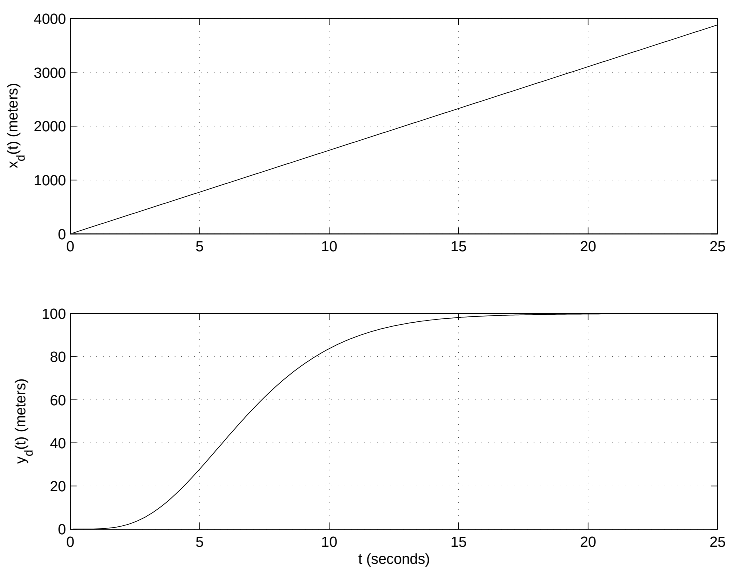

Figure 7.2: Desired CTOL Trajectory

We start the simulation with $(x(0), y(0)) = (0, 0)$ and the other initial conditions set to equilibrium values corresponding to the steady horizontal glide with a speed of $\frac{0.85}{\sqrt{a_L}}$. We set $\Delta t_k = 0.1$ s for all k. The control gains k_1 and k_2 are determined at every t_k by solving equations (7.21)-(7.23) for the calculated steady glide between t_k and t_{k+1}. The remaining control gains are set to $k_3 = 7\exp(5)$ and $k_4 = 2.5\exp(2)$.

The position tracking error components are plotted in Figure 7.3 and the control effort is plotted in Figure 7.4. The desired trajectory is tracked with good accuracy. The trade-off between tracking error and control effort may be adjusted through control gains k_3 and k_4. Our choice of k_3 and k_4 yields control effort lower than what is required for tracking using the methods of [63, 64, 142], applied to tracking the desired trajectory of Figure 7.2 in [36]. While the method of [142] finds an exact solution by inverting the dynamics, the methods of [63, 64] are based on minimum phase approximation of the non-minimum phase system. In the method of [63], the coupling between the control input u_2 and the vertical acceleration is neglected for control design based on feedback linearization via dynamic extension, and in the method of [64] an approximation to the Jacobian linearization of the original system obtained by neglecting the right-half plane zeros is used.

The desired trajectory tracked in the simulation is not a constant velocity trajectory, so our simulation illustrates the potential usefulness of the steady gliding based tracking approach beyond what is proven in this chapter. The results of this chapter are also very relevant to trajectory tracking for underwater gliders. Derivation of tracking error boundedness results using the limited control actuation available for underwater gliders is a subject of future work.

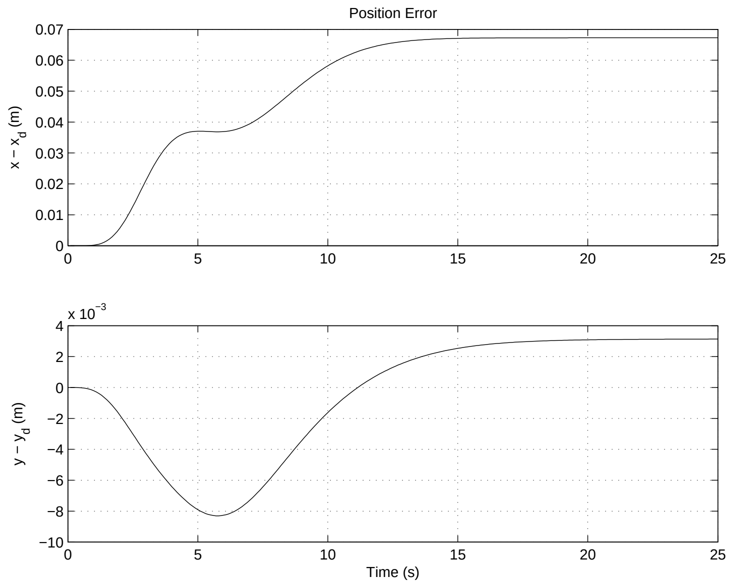

Figure 7.3: CTOL Aircraft Position Tracking Error

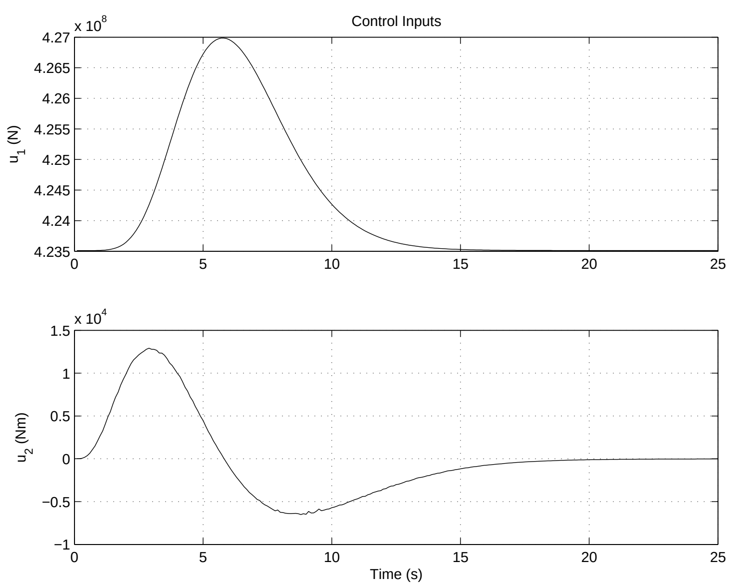

Figure 7.4: Thrust and Pitching Moment Control Inputs

Chapter 8

Three-Dimensional Steady Motions of Underwater Gliders

In this chapter we focus on studying motions of the underwater glider in the three dimensional space, governed by equations (2.1)-(2.6) presented in Chapter 2. Recall that the underwater glider equations of motion were derived from Kirchhoff's equations, by introducing the gravity and viscous effects in the form of external forces and moments, and by incorporating additional dynamics due to the motion of an internal point mass. Kirchhoff's equations and the dynamics of a constant-buoyancy, fixed center of gravity underwater glider are examples of dynamics of systems defined on the configuration manifold $SE(3)$, whose elements are 4×4 matrices of the form

$$\begin{bmatrix} R & \boldsymbol{b} \\ 0_{1\times 3} & 1 \end{bmatrix},$$

where R is a rotation matrix, $\boldsymbol{b} \in \mathbb{R}^3$ and $0_{1\times 3}$ is a 1×3 zero matrix. In §8.1, we calculate all possible relative equilibria motions under the action of $SE(3)$ on itself. A subset of these relative equilibria motions are steady motions of underwater glider dynamics. We focus on steady, circular helical motions of underwater gliders in

§8.2. We discuss how a circular helix traced by the glider depends on the parameters of the vehicle. We also present a numerical simulation of a circular helical motion using model parameters reflecting a Slocum glider, and we compute different possible circular helical motions by adjusting the buoyancy mass m_0 and the position $\boldsymbol{r}_P$ of the internal point mass $\bar{m}$. We note that some of the possible circular helical motions may be unstable. For example, motions may diverge from steady circular helical motions to unsteady or periodic motions. The stability of circular helical motions depend on several parameters of the glider. In §8.3 we discuss how stability changes with respect to a vehicle bottom-heaviness parameter. The results discussed in this chapter follow the presentation in [143].

8.1 Rigid Body Relative Equilibria

We consider the motion of an underwater glider with a constant buoyancy mass and fixed internal mass. This vehicle is essentially a rigid body in water, with non-coincident centers of gravity and buoyancy. The configuration space used to describe the motion of such a glider is $SE(3)$, the space of all rigid body motions. In this section we derive all possible relative equilibria corresponding to the left action of $SE(3)$ on itself.

An element of $SE(3)$ may be represented as $(\boldsymbol{b}, R)$ where $\boldsymbol{b} \in \mathbb{R}^3$ is a vector and $R \in SO(3)$ is a rotation matrix. We use inertial coordinates (x, y, z) to describe $\boldsymbol{b}(t)$ and the yaw-pitch-roll Euler angle coordinates to describe R locally for writing the equations of motion of the underwater glider in §8.2.

Curves in three-dimensional space may be uniquely determined (except for their position in the space) by their curvature, κ, and torsion, τ. The curvature of the curve is defined as the norm of the derivative of the tangent vector of the curve with respect to its arc length (s), whereas torsion measures the deviation of the curve

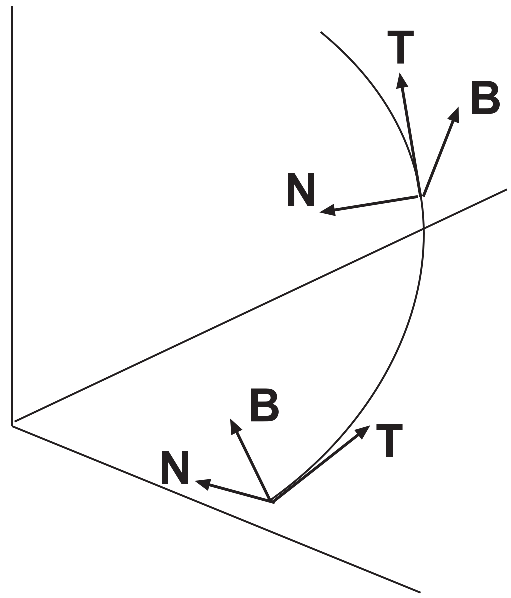

Figure 8.1: Frenet-Serret frames at two points on a three-dimensional curve.

from a plane, called the osculating plane. Reference [144] provides definitions of $\kappa(s)$, $\tau(s)$ for a general curve. We consider a time (t) parametrization of the curve in the following section and describe how $\kappa(t)$ and $\tau(t)$ are related to $\boldsymbol{b}(t)$. This relation is defined through the Frenet-Serret equations, which are presented in the following subsection.

8.1.1 Frenet-Serret Equations

The Frenet-Serret equations describe the motion of a triad of (unit) basis vectors as shown in Figure 8.1, called the Frenet-Serret frame, along a curve in three-dimensional space [144]. We can imagine a Frenet-Serret frame attached to the underwater glider. The first of the three basis vectors, $\boldsymbol{T}$, of the Frenet-Serret frame is chosen along the tangent of the path traced by the frame. Thus,

$$\boldsymbol{T}(t) = \frac{\dot{\boldsymbol{b}}(t)}{\|\dot{\boldsymbol{b}}(t)\|}. \tag{8.1}$$

The other two vectors of the Frenet-Serret frame are chosen as follows:

$$\boldsymbol{N}(t) = \frac{\dot{\boldsymbol{T}}(t)}{\|\dot{\boldsymbol{T}}(t)\|}, \tag{8.2}$$

$$\boldsymbol{B}(t) = \boldsymbol{T}(t) \times \boldsymbol{N}(t). \tag{8.3}$$

The evolution of the Frenet-Serret frame with time may be described in terms of $\tau(t)$ and $\kappa(t)$ as follows:

$$\frac{d\boldsymbol{T}}{dt} = V\kappa(t)\boldsymbol{N} \tag{8.4}$$

$$\frac{d\boldsymbol{N}}{dt} = -V\kappa(t)\boldsymbol{T} + V\tau(t)\boldsymbol{B} \tag{8.5}$$

$$\frac{d\boldsymbol{B}}{dt} = -V\tau(t)\boldsymbol{N}, \tag{8.6}$$

where $V = \|\dot{\boldsymbol{b}}\|$ is the speed of the frame.

Thus the path traced by the glider in the three-dimensional space may be described by specifying $\tau(t)$ and $\kappa(t)$. In the next subsection we compute all possible relative equilibria paths in the three-dimensional space corresponding to dynamics on $SE(3)$ in terms of $\kappa(t)$, $\tau(t)$.

8.1.2 Relative Equilibrium Solutions

The dynamics of rigid body motion are described on the phase space $TSE(3)$, the tangent bundle of $SE(3)$. A point belonging to $TSE(3)$ may be described by (g, ξ), where $g \in SE(3)$ and $\xi \in \mathfrak{se}(3)$. $\mathfrak{se}(3)$ is the Lie algebra corresponding to the Lie group $SE(3)$ (see Appendix B for a brief introduction to Lie groups and Lie algebras). The Lie algebra element ξ may be written as a 4×4 matrix:

$$\xi = \begin{bmatrix} \hat{\boldsymbol{\Omega}} & \boldsymbol{v} \\ 0 & 0 \end{bmatrix},$$

where $\mathbf{\Omega} \in \mathbb{R}^3$ is the rigid body angular velocity in body-coordinates and $\boldsymbol{v} \in \mathbb{R}^3$ is the translational velocity in body coordinates.

The Lie algebra element determines the evolution of the Lie group element g,

$$\dot{g} = g\xi \in TSE(3).$$

Thus, the kinematics of rigid body motion are given by the following equations:

$$\dot{R} = R\hat{\mathbf{\Omega}} \tag{8.7}$$

$$\dot{\boldsymbol{b}} = R\boldsymbol{v}. \tag{8.8}$$

The conditions for relative equilibria of $SE(3)$ are as follows [143]:

$$\dot{\boldsymbol{v}} = \mathbf{0} \tag{8.9}$$

$$\dot{\mathbf{\Omega}} = \mathbf{0}. \tag{8.10}$$

We note that the above conditions and the kinematics are a result of the system evolving on the $SE(3)$ configuration space. They are valid irrespective of the exact forces and moments acting on the rigid body. This remark also applies to the statement of the following theorem, which lists all possible relative equilibria on $SE(3)$.

Theorem 7. *The following types of motion describe all possible $SE(3)$ relative equilibria that satisfy conditions (8.9)-(8.10):*

1. *Motion along a straight line without any rotation.*

2. *Pure rotation.*

3. *Motion along a straight line with rotation about the direction of motion.*

4. *Motion along a circular helix.*

Proof: First, we derive a set of identities that we will later use to classify all possible relative equilibria.

Constancy of speed: Since $\boldsymbol{v}$ is constant for a relative equilibrium we can conclude from equation (8.8) that

$$\| \dot{\boldsymbol{b}} \| = \text{constant.} \tag{8.11}$$

Constancy of acceleration magnitude: Differentiating equation (8.8) we get

$$\begin{aligned} \ddot{\boldsymbol{b}} &= \dot{R}\boldsymbol{v} + R\dot{\boldsymbol{v}} \\ &= R\hat{\boldsymbol{\Omega}}\boldsymbol{v} \quad \because \dot{\boldsymbol{v}} = \boldsymbol{0} \qquad (8.12) \\ \Rightarrow \quad \| \ddot{\boldsymbol{b}} \| &= \text{constant.} \qquad (8.13) \end{aligned}$$

From equation (8.12) we can also calculate

$$\begin{aligned} \ddot{\boldsymbol{b}} &= R\hat{\boldsymbol{\Omega}}R^{-1}R\boldsymbol{v} \\ &= \widehat{R\boldsymbol{\Omega}}R\boldsymbol{v} \\ &= \hat{\boldsymbol{\omega}}\dot{\boldsymbol{b}}. \qquad (8.14) \end{aligned}$$

Orthogonality of acceleration and angular velocity:

$$\begin{aligned} \boldsymbol{\omega} \cdot \ddot{\boldsymbol{b}} &= R\boldsymbol{\Omega} \cdot R\hat{\boldsymbol{\Omega}}\boldsymbol{v} \\ &= R\boldsymbol{\Omega} \cdot \widehat{R\boldsymbol{\Omega}}R\boldsymbol{v} = 0. \qquad (8.15) \end{aligned}$$

Equations (8.12)-(8.15) must be satisfied by all $SE(3)$ relative equilibria. We first consider relative equilibria without spin ($\boldsymbol{\omega} = \boldsymbol{0}$). Since $\boldsymbol{\Omega} = R^{-1}\boldsymbol{\omega}$, $\boldsymbol{\omega} = \boldsymbol{0}$ implies $\boldsymbol{\Omega} = \boldsymbol{0}$. Thus, from equation (8.12) we have $\ddot{\boldsymbol{b}} = \boldsymbol{0}$, i.e., $\dot{\boldsymbol{b}}$ =constant, which corresponds to motion along a straight line (case 1 of Theorem 7).

When $\boldsymbol{\omega} \neq \mathbf{0}$ we can consider two subcases: from equation (8.15) either $\ddot{\boldsymbol{b}} = \mathbf{0}$ or $\ddot{\boldsymbol{b}}$ is perpendicular to $\boldsymbol{\omega}$. When $\ddot{\boldsymbol{b}} = \mathbf{0}$, $\dot{\boldsymbol{b}} =$ constant and we can employ equation (8.12) to conclude that either $\boldsymbol{v} = \mathbf{0}$ or $\boldsymbol{\Omega}$ is parallel to $\boldsymbol{v}$. The situation of $\boldsymbol{v} = \mathbf{0}$ corresponds to a pure rotation of the rigid body (case 2 of Theorem 7). The situation of $\boldsymbol{\Omega} \parallel \boldsymbol{v}$ is rotation of the rigid body about the direction of translation (case 3 of Theorem 7).

In the rest of the proof we show that $\ddot{\boldsymbol{b}}$ perpendicular to $\boldsymbol{\omega}$ corresponds to the motion of the rigid body along a circular helix by showing that the curvature κ and the torsion τ are constant for this case.

Using the definition of $\boldsymbol{N}$ (equation (8.2)) and the first Frenet-Serret equation (8.4) we have the following definition of $\kappa(t)$:

$$\kappa(t) = \frac{1}{V}\left\|\frac{d\boldsymbol{T}}{dt}\right\|. \tag{8.16}$$

Using equation (8.1) we calculate

$$\begin{aligned}
\kappa(t) &= \frac{1}{V}\left\|\frac{d}{dt}\left(\frac{\dot{\boldsymbol{b}}}{V}\right)\right\| \\
&= \frac{\|\ddot{\boldsymbol{b}}\|}{V^2} \quad \because\ V \text{ is constant from equation (8.11)} \\
&= \text{constant} \quad \because\ \|\ddot{\boldsymbol{b}}\| \text{ is constant from equation (8.14).}
\end{aligned} \tag{8.17}$$

From equation (8.12) we have $\|\ddot{\boldsymbol{b}}\| = \|\hat{\boldsymbol{\Omega}}\boldsymbol{v}\| = \|\boldsymbol{\Omega}\|\, V|\sin\xi|$, where ξ is the angle between $\boldsymbol{v}$ and $\boldsymbol{\Omega}$. Thus,

$$\kappa(t) = \frac{\|\boldsymbol{\Omega}\|}{V}|\sin\xi|. \tag{8.18}$$

Furthermore, from the definition of $\boldsymbol{N}$ (equation (8.2))

$$\boldsymbol{N} = \frac{d/dt\left(\dot{\boldsymbol{b}}/\|\dot{\boldsymbol{b}}\|\right)}{\|d/dt\left(\dot{\boldsymbol{b}}/\|\dot{\boldsymbol{b}}\|\right)\|}. \tag{8.19}$$

Since $\|\dot{\boldsymbol{b}}\|$ is constant (from equation (8.14)) we have $d/dt\left(\dot{\boldsymbol{b}}/\|\dot{\boldsymbol{b}}\|\right) = \ddot{\boldsymbol{b}}/\|\dot{\boldsymbol{b}}\|$. Thus,

$$\begin{aligned}
\boldsymbol{N} &= \frac{\ddot{\boldsymbol{b}}/\|\dot{\boldsymbol{b}}\|}{\|\ddot{\boldsymbol{b}}/\|\dot{\boldsymbol{b}}\|\|} \\
&= \frac{\ddot{\boldsymbol{b}}}{\|\ddot{\boldsymbol{b}}\|}. \qquad (8.20)
\end{aligned}$$

We evaluate $\tau(t)$ using the third Frenet-Serret equation (8.6). We have

$$\begin{aligned}
\frac{d\boldsymbol{B}}{dt} &= \dot{\boldsymbol{T}} \times \boldsymbol{N} + \boldsymbol{T} \times \dot{\boldsymbol{N}} \quad \text{(according to the definition of } \boldsymbol{B}\text{)} \\
&= \frac{\ddot{\boldsymbol{b}}}{V} \times \frac{\ddot{\boldsymbol{b}}}{\|\ddot{\boldsymbol{b}}\|} + \frac{\dot{\boldsymbol{b}}}{V} \times \frac{d}{dt}\left(\frac{\ddot{\boldsymbol{b}}}{\|\ddot{\boldsymbol{b}}\|}\right) \\
&= \frac{1}{V\|\ddot{\boldsymbol{b}}\|}\left(R\boldsymbol{v} \times \frac{d}{dt}(R\hat{\boldsymbol{\Omega}}\boldsymbol{v})\right) \quad \text{(using equation (8.12))} \\
&= \frac{1}{V\|\ddot{\boldsymbol{b}}\|}\left(R\boldsymbol{v} \times R\hat{\boldsymbol{\Omega}}\boldsymbol{y}\right) \text{ where } \boldsymbol{y} = \hat{\boldsymbol{\Omega}}\boldsymbol{v} \\
&= \frac{R\hat{\boldsymbol{v}}\hat{\boldsymbol{\Omega}}\boldsymbol{y}}{V\|\ddot{\boldsymbol{b}}\|} = \frac{R}{V\|\ddot{\boldsymbol{b}}\|}((\boldsymbol{v}\cdot\boldsymbol{y})\boldsymbol{\Omega} - (\boldsymbol{v}\cdot\boldsymbol{\Omega})\boldsymbol{y}) = -\frac{(\boldsymbol{v}\cdot\boldsymbol{\Omega})R\hat{\boldsymbol{\Omega}}\boldsymbol{v}}{V\|\ddot{\boldsymbol{b}}\|} \\
&= -\frac{(\boldsymbol{v}\cdot\boldsymbol{\Omega})\ddot{\boldsymbol{b}}}{V\|\ddot{\boldsymbol{b}}\|} = -\frac{(\boldsymbol{v}\cdot\boldsymbol{\Omega})}{V}\boldsymbol{N}. \qquad (8.21)
\end{aligned}$$

Thus, we infer

$$\begin{aligned}
\tau(t) &= \frac{(\boldsymbol{v}\cdot\boldsymbol{\Omega})}{V^2} = \text{ constant.} \\
&= \frac{|\boldsymbol{\Omega}|}{V}\cos\xi. \qquad (8.22)
\end{aligned}$$

Since $\kappa(t)$ and $\tau(t)$ are constants, the relative equilibrium motion is along a circular helix (case 4 of Theorem 7).

Thus, we have shown that all possible relative equilibria motions belong to the classes listed in the statement of Theorem 7. □

8.1.3 Relative Equilibria Realized by Underwater Glider Dynamics

The possible relative equilibrium motions corresponding to underwater glider dynamics (with constant buoyancy and a fixed internal mass position) are a subset of the motions listed in Theorem 7. We have already seen that motion along a straight line with constant speed is a possible relative equilibrium motion of the glider. In the next section we will show that circular helical motions are also steady solutions of underwater glider dynamics. But the other two types of motions listed in Theorem 7 are not steady motions of underwater glider dynamics. We note that all external forces and moments acting on the glider except gravitational force and rotational damping moment require some nonzero V. Gravitational force and rotational damping alone cannot produce a steady, rotational motion. This accounts for pure rotation not being one of the relative equilibrium solutions. Steady rotation about the translational direction of motion cannot be sustained due to the presence of damping. Although the moment due to the offset of CB and CG could balance the damping torque instantaneously, the magnitude of the CB-CG offset moment changes with rotation; hence, a steady motion cannot be realized.

8.2 Circular Helical Motions

In this section we focus on the steady, circular helical motions of underwater glider dynamics. First we write out equations (2.1)-(2.6) describing the three-dimensional dynamics of the glider for the case of constant buoyancy mass and fixed internal mass ($\bar{m}$) in §8.2.1. We interpret the buoyancy mass m_0 and position r_P of $\bar{m}$ as our control parameters in the present discussion. We solve the equilibrium equations of glider dynamics numerically for a number of control parameter sets in §8.2.2 to illustrate how the resulting circular helix may be regulated by adjusting the control parameters.

8.2.1 Three-Dimensional Equations of Motion

We presented the longitudinal plane equations of motion in §2.3 and discussed the transformation from force to acceleration control (of the internal mass $\bar{m}$) for longitudinal dynamics in §2.3.2. The force to acceleration transformation may be extended to the dynamics representing three-dimensional motion of the glider also [5]. Employing this transformation and assuming that the position $\boldsymbol{r}_P$ of the internal mass $\bar{m}$ is constant (implying that acceleration control inputs are zero) and a constant buoyancy mass, we arrive at the following equations of motion for $SE(3)$ dynamics of the underwater glider [5]:

$$\begin{pmatrix} \dot{\boldsymbol{v}} \\ \dot{\boldsymbol{\Omega}} \end{pmatrix} = \begin{bmatrix} (M+\bar{m}) & -\bar{m}\hat{\boldsymbol{r}}_P \\ \bar{m}\hat{\boldsymbol{r}}_P & J-\bar{m}\hat{\boldsymbol{r}}_P\hat{\boldsymbol{r}}_P \end{bmatrix}^{-1} \begin{pmatrix} \bar{\boldsymbol{F}}' \\ \bar{\boldsymbol{T}}' \end{pmatrix}, \tag{8.23}$$

where

$$\bar{\boldsymbol{F}}' = \Big[M\boldsymbol{v} + \bar{m}(\boldsymbol{v} + \hat{\boldsymbol{\Omega}}\boldsymbol{r}_P)\Big] \times \boldsymbol{\Omega} + m_0 g R^T \boldsymbol{k} + \boldsymbol{F_{ext}} \tag{8.24}$$

$$\begin{aligned} \bar{\boldsymbol{T}}' &= \Big[J\boldsymbol{\Omega} + \bar{m}\hat{\boldsymbol{r}}_P(\boldsymbol{v} + \hat{\boldsymbol{\Omega}}\boldsymbol{r}_P)\Big] \times \boldsymbol{\Omega} - \hat{\boldsymbol{v}}M\boldsymbol{v} - \bar{m}\hat{\boldsymbol{v}}\hat{\boldsymbol{\Omega}}\boldsymbol{r}_P \\ &+ \ \bar{m}g\hat{\boldsymbol{r}}_P(R^T\boldsymbol{k}) + \boldsymbol{T_{ext}}. \end{aligned} \tag{8.25}$$

The external force $\boldsymbol{F_{ext}}$ and moment $\boldsymbol{T_{ext}}$ include the hydrodynamic forces and moments described by equations (2.9)-(2.14). We note that equation (8.23) is a specialization of equations (2.4)-(2.6) presented in §2.2.

In addition to equation (8.23) we also need to consider equations (2.1)-(2.2), which describe the kinematics of the underwater glider.

We use the Yaw-Pitch-Roll (YPR) Euler angle convention to describe the rotation matrix R. In this convention the rotation from the inertial frame to the body-fixed frame is performed by first rotating about the 3-axis of the body by an angle ψ (yaw), then rotating about the 2-axis of the body by an angle θ (pitch) and finally rotating about the 1-axis of the body by an angle φ (roll), all in the counterclockwise direction. The rotation matrix in terms of (ψ, θ, φ) is

$$R = \begin{bmatrix} \cos\psi\cos\theta & -\sin\psi\cos\varphi + \cos\psi\sin\theta\sin\varphi & \sin\psi\sin\varphi + \cos\psi\sin\theta\cos\varphi \\ \sin\psi\cos\theta & \cos\psi\cos\varphi + \sin\psi\sin\theta\sin\varphi & -\cos\psi\sin\varphi + \sin\psi\sin\theta\cos\varphi \\ -\sin\theta & \cos\theta\sin\varphi & \cos\theta\cos\varphi \end{bmatrix} \tag{8.26}$$

We note that the above rotation matrix takes vectors described in body-frame coordinates to inertial coordinates.

Let us closely observe the right-hand-side of equation (8.23). We know that for relative equilibrium motion $\dot{\boldsymbol{v}} = \dot{\boldsymbol{\Omega}} = 0$, i.e., $\boldsymbol{v}$ and $\boldsymbol{\Omega}$ are constant. Since $\boldsymbol{v}$ is constant, the angles α and β, which are defined entirely by the components of $\boldsymbol{v}$, are also constant. This implies that the external (hydrodynamic) force $\boldsymbol{F_{ext}}$ and torque $\boldsymbol{T_{ext}}$ are also constant. Thus, we see that all terms of $\bar{\boldsymbol{F}}^{'}$ and $\bar{\boldsymbol{T}}^{'}$ except possibly those involving $R^T\boldsymbol{k}$ are constant. But since we require $\bar{\boldsymbol{F}}^{'} = \bar{\boldsymbol{T}}^{'} = 0$ for relative equilibrium, we can infer that $R^T\boldsymbol{k}$ must be constant at relative equilibrium, i.e.,

$$R^T\boldsymbol{k} = \begin{pmatrix} -\sin\theta \\ \cos\theta\sin\varphi \\ \cos\theta\cos\varphi \end{pmatrix} = \text{ constant.} \tag{8.27}$$

Thus, we can conclude that the pitch angle θ and roll angle φ are constants for relative equilibrium motion.

We note the general relation between the body-coordinates angular velocity vector

$\boldsymbol{\Omega}$ and the YPR Euler angle rates:

$$\boldsymbol{\Omega} = \begin{bmatrix} 1 & 0 & -\sin\theta \\ 0 & \cos\varphi & \cos\theta\sin\varphi \\ 0 & -\sin\varphi & \cos\theta\cos\varphi \end{bmatrix} \begin{pmatrix} \dot{\varphi} \\ \dot{\theta} \\ \dot{\psi} \end{pmatrix}. \tag{8.28}$$

Since $\boldsymbol{\Omega}$, φ and θ are constant we require

$$\dot{\psi}_e = \text{ constant} \tag{8.29}$$

for equation (8.28) to be satisfied.

From equation (8.28) we can readily see that $\dot{\psi}_e = 0$ corresponds to $\boldsymbol{\Omega}_e = \mathbf{0}$. Since $\theta_e =$ constant and $\phi_e =$ are constant $\dot{\theta}_e = \dot{\phi}_e = 0$. $\boldsymbol{\Omega}_e = \mathbf{0}$ corresponds to steady gliding along a straight line. When $\dot{\psi}_e \neq 0$ we have $\boldsymbol{\Omega}_e \neq \mathbf{0}$. This motion corresponds to one of the last three cases of Theorem 7. $\boldsymbol{v}_e = \mathbf{0}$ would correspond to case 2 of Theorem 7 and a $\boldsymbol{v}$ of the form

$$\boldsymbol{v}_e = \|\boldsymbol{v}_e\| \begin{pmatrix} -\sin\theta_e \\ \cos\theta_e\sin\phi_e \\ \cos\theta_e\cos\phi_e \end{pmatrix} \tag{8.30}$$

so that $\boldsymbol{\Omega}_e$ is parallel to $\boldsymbol{v}_e$ would correspond to case 3 of Theorem 7. However, as noted in §8.1.3 $\boldsymbol{v}_e = \mathbf{0}$, $\boldsymbol{\Omega}_e \neq \mathbf{0}$ or $\boldsymbol{v}_e$ of the form in the above equation are not solutions of the glider equilibrium equations. Thus, the only possible steady solutions for the underwater glider are straight line motions and circular helix motions.

The axis of the circular helix traced by the relative equilibrium motion of the glider is determined by the direction of gravity. To see this let us differentiate $R^T\boldsymbol{k}$.

Since $R^T\boldsymbol{k}$ is constant we have

$$\begin{aligned} \frac{d}{dt}\left(R^T\boldsymbol{k}\right) &= 0 \\ \Rightarrow \left(R\hat{\boldsymbol{\Omega}}\right)^T\boldsymbol{k} &= 0 \\ \Rightarrow -\hat{\boldsymbol{\Omega}}R^T\boldsymbol{k} &= 0 \\ \text{i.e., } \boldsymbol{\Omega}\times(R^T\boldsymbol{k}) &= 0 \\ \Rightarrow R^TR\boldsymbol{\Omega}\times(R^T\boldsymbol{k}) &= 0 \\ \Rightarrow R^T(\boldsymbol{\omega}\times\boldsymbol{k}) &= 0. \end{aligned} \tag{8.31}$$

The last equality implies that $\boldsymbol{\omega} = \mathbf{0}$ or $\boldsymbol{\omega}$ must be parallel to $\boldsymbol{k}$. The former is true for straight line motion and the latter for circular helix motion. Thus, for equilibrium motion along a circular helix, the axis of the helix must be aligned with the direction of gravity.

We summarize our observations about the circular helical relative equilibrium of underwater gliders:

1. The underwater glider moves with constant speed along a circular helix at relative equilibrium.

2. The pitch and roll angles are constant while the yaw changes at a constant rate.

3. The angle of attack and side-slip angle remain constant. This implies that the total viscous forces and moments relative to vehicle are constant.

4. The axis of the circular helix is aligned with the direction of gravity.

In the following subsection we illustrate how the glider speed, the radius, time period and pitch of the circular helix traced by the glider depend on vehicle parameters.

m	50 kg
m_h	40 kg
$\bar{m}$	9 kg
m_{f1}	5 kg
m_{f2}	60 kg
m_{f3}	70 kg
J_1	4 kgm^2
J_2	12 kgm^2
J_3	11 kgm^2
K_{L0}	0 kg/m
K_L	135 kg/m/rad
K_{D0}	2 kg/m
K_D	45 kg/m/rad^2
K_β	20 kg/m/rad
K_{M0}	0 kg
K_M	-50 kg/rad
K_{MY}	100 kg/rad
K_{MR}	-60 kg/rad
$K_{\Omega_{11}}$	-20 kg.s/rad
$K_{\Omega_{12}}$	-60 kg.s/rad
$K_{\Omega_{13}}$	-20 kg.s/rad
$K_{\Omega_{21}}$	0 kg.s/rad^2
$K_{\Omega_{22}}$	0 kg.s/rad^2
$K_{\Omega_{23}}$	0 kg.s/rad^2

Table 8.1: Underwater glider parameters for study of dependence of circular helices on control parameters $\boldsymbol{r}_P$ and m_0.

8.2.2 Parameter Dependence of Circular Helices

We consider the underwater glider model with parameters reflecting the Slocum glider [14]. Some of the Slocum parameters were estimated using data from sea trials in [46] and using wind tunnel experiments in [45]. Other Slocum parameters were chosen to reflect observed qualitative behavior of the glider, as in [5]. The parameter mapping presented here is meant to serve as a qualitative illustration of the effect of vehicle parameters on resulting steady motions. Accurate prediction of glider motions would require experiment-based estimation of all vehicle parameters.

For our example we pick vehicle parameters as indicated in Table 8.2.2. We interpret the buoyancy mass m_0 and the position $\boldsymbol{r}_P$ of the internal mass $\bar{m}$ as control parameters. By varying the control parameters we can influence the steady circular helical motion of the underwater glider. Before presenting the influence of varying control parameters we present a simulation of 3D glider dynamics with a nominal set of control parameters for the purpose of illustration. We set the control parameters to be $r_{P1} = 2$ cm, $r_{P2} = 2$ cm, $r_{P3} = 4$ cm and $m_0 = 0.25$ kg. The initial conditions for the simulation are $x(0) = 0$ m, $y(0) = 0$ m, $z(0) = 0$ m, $\psi(0) = 0^o$, $\theta(0) = -26.654^o$, $\phi(0) = 14.419^o$, $v_1 = 0.802$ m/s, $v_2 = 0.014$ m/s, $v_3 = 0.025$ m/s, $\Omega_1(0) = 0.0046$ rad/s, $\Omega_2(0) = 0.0025$ rad/s and $\Omega_3(0) = 0.0077$ rad/s. The simulation is run for 2000 s. Figure 8.2 shows the trajectory followed by the underwater glider in 3D space. The glider converges to the equilibrium circular helical motion, indicating that the equilibrium is stable. The steady circular helix has a radius of 66.60 m and the equilibrium speed of the glider is 0.729 m/s. The pitch of the circular helix is 206.2 m and the time period of motion is 639.6 s. Figures 8.3 and 8.4 shows plots of all states of the glider dynamics for the first 300 s of the simulation.

We compute the equilibrium circular helical motion for different positions $\boldsymbol{r}_P$ of the internal mass $\bar{m}$ and different values of m_0. The parameters of a steady helix (radius, speed, pitch, period) depend on the equilibrium values of the glider velocity, angular velocity, angle of attack and side-slip angle. Figures 8.5 and 8.6 show the variation of the circular helix parameters with respect to r_{P1}. In Figure 8.5 we consider positive values of r_{P1} and negative buoyancy (heavy glider, $m_0 > 0$) with $r_{P2} = 2$ cm, $r_{P3} = 4$ cm and $m_0 = 0.25$ kg and in Figure 8.6 we consider negative values of r_{P1} and positive buoyancy (light glider, $m_0 < 0$) with $r_{P2} = 2$ cm, $r_{P3} = 4$ cm and $m_0 = -0.25$ kg. We could not find any equilibrium solutions for a combination of negative buoyancy ($m_0 > 0$) and aft center of gravity ($r_{P1} < 0$) or for a combination of positive buoyancy ($m_0 < 0$) and fore center of gravity ($r_{P1} > 0$). For $m_0 > 0$ as r_{P1} increases the equilibrium pitch angle as well as the flight path angle become

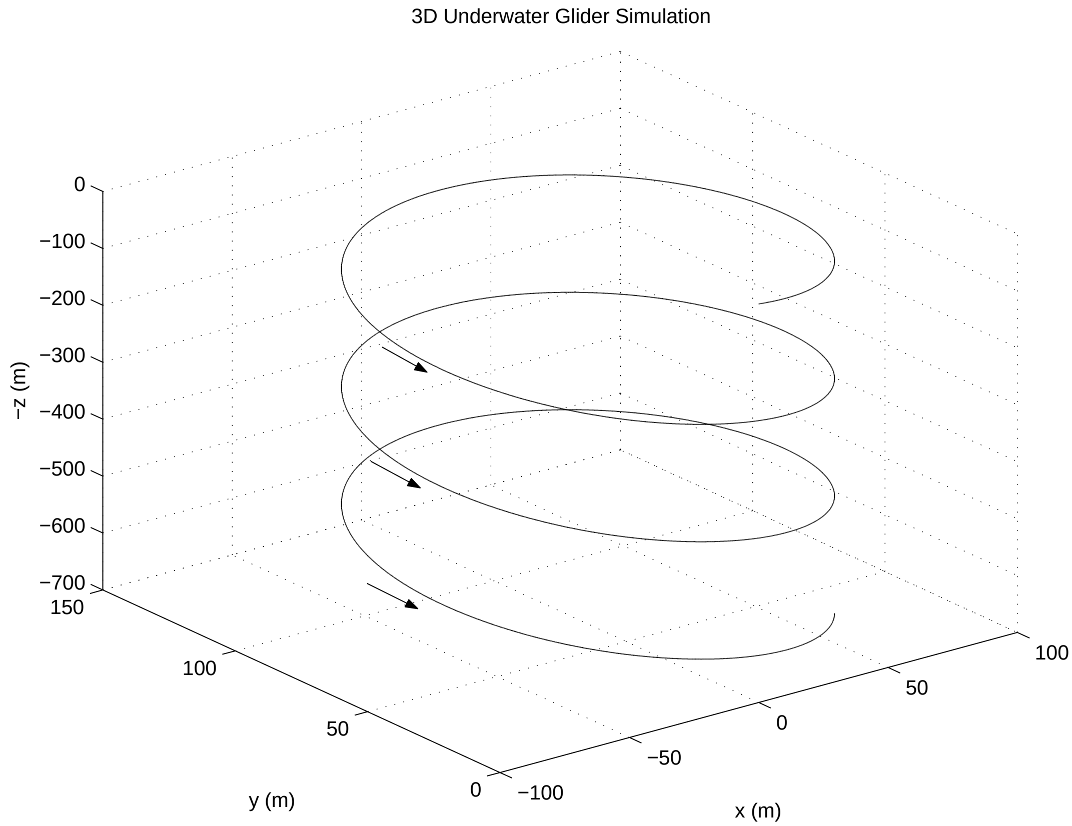

Figure 8.2: Simulation of underwater glider dynamics showing the motion converging to a steady circular helix in 3D space.

more negative, as expected. The equilibrium angle of attack α_e and side-slip angle β_e become lower (both are positive). The smaller α_e causes a lower drag force, which leads to a greater equilibrium speed V_e. On the other hand, increasing r_{P1} also leads to smaller angular speed $\|\boldsymbol{\Omega}_e\|$. Smaller $\|\boldsymbol{\Omega}_e\|$ and greater V_e both contribute towards greater helical radius, as well as greater pitch and period of the helix. For $m_0 < 0$ both α_e and β_e are negative. For small $|r_{P1}|$, as r_{P1} is decreased, α_e initially decreases (i.e., more negative) causing greater equilibrium drag, and consequently smaller V_e. Beyond a critical value decreasing r_{P1} leads to greater α_e (i.e., less negative) and greater V_e.

Figures 8.7 and 8.8 show variation of helix parameters for different positions of $\bar{m}$ along the body 2-direction. Figure 8.7 corresponds to negative buoyancy with

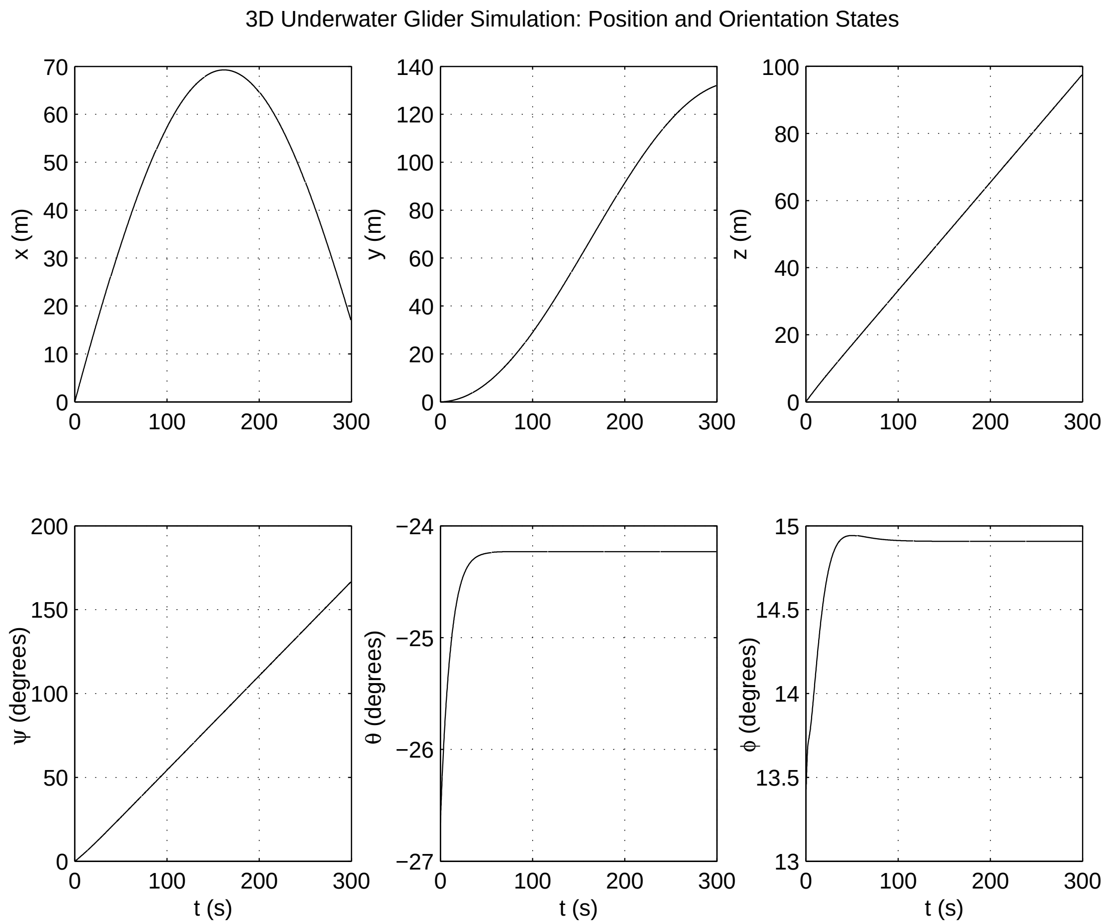

Figure 8.3: Underwater glider simulation: position and orientation states.

$r_{P1} = 2$ cm, $r_{P3} = 4$ cm and $m_0 = 0.25$ kg, and Figure 8.8 corresponds to positive buoyancy with $r_{P1} = -2$ cm, $r_{P3} = 4$ cm and $m_0 = -0.25$ kg. The radius of the helix tends to ∞ as r_{P2} approaches 0. An infinite radius is a result of the equilibrium angular velocity being equal to the zero vector. This corresponds to steady gliding along a straight line in the longitudinal plane of the glider (the equilibrium side-slip angle tends to zero as r_{P2} tends to zero). For nonzero r_{P2} the range of variation of the equilibrium roll angle is smaller for $m_0 = 0.25$ kg than for $m_0 = -0.25$ kg. The sign of β_e depends on the signs of both m_0 and r_{P2}. β_e is positive when m_0 and r_{P2} have opposite signs and negative otherwise. For example a positive β_e is realized for a heavy vehicle ($m_0 > 0$) rolled to the left or for a light vehicle ($m_0 < 0$) rolled to the

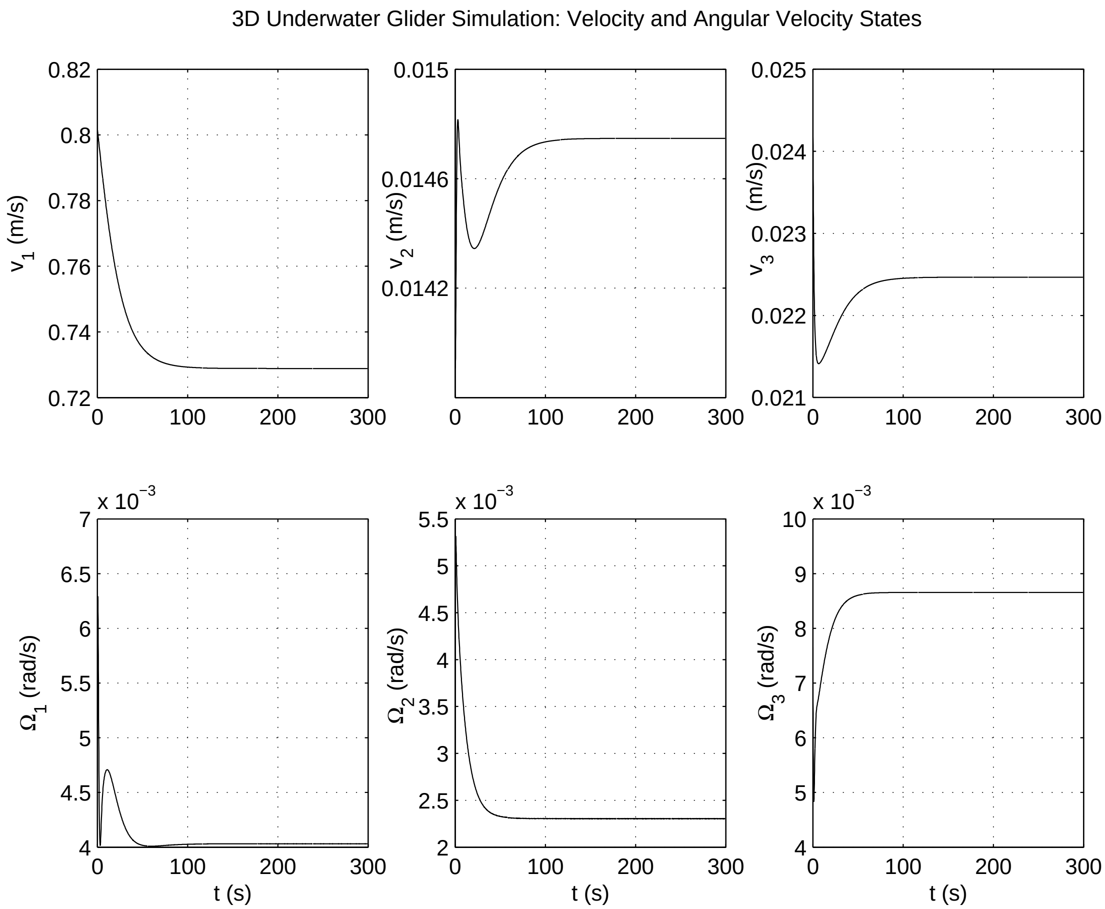

Figure 8.4: Underwater glider simulation: velocity and angular velocity states.

right. Thus, we get different equilibrium solutions for the same r_{P2} for different signs of m_0. But for a given m_0 the equilibrium solutions are symmetric about $r_{P2} = 0$.

Figures 8.9 and 8.10 show the variation of helix parameters for varying r_{P3}. Figure 8.9 corresponds to negative buoyancy with $r_{P1} = 2$ cm, $r_{P2} = 2$ cm and $m_0 = 0.25$ kg, and Figure 8.10 corresponds to positive buoyancy with $r_{P1} = -2$ cm, $r_{P2} = 2$ cm and $m_0 = -0.25$ kg. For the latter case the helix parameters vary smoothly with r_{P3} while for the former case there is a critical value of r_{P3} that corresponds to steady, straight-line gliding motion due to zero equilibrium angular velocity. However, this straight line motion is not in the longitudinal plane of glider (the equilibrium side-slip angle is not zero).

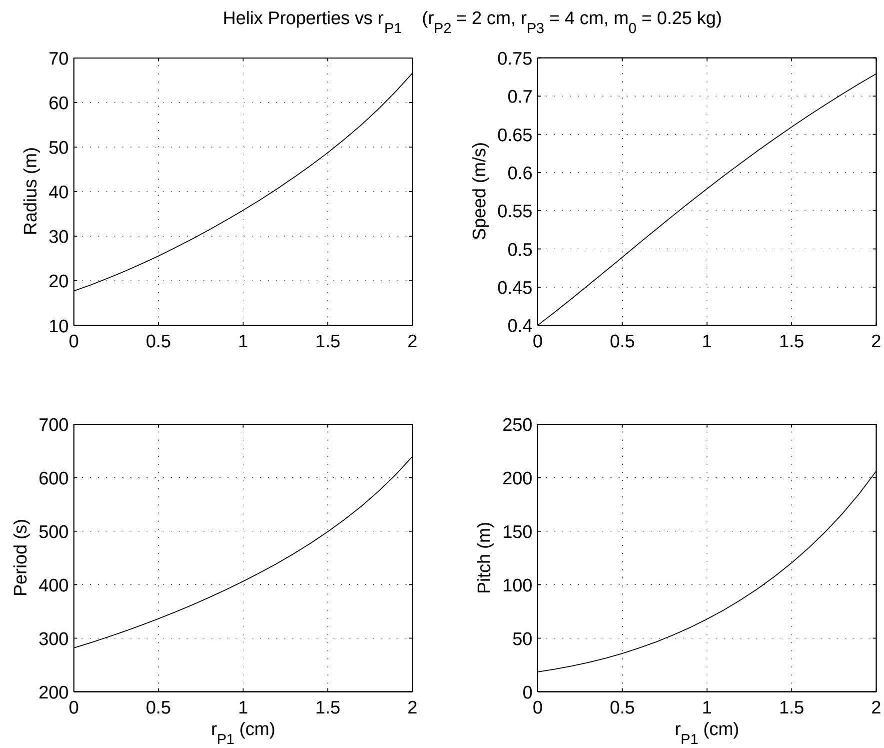

Figure 8.5: Variation of Helix Parameters With Respect to r_{P1} for $m_0 > 0$.

Figures 8.11 and 8.12 show the variation of helix parameters with respect to m_0 for negative and positive buoyancies, respectively. m_0 does not directly influence the moment balance. For force balance, greater $|m_0|$ implies greater net gravitational force that can balance larger magnitudes of other forces due to greater equilibrium translational and angular speeds. The variation of translational speed versus $|m_0|$ is almost linear. The equilibrium angular speed grows at a faster rate than the equilibrium translational speed, causing the radius of the circular helix to decrease with $|m_0|$.

The parametric study presented here reveals some interesting trends in the dependence of the equilibrium circular helical motion on control adjustments. It shows that a wide range of circular helices may be obtained by small variations of $\boldsymbol{r}_P$ and m_0 for the vehicle parameters considered in the study. This is very encouraging from a control standpoint. The complex dependence of the equilibrium circular helical motion

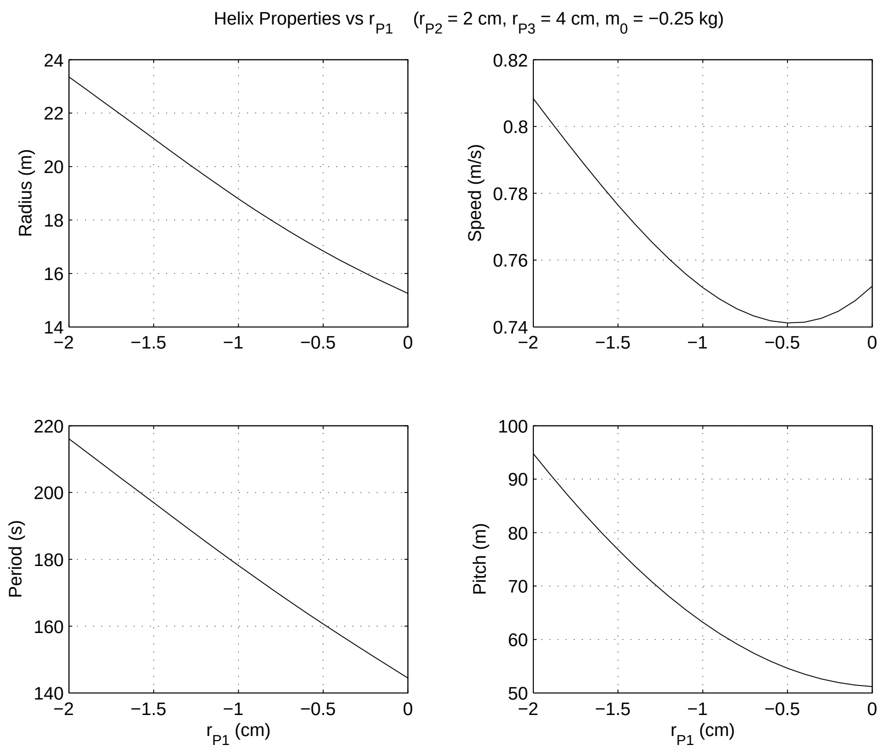

Figure 8.6: Variation of Helix Parameters With Respect to r_{P1} for $m_0 < 0$.

needs to be further investigated using analytical results from equilibrium equations ($\boldsymbol{F}' = \boldsymbol{0}$, $\boldsymbol{T}' = \boldsymbol{0}$), which is a subject of future work. Another future work direction is to consider linear dependencies of equilibrium states on control parameter $(\boldsymbol{r}_P, m_0)$ variation about nominal circular helix motions. The latter type of work, which has been done for aircraft flying in constant circles, would aid in developing further insight for designing control laws for regulating more complex maneuvers of the underwater glider.

8.3 Stability of Circular Helix Motion

In this section we present a numerical example that illustrates how the stability of circular helical steady motions of the glider is affected by the vehicle bottom-

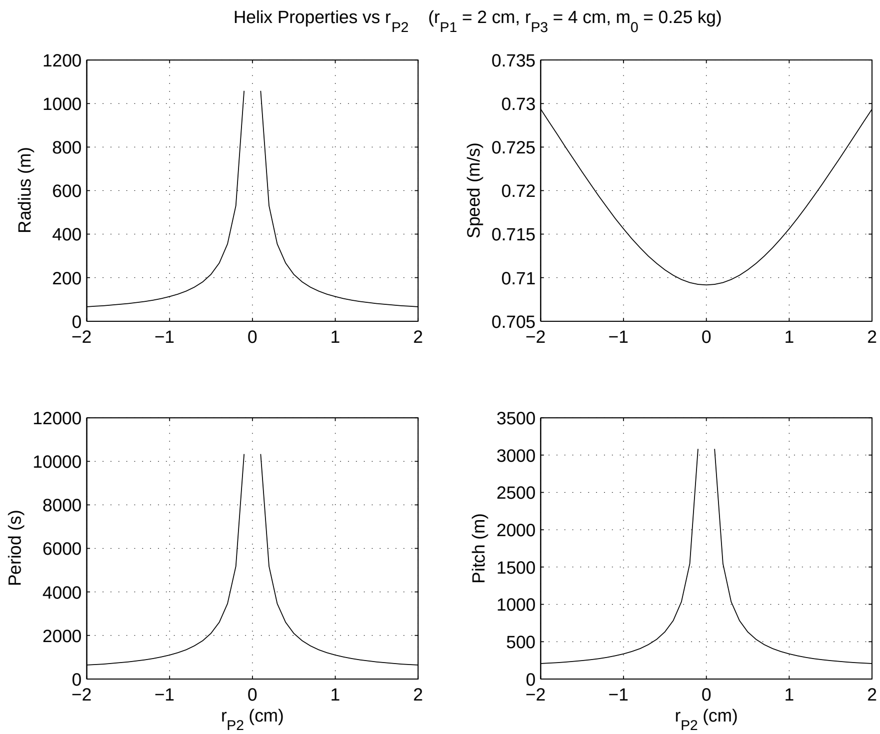

Figure 8.7: Variation of Helix Parameters With Respect to r_{P2} for $m_0 > 0$.

heaviness, parameterized by r_{bh}, defined as follows:

$$r_{bh} := \boldsymbol{r}_P \cdot R^T \boldsymbol{k},$$

where $\boldsymbol{r}_P$ is the position of $\bar{m}$ with respect to the CB, in body coordinates. Thus, r_{bh} is the component of $\boldsymbol{r}_P$ in the direction of gravity.

We note that the bottom-heaviness parameter does not affect the relative equilibrium solution of glider dynamics. This is because the moment due to $\bar{m}$ in equilibrium depends only on the component of $\boldsymbol{r}_P$ perpendicular to the direction of gravity. But r_{bh} *does* affect the stability of the relative equilibrium, quite like in the case of an underwater rigid body without viscous forces and moments studied in [47].

We consider an underwater glider example with the same vehicle parameters as in the previous section. We fix $m_0 = 0.25$ kg. We start with a nominal case of $r_{P1} =$

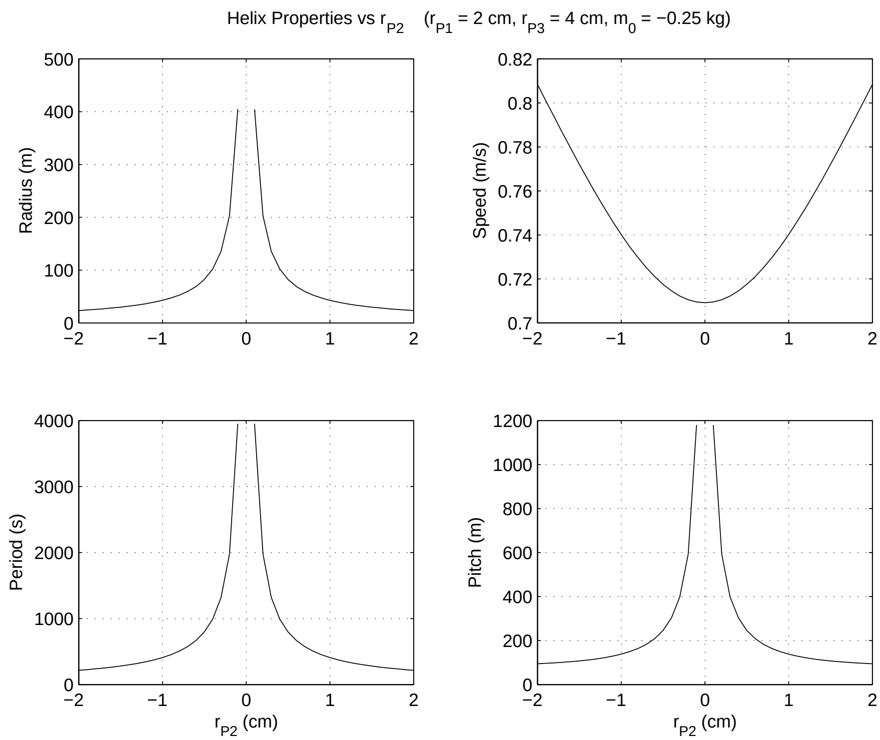

Figure 8.8: Variation of Helix Parameters With Respect to r_{P2} for $m_0 < 0$.

0.02 m, r_{P2} = -0.02 m and r_{P3} = 0.04 m. This corresponds to r_{bh} = 0.0481 m. We then vary r_{bh} and study the eigenvalues of the linearization of the dynamics about the relative equilibrium solution over a range of r_{bh}. Figures 8.13 and 8.14 show plots of real part of the eigenvalues of the linearized system versus r_{bh}. Near r_{bh} = -0.004 m (indicated by letter A in Figure 8.14) one of the purely real eigenvalues crosses over the imaginary axis, and the circular helix steady motion becomes unstable. Near this bifurcation value of r_{bh}, the glider dynamics is structurally unstable [145], i.e., the nature of glider dynamics changes drastically for small changes in a system parameter (r_{bh}). This structural instability was also reflected in the instability of numerical computations for parameter values around the bifurcation value of r_{bh}.

Near parameter values indicated by letters B and D, in Figure 8.14 two purely real eigenvalues come together to form a complex conjugate pair as r_{bh} increases. On the other hand, near the parameter value indicated by C a complex conjugate pair

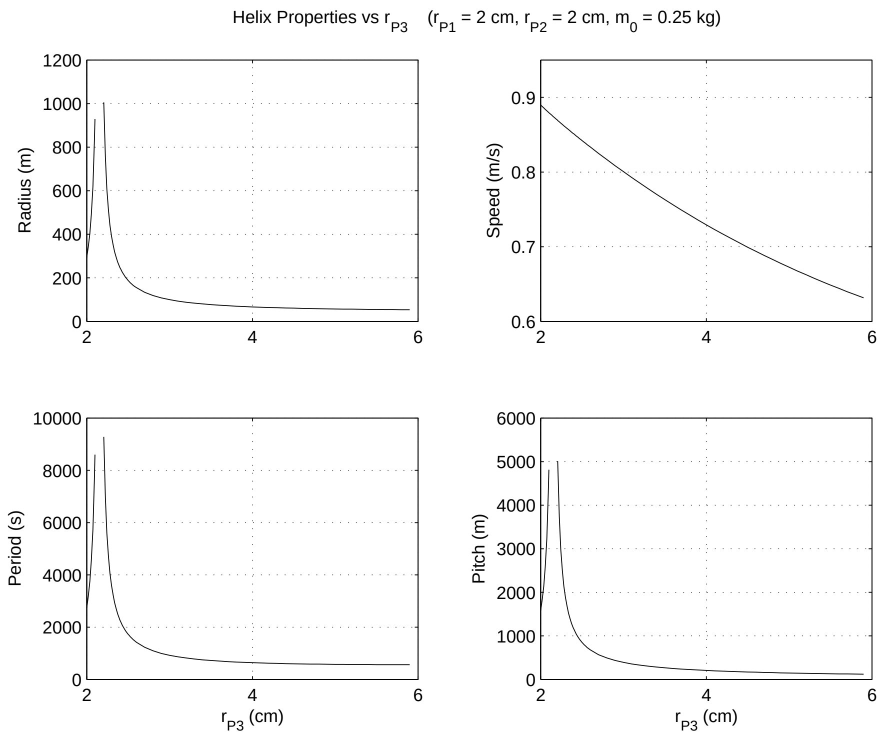

Figure 8.9: Variation of Helix Parameters With Respect to r_{P3} for $m_0 > 0$.

of eigenvalues breaks into two purely real eigenvalues. Thus, B and D correspond to break-away points and C corresponds to a break-in point on the root locus plot [146] of the linearization of glider dynamics with respect to r_{bh}.

From this numerical example we note that the circular helix motion is stable provided $\bar{m}$ is placed such that r_{bh} is large enough, or in other words if the underwater glider is sufficiently bottom-heavy. Furthermore we see that the stability properties of the circular helix vary smoothly with respect to r_{bh}.

The numerical study presented in this chapter indicates that a wide range of steady circular helices can be realized by adjusting the control parameters $\boldsymbol{r_P}$ and m_0. We have also seen that the stability of the circular helix may be regulated by the parameter r_{bh} without changing other specifications of the helix. A subject of future work is to support the numerical results of this chapter by analytical computations. Analytical computations of circular helix steady motions are much harder than com-

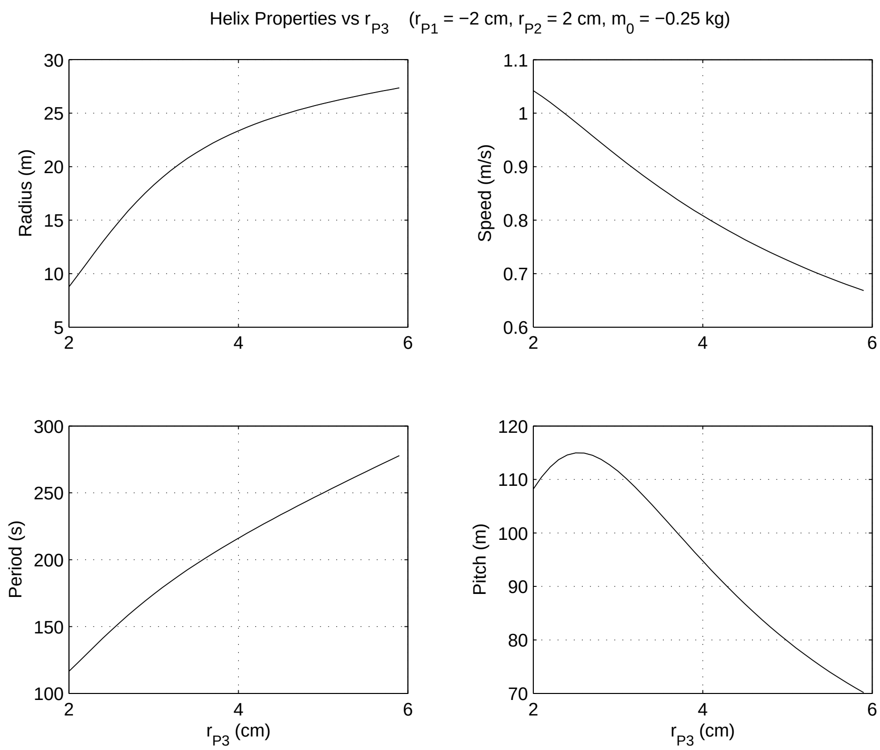

Figure 8.10: Variation of Helix Parameters With Respect to r_{P3} for $m_0 < 0$.

puting steady straight line glides. However, analytical results will aid in exploring the 3D operating envelope of a given underwater glider and in glider design studies for particular applications that use 3D steady motions.

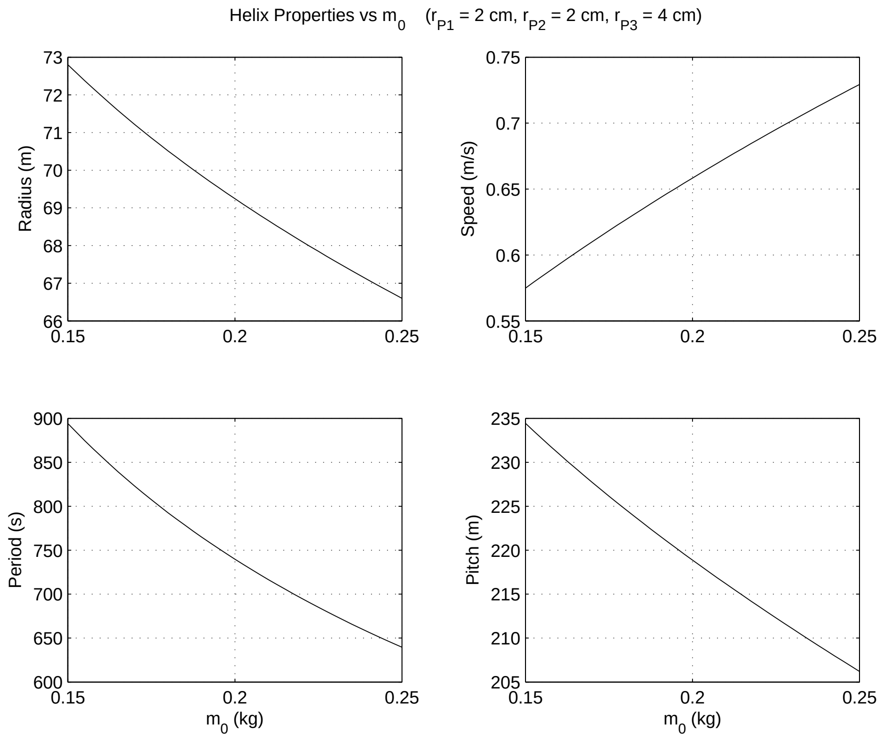

Figure 8.11: Variation of Helix Parameters With Respect to m_0 for $m_0 > 0$.

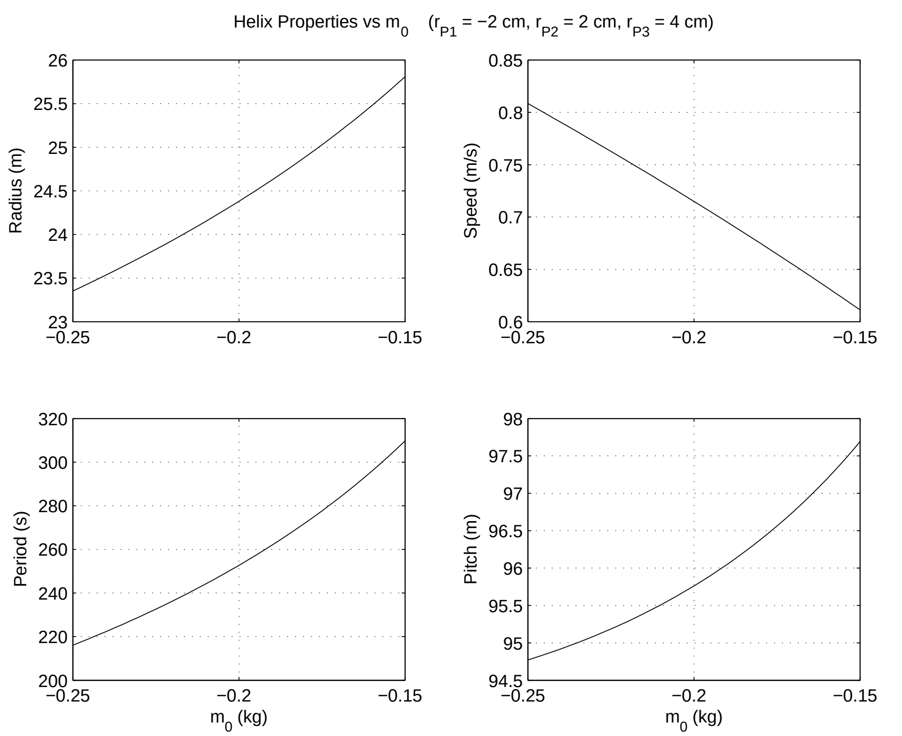

Figure 8.12: Variation of Helix Parameters With Respect to m_0 for $m_0 < 0$.

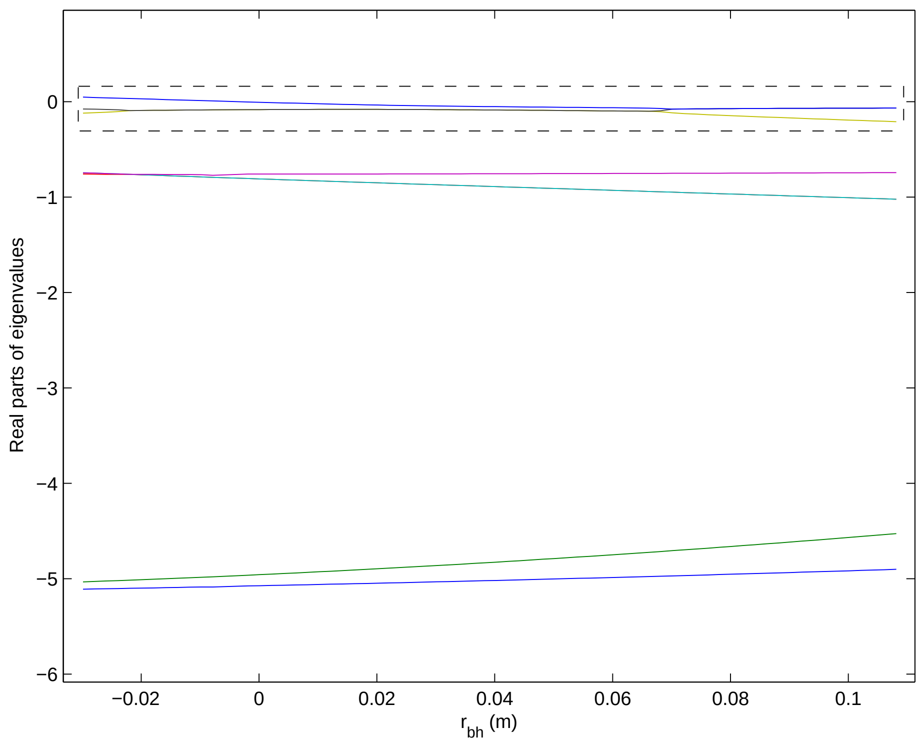

Figure 8.13: Variation of real parts of eigenvalues of the circular helix equilibrium with respect to the bottom-heaviness parameter r_{bh}. The area within the dashed rectangular box is zoomed into in Figure 8.14.

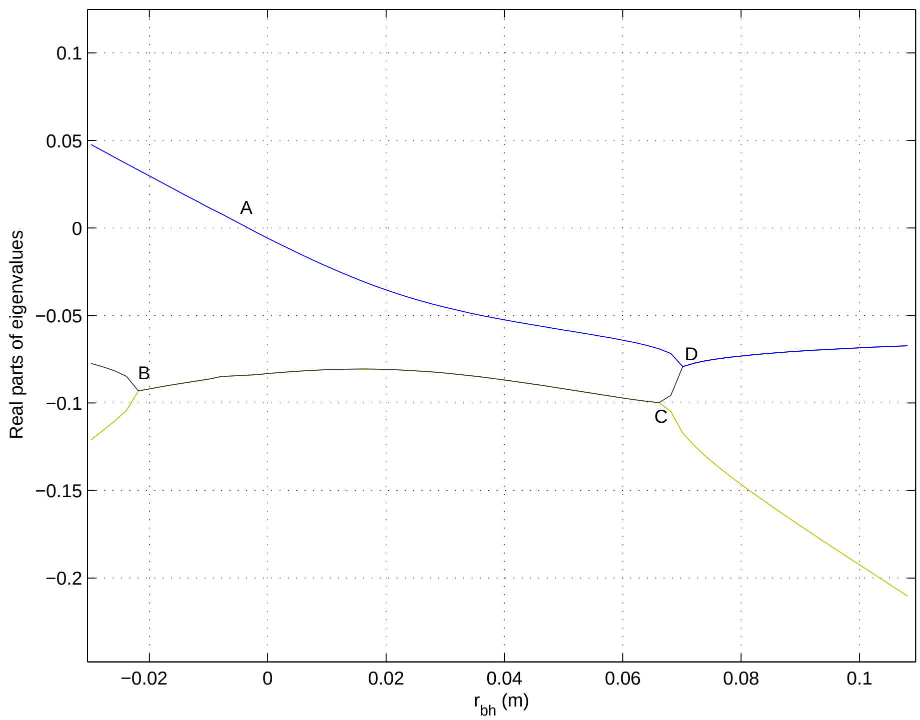

Figure 8.14: A more detailed view of Figure 8.13 in the area enclosed by the dashed rectangular box. This figure shows the real part of one of the eigenvalues crossing zero. This happens when r_{bh} is approximately equal to -0.004 m. This is the bifurcation value of r_{bh}.

Chapter 9

Conclusions and Future Directions

We have adopted a nonlinear systems approach to the study of dynamics and design of control laws for vehicles subject to aerodynamic forcing. The work presented in this thesis was motivated by the underwater glider application. Many of the results derived were specialized to underwater gliders but, in principle, analogous results can be obtained for vehicles with similar dynamics such as airships, aircraft, and other autonomous underwater vehicles. In this chapter, we present a brief summary of the approach, results, and conclusions presented in this thesis, as well as possible directions for future work.

9.1 Conclusions

Our approach in this thesis is based on determining the stability of steady motions associated with vehicle dynamics and then choosing control actions to regulate vehicle motion to these steady motions, or track desired trajectories using steady motions. As a result, the control laws we present do not require large magnitude actuation. They attempt to beneficially use the natural dynamics of the vehicle to achieve a desired motion. Our stability analysis method classifies different subsystems of vehicle dynamics. The subsystems are shown to be stable using individual Lyapunov functions, which are combined together to construct a composite Lyapunov function for proving the stability of steady motion of the full vehicle dynamics.

Using linear analysis, we initially show that a typical underwater glider design is an open-loop stable system if we consider the control inputs to be internal mass acceleration and buoyancy rate. We review linear controllability and observability results for underwater glider longitudinal dynamics.

We study the phugoid-mode approximation of underwater glider dynamics with a view of developing further insight into the geometric structure induced by the hydrodynamic lift force. We present multiple Hamiltonian formulations of the phugoid-mode model. The Hamiltonian function of a 2-dimensional Hamiltonian formulation provides us with a Lyapunov function candidate for proving the stability of the translational subsystem of the underwater glider, and eventually the stability of steady glides.

Using singular perturbation theory, we reduce the dynamics of an underwater glider to a 2-dimensional system describing the phugoid mode of the vehicle. We derive conditions under which such a reduction is valid. For applying singular perturbation theory, we prove exponential stability of the boundary-layer and reduced system equilibria using separate Lyapunov functions. These functions are later combined in a composite Lyapunov function, used for proving the stability of steady glides as well as for computing region of attraction guarantees. This Lyapunov-based stability result is useful for developing control methods that employ steady gliding motions. We consider different control configurations of an underwater glider, and design specific control laws for stabilizing desired steady glides.

We present a trajectory tracking methodology based on exponential stability of steady gliding motions, and apply this methodology to a CTOL aircraft model. We prove exponential stability of desired steady glides for a CTOL aircraft using an interconnected system framework. Lyapunov functions for the individual subsystems of the aircraft are combined to construct a composite Lyapunov function that proves the stability of all closed-loop steady glides. Adjustable control gains in our tracking formulation allow us determine a suitable compromise between position tracking error and control effort. The use of steady gliding motions makes this tracking method attractive for the underwater glider application.

We present results pertaining to steady motions of underwater gliders in three dimensions. We show that the only possible relative equilibrium motions for the glider are the straight-line motion and the motion along a circular helix. We study the dependence of circular helix properties on vehicle control parameters for a model reflecting one of the commercially available underwater gliders. We show that small changes in control parameters lead to significant changes in the circular helix properties, which is encouraging from a control standpoint. We also demonstrate how the bottom-heaviness of the underwater glider, which does not determine the circular helix solution, but influences its stability.

The work presented in this thesis may be extended in several directions to further analysis of underwater and aerospace vehicle dynamics, and to design control laws that can be implemented on such vehicles. We list some directions for future work in the following section.

9.2 Future Directions

The singular perturbation results of Chapter 5 were derived for the case of an underwater glider with coincident centers of gravity and buoyancy. Although most results are expected to hold for the general case of noncoincident CB and CG, verification of Theorem 2 for this case presents additional technical difficulties. We may conclude stability of steady glides for slightly noncoincident CB and CG by continuous dependence of eigenvalues on vector field parameters [145]. A more systematic procedure may involve the application of regular perturbation theory to calculate a bound on $\boldsymbol{r_P}$ within which the stability of steady glides may be guaranteed by a composite Lyapunov function of the form presented in Chapter 5.

The effect of noncoincidence of CB and CG was modelled as a torque control in Chapter 6. This was an approximation to the coupling between dynamics of $\bar{m}$ and the rigid body dynamics, fully represented by equations (2.18)-(2.24). Extension of stability results to the case of noncoincident centers would let us consider alternative models of actuation for nonlinear control design.

The approximate tracking result presented in Chapter 7 is derived for the case of a straight line desired trajectory. It may be extended to more general trajectories. A general desired trajectory may be first approximated by a set of straight line segments. Each of these individual segments may be tracked approximately as in Chapter 7. However, further calculations are required to compute the maximal upper bound on the position tracking error for tracking general trajectories. This bound will depend on the highest curvature of the desired trajectory. A simulation demonstration of the CTOL aircraft approximately tracking a curvy trajectory was presented in §7.3.3. The calculation of position error bounds is the subject of a future publication.

The tracking result of Chapter 7 assumed an ability to stabilize to any desired steady glide. Any steady glide may be realized by a CTOL aircraft equipped with (unlimited) thrust and torque controls. Presence of control saturation limits the set of steady glides that can be achieved. However, a wide range of desired trajectories may be approximately tracked with very low thrust and torque control actuation. On the other hand an underwater gilder is not equipped with thrust control. The size of the glider limits the maximum buoyancy control magnitude and the maximum control torque due to $\bar{m}$. These limits determine the range of steady glides that may be realized by an underwater glider. With a limited set of steady glides possible the underwater glider will only be able to track a restricted class of desired trajectories.

Such a class may be characterized by bounds on speed, curvature and slope of the desired trajectory. A useful calculation will provide a mapping between these bounds and glider control saturation limits.

An alternative to trajectory tracking is path following, which has been considered for aircraft. Trajectory tracking requires the vehicle to be at a certain position at a certain time whereas the path following problem only concerns following a desired path. The vehicle is allowed to track the path at any speed in the latter problem. This easing of requirements may be highly justified in many surveying/data gathering applications where underwater gliders are employed. Dependence of the set of paths that can be approximately tracked on glider parameters and the associated position error bounds need to be calculated.

In Chapter 8 we considered the influence of the position r_P of the internal mass and the buoyancy m_0 on the resulting steady state circular helix for an underwater glider example. It appears intractable to solve the mapping symbolically for a general underwater glider, but further simulations and analysis are required to better understand how best we can regulate three-dimensional steady motions using our control parameters $\boldsymbol{r_p}$ and m_0.

Many results presented in this thesis depend on the estimates of the hydrodynamic moment and force coefficients. Small uncertainties in these parameters do not adversely affect vehicle stability determination. But accurate calculation of relative equilibria requires accurate estimates of moment and force coefficients. Parameter identification experiments presented in [46] were based on steady gliding data and only provided estimates of parameters pertaining to longitudinal-plane dynamics. Dynamic system identification that incorporate adequate excitation of glider dynamics would provide a more accurate and comprehensive estimate of glider parameters. Methods such as those used in [147, 148] for system identification of aircraft may be applied to identify hydrodynamic parameters of the underwater glider.

One of the motivating problems for nonlinear systems analysis of underwater glider dynamics is coordination of multiple vehicles. Coordination problems have been posed and successful solutions have been implemented at a high level in the Autonomous Ocean Sampling Network (AOSN) and Adaptive Sampling And Prediction (ASAP) projects. The spatial and time scales of importance for these projects were much larger than those of underwater glider dynamics to allow for a high level consideration of glider motion. For applications involving multiple gliders required to coordinate at similar spatial and time scales as the vehicle dynamics we would need to consider both transient and steady motions. For example, we may coordinate multiple gliders to converge to a synchronized relative equilibrium motion by regulating the relative positions of their internal masses [50]. In the context of multi-vehicle coordination it may be useful to consider natural motions of the glider to switch between different relative equilibria motion.

Appendix A

Geometric Mechanics Definitions

In this appendix we briefly introduce some topics from geometric mechanics that have been used in this thesis. The definitions we provide are based on [22, 149], and we refer the reader to these references for more details. We start with the notion of a manifold. A manifold is essentially any space that locally looks like a Euclidean space. The precise definition follows.

Definition [149]: A **manifold** M of dimension n is a topological space (i.e., a set endowed with a means of defining neighborhoods for its elements) having the following three properties:

1. M is Hausdorff, i.e., it is possible to find disjoint neighborhoods for any two distinct points of the space.

2. M is locally Euclidean of dimension n, i.e., it is possible to find an invertible transformation from any open neighborhood of P to an open set in $\mathbb{R}^n$ such that the transformation is a bijection, continuous, and has a continuous inverse (in other words, the transformation is homeomorphic).

3. M has a countable basis of open sets, i.e., any open subset of M may be specified as a union of a countable number of (basis) open sets. □

Our next goal is to strengthen the definition of a manifold to that of a differentiable manifold. This requires introduction of the notion of a chart and the property of $\mathcal{C}^\infty$ compatibility between different charts of a manifold. Let us consider a neighborhood $U \in M$ and a homeomorphic map f from U to $\mathbb{R}^n$. Together they form a chart (U, f) of M. Let us also consider another neighborhood $V \in M$ and an associated homeomorphic map g. The images of both U and V, through transformations f and g respectively, are open sets in $\mathbb{R}^n$. Now, we wish to consider the mappings that take us between the intersection of these images. For instance, the mapping that takes us from the image of U to that of V is $g \circ f^{-1}$. The domain of this mapping is non-empty if the intersection of the images of U and V is non-empty. If this mapping is $\mathcal{C}^\infty$ for a non-empty domain we say that U and V are $\mathcal{C}^\infty$-compatible. Now, we are ready to give a definition of a differentiable manifold.

Definition [149]: A **differentiable manifold** is a manifold equipped with a family of charts $\mathcal{U} = (U_\alpha, f_\alpha)$ such that

1. The U_α cover M.
2. For any α, β, the charts (U_α, f_α) and (U_β, f_β) are $\mathcal{C}^\infty$-compatible.
3. Any chart (V, g) that is $\mathcal{C}^\infty$-compatible with every (U_α, f_α) is itself in $\mathcal{U}$. □

Before proceeding to the definition of a Lie group, we provide the familiar definition of a general group.

Definition: A **group** is a non-empty set G, endowed with a binary operation $* : G \times G \to G$, called the group operation, such that

1. $*$ is associative, i.e., $\forall\, a, b, c \in G,\ a * (b * c) = (a * b) * c$.
2. G has an identity element, i.e., $\exists\, e \in G$ such that $a * e = e * a = a,\ \forall\, a \in G$.
3. For every $a \in G$, $\exists\, a^{-1} \in G$ such that $a * a^{-1} = a^{-1} * a = e$. □

A Lie group is a special type of a group, as described by the following definition.

Definition: A **Lie group** is a group which is also a manifold such that the group operation is smooth (i.e., $\mathcal{C}^\infty$). $\square$

The Euclidean space $\mathbb{R}^n$ is an example of a Lie group. Other examples of Lie groups are $SO(3)$ and $SE(3)$[1] that are defined below.

Definition: The group $\boldsymbol{SO(3)}$ is the set of 3×3 matrices such that $R^T R = I_3$ and $\det(R) = 1$, where R is any element of the group and I_3 is the 3×3 identity matrix. The group $\boldsymbol{SE(3)}$ is the set of all 4×4 matrices of the form

$$\begin{bmatrix} R & \boldsymbol{b} \\ 0_{1\times 3} & 1 \end{bmatrix},$$

where $R \in SO(3)$, $\boldsymbol{b} \in \mathbb{R}^3$ and $0_{1\times 3}$ is the 1×3 zero matrix. For both $SO(3)$ and $SE(3)$, the group binary operation is the usual matrix multiplication. $\square$

In order to talk about dynamics on a manifold, we need to use the notion of a tangent vector. The tangent vector may be defined in many equivalent ways. Here, we provide a definition based only on parameterized curves on manifolds. Consider a manifold M and two curves $c_1(t)$ and $c_2(t)$ in M. The two curves are considered equivalent at m if

1. $c_1(0) = c_2(0) = m \in M$.

2. $(f \circ c_1)'(0) = (f \circ c_2)'(0)$,

where f denotes the mapping of a local chart and $()'$ is the derivative with respect to the parameter t. Now, we are ready to define a tangent vector.

Definition: A **tangent vector** at $m \in M$ is an equivalence class of curves $[c]_m$, i.e., it denotes the set of all curves equivalent to $c(t)$ at m. $\square$

[1]The acronyms SO and SE stand for 'Special Orthogonal' and 'Special Euclidean' respectively. Generally speaking $SO(n)$ is a group consisting of $n \times n$ orthogonal matrices having a special property, that their determinant is equal to 1. $SE(n)$ is a matrix group constructed using elements of $SO(n)$ and $\mathbb{R}^n$.

Next, we define the tangent space, the tangent bundle, and vector fields.

Definition: The **tangent space** at m is the collection of all tangent vectors that can be defined at m. It is denoted as $T_m M$. $\square$

Definition: We call $TM = \bigcup_{m \in M} (T_m M)$ the **tangent bundle** of M. $\square$

According the above definition the tangent bundle is a disjointed union of tangent spaces along with the corresponding base points. For example, we could consider the manifold $M = S^1$, which contains the points on a circle. The tangent space at any point m on the circle is essentially the infinitely-long tangent line at that point. This tangent line is the tangent space $T_m M$. Any subset of the tangent line represents a tangent vector at m. The tangent bundle TM is essentially the collection of all points m with their attached tangent lines $T_m M$. Sometimes the manifold M is called the "base manifold", point m a "base point" and the tangent space at m is called a "fiber". So the tangent bundle is the collection of base points and its attached fibers.

Definition: A **vector field** X on a manifold M is a map $X\colon M \to TM$ that assigns a vector $X(m)$ at the point $m \in M$. $\square$

We note that the tangent space is a vector space. We can consider a dual space of this vector space. The dual space of the tangent space is called the cotangent space and its elements are called cotangent vectors, or simply covectors. The cotangent space at m is denoted by $T_m^* M$. The space $T^* M = \bigcup_{m \in M} (T_m^* M)$ is the cotangent bundle of M.

Before concluding this chapter we introduce some differential forms that are used in the following appendix chapter, and present definitions of related operations.

Definition: A **0-form** on a manifold M maps $m \in M$ to a real number.

$$\text{0-form: } M \to \mathbb{R} \quad \square$$

An example of 0-forms is a function f that maps $m \in M$ to $f(m) \in \mathbb{R}$.

Definition: A **1-form** on a manifold M maps every tangent vector in T_mM for every $m \in M$ to a real number.

$$\text{1-form: } T_mM \to \mathbb{R} \qquad \square$$

An example of 1-forms is the differential df of a function f on M that maps $v \in TM$ to $df(v) =< df(m), v_m >\in \mathbb{R}$.

Definition: A **2-form** on a manifold M is a map $\Omega(m)$: $T_mM \times T_mM \to \mathbb{R}$ that assigns to each $m \in M$ a skew symmetric, bilinear form on T_mM, i.e.,

$$\Omega(m)\colon T_mM \times T_mM \to \mathbb{R}$$

such that

$$\begin{aligned} \Omega(m)(v_1, v_2) &= -\Omega(m)(v_2, v_1) \quad \text{[skew symmetry]} \\ \Omega(m)(\alpha v_1 + \beta v_2, v_3) &= \alpha\Omega(v_1, v_3) + \beta\Omega(v_2, v_3) \quad \text{[bilinearity]} \end{aligned}$$

for all v_1, v_2, $v_3 \in T_mM$. $\square$

The 2-form may be considered as a skew symmetric, bilinear matrix that may vary over the manifold M. The definition of the 2-form may be further generalized to k-forms [22].

The wedge product (denoted by the symbol $\wedge$) is an operation that can be used to obtain a $(k + l)$-form from a $k-$form and an $l-$form. Below we define only the wedge product of two 1-forms.

Definition: The **wedge product**, $\alpha \wedge \beta$, of two 1-forms α and β is a 2-form defined as follows:

$$(\alpha \wedge \beta)(v_1, v_2) = \alpha(v_1)\beta(v_2) - \alpha(v_2)\beta(v_1) \qquad \square$$

For example, if we consider 1-forms $\alpha = [1\ 0]$ and $\beta = [0\ 1]$ that map every tangent vector $v_1 = [v_{11}\ \ v_{12}]^T$ in $T_m\mathbb{R}^2$ for all $m \in \mathbb{R}^2$ to the real numbers v_{11} and v_{12} respectively, the wedge product $\alpha \wedge \beta$ is the 2-form

$$\alpha \wedge \beta = \begin{bmatrix} 0 & 1 \\ -1 & 0 \end{bmatrix}.$$

The above 2-form takes two vectors $v_1 = [v_{11}\ v_{12}]^T$, $v_2 = [v_{21}\ v_{22}]^T$ and yields the real number $v_{11}v_{22} - v_{12}v_{21}$.

The interior product operation yields $(k-1)$ forms from $k-$forms $(k > 0)$. We define the interior product of a 2-form below.

Definition: The **interior product** of a 2-form Ω with respect to a vector field X defined on the manifold M is a 1-form $i_X\Omega$ such that

$$i_X\Omega(v) = \Omega(X(m), v),$$

for all $v \in T_mM$ and all $m \in M$. $\square$

Appendix B

Hamiltonian Systems

The familiar form of Hamilton's equations are

$$\boldsymbol{q} = \frac{\partial H}{\partial \boldsymbol{p}} \tag{B.1}$$

$$\boldsymbol{p} = -\frac{\partial H}{\partial \boldsymbol{p}}, \tag{B.2}$$

where $\boldsymbol{p}$, $\boldsymbol{q} \in \mathbb{R}^n$ are the configuration and conjugate momentum vectors respectively. The function $H(p, q) : \mathbb{R}^{2n} \to \mathbb{R}$ is called the Hamiltonian function. A dynamical system whose equations have the above form is called a (canonical) Hamiltonian system. In the rest of this chapter we present a generalization of the Hamiltonian system to include systems with a more general structure, as well as systems defined on sets other than $\mathbb{R}^{2n}$.

First, we define a special type of manifold (see Appendix A for the definitions of a manifold and a 2-form) called the Symplectic manifold.

Definition: A **symplectic manifold** is a manifold P together with a closed, non-degenerate, 2-form Ω. A symplectic manifold is represented as (P, Ω). $\square$

The 2-form Ω essentially determines a bilinear map Ω_z at each point z on the manifold. The bilinear map Ω_z takes two elements from the tangent space of P at z

and yields a real number:

$$\Omega_z : T_zP \times T_zP \to \mathbb{R}$$
$$(v_z, w_z) \mapsto \Omega_z(v_z, w_z).$$

We note that the bilinear map Ω_z does not have to be constant over the manifold. Next, we provide a definition of a symplectic Hamiltonian system.

Definition: Let (P, Ω) be a symplectic manifold. A vector field X on P describes a **symplectic Hamiltonian system** if there exists a function $H : P \to \mathbb{R}$ such that $\forall v \in T_zP$

$$\Omega_z(X(z), v) = dH(z) \cdot v.$$

Equivalently, using the notion of the interior product, a vector field X is Hamiltonian if

$$i_X\Omega = dH$$

for some $H : P \to \mathbb{R}$. $\square$

The equations (B.1)-(B.2) are a special case of the symplectic Hamiltonian system defined above. They correspond to a Hamiltonian system defined on a vector space (a special case of a manifold) $P = \mathbb{R}^{2n}$, with a constant symplectic form

$$\Omega_b = \begin{bmatrix} 0_{n\times n} & -\mathbb{I}_{n\times n} \\ \mathbb{I}_{n\times n} & 0_{n\times n} \end{bmatrix},$$

where $0_{n\times n}$ and $\mathbb{I}_{n\times n}$ are the $n \times n$ zero matrix and the $n \times n$ identity matrix, respectively.

The concept of a Hamiltonian system can be further generalized using Poisson brackets and Poisson manifolds, defined below.

Definition: A **Poisson bracket**, denoted $\{,\} : \mathcal{F}(P) \times \mathcal{F}(P) \to \mathcal{F}(P)$, is a map that takes two differentiable functions defined on the manifold P and yields a function defined on P, and satisfies the following properties -

1. Bilinearity: $\forall F, K, L \in \mathcal{F}(P)$ and $\alpha,\ \beta \in \mathbb{R}$, $\{\alpha F + \beta K, L\} = \alpha\{F, L\} + \beta\{K, L\}$.

2. Skew Symmetry: $\forall F, K \in \mathcal{F}(P)$, $\{F, K\} = -\{K, F\}$.

3. Jacobi's Identity: $\forall F, K, L \in \mathcal{F}(P)$, $\{F, \{K, L\}\} + \{K, \{L, F\}\} + \{L, \{F, K\}\} = 0$.

4. Derivation: $\forall F, K, L \in \mathcal{F}(P)$, $\{FK, L\} = F\{K, L\} + K\{F, L\}$. □

Definition: A **Poisson manifold** is a manifold P along with a Poisson bracket operation $\{,\}$ for differentiable functions defined on P. A Poisson manifold is denoted by $(P, \{,\})$. □

Now, we are ready to define a Hamiltonian system on a Poisson manifold.

Definition: A **vector field** X **on a Poisson manifold** $(P, \{,\})$ **is Hamiltonian** if there is a function $H : P \to \mathbb{R}$ such that for all differentiable functions $G \in \mathcal{F}(P)$

$$dG \cdot X = \{G, H\}. \qquad \square$$

We note that a symplectic manifold is also a Poisson manifold. This is true because it is always possible to define a Poisson bracket operation using the symplectic form. Given differentiable functions $F, G \in \mathcal{F}(P)$ the Poisson bracket operation corresponding to the symplectic form Ω is

$$\{F, G\}(z) = \Omega(z)(X_F(z), X_G(z)),$$

for all $z \in P$, where $X_F(z)$ and $X_G(z)$ are the symplectic Hamiltonian vector fields corresponding to Hamiltonian functions F and G, respectively. On the other hand, all Poisson manifolds are not symplectic manifolds. The key difference is with regard to the degeneracy property of the corresponding structures. Recall from the definition of a symplectic manifold that the symplectic 2-form Ω must be non-degenerate. The Poisson bracket is allowed to be degenerate in general (although Poisson brackets derived from symplectic forms will be non-degenerate).

Hamiltonian systems have been widely studied and many tools have been developed that make use of geometric structures summarized in this chapter. The interested reader is referred to [22, 150, 151] for a number of analysis and design tools for Hamiltonian systems.

Appendix C

Theorem 5 Calculations

In this appendix we present details of the calculations related to the Lyapunov function for the translational subsystem of the CTOL aircraft model presented in Chapter 7. In §7.2.4 we present the Lyapunov function candidate

$$Q_1 = \frac{1}{3}(1+\bar{V})^3 - (1+\bar{V})\cos\bar{\gamma} + \frac{2}{3}$$

for proving the stability of the translational subsystem, defined by equation (7.68). In this appendix we show that Q_1 satisfies conditions (7.41)-(7.42) of Theorem 5 for the translational subsystem (7.68).

First, we compute $\dot{Q}_1 = \frac{\partial Q_1}{\partial x_1} f(x_1)$:

$$\begin{aligned}
\dot{Q}_1 \;=\; V_e\Big[& -K_{Dr_e}\left((\bar{V}^2+2\bar{V})^2 + 4(1+\bar{V})^2\sin^2\frac{\bar{\gamma}}{2}\right) - a_L c(1+\bar{V})^2\bar{\gamma}\sin\bar{\gamma} \\
& - a_D bc^2\bar{\gamma}^2\left(\bar{V}^2+2\bar{V}\right)^2 - 2a_D bc^2\bar{\gamma}^2\left(1+\bar{V}\right)^2\sin^2\frac{\bar{\gamma}}{2} \\
& - 2a_D bc^2\bar{\gamma}^2\left(\bar{V}^2+2\bar{V}\right) + 2a_D bc\left(c\alpha_e+1\right)\bar{\gamma}\left(\bar{V}^2+2\bar{V}\right)^2 \\
& + 4a_D bc(c\alpha_e+1)\left(1+\bar{V}\right)^2\bar{\gamma}\sin^2\frac{\bar{\gamma}}{2} + 2a_D bc\left(c\alpha_e+1\right)\bar{\gamma}\left(\bar{V}^2+2\bar{V}\right)\Big]
\end{aligned}$$

Let us consider $\|x\| \leq r < 1$. Since $a_L, c > 0$ we can deduce the following inequalities for the terms of the above equation within the square parentheses -

$$
\begin{aligned}
-K_{Dr_e}\left(\bar{V}^2+2\bar{V}\right)^2 &= -K_{Dr_e}(2+\bar{V})^2\bar{V}^2 \\
&\leq -K_{Dr_e}(2-r)^2\bar{V}^2. \\
-4K_{Dr_e}(1+\bar{V})^2\sin^2\frac{\bar{\gamma}}{2} &\leq -4K_{Dr_e}(1-r)^2\sin^2\frac{\bar{\gamma}}{2} \\
&\leq -4K_{Dr_e}(1-r)^2\frac{\sin^2(r/2)}{(r/2)^2}\frac{\bar{\gamma}^2}{4} \\
&= -K_{Dr_e}(1-r)^2\frac{\sin^2(r/2)}{(r/2)^2}\bar{\gamma}^2 \\
-a_Lc(1+\bar{V})^2\bar{\gamma}\sin\bar{\gamma} &= -a_Lc(1+\bar{V})^2|\bar{\gamma}\sin\bar{\gamma}| \\
&\leq -a_Lc(1+\bar{V})^2\left|\bar{\gamma}\frac{\sin r}{r}\bar{\gamma}\right| \\
&\leq -a_Lc\frac{\sin r}{r}\bar{\gamma}^2(1-r)^2 \qquad \because |\bar{V}|\leq r. \\
-a_Dbc^2\bar{\gamma}^2\left(\bar{V}^2+2\bar{V}\right)^2 &\leq 0. \\
-2a_Dbc^2\bar{\gamma}^2\left(1+\bar{V}\right)^2\sin^2\frac{\bar{\gamma}}{2} &\leq 0. \\
-2a_Dbc^2\bar{\gamma}^2\left(\bar{V}^2+2\bar{V}\right) &= -a_Dbc^2\left(1+\bar{V}\right)^2\bar{\gamma}^2+a_Dbc^2\bar{\gamma}^2 \\
&\leq -a_Dbc^2\left((1-r)^2-1\right)\bar{\gamma}^2 \\
&= -a_dbc^2(r^2-2r)\bar{\gamma}^2. \\
2a_Dbc\left(c\alpha_e+1\right)\bar{\gamma}\left(\bar{V}^2+2\bar{V}\right)^2 &\leq 2a_Dbc|c\alpha_e+1|r(2+r)\bar{V}^2. \\
4a_Dbc(c\alpha_e+1)\left(1+\bar{V}\right)^2\bar{\gamma}\sin^2\frac{\bar{\gamma}}{2} &\leq 4a_Dbc|c\alpha_e+1|(1+r)^2r\frac{\bar{\gamma}^2}{4} \\
&\leq a_Dbc|c\alpha_e+1|(1+r)^2r\bar{\gamma}^2. \\
2a_Dbc\left(c\alpha_e+1\right)\bar{\gamma}\left(\bar{V}^2+2\bar{V}\right) &\leq 2a_Dbc|\left(c\alpha_e+1\right)|r\bar{V}^2+4a_Dbc\left(c\alpha_e+1\right)\bar{\gamma}\bar{V} \\
&\leq 2a_Dbc|\left(c\alpha_e+1\right)|r\bar{V}^2+2a_Dbc|\left(c\alpha_e+1\right)|(\bar{V}^2+\bar{\gamma}^2) \\
&= 2a_Dbc|\left(c\alpha_e+1\right)|\left((1+r)\bar{V}^2+\bar{\gamma}^2\right)
\end{aligned}
$$

Substituting the above inequalities in the expression for $\dot{Q}_1$ we get

$$\begin{aligned}
\dot{Q}_1 \;\; &\leq \;\; -\Big(K_{Dr_e}(2-r)^2 - 2a_D bc|c\alpha_e + 1|(1+3r+r^2)\Big)\bar{V}^2 \\
&\quad -\Big(K_{Dr_e}(1-r)^2\frac{\sin^2(r/2)}{(r/2)^2} + a_L c\frac{\sin r}{r}(1-r)^2 + a_d bc^2(r^2-2r) \\
&\qquad - \;\; a_D bc|c\alpha_e + 1|((1+r)^2 r + 2)\Big)\bar{\gamma}^2.
\end{aligned}$$

Thus, the Lyapunov function candidate Q_1 for the translational subsystem (7.68) satisfies condition (7.41) of Theorem 5 with λ_1 given by equation (7.70).

Next, we simplify the inequality (7.73):

$$\left\|\frac{\partial Q_1}{\partial x_1}\right\| \;\; \leq \;\; \left\{2(\bar{V}^2 + 2\bar{V})^2 + 8\sin^4\frac{\bar{\gamma}}{2} + (1+\bar{V})^2\sin^2\bar{\gamma}\right\}^{\frac{1}{2}}. \tag{C.1}$$

We examine the terms within the flower parentheses of the above inequality separately for $\|x\| \leq r < 1$:

$$\begin{aligned}
2(\bar{V}^2 + 2\bar{V})^2 \;\; &= \;\; 2(2+\bar{V})^2\bar{V}^2 \\
&\leq \;\; 2(2+r)^2\bar{V}^2 \\
8\sin^4\frac{\bar{\gamma}}{2} \;\; &\leq \;\; 8\left(\frac{\bar{\gamma}}{2}\right)^2\sin^2\frac{\bar{\gamma}}{2} \\
&= \;\; 8\left(\frac{r}{2}\right)^2\sin^2\frac{\bar{\gamma}}{2} \\
&\leq \;\; 2r^2\left(\frac{\bar{\gamma}}{2}\right)^2 = \frac{r^2\bar{\gamma}^2}{2}. \\
(1+\bar{V})^2\sin^2\bar{\gamma} \;\; &\leq \;\; (1+r)^2\bar{\gamma}^2.
\end{aligned}$$

Substituting the above relations in (C.1) we have

$$\begin{aligned}
\left\|\frac{\partial Q_1}{\partial x_1}\right\| \;\; &\leq \;\; \left\{2(2+r)^2\bar{V}^2 + \left(\frac{r^2}{2} + (1+r)^2\right)\bar{\gamma}^2\right\}^{\frac{1}{2}} \\
&\leq \;\; \max\left\{2(2+r)^2, \left(\frac{r^2}{2} + (1+r)^2\right)\right\}^{\frac{1}{2}}\left(\bar{V}^2 + \bar{\gamma}^2\right)^{\frac{1}{2}}
\end{aligned}$$

For $r < 1$, we have

$$\max\left\{2(2+r)^2, \left(\frac{r^2}{2} + (1+r)^2\right)\right\} = 2(2+r)^2.$$

Thus,

$$\left\|\frac{\partial Q_1}{\partial x_1}\right\| \;\; \leq \;\; \sqrt{2}(2+r)\left(\bar{V}^2 + \bar{\gamma}^2\right)^{\frac{1}{2}},$$

i.e., Q_1 satisfies condition (7.42) of Theorem 5 for the boundary layer subsystem (7.68) with

$$\beta_1 = \sqrt{2}(2+r).$$

Bibliography

[1] D. L. Rudnick, R. E. Davis, C. C. Eriksen, D. M. Fratantoni, and M. J. Perry, "Underwater gliders for ocean research," *Marine Technology Society Journal*, vol. 38, no. 1, pp. 48–59, 2004.

[2] R. Bachmayer, N. E. Leonard, P. Bhatta, E. Fiorelli, and J. Graver, "Dynamics, control and cordination of underwater gliders," in *Advances in Unmanned Marine Vehicles, edited by G. Roberts and R.Sutton*, (London, UK), pp. 407–432, 2005. IEE Control Series 69.

[3] "Autonomous Ocean Sampling Network II (AOSN-II), collaborative project." http://www.mbari.org/aosn/.

[4] "Adaptive Sampling And Prediction (ASAP), collaborative project." http://www.princeton.edu/∼dcsl/asap.

[5] J. G. Graver, *Underwater Gliders: Dynamics, Control and Design.* 2005. Princeton University PhD Thesis, Department of Mechanical and Aerospace Engineering designation 3131T.

[6] N. E. Leonard and J. G. Graver, "Model-based feedback control of autonomous underwater gliders," *IEEE Journal of Oceanic Engineering*, vol. 26, no. 4, pp. 633–645, 2001.

[7] M. Gertler and G. Hagen. Technical Report, David Taylor Naval Ship Research and Development Center. Defense Technical Information Center Document # 653861.

[8] J. P. Feldman. Technical Report, David Taylor Naval Ship Research and Development Center. Defense Technical Information Center Document # A071804.

[9] S. A. Jenkins, D. E. Humphreys, J. Sherman, J. Osse, C. Jones, N. E. Leonard, R. Bachmayer, J. Graver, T. Clem, P. Carroll, P. Davis, J. Berry, P. Worley, and J. Wasyl, "Underwater glider system study." Technical Report, Office of Naval Research, 2003.

[10] T. J. Prestoro, *Verification of a six-degree of freedom simulation model for the REMUS AUV.* 2001. Master's Thesis, Massachusetts Institute of Technology/Woods Hole Oceanographic Institution.

[11] C. von Alt, B. Allen, T. Austin, and R. Stokey, "Remote environmental measuring units," in *Proc. Autonomous Underwater Vehicle Conference*, (Cambridge, MA), 1994.

[12] J. Kim, K. Kim, H. S. Choi, W. Seong, and K. Lee, "Estimation of hydrodynamic coefficients for an AUV using nonlinear observers," *IEEE Journal of Oceanic Engineering*, vol. 27, no. 4, pp. 830–840, 2002.

[13] H. K. Khalil, *Nonlinear Systems.* Upper Saddle River, NJ: Prentice Hall, 3rd ed., 2002.

[14] D. C. Webb, P. J. Simonetti, and C. P. Jones, "SLOCUM: An underwater glider propelled by environmental energy," *IEEE Journal of Oceanic Engineering*, vol. 26, no. 4, pp. 447–452, 2001.

[15] J. Sherman, R. E. Davis, W. B. Owens, and J. Valdes, "The autonomous underwater glider 'Spray'," *IEEE Journal of Oceanic Engineering*, vol. 26, no. 4, pp. 437–446, 2001.

[16] C. C. Eriksen, T. J. Osse, R. D. Light, T. Wen, T. W. Lehmann, P. L. Sabin, J. W. Ballard, and A. M. Chiodi, "Seaglider: A long range autonomous underwater vehicle for oceanographic research," *IEEE Journal of Oceanic Engineering*, vol. 26, no. 4, pp. 424–436, 2001.

[17] B. Allen, R. Stokey, T. Austin, N. Forrester, R. Goldsborough, M. Purcell, and C. von Alt, "REMUS: A small, low cost AUV; system description, field trials and performance results," in *Proc. IEEE/MTS OCEANS'97*, (Halifax, Nova Scotia), pp. 997–1000, 1997.

[18] M. Dunbabin, J. Roberts, K. Usher, and P. Corke, "A new robot for environmental monitoring on the Great Barrier Reef," in *Proc. Australian Conference on Robotics and Automation*, (Canberra, Australia), 2004.

[19] H. Singh, R. Armstrong, F. Gilbes, R. Eustice, C. Roman, O. Pizarro, and J. Torres, "Imaging coral i: Imaging coral habitats with the SeaBED AUV," *Subsurface Sensing Technologies and Applications*, vol. 5, no. 1, pp. 25–42, 2004.

[20] A. S. Gadre, J. J. Mach, D. J. Stilwell, and C. E. Wick, "Design of a prototype miniature underwater vehicle," in *Proc. 2003 IEEE/RSJ International Conference on Intelligent Robots and Systems*, (Las Vegas, NV), 2003.

[21] C. E. Wick and D. J. Stilwell, "USNA-1: A miniature, low-cost autonomous underwater vehicle," *Sea Technology*, vol. 43, no. 6, pp. 17–25, 2002.

[22] J. E. Marsden and T. S. Ratiu, *Introduction to Mechanics and Symmetry*. New York, NY: Springer-Verlag, 2nd ed., 1999.

[23] A. M. Bloch, D. E. Chang, N. Leonard, and J. E. Marsden, "Controlled Lagrangians and the stabilization of mechanical systems II: Potential shaping," *IEEE Transactions on Automatic Control*, vol. 46, no. 10, pp. 1556–1571, 2001.

[24] R. Ortega, M. W. Spong, F. Gómez-Estern, and G. Blankenstein, "Stabilization of underactuated mechanical systems via interconnection and damping assignment," *IEEE Transactions on Automatic Control*, vol. 47, no. 8, pp. 1218–1233, 2002.

[25] G. A. Khoury and J. D. Gillett, *Airship Technology.* Cambridge, UK: Cambridge University Press, 1999. Cambridge Aerospace Series (No. 10).

[26] B. L. Nagabhushan and N. P. Tomlinson, "Flight dynamics simulation of a heavy lift airship," *Journal of Aircraft*, vol. 18, no. 2, pp. 96–102, 1981.

[27] H. Zhang and J. P. Ostrowski, "Visual servoing with dynamics: Control of an unmanned blimp," in *Proc. International Conference on Robotics and Automation*, (Detroit, MI), pp. 618–623, 1999.

[28] A. Elfes, S. S. Bueno, J. J. G. Ramos, E. C. de Paiva, M. Bergerman, J. R. H. Carvalho, S. M. Maeta, L. G. B. Mirisola, B. G. Faria, and J. R. Azinheira, "Modelling, control and perception for an autonomous robotic airship," in *Lecture Notes in Computer Science, Volume 2238*, pp. 216–244, 2002. Published by Springer Berlin / Heidelberg.

[29] J. Kim, J. Keller, and V. Kumar, "Design and verification of controllers for airships," in *Proc. International Conference on Intelligent Robots and Systems*, (Las Vegas, NV), pp. 54–60, 2003.

[30] J. B. Mueller, M. A. Paluszek, and Y. J. Zhao, "Development of an aerodynamic model and control law design for a high altitude airship," in *Proc. AIAA Unmanned Unlimited Conference*, (Chicago, IL), 2004.

[31] J. Graver, J. Liu, C. Woolsey, and N. E. Leonard, “Design and analysis of an underwater vehicle for controlled gliding,” in *Proc. 32nd Conference on Information Sciences and Systems*.

[32] E. Fiorelli, N. E. Leonard, P. Bhatta, D. Paley, R. Bachmayer, and D. M. Fratantoni, “Multi-AUV control and adaptive sampling in Monterey Bay,” *IEEE Journal of Oceanic Engineering*, 2006.

[33] R. von Mises, *Theory of Flight*. New York, NY: Dover, 1959.

[34] F. W. Lanchester, *Aerodonetics*. London, UK: A. Constable and Co., 1908.

[35] P. Kokotović, H. K. Khalil, and J. O’Reilly, *Singular Perturbation Methods in Control: Analysis and Design*. Philadelphia, PA: SIAM, 2nd ed., 1999.

[36] C. Tomlin, J. Lygeros, L. Benvenuti, and S. Sastry, “Output tracking for a non-minimum phase dynamic CTOL aircraft model,” in *Proc. 34th IEEE Conference on Decision and Control*, (New Orleans, LA), pp. 1867–1872, 1995.

[37] M. Morrow, *A self-sustaining, boundary-layer-adapted system for terrain exploration and environmental sampling*. 2005. Master’s Thesis, Virginia Polytechnic Institute and State University.

[38] H. Stommel, “The Slocum mission.,” *Oceanography*, vol. 2, no. 1, pp. 22–25, 1989.

[39] T. Curtin, J. G. Bellingham, J. Catipovic, and D. Webb, “Autonomous ocean sampling networks.,” *Oceanography*, vol. 6, no. 3, pp. 86–94, 1993.

[40] H. Lamb, *Hydrodynamics*. New York, NY: Dover, 6th ed., 1932.

[41] I. A. Kibel, N. E. Kochen, and N. V. Roze, *Theoretical Hydromechanics*. New york, NY: Wiley, 1964.

[42] R. F. Stengel, *Flight Dynamics.* Princeton, NJ: Princeton University Press, 2004.

[43] B. L. Stevens and F. L. Lewis, *Aircraft Control and Simulation.* Hoboken, NJ: Wiley-Interscience, 2nd ed., 2002.

[44] J. Roskam, *Flight Dynamics of Rigid and Elastic Airplanes.* 1973. Roskam Aviation and Engineering Corporation, Lawrence, KS.

[45] S. Berman, "Comparison of the lift, drag and pitch moment coefficients of a slocum glider wind tunnel model with computational results by vehicle control technologies, inc." Princeton University MAE 222 Course Project Report, 2003.

[46] J. G. Graver, R. Bachmayer, N. E. Leonard, and D. M. Fratantoni, "Underwater glider model parameter identification," in *Proc. 13th Int. Symposium on Unmanned Untethered Submersible Tech.*, (Durham, NH), 2003.

[47] N. E. Leonard, "Stability of a bottom-heavy underwater vehicle," *Automatica*, vol. 33, no. 3, pp. 331–346, 1997.

[48] J. G. Graver and N. E. Leonard, "Underwater glider dynamics and control," in *Proc. 12th Int. Symposium on Unmanned Untethered Submersible Tech.*, (Durham, NH), 2001.

[49] M. J. Abzug, "Fuel slosh in skewed tanks," *Journal of Guidance, Control and Dynamics*, vol. 19, no. 5, pp. 1172–1177, 1996.

[50] P. Bhatta and N. E. Leonard, "Stabilization and coordination of underwater gliders," in *Proc. 41st IEEE Conference on Decision and Control*, (Las Vegas, NV), pp. 2081–2086, 2002.

[51] S. H. Lane and R. F. Stengel, "Flight control design using non-linear inverse dynamics," *Automatica*, vol. 24, no. 4, pp. 471–483, 1988.

[52] S. A. Snell, D. F. Enns, and W. L. Garrard Jr., “Nonlinear inversion flight control for a supermaneuverable aircraft,” *Journal of Guidance, Control and Dynamics*, vol. 15, no. 4, pp. 976–984, 1992.

[53] M. Azam and S. N. Singh, “Invertibility and trajectory control for nonlinear maneuvers of aircraft,” *Journal of Guidance, Control and Dynamics*, vol. 17, no. 1, pp. 192–200, 1994.

[54] Q. Wang and R. F. Stengel, “Robust nonlinear control of a hypersonic aircraft,” *Journal of Guidance, Control and Dynamics*, vol. 23, no. 4, pp. 577–585, 2000.

[55] Q. Wang and R. F. Stengel, “Robust nonlinear flight control of a high-performance aircraft,” *IEEE Transactions on Control Systems Technology*, vol. 13, no. 1, pp. 15–26, 2005.

[56] O. Härkegard, *Backstepping and Control Allocation with Applications to Flight Control*. 2003. Linkoping University Thesis.

[57] M. Sharma, J. A. Farrell, M. M. Polycarpou, N. D. Richards, and D. G. Wang, “Backstepping flight control using on-line function approximation,” (Austin, TX), 2003. AIAA Guidance, Navigation, and Control Conference and Exhibit, paper number - 5713.

[58] R. Akmeliawati and I. Mareels, “Nonlinear energy-based control method for aircraft dynamics,” in *Proc. 40th IEEE Conference on Decision and Control*, (Orlando, FL), pp. 658–663, 2001.

[59] G. Meyer, L. R. Hunt, and R. Su, “A different look at output tracking: control of a VTOL aircraft,” in *Proc. 33rd IEEE Conference on Decision and Control*, (Lake Buena Vista, FL), pp. 2376–2381, 1994.

[60] S. Devasia and B. Paden, "Stable inversion for nonlinear nonminimum-phase time-varying systems," vol. 43, no. 2, pp. 283–288, 1998.

[61] L. R. Hunt and G. Meyer, "Stable inversion for nonlinear systems," *Automatica*, vol. 33, no. 8, pp. 1549–1554, 1997.

[62] C. J. Tomlin and S. S. Sastry, "Bounded tracking for non-minimum phase nonlinear systems with fast zero dynamics," *International Journal of Control*, vol. 68, no. 4, pp. 819–847, 1997.

[63] J. Hauser, S. Sastry, and G. Meyer, "Nonlinear control design for slightly nonminimum phase systems: Application to V/STOL aircraft," *Automatica*, vol. 28, no. 4, pp. 665–679, 1992.

[64] L. Benvenuti, M. D. D. Benedetto, and J. W. Grizzle, "Approximate output tracking for nonlinear non-minimum phase systems with an application to flight control," *International Journal of Robust and Nonlinear Control,*, vol. 4, pp. 397–414, 1994.

[65] E. Fiorelli, N. E. Leonard, P. Bhatta, D. Paley, R. Bachmayer, and D. M. Fratantoni, "Multi-AUV control and adaptive sampling in Monterey Bay," in *Proc. IEEE Autonomous Underwater Vehicles 2004: Workshop on Multiple AUV Operations (AUV'04)*, (Sebasco, ME), pp. 134–147, 2004.

[66] B. Allen, R. Stokey, N. Forrester, R. Gouldsborough, M. Purcell, and C. von Alt, "REMUS: a small, low cost auv; system description, field trials and performance results," in *Proc. IEEE/MTS OCEANS*, (Halifax, Nova Scotia), pp. 994–1000, 1997.

[67] M. Sibenac, W. J. Kirkwood, R. McEwen, F. Shane, R. Henthorn, D. Gashler, and H. Thomas, "Modular AUV for routine deep water science operations," in *Proc. IEEE/MTS OCEANS*, (Biloxi, MS).

[68] A. R. Robinson, “Forecasting and simulating coastal ocean processes and variabilities with the harvard ocean prediction system,” in *Coastal Ocean Prediction (Editied by C.N.K. Mooers)*, (Washington, DC), pp. 77–100, 1999. AGU Coastal and Estuarine Studies Series, Volume 56.

[69] A. F. Shchepetkin and J. C. McWilliams, “The Regional Ocean Modeling System (ROMS): A split-explicit, free-surface, topography-following-coordinate oceanic model,” *Ocean Modeling*, vol. 9, no. 4, pp. 347–404, 2005.

[70] I. Shulman, C. R. Wu, J. D. Paduan, L. K. Rosenfeld, J. C. Kindle, S. R. Ramp, and C. A. Collins, “High resolution modeling and data assimilation in the Monterey Bay area,” *Continental Shelf Research*, vol. 22, no. 8, pp. 1129–1151, 2002.

[71] R. Bachmayer, N. E. Leonard, J. Graver, E. Fiorelli, P. Bhatta, and D. Paley, “Underwater gliders: Recent developments and future applications,” in *Proc. IEEE International Symposium on Underwater Technology (UT'04)*, (Taipei, Taiwan), 2004.

[72] E. Fiorelli, P. Bhatta, N. E. Leonard, and I. Shulman, “Adaptive sampling using feedback control of an autonomous underwater glider fleet,” in *Proc. 13th Int. Symposium on Unmanned Untethered Submersible Tech.*, (Durham, NH), 2003.

[73] P. Ögren, E. Fiorelli, and N. E. Leonard, “Coperative control of mobile sensor networks: Adaptive gradient climbing in a distributed environment,” *IEEE Transactions on Automatic Control*, vol. 49, no. 8, pp. 1292–1302, 2004.

[74] E. Fiorelli, *Cooperative Vehicle Control, Feature Tracking and Ocean Sampling.* 2005. Princeton University PhD Thesis, Department of Mechanical and Aerospace Engineering designation 3160T.

[75] P. Bhatta, E. Fiorelli, F. Lekien, N. E. Leonard, D. A. Paley, F. Zhang, R. Bachmayer, R. E. Davis, D. M. Fratantoni, and R. Sepulchre, "Coordination of an underwater glider fleet for adaptive sampling," in *Proc. Internaltional Workshop on Underwater Robotics*, (Genoa, Italy), pp. 61–69, 2005.

[76] N. E. Leonard and E. Fiorelli, "Virtual leaders, artificial potentials and coordinated control of groups," in *Proc. 40th IEEE Conference on Decision and Control*, (Orlando, FL), pp. 2968–2973, 2001.

[77] P. Ögren, E. Fiorelli, and N. E. Leonard, "Formations with a mission: Stable coordination of vehicle group maneuvers," in *Proc. Symposium of Mathematical Theory of Networks and Systems*, (Notre Dame, IN), 2002.

[78] N. Leonard, D. Paley, F. Lekien, R. Sepulchre, and D. M. Fratantoni, "Collective motion, sensor networks and ocean sampling," *Proceedings of the IEEE*, 2005. special issue on "The Emerging Technology of Networked Control Systems".

[79] R. Sepulchre, D. Paley, and N. E. Leonard, "Stabilization of planar collective motion, part I: All-to-all communication," *IEEE Transactions on Automatic Control*, 2006. Accepted.

[80] D. Paley, N. E. Leonard, and R. Sepulchre, "Oscillator models and collective motion: Splay state stabilization of self-propelled particles," in *Proc. 44th IEEE Conference on Decision and Control*, (Seville, Spain), 2005.

[81] L. Gandin, *Objective Analysis of Meteorological Fields*. Jerusalem: Translated from Russian by R. Hardin; Israel Program for Scientific Translations, 1963.

[82] F. P. Bretherton, R. E. Davis, and C. B. Fandry, "A technique for objective analysis and design of oceanographic experiments applied to MODE-73," *Deep Sea Research*, vol. 23, no. 7, pp. 559–582, 1976.

[83] H. Goldstein, *Classical Mechanics*. San Francisco, CA: Addison Wesley, 3rd ed., 2002.

[84] D. E. Chang and N. E. Leonard. unpublished notes, 2000.

[85] P. K. Newton, *The N-Vortex Problem*. New York, NY: Springer-Verlag, 2001.

[86] A. E. Love, *Treatise on the Mathematical Theory of Elasticity*. New York, NY: Dover, 4th ed., 1927.

[87] G. Kirchhoff, "Über das gleichgewicht und die bewegung eines unendlich dünnen elastischen stabes," *Journal für Mathematik (Crelle)*, vol. 56, pp. 285–313, 1859.

[88] D. S. Naidu and A. J. Calise, "Singular perturbations and time scales in guidance and control of aerospace systems: A survey," *Journal of Guidance, Control and Dynamics*, vol. 24, no. 6, pp. 1057–1078, 2001.

[89] H. J. Kelley and T. N. Edelbaum, "Energy climbs, energy turns and asymptotic expansions," *Journal of Aircraft*, vol. 7, no. 1, pp. 93–95, 1970.

[90] H. J. Kelley, "Boundary-layer approximation to powered-flight attitude transients," *Journal of Spacecraft and Rockets*, vol. 7, no. 7, pp. 879–879, 1970.

[91] H. J. Kelley, "Flight path optimization with multiple time scales," *Journal of Aircraft*, vol. 8, no. 4, pp. 238–240, 1971.

[92] H. J. Kelley, "Reduced order modeling in aircraft mission analysis," *AIAA Journal*, vol. 9, no. 2, pp. 349–350, 1971.

[93] H. J. Kelley, "Aircraft maneuver optimization by reduced order approximations," in *Control and Dynamical Systems, edited by C. T. Leondes*, pp. 131–178, 1973. Academic Press, New York.

[94] M. D. Ardema, "Solution to the minimum time-to-climb problem by matched asmptotic expansion," *AIAA Journal*, vol. 14, no. 7, pp. 843–850, 1976.

[95] M. D. Ardema, "Singular perturbation in flight mechanics," 1977. NASA TM X 62, 380.

[96] A. J. Calise, "Singularly perturbation methods for variational problems in aircraft flight," *IEEE Transactions on Automatic Control*, vol. 21, no. 3, pp. 345–352, 1976.

[97] A. J. Calise, "Extended energy management methods for flight performance optimization," *AIAA Journal*, vol. 15, no. 3, pp. 314–321, 1977.

[98] A. J. Calise, "A new boundary layer matching procedure for singularly perturbed systems," *IEEE Transactions on Automatic Control*, vol. 23, no. 3, pp. 434–438, 1978.

[99] A. J. Calise, "A singularly perturbation analysis of optimal aerodynamic and thrust magnitude control," *IEEE Transactions on Automatic Control*, vol. 24, no. 5, pp. 720–729, 1979.

[100] J. V. Breakwell, "Optimal flight-path-angle transitions in minimum time airplane climbs," *Journal of Aircraft*, vol. 14, no. 8, pp. 782–786, 1977.

[101] J. V. Breakwell, "More about flight-path-angle transitions in optimal airplane climbs," *Journal of Guidance and Control*, vol. 1, pp. 205–208, 1978.

[102] A. J. Calise, N. Markopoulos, and J. F. Corban, "Nondimensional forms for singular perturbation analysis of aircraft energy climbs," *Journal of Guidance Control and Dynamics*, vol. 17, no. 3, pp. 584–590, 1994.

[103] A. J. Calise, "Singular perturbation techniques for on-line optimal flight-path control," *Journal of Guidance and Control*, vol. 4, no. 4, pp. 398–405, 1981.

[104] A. J. Calise and J. F. Corban, "Optimal control of two-timescale systems with state-variable inequality constraints," *Journal of Guidance Control and Dynamics*, vol. 15, no. 2, pp. 468–476, 1992.

[105] J. Shinar and N. Farber, "Horizontal variable speed interception game solved by forced singular perturbation technique," *Journal of Optimization Theory and Applications*, vol. 42, no. 4, pp. 603–636, 1984.

[106] H. G. Visser and J. Shinar, "First-order corrections in optimal feedback control of singularly perturbed nonlinear systems," *IEEE Transactions on Automatic Control*, vol. 31, no. 5, pp. 387–393, 1986.

[107] M. A. van Buren and K. D. Mease, "Aerospace plane guidance using timescale decomposition and feedback linearization," *Journal of Guidance, Control and Dynamics*, vol. 15, no. 5, pp. 1166–1174, 1992.

[108] M. A. van Buren, *Robust Nonlinear Feedback Guidance for an Aerospace Plane: A Geometric Approach*. 1992. Princeton University PhD Thesis, Department of Mechanical and Aerospace Engineering designation 1935T.

[109] K. D. Mease and M. A. van Buren, "Geometric synthesis of aerospace plane ascent guidance logic," *Automatica*, vol. 30, no. 12, pp. 1839–1849, 1994.

[110] J. P. Kremer, *Studies in flight guidance involving nonlinear techniques and optimization*. 1996. Princeton University PhD Thesis, Department of Mechanical and Aerospace Engineering designation 2041T.

[111] J. P. Kremer and K. D. Mease, "Near-optimal control of altitude and path angle during aerospace plane ascent," *Journal of Guidance, Control and Dynamics*, vol. 20, no. 4, pp. 789–796, 1997.

[112] N. X. Vinh and Z. S. Kuo, "Improved matched asymptotic solutions for deceleration control during atmospheric entry," *Acta Astronautica*, vol. 40, no. 1, pp. 1–11, 1997.

[113] N. X. Vinh, K. D. Mease, and J. M. Hanson, "Explicit guidance of drag-modulated aeroassisted transfer between elliptical orbits," *Journal of Guidance, Control and Dynamics*, vol. 9, no. 3, pp. 274–280, 1986.

[114] S. Kamesh and S. Pradeep, "Phugoid approximation revisited," *Journal of Aircraft*, vol. 36, no. 2, pp. 465–467, 1999.

[115] W. F. Phillips, "Phugoid approximation for conventional airplanes," *Journal of Aircraft*, vol. 37, no. 1, pp. 30–36, 2000.

[116] N. Ananthkrishnan and P. Ramadevi, "Phugoid approximation revisited," *Journal of Guidance, Control and Dynamics*, vol. 25, no. 4, pp. 820–824, 2002.

[117] M. Suzuki and M. Miura, "Stabilizing feedback controllers for singularly perturbed systems," *IEEE Transactions on Automatic Control*, vol. 21, no. 1, pp. 123–124, 1976.

[118] J. H. Chow and P. V. Kokotovic, "A decomposition of near-optimum regulators for systems with slow and fast modes," *IEEE Transactions on Automatic Control*, vol. 21, no. 5, pp. 701–705, 1976.

[119] H. K. Khalil and P. V. Kokotovic, "Control of linear systems with multiparameter singular perturbations," *Automatica*, vol. 15, no. 2, pp. 197–207, 1979.

[120] P. Y. Xu, "Singular perturbation theory of horizontal dynamic stability and response of aircraft," *Aeronautical Journal*, vol. 89, no. 885, pp. 179–184, 1985.

[121] H. K. Khalil, "Output feedback control for linear two time-scale systems," *IEEE Transactions on Automatic Control*, vol. 32, no. 9, pp. 782–792, 1987.

[122] H. K. Khalil, “Feedback control of nonstandard singularly perturbed systems,” *IEEE Transactions on Automatic Control*, vol. 34, no. 10, pp. 1052–1060, 1989.

[123] F. Chen and H. K. Khalil, “Two-time-scale longitudinal control of airplanes using singular perturbation,” *Journal of Guidance Control and Dynamics*, vol. 13, no. 6, pp. 952–960, 1990.

[124] N. Markopoulos and K. D. Mease, “Thrust law effects on the longitudinal stability of hypersonic cruise,” in *Proc. AIAA Atmospheric Flight Mechanics Conference*, (Portland, OR), pp. 141–155, 1990.

[125] K. Shim and M. E. Sawan, “Approximate controller design for singularly perturbed aircraft systems,” *Aircraft Engineering and Aerospace Technology*, vol. 77, no. 4, pp. 311–316, 2005.

[126] H. K. Khalil, “Asymptotic stability of nonlinear multiparameter singularly perturbed systems,” *Automatica*, vol. 17, no. 6, pp. 797–804, 1981.

[127] A. Saberi and H. Khalil, “Quadratic-type Lyapunov functions for singularly perturbed systems,” *IEEE Transactions on Automatic Control*, vol. 29, no. 6, pp. 542–550, 1984.

[128] H. K. Khalil, “Stability analysis of nonlinear multiparameter singularly perturbed systems,” *IEEE Transactions on Automatic Control*, vol. 32, no. 3, pp. 260–263, 1987.

[129] P. Bhatta and N. E. Leonard, “A Lyapunov function for vehicles with lift and drag: Stability of gliding,” in *Proc. 43rd IEEE Conference on Decision and Control*, (Paradise Island, Bahamas), pp. 4101–4106, 2004.

[130] P. Bhatta and N. E. Leonard, “Nonlinear gliding stability and control for vehicles with aerodynamic forcing,” 2006. To be Submitted.

[131] A. Miele, T. Wang, and W. Melvin, "Guidance strategies for near-optimum takeoff performance in wind shear," *Journal of Optimization Theory and Applications*, vol. 50, no. 1, pp. 1–47, 1986.

[132] M. L. Psiaki, *Control of Flight Through Microburst Wind Shear Using Deterministic Trajectory Optimization.* 1987. Princeton University PhD Thesis, Department of Mechanical and Aerospace Engineering designation 1787T.

[133] Y. Zhao and A. E. Bryson, "Control of an aircraft in downbursts," *Journal of Guidance, Control and Dynamics*, vol. 13, no. 5, pp. 813–818, 1990.

[134] S. S. Mulgund and R. F. Stengel, "Aircraft flight control in wind shear using sequential dynamic inversion," *Journal of Guidance, Control and Dynamics*, vol. 18, no. 5, pp. 1084–1091, 1995.

[135] S. S. Mulgund and R. F. Stengel, "Optimal nonlinear estimation for aircraft flight control in wind shear," *Automatica*, vol. 32, no. 1, pp. 3–13, 1996.

[136] S. A. Al-Hiddabi and N. H. McClamroch, "Trajectory tracking control and maneuver regulation control for the CTOL aircraft model," in *Proc. 38th IEEE Conference on Decision and Control*, (Phoenix, AZ), pp. 1958–1963, 1999.

[137] S. A. Al-Hiddabi and N. H. McClamroch, "A study of longitudinal flight maneuvers for the CTOL aircraft model," in *Proc. IEEE Conference on Control Applications*, (Kohula Coast-Island of Hawaii, HI), pp. 1199–1204, 1999.

[138] P. Bhatta and N. E. Leonard, "Controlled steady gliding and approximate trajectory tracking for vehicles subject to aerodynamic forcing," in *Proc. American Control Conference*, (Minneapolis, MN), 2006.

[139] S. Sastry, *Nonlinear Systems: Analysis, Stability and Control.* New York, NY: Springer-Verlag, 1999.

[140] G. Meyer, L. R. Hunt, and R. Su, "Nonlinear system guidance," in *Proc. 34rd IEEE Conference on Decision and Control*, (New Orleans, LA), pp. 590–595, Dec. 1995.

[141] S. A. Al-Hiddabi and N. H. McClamroch, "A decomposition approach to output tracking for multivariable nonlinear nonminimum phase systems," in *Proc. American Control Conference*, (Philadelphia, PA), pp. 1128–1132, 1998.

[142] S. Devasia and B. Paden, "Exact output tracking for nonlinear time-varying systems,"

[143] P. Bhatta, N. E. Leonard, M. Schilthuis, and F. Zhang. Princeton University MAE Technical Report. In preparation.

[144] E. Kreyszig, *Introduction to Differential Geometry and Riemannian Geometry.* Toronto, ON: University of Toronto Press, 1968.

[145] J. Guckenheimer and P. Holmes, *Nonlinear Oscillations, Dynamical Systems and Bifurcations of Vector Fields.* New York, NY: Springer-Verlag, 1983.

[146] K. Ogata, *Modern Control Engineering.* Upper Saddle River, NJ: Prentice Hall, 2001.

[147] M. Sri-Jayantha and R. F. Stengel, "Determination of nonlinear aerodynamic coefficients using the estimation-before-modeling method," *Journal of Aircraft*, vol. 25, no. 9, pp. 796–804, 1988.

[148] K. W. Iliff and R. E. Maine, "NASA Dryden's experience in parameter estimation and its uses in flight test," Aug. 1982. AIAA Paper N0. 82-1373.

[149] W. M. Boothby, *An Introduction to Differentiable Manifolds and Riemannian Geometry.* San Diego, CA: Academic Press, 2nd ed., 2003.

[150] J. E. Marsden, *Lectures on Mechanics.* Cambridge, UK: Cambridge University Press, 1992.

[151] H. Nijmeijer and A. van der Schaft, *Nonlinear Dynamical Control Systems.* New York, NY: Springer, 1996.